2020

Control of charged particle dynamics and electron power absorption dynamics utilizing voltage waveform tailoring in capacitively driven radio-frequency plasmas

Steven W. Brandt
West Virginia University, sbrandt1@mix.wvu.edu

2020

Control of charged particle dynamics and electron power absorption dynamics utilizing voltage waveform tailoring in capacitively driven radio-frequency plasmas

Steven W. Brandt

Control of charged particle dynamics and electron power absorption dynamics utilizing voltage waveform tailoring in capacitively driven radio-frequency plasmas

Steven Brandt

Dissertation submitted
to the Eberly College of Arts and Sciences
at West Virginia University
in partial fulfillment of the requirements for the degree of
Doctor of Philosophy in
Physics

Julian Schulze, Ph.D., Chair
Mark Koepke, Ph.D., Co-Chair
Paul Cassak, Ph.D.
Charter Stinespring, Ph.D.

Department of Physics and Astronomy

West Virginia University
Morgantown, West Virginia
United States of America
April 28th, 2020

Keywords: Capacitively coupled plasmas, multi-frequency capacitive discharges, voltage waveform tailoring, electrical asymmetry effect, plasma series resonance, electron heating in CCRF plasmas, electronegative plasmas, secondary electron emission, plasma-surface interactions, PIC/MCC simulations, discharge modeling

Abstract

Control of charged particle dynamics and electron power absorption dynamics utilizing voltage waveform tailoring in capacitively driven radio-frequency plasmas

Steven Brandt

In this work, experimental measurements and analysis of numerical simulations are performed for capacitively coupled plasmas driven by tailored voltage waveforms under conditions which examine complicating factors present in industrial processes, including the influence of resonance effects, electronegative gases or gas mixtures, and plasma-surface interactions at a changing plasma-surface interface. Furthermore, the influence of different tailored voltage waveforms on the spatio-temporal electron power absorption, the generation of a DC self-bias, and on process relevant plasma parameters like ion energy distribution functions is investigated to provide a more complete understanding of the underlying fundamental plasma physics responsible for sustaining the discharge. It is found that these complicating factors can dramatically alter the operation of discharges under conditions that are highly relevant to many industrial processes. First, it is demonstrated that tailored voltage waveforms provide improved control over the charged particle dynamics and process-relevant plasma parameters of electropositive argon discharges. The self-excitation of the plasma series resonance and its subsequent influence on the charged particle dynamics is then analyzed using numerical simulations of geometrically symmetric but electrically asymmetric argon discharges. The influence of negative ions and electronegativity on the charged particle dynamics produced by various tailored voltage waveforms is investigated for tetrafluoromethane discharges and argon-tetrafluoromethane gas mixtures. It is found that the discharge electronegativity and the presence of the drift-ambipolar heating mode dramatically alter the operation of the discharge. Lastly, the dependence of secondary electron emission on the surface characteristics (surface roughness, film thickness) of aluminum and aluminum oxide surfaces is demonstrated to be non-negligible and hypotheses for the underlying physical mechanisms behind these dependencies are presented. Thus, several important factors frequently used in industrial processing which are usually omitted from fundamental studies of capacitively coupled plasmas are shown to significantly modify the associated spatio-temporal charged particle dynamics and should not be neglected in future research.

Acknowledgments

I would like to acknowledge the funding by WVU startup fund for Dr. Julian Schulze's research group, the US National Science Foundation under the grant PHY 1601080, the Deutsche Forschungsgemeinschaft (DFG, German Research Foundation) within the framework of the Sonderforschungsbereich (SFB TR 87), the Hungarian Nation Research, Development, and Innovation Office (NFKIH K 119357), and the donations and support by the Lam Research Corporation. Without all of this, none of my research could have been possible.

I would like to deeply thank my supervisor, Dr. Julian Schulze, for his endless guidance and support throughout my graduate career. For motivating me and helping to define the path of my research, I am extremely grateful.

I would like to also deeply thank Dr. Mark Koepke, who has been instrumental throughout my academic career in guiding me, motivating me, and keeping me sane for so many years. I would have found myself quite lost many times in my life without his help.

I want to acknowledge Dr. Zoltan Donkó and his group at the Wigner Research Centre for Physics for their extensive collaborations with our group at WVU.

I also want to acknowledge Douglas Keil and the Lam Research Corporation for their collaboration and support with our group at WVU.

I would also like to acknowledge Dr. Paul Cassak, who inspired my interest in physics in my undergraduate studies and who continues to be supportive to this day.

I wish to give special thanks to Birk Berger, Dr. Edmund Schüngel, Manaswi Daksha, Thomas Steinberger, and Sam Nogami for their help in the laboratory and countless scientific discussions that has made my work possible.

I would like to thank all of my fellow colleagues who have supported and collaborated with me over the years, including James Franek, Aranka Derzsi, Ihor Korolov, and Bastien Bruneau.

I would like to thank all of my friends and family who have spent years supporting, motivating, and inspiring me to achieve something just that much greater.

Table of Contents

List of Figures

List of Tables

List of Symbols and Constants

Symbol	Description	Symbol	Description
t	Time	f	Fundamental applied frequency
$\varphi = 2\pi f t$	Radio-frequency phase	$\omega_{\mathrm{RF}} = 2\pi f$	Applied fundamental frequency in radians/s
$T = \frac{1}{f}$	Radio-frequency period	x	Inter-electrode position
$\widetilde{\phi}(t)$	Applied voltage waveform	ϕ_{tot}	Total possible applied voltage amplitude
N	Number of consecutive applied harmonic frequencies	k	Harmonic index number
ϕ_k	Individual harmonic voltage amplitudes	θ_k	Individual harmonic phases, relative to $\theta_{k=1} = 0°$
$\widetilde{\phi}_{\mathrm{max/min}}$	Extrema of applied voltage waveform	ε_0	Vacuum permittivity (8.854×10^{-12} Fm^{-1})
p	Neutral gas pressure	e	Elementary charge (1.602×10^{-19} C)
m	Mass of an electron (9.109×10^{-31} kg)	m_{i}	Mass of a given ion
n_{e}	Number density of electrons	n_{i}	Number density of a given ion species
$n_{\mathrm{e}}(x)$	Electron density profile	$n_{\mathrm{i}}(x)$	Density profile of a given ion species
$\omega_{\mathrm{pe}} = \sqrt{\frac{e^2 n_{\mathrm{e}}}{\varepsilon_0 m}}$	Electron plasma frequency	$\omega_{\mathrm{pi}} = \sqrt{\frac{e^2 n_{\mathrm{i}}}{\varepsilon_0 m_{\mathrm{i}}}}$	Ion plasma frequency for a given ion species
ν_{m}	Electron-neutral momentum transfer collision frequency	η	DC self-bias voltage
ε	Symmetry parameter	s	Plasma sheath width

Continued on next page

Continued from previous page

Symbol	Description	Symbol	Description
$s_{\mathrm{p}}(t)$, $s_{\mathrm{g}}(t)$	Time-dependent sheath width of powered (p) or grounded (g) sheath	s_{m}	Minimum sheath width in section 2.1
λ_{D}	Debye length-scale	$\Phi(x,t)$	Time-dependent plasma potential profile
ϕ_{sp}, ϕ_{sg}	Electric potential (voltage) drop across each electrode sheath (p, g)	$\phi_{\mathrm{s,max/min}}$	Maximum/minimum potential drop across a given sheath
ϕ_{b}	Potential drop across bulk plasma	$\phi^{\mathrm{b}}_{\mathrm{max/min}}$	Potential drop across bulk plasma during times of maximum and minimum applied voltage
A_{p}, A_{g}	Effective areas of the powered and grounded electrodes	d	Electrode gap separation distance
n_{i0}	Matrix sheath ion density profile (constant)	Q_0	Charge normalization factor; Maximum charge in the powered sheath
Q_{sp}	Uncompensated space charge in powered sheath	q_{tot}	Total normalized net charge in whole plasma (assumed constant)
$q = q_{\mathrm{sp}}$	Normalized charge in the powered sheath	$q_{\mathrm{sg}} = q_{\mathrm{tot}} - q$	Normalized charge in the grounded sheath
$q_{\mathrm{sp,max/min}}$, $q_{\mathrm{sg,max/min}}$	Max./min. normalized charge in each sheath (p, g)	s_{p}, s_{g}	Maximum sheath widths for each sheath (p, g)
u	Electron velocity	u_{d}	Electron drift velocity
u_{r}	Reflected electron velocity from sheath expansion in "hard wall" model	$u_{\mathrm{es}}(t)$	Time-dependent sheath expansion velocity in "hard wall" model
E	Electric field	E_{b}	Electric field in bulk plasma
j	Electron conduction current density	$j_{\max}$	Maximum possible electron conduction current density for a given $n_{\mathrm{e,max}}$
ζ	Global electronegativity	$\phi^{\mathrm{f}}_{\mathrm{sp}}$, $\phi^{\mathrm{f}}_{\mathrm{sg}}$	Floating potentials at each electrode (p, g)
η_{vw}, η_{f}, η_{b}	DC self-bias components due to $\widetilde{\phi}(t)$, ϕ_{b}, and $\phi^{\mathrm{f}}_{\mathrm{sp,sg}}$, respectively	$\bar{n}_{\mathrm{sp,sg}}$	Mean net charged particle densities in each sheath (p, g)
$Q_{\mathrm{mp,mg}}$	Max uncompensated charge in each sheath (p, g)	$I_{\mathrm{sp,sg}}$	Sheath integrals for each sheath (p, g)

Continued on next page

Continued from previous page

Symbol	Description	Symbol	Description
γ	Secondary electron emission coefficient (SEEC)	L_{bulk}	Length of the bulk region (in x) defined by the momentary sheath edges
$\bar{A}$	Effective discharge area	A_s	Area of sheath surface
n_{s}	plasma density in a given sheath	ϕ_0	Example ϕ_{tot} in subsection 2.5.1
$s_{\max}$	Maximum sheath width in subsection 2.5.1	χ	Dimensionless geometric parameter in subsection 2.5.1
$\omega_0 = \omega_{\text{pe}}\chi$	Normalization frequency for a given n_{e} in subsection 2.5.1	$\Omega = \frac{\omega_{\text{RF}}}{\omega_0}$	Dimensionless applied frequency parameter in subsection 2.5.1
$\kappa_0 = \frac{\nu_{\text{m}}}{\omega_0}$	Dimensionless momentum transfer collision frequency parameter for single-frequency discharge discussed in subsection 2.5.1	$\tau = \omega_0 t$	Dimensionless time parameter in subsection 2.5.1
q_0	Unperturbed normalized charge in powered sheath	q_1	Perturbation to normalized charge in powered sheath due to plasma series resonance
j_0	Unperturbed current density	j_1	Perturbation to current density due to plasma series resonance
$\pm\Delta\tau$	Small interval around $\tau = 0$ in subsection 2.5.1	f_1	Function in q_1 by ansatz in subsection 2.5.1
ω_{PSR}	Resonant frequency of the plasma series resonance circuit	$\widetilde{\Omega}_{\text{PSR}} = \frac{\omega_{\text{PSR}}}{\omega_0}$	Dimensionless resonant frequency in subsection 2.5.1
$\bar{\phi}_{\text{sp}}$, $\bar{\phi}_{\text{sg}}$	Normalized (by ϕ_{tot}) sheath voltage drops across each sheath (p, g)	$\bar{\phi}_{\text{b}} = \frac{\phi_{\text{b}}}{\phi_{\text{tot}}}$	Normalized voltage drop across bulk plasma
a, b	Cubic parameters in sheath charge-voltage relation	$\kappa = \frac{\nu_{\text{m}}}{\omega_{\text{RF}}}$	Dimensionless momentum transfer collision frequency parameter for multi-frequency discharges
β	Bulk parameter associated with electron inertia in plasma series resonance model	$\omega_{\text{PSR,max/min}}$	Max./min. possible resonant frequency of plasma series resonance

Continued on next page

Continued from previous page

Symbol	Description	Symbol	Description
$\bar{\omega}_{\mathrm{pe}}(t)$	Time-dependent, spatially averaged, effective bulk electron plasma frequency	$\bar{j}$	Normalized current density determined from time derivative of q
j_{tot}	Normalized current density with ϕ_{b} included in the global circuit model	j_{sim}	Normalized current density excluding ϕ_{b} from the global circuit model; i.e., unperturbed $\bar{j}$
j_{PSR}	Normalized current density perturbation resulting from the plasma series resonance	P	Power/electron heating rate
P_{tot}	Total electron heating rate	P_{sim}	Electron heating rate without the plasma series resonance
P_{PSR}	Electron heating rate caused by plasma series resonance perturbation	P_{p}, P_{g}	Electron heating rate in the powered and grounded discharge "halves"
$P(x,t)$	Spatio-temporal electron heating rate	Θ	Heaviside function
θ_{inc}	Incident angle of incoming particle during secondary electron emission	$S(\vec{x})$	Physical surface profile as a function of position on surface ($\vec{x}$)
γ_0	Minimum SEEC at normal incidence during kinetic secondary electron emission	ϕ_{W}	Work function of a given surface
ϵ_0	Potential well depth for a given surface's density of states	E_{i}	ionization energy of a given ion
E_{x}	Excitation energy of a given ion	ϵ	Initial energy of a electron before a secondary electron emission process
ϵ_{k}	Energy of an excited electron during secondary electron emission	E_{k}	Energy of an escaped electron after secondary electron emission
ϵ_{F}	Fermi energy of a given surface	z	Distance between surface and ion during secondary electron emission
$N_{\mathrm{c}}(\epsilon)$	Initial density of states in the conduction band	$N_{\mathrm{i}}(\epsilon_{\mathrm{k}})$	Energy distribution of excited electrons in a surface

Continued on next page

Continued from previous page

Symbol	Description	Symbol	Description
$N_0(E_\mathrm{k})$	Energy distribution of escaped electrons	$P_\mathrm{e}(\epsilon_\mathrm{k})$	Probability of an excited electron escaping a surface during secondary electron emission
$P_{\mathrm{e},\Omega}(\theta, \epsilon_\mathrm{k})$	Probability of an excited electron escaping a surface at a given angle	$\epsilon^{'}$, $\epsilon^{''}$	Initial energies of surface electrons in Auger neutralization
$\epsilon^{'''}$	Initial energy of surface electron in Auger de-excitation	ϕ_N	ϕ_tot for the Sawtooth waveforms, changes with N
$n_{i,\mathrm{exc}}$	Population density of excited state i in subsection 3.2.2	n_{E0}	Population density of ground state in subsection 3.2.2
n_M	Population density of relevant metastable levels (M) in subsection 3.2.2	$n_c(t)$	Time-dependent population density of relevant cascade levels (c) in subsection 3.2.2
$\hat{E}_{0,i}(t)$	Excitation rate from ground state to excited state i in subsection 3.2.2	$\hat{E}_{M,i}(t)$	Excitation rate from a metastable level M to excited state i in subsection 3.2.2
R_{ci}	Decay rate of level c into level i in subsection 3.2.2	R_i	Effective decay rate of excited state i in subsection 3.2.2
T_i	Lifetime of excited state i in subsection 3.2.2	R_{ih}	Probability for spontaneous emission from level i to level h in subsection 3.2.2
K_q	Quenching coefficient associated with a given collision partner in subsection 3.2.2	n_q	density of collision partner in subsection 3.2.2
G_{ih}	Escape factors reflecting the probability of an emitted photon escaping the plasma in subsection 3.2.2	$\dot{n}_{ph,i}(t)$	Measured photon counts per unit time; i.e., measured emission in subsection 3.2.2
ϕ_H	Potential of RFEA housing (i.e., of G1 in RFEA)	ϕ_R	Electron repelling potential (i.e., of G2 in RFEA)
ϕ_D	Discriminating potential (i.e., of G3 in RFEA)	ϕ_C	Collector plate potential in RFEA
ϵ_i	Ion energy at a given surface	$\epsilon_\mathrm{i,max}$	Maximum ion energy in ion flux-energy distribution

Continued on next page

Continued from previous page

Symbol	Description	Symbol	Description
$F(\epsilon_{\mathrm{i}})$	Ion flux-energy distribution function	Γ_{i}	Total ion flux
I_α	Intensity of α-mode excitation rate maxima	I_γ	Intensity of γ-mode excitation rate maxima
E_0	Energy threshold of collisional processes in section 3.3	Q_{p}	Polarization spiraling cross-section in section 3.3
Q_{i}	Isotropic scattering cross-section in section 3.3	Q_{m}	Momentum transfer cross-section in section 3.3
Q_{b}	Backwards scattering cross-section in section 3.3	$P_{\mathrm{e}}^{+}(x,t)$	Positive electron heating rate determined from the simulations; excludes electron cooling
σ_L	Langevin-type cross-sections used in subsection 3.3.2	α_p	Polarizability used in σ_L
g	Relative velocity of colliding partners used in σ_L	β_∞	Dimensionless impact parameter used in σ_L

Chapter 1

Introduction to radio-frequency capacitively coupled plasmas driven by tailored voltage waveforms

Industrial manufacturing of many important modern technological products frequently requires processes involving treatment of a surface or material by exposure to a low temperature radio-frequency (RF) plasma. Low temperature plasmas are defined by a thermal non-equilibrium between hot electrons and cold heavy particles, such as ions, atoms, molecules, and reactive radicals. This allows for the treatment of sensitive surfaces as the fluxes and energies of reactive or ion particle species to the surface do not result in uncontrollable damage to the surface by energetic heavy particle bombardment or plasma-surface chemistry. This is due to the fact that the dynamics of these heavy particles occur over a significantly longer time-scale than the sustainment of the plasma by the hot electrons. The heavy particle flux-energy distributions can also be adjusted to suit a given application by carefully choosing the conditions under which the plasma is generated. Furthermore, these industrial plasmas are typically generated by the application of radio-frequency power since the application of direct current (DC) causes dielectric materials to continually accumulate charge which can disrupt this control of heavy particles. Therefore, RF coupling which ensures a particle flux balance to each surface is necessary to process dielectrics, but it also introduces additional parameters for controlling the discharge such as applied frequency or frequencies. Processing rates at a surface in such plasmas can then be controlled by careful selection of discharge conditions such as background gas pressure and composition and the applied RF power. This is, however, a vastly oversimplified view of how such processing rates are obtained from the fundamental physics that generate and sustain such discharges.

There are numerous applications of such plasma treatments, including anisotropic dielectric etching for integrated circuits [1–3], reactive sputter deposition [4], plasma enhanced chemical vapor deposition (PECVD) of nano-scale structures, solar cell materials, or bio-compatible surfaces [5–13], applications in plasma medicine [14–17], and modification

of surface properties via ion implantation. Furthermore, improvements in such applications are critical for advancements in these fields, such as the continual need to realize smaller feature dimensions in semiconductor etching in accordance with Moore's law [18]. Such technological plasmas often require customized local plasma parameters such as the ion flux, the particle energy distribution function, and the plasma chemistry at a substrate surface, potentially under highly complex discharge conditions. These plasma parameters are a product of how the discharge is operated, i.e., its exact spatio-temporal ionization profile, and therefore on the fundamental plasma physics mechanisms which enable the generation and sustainment of the discharge. The ionization profile of such discharges is furthermore determined by the acceleration of charged particles, particularly electrons, prominently via interactions with the plasma sheath electric fields present adjacent to each boundary surface (but also occasionally other electric fields in the plasma). Importantly, these electron power absorption dynamics (also known as electron heating dynamics) are thus critical to nearly all aspects of these technological plasmas. However, these dynamics are typically very complicated, including both space and time dependence, and can be highly diverse across a broad array of discharge conditions. Optimized process control in such applications therefore necessitates specific particle flux-energy distributions for electrons, ions and neutrals produced on the basis of a complete understanding of these physical mechanisms. That is, advanced methods for controlling such plasma parameters and the particle energy distribution functions of different particle species both in the plasma bulk and near boundary surfaces for a very wide range of discharge conditions are highly incentivized throughout these fields of study [19].

This level of control traditionally is not possible in many conventionally utilized types of discharges, including radio-frequency capacitively coupled plasmas (RF-CCPs) driven by single-frequency voltage waveforms or inductively coupled plasmas (ICPs) [20–26], as such discharges are limited by the strong coupling between the discharge's ionization to the resulting ion flux-energy distributions at the electrodes. The charged particle distributions can be manipulated by controlling the spatio-temporal distribution of the electric field in the sheaths adjacent to the surfaces and in the plasma bulk. Limited control is possible for conventional dual frequency discharges operated at significantly different frequencies [26–31] but only in a limited range of operating conditions. RF substrate biasing also allows ICPs to change the average ion energy at the substrate surface in a controlled way [32, 33]. Despite these improvements, however, the need for even more advanced plasma processing discharges continue to increase.

Capacitively coupled radio frequency discharges are traditionally operated by applying a time-dependent (t) voltage waveform $\widetilde{\phi}(t)$ to one or both electrodes of a parallel plate capacitor inside a vacuum chamber in order to ionize the neutral background gas and sustain a plasma created from the chosen gases present between the electrodes. Townsend breakdown [34] occurs in order to initially generate the plasma which is thereafter sustained by charged particle interactions with electric fields either in the plasma sheaths which form at the electrodes or in the bulk plasma. The power transferred to particles in the plasma is primarily dominated by the acceleration of ions in these sheath electric fields, but the generation and sustainment of the plasma is due to the power absorption by electrons in these fields as they

can respond to the changes in the applied voltage waveform and thus the changing sheath voltages. The way in which the discharge is sustained is therefore referred to as the electron power absorption mode. Furthermore, previous works in single-frequency and dual-frequency RF-CCPs [20–23, 26–31] have demonstrated that there is a very strong coupling between the electron power absorption dynamics, which dictates key plasma parameters such as the plasma density and ion fluxes, and the mean sheath voltages at the electrodes [26], which themselves are dependent on the applied $\widetilde{\phi}(t)$. This coupling limits the independent control of the mean ion energy and the ion flux, i.e., control over ion flux-energy distribution functions (ion FEDFs), which is often necessary for many plasma processing discharges [26–28, 35]. The spatio-temporal plasma dynamics which shape these plasma parameters that are critically important to RF-CCPs in plasma processing are heavily reliant on the operating conditions, i.e., the applied voltage waveform, the discharge's geometry, and the choice of gases and gas pressures used.

A highly promising way to achieve an advanced control of distribution functions is driving radio-frequency plasmas with *tailored voltage waveforms* [7, 8, 13, 32, 36–66, FJ15, 67, 68, SE15a, BS16, 69–72]. This idea was initially conceived based on the work of Wendt *et al.* [33, 73] and Baloniak *et al.* [74], who introduced unmatched customized low frequency (in the kHz range) voltage waveforms used as a substrate bias to control the shape of the ion flux-energy distribution functions in high density remote plasma sources. This idea of applying customized voltage waveforms is now applied instead to the direct operation of RF-CCP discharges in the form of voltage waveform tailoring (VWT). The VWT technique allows for customization of each sheath voltage waveform as well as the time-dependence of the electric field in each sheath and in the plasma bulk on a nano-second timescale. The ion and electron power absorption dynamics, as well as the distribution functions of different particle species, can be controlled as a result [32, 36–40, 43–53, 56–58, BS16, 69–72]. Such voltage waveforms can be generated as a superposition of multiple harmonics of a fundamental driving frequency and can be tailored by individually adjusting each harmonic's voltage amplitude and phase. The possible driving waveforms are limited only by the number of applied harmonics. Effective impedance matching of such waveforms is possible with novel RF supply and matching systems [FJ15, 67, 68]. Tailored voltage waveforms are also now being applied to the operation of micro-atmospheric pressure plasmas [75, 76]. This technology is currently an appealing alternative for many industrial applications, and therefore is the subject of study throughout this work.

The applied voltage waveform can be tailored utilizing this technique with a Fourier series of consecutive harmonics of a given fundamental frequency f [45–52, 58]:

$$\widetilde{\phi}(t) = \sum_{k=1}^{N} \phi_k \cos(2\pi f k t + \theta_k), \tag{1.1}$$

where N is the total number of harmonics, ϕ_k and θ_k are the voltage amplitudes and phases, respectively, of each harmonic (k), and t is time. Note that the RF phase $\varphi = 2\pi f t$ is occasionally used to describe a given point in time during the RF period (i.e., from $\varphi = 0$ to $\varphi = 2\pi$) since these voltage waveforms are periodic. The duration of the RF period is thus

denoted $T = 1/f$. The first harmonic's phase is defined as $\theta_1 = 0°$ in equation (1.1) such that all other harmonic phases ($\theta_{k\neq 1}$) are defined relative to the first harmonic's phase. The maximum possible voltage amplitude of the applied waveform is defined as $\phi_{\text{tot}} = \sum_{k=1}^{N} \phi_k$ for a given set of ϕ_k. Traditionally, most RF-CCPs utilize fundamental frequencies (f) in the MHz range in order to utilize the conditions $\omega_{\text{pe}}^2 \gg \omega_{\text{RF}}^2 \left(1 + \frac{\nu_{\text{m}}^2}{\omega_{\text{RF}}^2}\right)^2$ and $\omega_{\text{pi}}^2 \ll \omega_{\text{RF}}^2$ [2, p. 389], where $\omega_{\text{pe}} = \sqrt{\frac{e^2 \bar{n}_{\text{e}}}{\varepsilon_0 m}}$ is the electron plasma frequency, $\omega_{\text{pi}} = \sqrt{\frac{e^2 \bar{n}_{\text{i}}}{\varepsilon_0 m_{\text{i}}}}$ is the ion plasma frequency, and ν_{m} is the electron neutral momentum transfer collision frequency, such that only the electrons are able to respond to the applied frequencies represented here by $\omega_{\text{RF}} = 2\pi f$. Here, n_{e}, n_{i}, m_{e}, and m_{i} are the densities and masses of electrons and positive ions in the plasma, ε_0 is the vacuum permittivity, and e is the fundamental charge. The voltage amplitudes ϕ_k and the harmonic phases θ_k can then be chosen in order to specifically tailor the total voltage waveform as needed. Furthermore, the presence of a blocking capacitor in the plasma circuit allows for the generation of a DC self-bias η, which effectively acts as a DC offset to the applied voltage waveform. Only RF-CCPs which apply this voltage waveform to one electrode, i.e., the powered electrode, while the other electrode is kept grounded, are considered here.

Investigations of the effects of applying customized driving voltage waveform on the electron power absorption dynamics [45–52, 58, BS16, 72, 77–81] are then crucial to gain a fundamental understanding of how such plasmas are generated. These effects are the underlying basis for customizing electron and ion distribution functions, and therefore, process optimization based upon plasma science. One major stride towards this objective was the discovery of the electrical asymmetry effect (EAE) in a RF-CCP driven by two consecutive harmonics by Heil *et al.* [37, 82] which allowed the DC self-bias and spatial ionization asymmetry of the discharge, represented by the symmetry parameter ε, to be modified depending on the shape of the applied voltage waveform. An adjustable DC self-bias voltage is then generated as a function of the phase between the driving harmonics. The excitation waveform discussed in [37] generates an asymmetry due to the differing magnitudes of the maximum and minimum applied voltages, which was later referred to as the amplitude asymmetry effect (AAE). The performance of the EAE was verified by simulations [38, 40, 42–44, 60] and experiments [39–44, 59, 62] and was seen to be enhanced by the usage of more than two harmonics [32, 45–53, 56–58, FJ15, SE15a]. Another method of generating a discharge asymmetry by driving the plasma with a waveform that has same magnitude of the voltage maximum and minimum, but different "rising" and "falling" slopes, such as "sawtooth"-type waveforms, has been proposed by Bruneau *et al.* and named as the slope asymmetry effect (SAE) [63–66].

There are many extensive studies utilizing voltage waveform tailoring and the EAE exploring a variety of discharge conditions and applications [36, 45–52, 58–60, 63–66, BS16, 69–72, 75–81, 83–92], but frequently fundamental investigations of the plasma physics are limited in scope (e.g., to single gases or admixtures) and frequently omit or assume a variety of industry-relevant factors. Such factors include, but are certainly not limited to, complicated mixtures of reactive and electronegative gases, resonance effects present under certain conditions, and changing plasma-facing surface and thus potentially changing plasma-

surface interactions. For example, many applications use complex gas mixtures that contain different admixtures of reactive and/or electronegative gases. Most previous investigations of VWT in RF-CCPs are restricted to a single gas that is either electropositive or -negative. The choice of the gas was found to drastically affect the spatio-temporal dynamics of energetic electrons and the control of process relevant flux-energy distribution functions [36, 60, 66, BS16, 93]. Fischer et al. [72] have, e.g., recently demonstrated that admixing electronegative SF_6 to a RF-CCP driven by tailored voltage waveforms and operated in O_2 drastically affects the DC self bias. This observation is explained by an electron heating mode transition induced by adding more electronegative gas to the plasmas. The spatio-temporal electron dynamics are, however, not studied explicitly in that work. Therefore, the application of such fundamental studies to industrial discharges is complicated in practice by these factors which may significantly influence a variety of process-relevant plasma parameters but are currently inadequately understood. Ultimately, this means that achieving peak optimization of processing rates and accounting for all possible effects could require exhaustive consideration of the underlying plasma physics. Building this fully complete understanding of RF-CCPs for an arbitrary set of discharge conditions (i.e., choice of gas or gas mixture, neutral gas pressure, chosen applied voltage waveform, electron power absorption mode, discharge geometry, and conditions at plasma-facing surfaces) is therefore a crucial step towards improvements in industrial applications and is highly incentivized by the desire for finely tuned plasma parameters in industrial applications [7–11]. It should be noted, however, that perfectly accurate models or numerical simulations, which could be difficult to implement due to their complexity (e.g., the time limitations associated with the execution of all these factors in a particle-in-cell simulation), are not necessarily the primary objective of such research. Rather, the effects of such industry-relevant factors should be known under a variety of conditions, such that when these effects become significant, they are not neglected. Additional research focused on such factors is thus highly relevant across the science of low temperature plasmas.

In this thesis, experimental and numerical studies are used to investigate the fundamental charged particle dynamics of RF-CCPs utilizing tailored voltage waveforms for the purpose of examining the effects of industry-relevant conditions and the subsequent fundamental plasma physics on discharge operation and the optimization of process-relevant plasma parameters. Therefore, the work in this thesis covers a significant range of important topics relevant to RF-CCPs. These topics include: the effects of VWT on the electron heating and plasma parameters of electropositive argon discharges [FJ15, BB15]; the self-excitation of the plasma series resonance in symmetric and asymmetric argon RF-CCPs and its subsequent influence on the electron heating dynamics [SE15a, SE15b]; the influence of electronegative gases and gas mixtures on the charged particle dynamics, the EAE, discharge asymmetry, and the generation of the DC self-bias [BS16, BS19]; and the effects of changing plasma-facing surfaces on secondary electron emission and the subsequent interaction such dependence has with the operation of the discharge. These complicated topics therefore also require extensive discussion of the underlying fundamental plasma physics responsible for generation and sustainment of the discharge and thus the subsequent observed plasma parameters.

This thesis is structured into chapters which either establish knowledge of known theoretical concepts and models, of the experimental setup and diagnostics, and of utilized numerical

simulations, or specifically investigate one of the key topics described above. Each chapter is further structured into sections and subsections to focus on particular aspects of discharge operation or topics of interest. The list of figures, list of tables, and list of mathematical symbols included in the work can be found after the table of contents. Furthermore, the contents of the individual chapters are summarized below.

The fundamental physical concepts, theories, and all relevant models pertaining to the operation of RF-CCPs and the associated charged particle dynamics are detailed in chapter 2. First, the general operation of a capacitively coupled plasma via application of a given voltage waveform to one electrode, while the other is kept grounded, is discussed in section 2.2 in the context of a global circuit model which analogizes the discharge to a complicated electrical circuit. The subsequent effects from applying a customized voltage waveform, i.e., of the electrical asymmetry effect on the discharge asymmetry and the generation of a DC self-bias, is explained in section 2.3. The effects of tailored voltage waveforms on the sustainment of the discharge via specific electron power absorption mechanisms and their associated ionization, as well as the subsequent influence of such charged particle dynamics on the discharge asymmetry and the EAE, is explored in section 2.4. The global circuit model of section 2.2 is further expanded upon in section 2.5 in order to accurately model the plasma series resonance (PSR); this expanded model is further utilized in chapter 5 in the analysis of the self-excitation of the PSR. Lastly, the quantum-mechanical basis for secondary electron emission due to low energy ion impact at a given surface is summarized in section 2.6 in order to provide context for the hypotheses stipulated in chapter 7 on the dependence of the SEE process on various surface characteristics.

The specific details of the experimental setup at West Virginia University (WVU), any relevant diagnostics, and the numerical simulations performed by the group of Zoltan Donkó at the Wigner Research Centre for Physics which are analyzed in this work are thoroughly explained in the appropriate sections of chapter 3. The experimental discharge and its associated matching network are detailed in section 3.1, with the specific kinds of applied voltage waveforms used throughout the other chapters outlined in subsection 3.1.1. The relevant experimental diagnostics utilized in the other chapters are detailed in section 3.2, including: a high voltage probe for voltage and DC self-bias measurements (subsection 3.2.1); an intensified charge-coupled device (ICCD) camera, digital delay generator, and optical filters for performing phase-resolved optical emission spectroscopy measurements (PROES, subsection 3.2.2); a retarding-field energy analyzer (RFEA) for measuring ion flux-energy distributions at each electrode surface (subsection 3.2.3); and the implementation of the experimental methodology of the γ-CAST diagnostic [94] using PROES measurements used to qualitatively investigate changes in secondary electron emission (subsection 3.2.4). Furthermore, the specific details of the numerical simulations analyzed in chapters 5 and 6 are outlined in section 3.3. Kinetic simulations involving only electropositive argon discharges are analyzed in chapter 5 to investigate the self-excitation of the PSR and are discussed in subsection 3.3.1. Details of the kinetic simulations of electronegative tetrafluoromethane (CF_4) discharges and discharges using a variety of gas mixtures of argon and CF_4 are similarly discussed in subsection 3.3.2. The exact experimental or analytical methodologies of chapters 4-7, including a detailed list of discharge and simulation conditions, is detailed in section 3.4.

The influence of various tailored voltage waveforms (TVWs), particularly those using three consecutive harmonics of a fundamental frequency of 13.56 MHz, on the experimental discharge's charged particle dynamics and plasma-processing relevant parameters is investigated for electropositive argon discharges at low and high neutral gas pressures. Specifically, the control ranges of the measured DC self-bias and ion FEDFs at the powered electrode produced by the application of the EAE are shown in section 4.1 to be significantly enhanced at low pressures (3 Pa and 5 Pa) compared to dual-frequency waveforms by applying multi-frequency waveforms, i.e., those using more than two applied harmonics, while retaining reasonably separate control over the total ion flux to the powered electrode. Subsection 4.1.1 considers measurements of the spatio-temporal excitation dynamics, the DC self-bias, and ion FEDFs at both electrodes for argon discharges operated by TVWs at 3 Pa, and thus describes the spatio-temporal charged particle dynamics of such discharges. Additional DC self-bias and ion FEDF measurements are similarly discussed in subsection 4.1.2 for argon discharges at 5 Pa. In each subsection, the control of these parameters via the relative harmonic phases at a fixed total applied voltage amplitude is also demonstrated. The ionization rate in the alpha-heating (α-) mode is shown to be enhanced by the changing sheath dynamics produced by such multi-frequency waveforms at specific harmonic phases, leading to a change in the shape of the ion FEDF and a subsequent increase in the total ion flux. Furthermore, it is found that the ionization rate in the α-heating mode can be enhanced for triple-frequency discharges compared to that of dual-frequency discharges by specifically tailoring the applied voltage waveform and subsequently the dynamics of each electrode sheath. This subsequently provides more detailed control over the shape of the ion FEDFs at each electrode and thus processing rates in applications. These results are further expanded upon by the additional investigations at 3 Pa of the complex electron power absorption dynamics for argon discharges operated by various dual- and triple-frequency tailored voltage waveforms. These dynamics are explained and correlated to important plasma parameters in subsection 4.1.1 using PROES measurements of the electron-impact excitation rate in addition to further DC self-bias and ion FEDF measurements. The excitation dynamics in the high pressure discharge are also investigated in section 4.2 where multiple transitions between the α- and gamma- (γ-) electron power absorption modes are observed as a function of both the relative harmonic phases and the number of applied harmonics. These transitions are explained as a result of the specific sheath dynamics associated with a given applied voltage waveform and are therefore demonstrated to be due to the specific shape of the applied voltage waveform in each case. The work of sections 4.1 and 4.2 is also published in Berger *et al.*, J. Appl. Phys. 118, 223302 (2015) [BB15] and is reproduced here with the permission of AIP Publishing. The work in subsection 4.1.2 is published separately in Franek *et al.*, Rev. Sci. Instrum. 86, 053504 (2015) [FJ15], again reproduced here with the permission of AIP Publishing.

The results of numerical simulations of low pressure (3 Pa) electropositive argon discharges are analyzed in comparison with the expanded global circuit model of section 2.5 in order to closely examine the self-excitation of the plasma series resonance (PSR) in RF-CCPs in chapter 5. The necessary requirements in the model for the self-excitation of the PSR in geometrically symmetric discharges driven by single- and multi-frequency waveforms are demonstrated in section 5.1 to be the inclusion of both a cubic contribution to the sheath

charge-voltage relations and a temporally varying bulk inductance and are supported by the corresponding simulations. Additionally, the simulations demonstrate that the bulk inductance significantly varies during the RF period, especially in discharges driven by multi-frequency waveforms, and thus should not be neglected when modeling the self-excitation of the PSR. The consequences of the self-excitation of the PSR on the electron power absorption dynamics in geometrically symmetric but potentially electrically asymmetric discharges driven by a variety of voltage waveforms are further expanded upon by analysis of the charged particle dynamics in additional numerical simulations in section 5.2. In subsection 5.2.1, the self-excitation and strength of the PSR perturbations are examined as a function of both the number of applied harmonics and the relative harmonic phases. Importantly, it is observed that the PSR can be weakly self-excited in perfectly symmetric ($\varepsilon = 1$) discharges driven by multi-frequency waveforms with four applied harmonics and that the amplitude of PSR oscillations is enhanced for asymmetric ($\varepsilon \neq 1$) discharges. These results are then correlated to changes in the spatio-temporal electron heating through the sheath dynamics and the mechanisms behind the α- and γ-mode heating in subsection 5.2.2 as a function of the number of applied harmonics. Notably, the overall discharge heating, in addition to the electrical asymmetry of the discharge, is found to be enhanced for specific multi-frequency waveforms because of the contribution of the high frequency PSR perturbations to the electron heating. The non-local ionization due to the low pressure, however, allows the ion flux to each electrode to be predominantly unaffected as a function of the second and fourth harmonic phases in spite of this highly asymmetric heating. The work presented in this chapter is co-authored alongside Edmund Schüngel. Section 5.1 is published in Schüngel *et al.*, Physics of Plasmas 22, 043512 (2015) [SE15a] and is reproduced here with the permission of AIP Publishing. The work in section 5.2 is published in Schüngel *et al.*, Plasma Sources Sci. Technol. 24, 044009 (2015) [SE15b].

The influence of electronegative gases and gas mixtures on the charged particle dynamics, the EAE, and the plasma parameters of multi-frequency RF-CCPs is investigated using a comparison of experimental measurements and numerical simulation results of CF_4 and Ar-CF_4 discharges driven by tailored voltage waveforms in chapter 6 as a function of the applied voltage waveform across a range of neutral gas pressures (10-100 Pa). The increased electronegativity at higher pressures (approximately > 50 Pa) and the subsequent presence of the drift-ambipolar (DA-) heating mode is found to significantly alter the discharge's spatio-temporal electron power absorption dynamics compared to the low pressure discharge and thus similarly alters the discharge's asymmetry and the EAE in section 6.1. The effects of gas pressure and harmonics' phases for voltage waveforms utilizing the amplitude asymmetry effect are investigated in subsection 6.1.1. Mode transitions between the α- and DA-modes are observed as a function of pressure and harmonics' phases. For specific harmonic phases, the discharge becomes uniquely split into an electropositive half and an electronegative half due to highly localized DA-mode heating producing a high negative ion density close to one electrode. This unique structure is caused by a relatively long time of sheath collapse at this electrode and the formation of a potential well for accelerated electrons. The changes in the charged particle dynamics due to the presence of negative ions is also correlated to the DA-mode heating mechanism and the particular shapes of the driving voltage waveforms. It is also demonstrated in subsection 6.1.2 that a transition from the α-mode to the DA-

mode with increasing pressure causes the discharge asymmetry and thus the sign of the DC self-bias to reverse for temporally asymmetric voltage waveforms, such as sawtooth waveforms, which utilize the slope asymmetry effect. In section 6.2, the spatio-temporal plasma dynamics from the experimental discharge and from numerical simulations at the same conditions are thoroughly examined for specific triple-frequency waveforms as a function of both pressure and the chosen Ar-CF_4 gas mixture to further clarify the influence of discharge electronegativity on the charged particle dynamics and the EAE. A fundamental understanding of the underlying plasma physics is obtained in subsection 6.2.1 using analysis of the simulated spatio-temporal excitation rate, electron attachment rate, bulk electric field, mean electron energy, and time-averaged densities of charged particle species in comparison to the experimentally measured spatio-temporal excitation rate distribution from PROES. The consequences of subsection 6.2.1 are then correlated to the observed changes in discharge asymmetry and in the generation of the DC self-bias through the EAE in subsection 6.2.2 based on the results of the experiments, simulations, and calculations utilizing the global circuit model. The work presented in section 6.1 is published in Brandt *et al.*, Plasma Sources Sci. Technol. 25, 045015 (2016) [BS16]. Similarly, the work of section 6.2 is published in Brandt *et al.*, Plasma Sources Sci. Technol. 28, 095021 (2019) [BS19].

The effects of a changing plasma-facing surface on secondary electron emission (SEE) in a high pressure (100-200 Pa) electropositive argon RF-CCP driven by a single-frequency waveform is experimentally investigated in chapter 7 for several aluminum and aluminum oxide (Al_2O_3) film surfaces of varying surface roughness via implementation of experimental PROES measurements to the experimental methodology of the γ-CAST diagnostic [94]. Through comparisons of the intensity of the α- and γ-mode excitation maxima for each surface as a function of increasing neutral gas pressure, qualitative hypotheses on the dependence of the secondary electron emission coefficient (SEEC) on the surface characteristics are drawn and correlated to the observed electron-impact excitation. Comparisons of measurements for clean aluminum surfaces and aluminum oxide film surfaces demonstrate that the effective SEEC (i.e., that suggested by the relative magnitude of the γ-mode excitation intensity) for the low incident ion energies under these conditions is comparably higher for clean aluminum surfaces in section 7.1. This is hypothesized to be due to changes in the electronic structure of the surface resulting from the formation of a semiconductor film layer over the conducting metal surface, and therefore corresponds to a dependence of the SEEC on not just the surface material, but also on the thickness of the given film on the surface. This is supported by an additional measurement for a surface with a significantly thicker Al_2O_3 film under otherwise similar surface conditions and identical discharge conditions. Comparisons of surfaces with varying surface roughness in section 7.2 demonstrate that the effective SEEC appears to increase at low surface roughness values (8-75 Ra) and eventually plateaus at higher surface roughness values (75-150 Ra). This dependence is hypothesized to be a quantum-mechanical SEE equivalent to the incident angle dependence observed for kinetic SEE processes, which is produced by the slopes of the surface profile (denoted $S(\vec{x})$) changing as a function of increasing surface roughness relative to the direction of the assumed anisotropic ion flux. The hypotheses of this chapter are, however, unconfirmed due to the lack of surface diagnostics

and therefore require further research.

The main conclusions drawn in chapters 4-7 are then summarized in chapter 8. Additionally, the impact of this work on future research and the implementation of these results into industrial applications is considered in the outlook presented in chapter 9. Lastly, any additional appendices, as well as the references used across all chapters, are included after chapter 9.

Chapter 2

Fundamental theory and modeling of radio-frequency capacitively coupled plasmas

The control of processing relevant plasma parameters and of the electron power absorption dynamics in capacitively coupled RF discharges is thoroughly explored in the following chapters for a number of important, industry-relevant situations, including considerations of the charged particle dynamics in electropositive (argon) plasmas, the effects of the plasma series resonance (PSR) in electropositive (argon) discharges, the charged particle dynamics in electronegative (CF_4) discharges, and the influence of the secondary electron emission plasma-surface interaction on RF-CCPs as a function of various surface parameters. A complete fundamental understanding of the effects of VWT on the plasma for arbitrary discharge conditions (choice of gas or gas mixture, neutral gas pressure, discharge geometry, chosen applied voltage waveform, electron power absorption mode, conditions at plasma-facing surfaces) has not yet been achieved, but is highly incentivized by the desire for finely tuned plasma parameters and the presence of complicated discharge and surface conditions. Furthermore, the influence of effects caused by complicated phenomena, such as the plasma series resonance or the secondary electron emission plasma-surface interaction, must similarly be understood in a fully complete way.

Therefore, in this chapter, the fundamental physical concepts utilized in the discussions of subsequent chapters and any relevant models are presented in detail. First, the generation of RF plasma boundary sheaths and the presence of a DC self-bias, which are both key to the operation of RF-CCPs, are briefly summarized in section 2.1. A global circuit model of a RF-CCP is presented in section 2.2, including the relationship between the applied voltage waveform and the individual voltage drops in the plasma sheaths and plasma bulk, as well as how these voltages are determined. The generation of a DC self-bias and the influence of a given plasma's spatial asymmetry on operation is discussed in section 2.3. The electron power absorption mechanisms which sustain the discharge by accelerating electrons which

cause subsequent ionization and excitation are explained in section 2.4. The expanded circuit model utilized to describe the plasma series resonance is detailed in section 2.5. Lastly, the secondary electron emission processes relevant to the discussions of chapter 7 are explained in section 2.6.

2.1 Radio-frequency plasma sheaths and particle flux balance in capacitively coupled plasmas

The operation of radio-frequency capacitively coupled plasmas is based on the application of oscillating potentials to generate and sustain a plasma. Typically, a RF voltage waveform is applied at one or more boundary surfaces in such discharges in order to couple energy from the voltage waveform to the charged particles in the plasma using electric fields. However, this capacitive coupling is complicated by the generation of plasma boundary sheaths which shield out such electric fields in most of the plasma. Thus, the interaction between the plasma and these boundary sheaths is critical to the operation of these plasmas. In this section, the idea of a plasma boundary sheath is briefly summarized in the context of the RF-CCPs discussed in this thesis.

Plasma boundary sheaths constitute regions in a plasma near plasma-facing boundary surfaces in which an electric field is shielded out over some length-scale, denoted as the sheath width s (which is typically much larger than the Debye length-scale λ_D [2, p. 38-39]), due to the separation of positively and negatively charged particle species via acceleration by the external field. Notably, the sheath width typically only reaches the scale of a few Debye lengths in the case where no external voltage is applied (i.e., for a "floating" potential; see later in this section). In the capacitively coupled plasmas discussed here, one plasma-adjacent electrode is driven by an applied voltage waveform. Therefore, this powered electrode has a time-dependent electric potential dictated by the applied waveform (i.e., $\widetilde{\phi}(t)$). The ions and electrons which make up the plasma react to the presence of this electric potential and the electric field it normally produces across the capacitor (i.e., the discharge electrodes) in the absence of the plasma.

For example, if the potential applied to the electrode is constant and negative, negatively charged particles such as electrons (or negative ions for electronegative gases) are repelled away from the electrode while positively charged particles such as positive ions are attracted to the electrode. Furthermore, the more mobile electrons in these low temperature plasmas react faster to the electrode potential due to their much lower mass and are repelled away from it. This leaves behind an uncompensated space charge density profile from the less mobile positive ions which shields the potential applied to the electrode. This creates a region where the normal charge quasi-neutrality of the plasma is violated, i.e., $-en_\mathrm{e} \neq en_\mathrm{i}$ for a singly-ionized atomic gas where n_e and n_i are the local electron and ion densities, respectively. According to Poisson's equation [2, p. 39], the externally applied potential is then shielded out by this uncompensated ion density profile over the sheath width. Notably, the assumed

shape of the ion density profile is then extremely important when discussing the total electric field in the sheath regions, as discussed in section 2.2. The plasma boundary sheath therefore acts as a mechanism to confine the plasma's electron density and sustain the discharge by avoiding a permanent loss of electrons to this electrode that exceeds the ion losses. The presence of such plasma sheaths also means that, generally, the "bulk" plasma (i.e., the quasi-neutral plasma outside these sheath regions) is shielded from the externally applied potentials, and it is therefore often the interaction of these sheaths with the plasma at the boundaries of this bulk region which is responsible for the sustainment of the plasma (see section 2.4).

Notably, a plasma sheath can be generated at any boundary, even ones that are not externally biased by an applied potential or electrically grounded, due to the flux of charged particles in the plasma to this surface through diffusion. If the positive and negative particle fluxes to this surface are not equal an unbiased surface will charge up either positively or negatively and subsequently generate an electric potential which is then shielded by the plasma. The plasma electrons can diffuse from the bulk plasma region to the surface faster than the ions in low-temperature plasmas, and thus typically the boundary charges up negatively, similar to the externally applied negative potential above. This potential attempts to ensure a flux-particle balance to the boundary surface on time average to prevent the continual build-up of excess charge. The potential which builds up on such a boundary surface due to this unequal flux is known as a floating potential, and it is this floating potential that attempts to ensure the flux-particle balance for these surfaces [2, p. 172, 393].

For an electrode surface which is grounded, the externally applied potential can be considered to be kept at effectively zero. In contrast to the floating potential case, this means that the electrode surface must remain at zero potential, such that any unbalanced charges at the surface will be sent to ground. However, a sheath can still form near this electrode if the potential profile of the plasma is not zero [2, p. 387-404]. For example, if the opposing electrode has an externally applied positive potential then bulk electrons are pulled towards this electrode and positive ions are repelled. However, since these ions are cold and move much slower than the electrons, a space charge density can only be generated on the time-scales of the ion motion. Therefore, since no electric field is present near this surface, the bulk plasma itself must also be at the same potential, since no voltage drop is achieved near this electrode or in the bulk plasma. However, near the grounded boundary surface, this potential must drop to zero. The difference in potential between the plasma potential and the grounded surface therefore causes, necessarily, an electric field and therefore a sheath region to develop. Again, this electric field causes electrons to be repelled back into the bulk plasma and positive ions to be accelerated to this grounded electrode.

It should be noted that the total electric field produced by this interaction between the externally applied (or floating) potential and the charged particles in the sheath regions will typically continuously accelerate positive particles towards the electrode surface and accelerate negatively charged particles away from the electrode surface. Therefore, it is the sheath electric field which is responsible for the acceleration of ions in many applications of such discharges. Additionally, secondary electrons emitted at this electrode surface will

be accelerated towards the bulk plasma, as discussed in section 2.4. Assuming the applied potential remains the same, this leads to a constant flux of accelerated positive ions to the electrode surface sustained by diffusion of ions in the bulk plasma towards the sheath region. It should be noted that these ions undergo some acceleration up to the Bohm velocity by passing through a pre-sheath region [2, p. 168-172]. Furthermore, the motion of charged particles and thus the generation of the plasma sheath itself also changes dramatically if the number of particle collisions occurring in this sheath region is not negligible [2, p. 173, 400–404, 411–414]. For example, positive ions accelerated in highly collisional sheaths frequently lose energy to collisions with other particles as they are accelerated through the sheath. This affects the transport of such particles and the resulting ion density profile that determines the shielding of the external potential and thus the definition of the sheath region. Similarly, secondary electrons traversing a collisional sheath region can lose energy by ionizing the background gas (see the γ-mode in section 2.4). The exact nature of each electrode sheath and the potential drop across each sheath is discussed in more detail in section 2.2. However, this over-simplified summary demonstrates that one major objective in controlling ion flux-energy distributions is controlling the potential drop across each sheath.

In capacitive discharges where the applied potential(s) and boundary surfaces are not time-dependent, i.e., DC plasmas, these plasma sheaths typically remain stable once an equilibrium is achieved. However, the application of a time-dependent potential, such as a radio-frequency sinusoidal potential, also causes the sheaths subsequently generated by this potential to also be time-dependent. Therefore, the time-dependent potential produced at a RF-biased electrode is again shielded by the acceleration of charged particles in the resulting electric field. The applied frequency of such a potential is, however, very important due to the high mobility of electrons and the low mobility of other heavier particles. For radio-frequency voltage waveforms in the discharges discussed in this work, sufficiently high frequencies are applied such that only the plasma electrons are able to react to the changes in the applied potential, while the ions can only react to the time-averaged potential. In most low pressure RF-CCPs, the contributions of collisions are negligible and the sheath can be modeled as a time-dependent, collisionless Child-law sheath [2, p. 400-403]. The specific model used for the sheaths in this work is discussed later in section 2.2. Schematic ion and electron density profiles of such a sheath are shown in figure 2.1. Notably, the electron density moves in time over the RF period, with the position of the edge of the sheath region $s(t)$ usually being defined by the location where the electron density profile drops off. The maximum sheath width (seen as zero in figure 2.1) for each sheath is obtained at a time corresponding to the maximum absolute value of the potential drop across the given sheath. Similarly, a minimum sheath width (seen as s_m in figure 2.1) is obtained at times where the voltage drop across the sheath is minimal. Notably, since floating potentials may exist even when the external potential goes to zero, this minimum sheath width is not necessarily zero. Furthermore, the n_e in figure 2.1 corresponds to a specific time in the RF period, while the RF period-averaged profile can be seen as $\bar{n}_\mathrm{e}$. The ion density profile, conversely, is typically not time-dependent.

Figure 2.2 shows the spatial variation of the total plasma potential profile between the electrodes, i.e., $\Phi(x)$ where x is inter-electrode distance, for the application of a sinusoidal voltage waveform. Consider then the application of such a sinusoidal potential at the powered

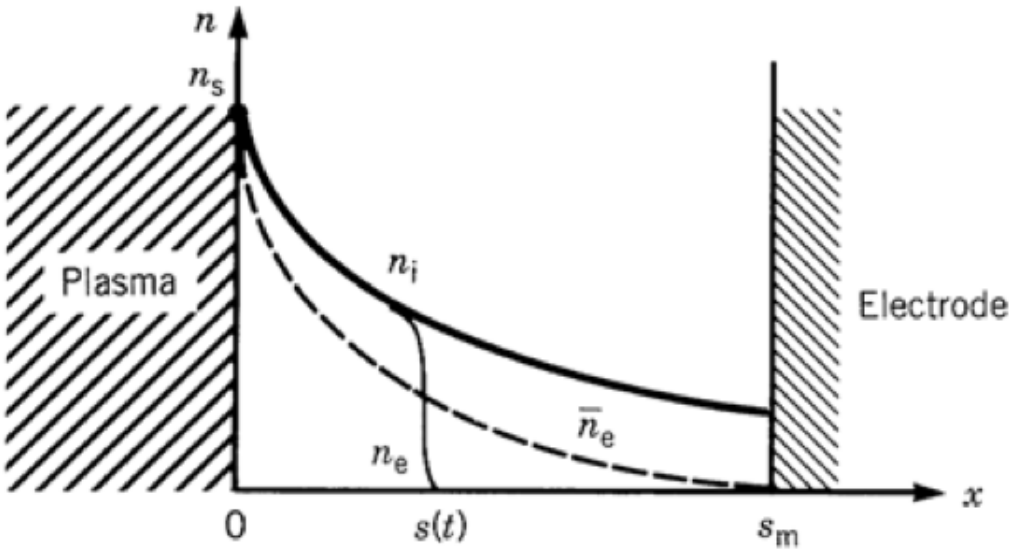

Figure 2.1: Schematic plot of the positive ion n_i and electron n_e density profiles in a high-voltage, capacitive radio-frequency sheath representative of the Child model. Here, $\bar{n}_e$ refers to the RF period averaged profile. Figure reproduced from "Principles of Plasma Discharges and Materials Processing", Lieberman and Lichtenberg, 2005 [2, p. 401] with the permission of Wiley Publishing.

electrode which begins at its minimum (i.e., most negative) value (i.e., the bottom potential plot of figure 2.2) while the second electrode is kept grounded. At first, the plasma sheath near the powered electrode would resemble that discussed above for an applied negative potential, but as the absolute value of this potential is decreased, less and less space charge density is required to shield out the applied potential. This allows bulk electrons to diffuse closer and closer to the electrode surface. This process where the sheath electric field, and thus the space charge region near the electrode, disappears is referred to as sheath collapse. Notably, the plasma potential profile changes as the collapse of this sheath occurs and this causes the generation of a sheath near the grounded electrode, as seen in the plot second from the bottom in figure 2.2. The increase in the bulk plasma's potential leads to a further increase in the strength of the electric field in the grounded electrode sheath. The grounded sheath region therefore has to extend further and further into the bulk plasma to be shielded by uncompensated space charge, and thus this sheath's electric field accelerates bulk electrons in these regions into the bulk plasma. This process where the sheath electric field increases and expands into the bulk plasma is referred to as sheath expansion. At zero applied potential, the plasma potential in the bulk plasma is similarly non-zero and therefore both sheath electric fields are still present. The collapse of the sheath at the powered electrode and the expansion of the sheath at the grounded electrode continues as the applied potential becomes positive. At the maximum (i.e., most positive) applied potential (second from the top in figure 2.2, the electron density profile has diffused to match the ion density profile near the powered electrode, i.e., this sheath has fully collapsed, while the sheath near the grounded electrode has fully expanded. The sheaths then act in reverse as the applied potential is decreased

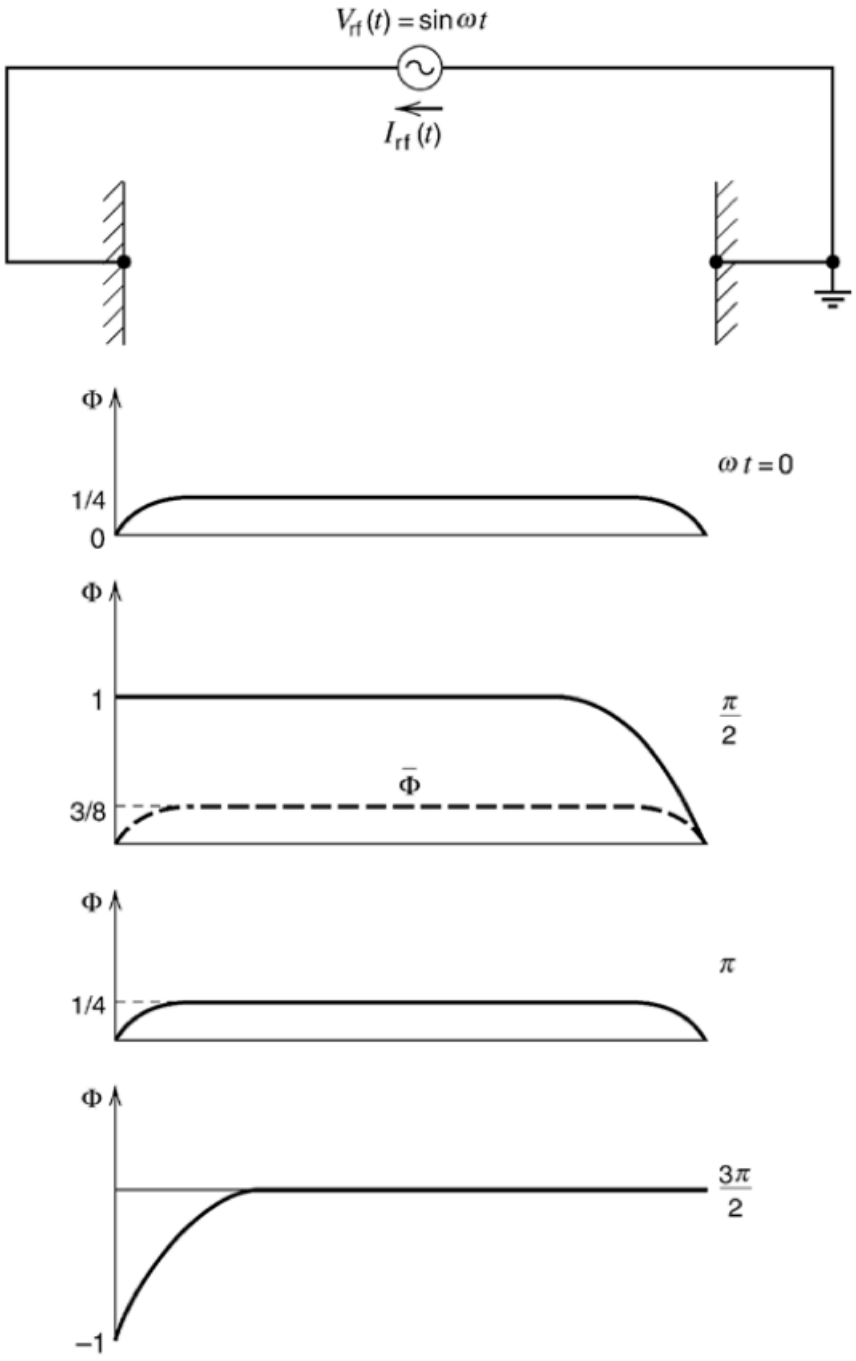

Figure 2.2: Schematic of the spatial variation of the total plasma potential $\Phi(x,t)$ (solid curves) at four different times in the RF cycle for a sinusoidal (single-frequency) voltage waveform. The dashed curves refer to the spatial variation for the RF period average potential $\bar{\Phi}(x)$. Here, the leftmost position is the powered electrode surface while the rightmost position is the grounded electrode surface. Figure reproduced from "Principles of Plasma Discharges and Materials Processing", Lieberman and Lichtenberg, 2005 [2, p. 395] with the permission of Wiley Publishing.

until the minimum applied potential is reached. Figure 2.2 can therefore be interpreted as a schematic of the temporal progression in the total plasma potential profile starting when the applied potential is zero and increasing positively. Therefore, over the course of a given sinusoidal oscillation in the applied potential, the boundary sheath near each electrode will expand into the plasma and collapse fully once.

It should be noted that in such capacitive discharges with a powered electrode and a grounded electrode that the sheath expansion of one sheath is usually accompanied by the collapse of the sheath at the opposing electrode. Therefore, the time-dependence of each sheath is approximately 180° out of phase with one another. The flux-particle balance discussed before is now only fulfilled over the course of one entire oscillation period, since the electrons generally cannot cross the sheath region unless the sheath is mostly or completely collapsed. Thus, during sheath collapse, enough electrons need to reach the associated electrode to compensate the positive ion flux to that surface accumulated while the sheath is expanded, as discussed in section 2.2. Notably, this situation is slightly more complicated for electronegative gases as negative (heavy) ions are also present. Since these negative ions generally cannot react to the applied frequencies, they are also confined to the bulk plasma by the time-averaged sheath electric fields. It should also be noted that negative ions tend to form through attachment processes (e.g., see subsection 3.3.2) which deplete the bulk electron density and thus affect the electron densities near the sheaths. Furthermore, it is the "motion" of the plasma boundary sheaths and the time-dependence of the sheath electric fields that are responsible for several mechanisms that sustain the plasma itself, as seen in section 2.4. This summary on RF sheath dynamics is vastly oversimplified, however, and is expanded upon in the subsequent sections of this chapter. A more complete description of radio-frequency sheaths can be found elsewhere (see, e.g., [2, p. 387-414] and [95]).

Lastly, it should be noted that directly supplying RF power to one electrode is not typically an efficient means of transferring power to the plasma due to an imaginary component of the plasma's impedance in the discharge circuit. In most RF-CCPs, a matching network which includes a "blocking" capacitor is placed between the power supply which generates the applied voltage waveform and the discharge itself [2, p. 430, 452–455]. For capacitive discharges where the maximum value of the potential drop across each sheath is identical, the voltage across this blocking capacitor relative to ground is the same as the difference between the applied potential relative to ground. However, many capacitively coupled plasmas are spatially asymmetric in their ionization and plasma density profiles (e.g., see sections 2.3 and 2.4) and, therefore, the potential drops across the powered and grounded sheaths are usually not the same. This leads to the build-up of a DC voltage on this blocking capacitor relative to ground [2, p. 430-432]. This effectively creates an additional plasma-generated bias voltage which must be considered in the circuit of the discharge. This voltage appears in practice as a DC voltage offset to the applied voltage waveform and is therefore referred to as the system's DC self-bias. The generation and modification of the DC self-bias is further discussed in section 2.3.

2.2 Circuit model of radio-frequency capacitively coupled plasmas using voltage waveform tailoring

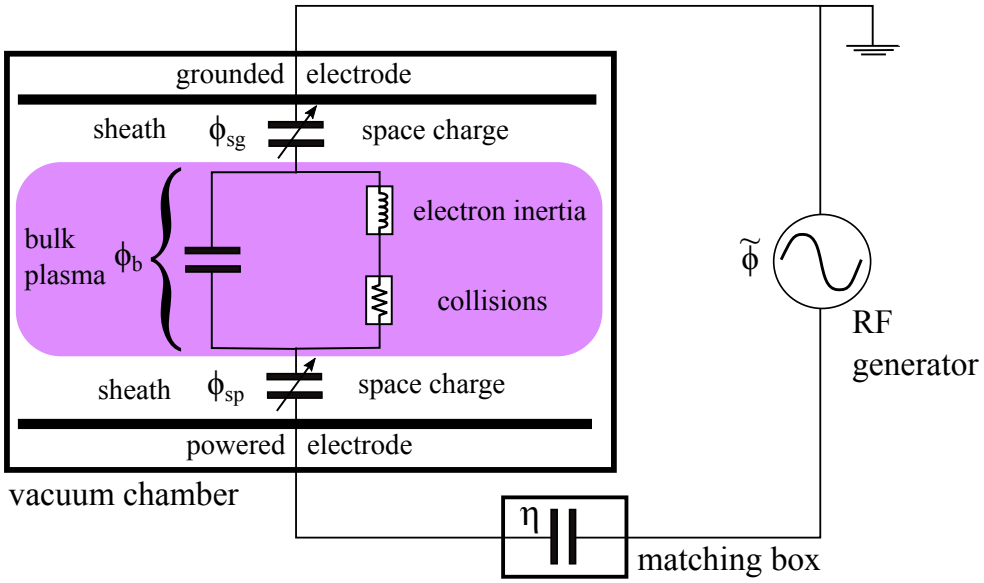

Figure 2.3: Schematic representation of an electrical circuit of an RF-CCP including the equivalent circuit components for the plasma bulk and sheaths. A similar figure is published in Schüngel *et al.*, Plasma Sources Sci. Technol. 24, 044009 (2015) [SE15b].

A RF-CCP can be modeled as a circuit, as seen in figure 2.3, by applying Kirchoff's rule for closed loops in order to obtain the voltage balance for the system [37, 40, 59, SE15a, SE15b, 96]:

$$\eta + \widetilde{\phi}(t) = \phi_{\mathrm{sp}}(t) + \phi_{\mathrm{b}}(t) + \phi_{\mathrm{sg}}(t), \tag{2.1}$$

where the sum of the applied voltage waveform $\widetilde{\phi}(t)$ and the DC self-bias η (discussed in section 2.3), equals the sum of the individual voltage drops across each electrode's sheath, i.e., ϕ_{sp} for the powered electrode sheath and ϕ_{sg} for the grounded electrode sheath, and the voltage drop across the bulk plasma region ϕ_{b}. A DC self-bias, i.e., a DC voltage drop across the discharge, builds up in the plasma as a by-product of placing a blocking capacitor in the matching network between the generators and the discharge itself [97]. Notably, the right hand side of equation (2.1) is also time-dependent, implying $\phi_{\mathrm{sp}}(t)$, $\phi_{\mathrm{sg}}(t)$, and $\phi_{\mathrm{b}}(t)$ because of the applied voltage waveform $\widetilde{\phi}(t)$. The applied voltage waveform therefore determines the voltages across each sheath and can be used to alter the dynamics of sheath expansion and collapse, which can strongly influence electron power absorption dynamics (see section 2.4). Traditionally, the bulk voltage ϕ_{b} can be neglected under certain conditions [97], but in cases where it is significant, such as those seen in chapters 5 and 6 for the plasma series resonance

and for electronegative gases, respectively, it must be included. The floating potentials at the electrode surfaces, which are a product of the electrodes becoming charged by bombardment of charged particles (e.g., ions when the sheath is expanded) are often very small compared to the applied voltages and are included in ϕ_{sp} and ϕ_{sg} (see equations (2.4) and (2.5) later in this section) in the voltage balance. This positive particle flux is normally balanced on RF period-average by a flux of bulk electrons that diffuse to the electrode during that electrode's sheath collapse. Notably, significant electric field reversals can occur in the sheath region at certain harmonic phase angles (θ_k) for some multi-frequency voltage waveforms due to the limited electron conduction current to the electrodes as a result of the shorter duration in which the sheath is collapsed [45]. That is, the floating potential is normally high with a sign that repels electrons at a given electrode for voltage waveforms which cause a long sheath collapse at that electrode, e.g., for a single low-frequency waveform, since without this potential too many electrons would overcome the sheath potential and reach the electrode during the collapse. The absolute value of this floating potential decreases as the duration of sheath collapse decreases since more electrons can be allowed to reach the electrode in the shorter time span. For very short sheath collapses, such as those generated by some multi-frequency waveforms (i.e., VWT), the sign of this floating potential can be reversed since the sheath collapse occurs too quickly for enough electrons to reach the electrode by diffusion. Thus, an electric field reversal in the sheath region is required to maintain the RF period-averaged flux balance of positive and negative particles to the electrode. This electric field reversal can be interpreted as a floating potential with reversed sign but does not correspond to a traditionally defined floating potential. The voltage drops associated with these electric field reversals must thus also be included in the model when necessary, but this consideration is neglected here since the results in the following chapters do not exhibit features indicative of sheath electric field reversals.

The sheath voltage drops $\phi_{\text{sp}}(t)$ and $\phi_{\text{sg}}(t)$ can be described as a function of the normalized charge in the powered electrode sheath q by defining the sheath regions and the net charge profile in the sheath, which is a function of the ion density n_{i} and the electron density $n_{\text{e}}(t)$ in the sheath depending on the sheath model utilized. The areas of the powered and grounded electrode surfaces, denoted A_{p} and A_{g}, respectively, at which these plasma sheaths form are dictated by the geometry of the discharge, as noted in section 3.1. The sheath regions can generally be assumed to be free of electrons (compared to the ion density) as the electric field in the sheath repels electrons back into the bulk plasma and only highly energetic electrons can cross the sheaths and interact with the electrodes while the sheath is not collapsed. This region is set between the electrode $x = 0$ and the momentary plasma sheath edge denoted by $x = s_{\text{p}}(t)$ for the powered electrode sheath, for example. The momentary plasma sheath edge $s(t)$ is calculated based on the integral criterion introduced by Brinkmann [98] wherein the electron density inside the sheath is balanced by the net charge on the bulk side taken up to half the fixed electrode gap length d:

$$\int_0^{s(t)} n_{\text{e}}(x,t)dx = \int_{s(t)}^{d/2} \left[n_{\text{i}}(x) - n_{\text{e}}(x,t)\right] dx. \tag{2.2}$$

The ion density is also assumed to not vary with time, which is satisfied for the applied fundamental frequencies used in this work. Then, by integrating Poisson's equation between

$x = 0$ and $x = s_{\mathrm{p}}(t)$, the charge $Q_{\mathrm{sp}}(t)$ within the powered electrode sheath for a given powered electrode area A_{p} is

$$Q_{\mathrm{sp}}(t) = eA_{\mathrm{p}} \int_0^{s_{\mathrm{p}}(t)} n_{\mathrm{i}}(x)dx, \tag{2.3}$$

and the voltage drop across the powered sheath becomes

$$\phi_{\mathrm{sp}}(t) = -\frac{e}{\varepsilon_0} \int_0^{s_{\mathrm{p}}} \int_x^{s_{\mathrm{p}}(t)} n_{\mathrm{i}}(x^{'})dx^{'}dx. \tag{2.4}$$

The shape of the ion density profile $n_{\mathrm{i}}(x)$ and thus the model used to represent it is highly important as a result. The matrix sheath model, for example, utilizes a homogeneous ion density profile $n_{\mathrm{i}}(x) = n_{\mathrm{i0}}$ which yields the quadratic charge-voltage relation $\phi_{\mathrm{sp}}(t) = -Q_{\mathrm{sp}}^2(t)/(2eA_{\mathrm{p}}^2\varepsilon_0 n_{\mathrm{i0}})$. This approximation is a strong simplification, however, and as discussed in section 2.5 and chapter 5 does not accurately reproduce real physical sheath behavior [SE15b]. This simplified model is, however, useful in the analytical treatment of the sheath voltages, such as in chapter 4. Once a charge-voltage relation for the powered electrode is obtained, the grounded sheath voltage drop $\phi_{\mathrm{sg}}(t)$ can then be defined as a function of the normalized total net charge within the discharge volume q_{tot}, which is assumed to be constant [25, 37, 40], and the normalized charge in the powered sheath q. The normalized charges q and q_{tot} are defined as $q(t) = Q_{\mathrm{sp}}(t)/Q_0$ and $q_{\mathrm{tot}} = Q_{\mathrm{tot}}/Q_0$ where $Q_0 = A_{\mathrm{p}}\sqrt{2e\varepsilon_0 n_{\mathrm{i0}}\phi_{\mathrm{tot}}}$ is the maximum charge in the powered sheath used as a charge normalization constant [97]. The normalized charge in the grounded sheath can then be easily defined as $q_{\mathrm{sg}} = q_{\mathrm{tot}} - q(t)$. Thus, as the powered electrode sheath oscillates between fully collapsed ($s_{\mathrm{p}}(t) \approx 0$) and fully expanded ($s_{\mathrm{p}}(t) = s_{\mathrm{p,max}}$) over one RF period, q varies from $q = 0$ to $q = 1$, respectively, in the case where both floating potentials are zero. The maximum powered and grounded sheath voltages $\phi_{\mathrm{sp}}^{\mathrm{max}}$ and $\phi_{\mathrm{sg}}^{\mathrm{max}}$ are additionally related via the symmetry parameter $\varepsilon = \left|\frac{\phi_{sg}^{max}}{\phi_{sp}^{max}}\right|$ discussed in section 2.3. For the simplified quadratic charge-voltage relations above, the max sheath voltages in this simplified case are expressed as $\left|\phi_{\mathrm{sp}}^{max}\right| \approx Q_{\mathrm{sp,max}}^2(t)/(2eA_{\mathrm{p}}^2\varepsilon_0 n_{\mathrm{i0,sp}})$ and $\left|\phi_{\mathrm{sg}}^{max}\right| \approx Q_{\mathrm{sg,max}}^2(t)/(2eA_{\mathrm{g}}^2\varepsilon_0 n_{\mathrm{i0,sg}})$, respectively.

The voltage balance can therefore be simplified for low pressure electropositive plasmas, where the bulk voltage ϕ_{b} is negligible, to the form:

$$\eta + \widetilde{\phi}(t) = \phi_{\mathrm{tot}} \left[-q^2(t) + \varepsilon(q_{\mathrm{tot}} - q(t))^2\right]. \tag{2.5}$$

Notably, the floating potentials are automatically included in equation (2.5) due to the use of $q_{\mathrm{sp}}(t) = q(t)$ and $q_{\mathrm{sg}}(t) = q_{\mathrm{tot}} - q(t)$ in the powered and grounded sheath voltages, respectively. This is because the minimum charges in each sheath obtained at the time of complete collapse of the respective sheath, e.g., $q_{\mathrm{sp,min}}$ for the powered sheath, are not necessarily zero. Therefore, the floating potentials are only neglected in this model when the minimum charge in each sheath is zero (e.g., $q_{\mathrm{sp,min}} = 0$). The applied voltage waveform $\widetilde{\phi}(t)$ and the total possible voltage amplitude ϕ_{tot} are easily obtainable from experimental voltage measurements and are frequently important input variables in simulations of RF-CCPs. The DC self-bias η can also be experimentally measured or can be output by such simulations

(see section 3.3). The symmetry parameter ε and total charge q_{tot} can therefore be calculated by rearranging equation (2.5) and using the global extrema of the applied voltage waveform, $\widetilde{\phi}_{\mathrm{max}}$ and $\widetilde{\phi}_{\mathrm{min}}$ [37, FJ15, 97]:

$$\varepsilon = -\frac{\eta + \widetilde{\phi}_{\mathrm{max}}}{\eta + \widetilde{\phi}_{min}}, \tag{2.6}$$

$$q_{\mathrm{tot}} = \sqrt{\frac{\widetilde{\phi}_{\mathrm{max}} - \widetilde{\phi}_{\mathrm{min}}}{\phi_{\mathrm{tot}}(1+\varepsilon)}}. \tag{2.7}$$

The sheath voltages can then be calculated in the forms $\phi_{\mathrm{sp}}(t) = -\phi_{\mathrm{tot}} q^2(t)$ and $\phi_{\mathrm{sg}}(t) = \varepsilon\phi_{\mathrm{tot}}\left[q_{\mathrm{tot}} - q(t)\right]^2$ by again rearranging equation (2.5) and using q_{tot} from equation (2.7) [42]. This yields

$$\phi_{\mathrm{sp}}(t) = -\phi_{\mathrm{tot}} \left[\frac{-\varepsilon q_{\mathrm{tot}} + \sqrt{\varepsilon q_{\mathrm{tot}}^2 - (1-\varepsilon)\frac{\eta+\widetilde{\phi}(t)}{\phi_{\mathrm{tot}}}}}{1-\varepsilon} \right]^2, \tag{2.8}$$

$$\phi_{\mathrm{sg}}(t) = \varepsilon\phi_{\mathrm{tot}} \left[\frac{q_{\mathrm{tot}} - \sqrt{\varepsilon q_{\mathrm{tot}}^2 - (1-\varepsilon)\frac{\eta+\widetilde{\phi}(t)}{\phi_{\mathrm{tot}}}}}{1-\varepsilon} \right]^2. \tag{2.9}$$

These sheath voltages, once calculated for a given applied voltage waveform, can then be correlated with spatio-temporal ionization or excitation dynamics in the plasma using experimental phase-resolved optical emission spectroscopy (PROES) measurements (see subsection 3.2.2) or via similar simulation outputs to further understand the influence of tailored voltage waveforms on the electron power absorption dynamics (see, for example, the results of chapter 4). If the bulk voltage is not negligible, such as in chapters 5 and 6, equations (2.5), (2.6), (2.7), (2.8), and (2.9) must be recalculated including the bulk voltage term $\phi_{\mathrm{b}}(t)$. For the plasma series resonance discussed in chapter 5, see section 2.5 for the appropriate model used. For the cases of electronegative gases and admixtures discussed in chapter 6, see the considerations laid out at the end of section 2.3.

The bulk voltage drop $\phi_{\mathrm{b}}(t)$ is modeled in a substantially different way and depends on the discharge conditions, the applied voltage waveform, and potentially the electronegativity of the bulk plasma. In traditional electropositive RF-CCPs, the plasma bulk is assumed to be a quasineutral region where the discharge current is purely conductive and the RF current is carried by the bulk electrons. The conduction current is then described based on the momentum balance equation:

$$m n_{\mathrm{e}} \frac{\partial u_{\mathrm{d}}}{\partial t} = -e n_{\mathrm{e}} E_{\mathrm{b}} - m n_{\mathrm{e}} \nu_{\mathrm{m}} u_{\mathrm{d}}, \tag{2.10}$$

where m, n_{e}, and u_{d} are the electron mass, density, and drift velocity in the x-direction perpendicular the electrode surfaces, respectively. E_{b} is the electric field in the bulk and ν_{m} is the electron collision frequency for momentum transfer. Notably, this momentum balance neglects the convective and force density terms, such as a pressure gradient, of the full momentum balance. This is a important limitation of this model since the pressure gradient term is related to the ambipolar electric field which is critical to the operation of

RF-CCPs, as seen in chapter 6, for example. This bulk voltage model is therefore not used for the discussions of PSR or electronegative plasmas (chapters 5 and 6). The bulk voltage in the PSR model can be found in section 2.5. For the electronegative plasmas in chapter 6, the bulk voltage is not analytically modeled due to the presence of the drift electric fields in the plasma bulk from the DA-heating mode (see section 2.4).

The electric field in the bulk $E_{\mathrm{b}}(t)$ can be found by solving equation (2.10) by setting the electron conduction current density as $j = -en_{\mathrm{e}}u$ (where u is electron velocity) and ignoring any time dependence for the electron density [96]:

$$E_{\mathrm{b}}(t) = \frac{m}{e^2 n_{\mathrm{e}}}\left[\frac{\partial j(t)}{\partial t} + \nu_{\mathrm{m}} j(t)\right]. \tag{2.11}$$

Here, the time derivative of $j(t)$ has a dependence on ω_{RF} corresponding to the applied frequency ($2\pi f$) in the single-frequency case as this current is driven across the plasma by the applied voltage waveform. For multi-frequency voltage waveforms, this ω_{RF} becomes a frequency space variable due to the application and excitation of higher harmonics (see section 2.5 and chapter 5). Note that in most asymmetric chamber configurations, this electric field would again be an over-simplification due to the presence of multiple potential current paths, such as coupling to the grounded chamber walls [39, 99, 100]. For this one-dimensional case the bulk voltage can then be found by integrating across the bulk region in the x-direction, yielding

$$\phi_{\mathrm{b}}(t) = -\int_{s_{\mathrm{p}}(t)}^{d-s_{\mathrm{g}}(t)} E_{\mathrm{b}}(t)dx, \tag{2.12}$$

where notably the bulk region is determined by the positions of the momentary sheath edges of the powered sheath and the grounded sheath, i.e., $x = s_{\mathrm{p}}(t)$ and $x = d - s_{\mathrm{g}}(t)$ respectively. This has significant implications for the bulk voltage as the bulk region sweeps back and forth through the sheath regions during sheath collapse and expansion, as discussed in section 2.5 and chapter 5.

The bulk voltage drop ϕ_{b} becomes significantly more complicated, however, for discharges which utilize electronegative gases or gas mixtures, which is often the case in industrial applications [7–11]. In electronegative plasmas, negative ions can form via electron attachment or dissociative molecular collision processes (e.g., [101, 102] for CF_4) and are often confined to the bulk plasma by the electric fields of the electrode sheaths. These negative ions are also much heavier than electrons and cannot react to the temporal variations of the applied voltage waveform. These ions therefore cannot carry the conduction current and can even reduce the conduction current in the bulk by reducing the electron density while maintaining quasi-neutrality. The global electronegativity ζ of a given discharge is defined using the ratio of the total number of negative ions to electrons:

$$\zeta = \frac{\int_0^d n_{\mathrm{i}}^- dx}{\int_0^d n_{\mathrm{e}} dx}, \tag{2.13}$$

For certain conditions, such as at high background gas pressures and/or highly electronegative gas admixtures for CF_4 [60, 89], the electronegativity of the discharge will increase as the

bulk electron density is depleted, resulting in a decrease of the conduction current across the bulk region. Note that not all electronegative gases are strongly electronegative under the same conditions, such as oxygen (O_2), which is significantly more electronegative at lower background gas pressures (e.g., see [84]). If a part of the bulk plasma is significantly more electronegative than another part, as discussed in the results of chapter 6, the conduction current will be significantly reduced in the region of depleted electron density. The bulk electric field must therefore act as a displacement current in these regions resulting in the behavior of the bulk drift electric fields observed in the Drift-Ambipolar power absorption mode discussed in section 2.4 [59, 60, 79, 83–85, 103–105]. The bulk voltage drop $\phi_b(t)$ thus becomes very important for the electron power absorption of this heating mode and is significantly enhanced when driving currents across the discharge bulk which exceed the maximum potential conduction current carried by the bulk electrons, i.e., $j_{max} = -en_e^{max}u$. In particular, certain tailored voltage waveforms which are particularly temporally asymmetric or have quick "rise" or "fall" times during times of sheath expansion, such as sawtooth waveforms [63–66], can drive such large currents across the bulk plasma and produce significant, time-asymmetric electric fields in the bulk region as a result.

The sheath voltage drops $\phi_{sp}(t)$ and $\phi_{sg}(t)$ and their dynamics are primarily responsible for several electron power absorption mechanisms, as discussed in section 2.4, as well as for several key plasma parameters such as the plasma density, the ion fluxes to each electrode, and the mean ion energies at the surface of substrates placed on a given electrode. The ability to customize the applied voltage waveform using tailored voltage waveforms enables the customization of the sheath voltage drops and the sheath dynamics to optimize the electron power absorption dynamics and the relevant plasma parameters. However, a key part of obtaining a full understanding of how the voltage waveform should be tailored for a given process is understanding the generation of the DC self-bias η (see section 2.3) and how both η and $\widetilde{\phi}(t)$ affect the electron power absorption dynamics under a given set of conditions (see section 2.4).

2.3 Electrical Asymmetry Effect: DC self-bias generation and discharge asymmetry in capacitively coupled plasmas using tailored voltage waveforms

The DC self-bias has been utilized for many years as a major control parameter of ion energy distribution functions at plasma-facing surfaces. However, it also has significant influence over the electron power absorption dynamics (see section 2.4) and is associated with any spatial asymmetry (geometrical or electrical) of the discharge [37, 97]. A complete fundamental understanding of how tailored voltage waveforms affect the spatio-temporal heating dynamics, the DC self-bias, and the discharge symmetry for any discharge conditions is therefore necessary to optimize process parameters. The voltage balance model [40] discussed

in section 2.2 is utilized here to analyze changes in the DC self-bias in terms of these effects at different conditions, including comparisons with simulations. The model allows for distinction between different mechanisms causing the generation of the DC self-bias by closely examining the discharge symmetry and the voltage drops across the electrode sheaths and the bulk plasma.

The DC self-bias, η, is obtained in the model based on the individual voltage drops across the sheaths adjacent to each electrode and across the bulk [37, 40]:

$$\eta = -\frac{\widetilde{\phi}_{\mathrm{max}} + \varepsilon\widetilde{\phi}_{\mathrm{min}}}{1+\varepsilon} + \frac{\phi^{\mathrm{f}}_{\mathrm{sp}} + \varepsilon\phi^{\mathrm{f}}_{\mathrm{sg}}}{1+\varepsilon} + \frac{\phi^{\mathrm{b}}_{\mathrm{max}} + \varepsilon\phi^{\mathrm{b}}_{\mathrm{min}}}{1+\varepsilon} = \eta_{\mathrm{vw}} + \eta_{\mathrm{f}} + \eta_{\mathrm{b}}, \tag{2.14}$$

where $\widetilde{\phi}_{\mathrm{max/min}}$ are the global maximum and minimum of the applied voltage waveform, $\phi^{\mathrm{f}}_{\mathrm{sp}}$ and $\phi^{\mathrm{f}}_{\mathrm{sg}}$ are the floating potentials at the powered and grounded electrodes, and $\phi^{\mathrm{b}}_{\mathrm{max/min}}$ are the voltage drops across the bulk at the times of maximum and minimum applied voltage, respectively. The DC self-bias terms have different origins: η_{vw} is due to the applied voltage waveform, η_{f} is due to the floating potentials at each electrode, and η_{b} is due to the voltage drop across the bulk plasma. The floating potentials are traditionally considered to be negligible when compared to the applied voltage waveform, such that the η_{f} term is neglected. The bulk voltage drops in equation (2.14) can usually be neglected for electropositive plasmas (e.g., argon) at low pressures [97], but cannot generally be ignored if an electronegative gas (e.g., CF_4) is present, as a significant drift electric field often exists in the bulk and a strong ambipolar field can be generated near the sheath edges [59, 60, 79, 83–85, 103–105]. The existence and strength of these electric field components as a function of the mixing ratio between the electronegative and electropositive component gases at a given pressure is not well understood at present and is discussed further in section 6.2. The term from the applied voltage waveform, η_{vw}, in equation (2.14) is typically dominant compared to the other terms, even in electronegative plasmas. The global extrema of the driving voltage waveform, $|\widetilde{\phi}_{\mathrm{max}}|$ and $|\widetilde{\phi}_{\mathrm{min}}|$, can be made unequal by applying two or more consecutive harmonics of a fundamental frequency with distinct relative phases θ_k. The effect of inducing a difference between the driving voltage waveform's global extrema on the η_{vw} self-bias term, via $\widetilde{\phi}_{\mathrm{max/min}}$, is known as the amplitude asymmetry effect (AAE).

The symmetry parameter in equation (2.14) is defined as

$$\varepsilon = \frac{|\phi_{\mathrm{sg,max}}|}{|\phi_{\mathrm{sp,max}}|} \approx \left(\frac{A_{\mathrm{p}}}{A_{\mathrm{g}}}\right)^2 \frac{\bar{n}_{\mathrm{sp}}}{\bar{n}_{\mathrm{sg}}} \left(\frac{Q_{\mathrm{mg}}}{Q_{\mathrm{mp}}}\right)^2 \frac{I_{\mathrm{sg}}}{I_{\mathrm{sp}}}, \tag{2.15}$$

where $|\phi_{\mathrm{sp,max}}|$ and $|\phi_{\mathrm{sg,max}}|$ are the maximum voltage drops across each sheath (note that $\phi_{\mathrm{sp,max}} < 0$ V and $\phi_{\mathrm{sg,max}} > 0$ V) [40]. The terms on the right hand side of equation (2.15) correspond to the ratios of the respective electrode surface areas, A_{p} and A_{g}, the respective mean net charged particle densities in each sheath, $\bar{n}_{\mathrm{sp}}$ and $\bar{n}_{\mathrm{sg}}$, the maximum uncompensated charges in each sheath, Q_{mp} and Q_{mg}, and the sheath integrals for each sheath, I_{sp} and I_{sg}, as discussed in [37, 40, 97, 106]. The symmetry parameter's dependence on the charge densities in each sheath suggests a dependence on the electron power-absorption mode through the localization of ionization, which is the basis for the slope asymmetry effect (SAE) described

in detail in the works of Bruneau *et al.* [63–66]. Voltage waveforms which are significantly time asymmetric, such as sawtooth waveforms and the "peaks-type" and "valleys-type" triple-frequency waveforms which have $\widetilde{\phi}(t) \neq \widetilde{\phi}(-t)$, frequently generate such spatially asymmetric ionization profiles as a product of strongly enhancing electron power absorption near only one electrode's sheath. This becomes particularly relevant in electronegative discharges at high pressures where the DA-mode is dominant, as the electron power absorption is primarily located at the collapsing sheath edge and in the bulk plasma in contrast with the α-mode, where maximum ionization is observed at the expanding sheath [BS16, 69]. The symmetry parameter ε is also a crucial parameter in the modeling of the plasma series resonance (see section 2.5).

It should be clarified that ε, the symmetry parameter, is regarded as defining the "discharge asymmetry." This implies that $\varepsilon = 1$ is the criterion for a symmetric discharge and $\varepsilon \neq 1$ is the criterion for an asymmetric discharge. The inequality for the latter further implies, as in equation (2.15), that the maximum sheath voltage for each sheath is not equal. This is most frequently due to a difference in the ion density profiles adjacent to each sheath under most conditions, as seen in section 6.2 with $\bar{n}_{\mathrm{sp}}/\bar{n}_{\mathrm{sg}}$ for example. The presence of a large DC self-bias, such as those commonly seen in geometrically asymmetric RF-CCPs, will also therefore correspond to an asymmetry of the potential profile. It does not, however, inherently correspond to an asymmetry of the density profile, although it is the product of ionization resulting from the electron power absorption mechanisms (see section 2.4). That said, a discharge can be asymmetric ($\varepsilon \neq 1$) even when the DC self-bias vanishes [44], again seen in the results of section 6.2.

In geometrically symmetric RF-CCPs, where $\left(\frac{A_{\mathrm{p}}}{A_{\mathrm{g}}}\right)^2 = 1$, the DC self-bias can thus be controlled using two mechanisms that aim to modify the η_{vw} self-bias term: $|\widetilde{\phi}_{\mathrm{max}}| \neq |\widetilde{\phi}_{\mathrm{min}}|$ (AAE) or $\varepsilon \neq 1$. One way to cause the symmetry parameter to deviate from unity is the use of the SAE, which can be induced by using temporally asymmetric waveforms. For geometrically asymmetric discharges, where usually the grounded area of the chamber is larger such that $\left(\frac{A_{\mathrm{p}}}{A_{\mathrm{g}}}\right)^2 < 1$, the same mechanisms can be used to control the DC self-bias with the notable inclusions that: i) the range of obtainable DC self-biases is now centered about a non-zero and negative voltage as a product of $\varepsilon < 1$ for the single-frequency case, such that the electron power absorption near the powered electrode is typically more favored for any applied waveforms (e.g., for the $\alpha-$mode), and ii) changes in the discharge symmetry due to the shape of the voltage waveform (i.e., the EAE) can be influenced by the presence of this inherent asymmetry, as discussed in section 6.2 for example. The DC self-bias and the associated extrema of the voltage waveform ($\widetilde{\phi}_{\mathrm{max}}$, $\widetilde{\phi}_{\mathrm{min}}$), furthermore, can be easily measured experimentally using a voltage probe (see subsection 3.2.1). Again, the symmetry parameter ε can also be calculated directly from the global extrema of the voltage waveform ($\widetilde{\phi}_{\mathrm{max}}$, $\widetilde{\phi}_{\mathrm{min}}$) and the DC self-bias η using equation (2.6) for discharges where the floating potential and bulk voltage DC self-bias terms are negligible (η_{f}, $\eta_{\mathrm{b}} = 0$).

For cases where the self-excitation of PSR oscillations is relevant, as in section 2.5 and chapter 5, or for electronegative RF-CCPs where the bulk voltage is not negligible, such

as the cases discussed in chapter 6, the η_{b} term must be included in equation (2.14) and its influence on the total DC self-bias, η, needs to be examined. The bulk voltage model for the PSR in electropositive discharges is outlined in section 2.5. For the electronegative plasmas in chapter 6, the bulk voltage is not analytically modeled due to the presence of the drift electric fields in the plasma bulk from the DA-heating mode (see section 2.4). Instead, in the frame of the DC self-bias analysis in section 6.2 the maximum and minimum bulk voltages $\phi^{\mathrm{b}}_{\mathrm{max,min}}$ in equation (2.14) are obtained from the spatio-temporal potential profile of the PIC/MCC simulations outlined in subsection 3.3.2. The "peaks-type" voltage waveform cases for $N = 3$ are examined for both 20 Pa and 60 Pa by using the results of the simulation discussed in subsection 3.3.2 as inputs to the voltage balance and the DC self-bias model in section 6.2. The sheath potentials ($\phi_{\mathrm{sp}}(t)$, $\phi_{\mathrm{sg}}(t)$), the applied voltage waveform ($\widetilde{\phi}(t)$), the DC self-bias (η), the symmetry parameter (ε), the floating potentials at each electrode ($\phi^{\mathrm{f}}_{\mathrm{sp}}$, $\phi^{\mathrm{f}}_{\mathrm{sg}}$), and the bulk voltage at the times of maximum and minimum applied voltage ($\phi^{\mathrm{b}}_{\mathrm{max/min}}$) are used as inputs into equations (2.14) and (2.15) in order to calculate the DC self-bias, η, based on equation (2.14). In this way, the contributions of η_{vw}, η_{b}, and η_{f} and the different mechanisms of DC self-bias generation can be separated. The evolution of η_{b} is then correlated to the changes in the global electronegativity (ζ) from equation (2.13), which is also extracted from the simulations. The evolution of the symmetry parameter ε from equation (2.15) with the changing gas mixture is also contextualized in the model by calculating each of its individual ratio components $\left(\frac{Q_{\mathrm{mg}}}{Q_{\mathrm{mp}}}\right)^2$, $\frac{\bar{n}_{\mathrm{sp}}}{\bar{n}_{\mathrm{sg}}}$, $\frac{I_{\mathrm{sg}}}{I_{\mathrm{sp}}}$, with $\left(\frac{A_{\mathrm{p}}}{A_{\mathrm{g}}}\right)^2 = 1$. The time-averaged charged particle density in each sheath, the uncompensated charge in each sheath ($Q_{\mathrm{sp}}(t)$, $Q_{\mathrm{sg}}(t)$), and the maximum sheath widths (l_{sp}, l_{sg}) from the simulation are used to calculate the symmetry parameter terms. Additionally, an example geometric asymmetry is implemented into the model by setting $\frac{A_{\mathrm{p}}}{A_{\mathrm{g}}} = 0.25$ but otherwise keeping the calculations for the symmetry parameter terms the same in order to study the effects of an exemplary geometric reactor asymmetry on the DC self-bias generation qualitatively.

The control of the DC self-bias is frequently a crucial variable for the operation of RF-CCP discharges which partially dictates the shape of the ion energy distribution function(s) such as those seen in chapter 4 and, in particular, the mean ion energy of ions accelerated through an electrode sheath towards a substrate. Therefore, the choice of the DC self-bias is a critical component of achieving separate control over the ion flux and ion energy, which is essential in many industrial discharges. This control is limited, however, by the influence of the DC self-bias on the electron power absorption dynamics and the discharge symmetry, as discussed in section 2.4.

2.4 Electron power absorption dynamics and modes of operation in capacitively coupled plasmas

In order to realize advanced control over plasma parameters and process rates, a detailed fundamental understanding of the plasma physics is required in RF-CCPs. The space and

time dependent charged particle power absorption dynamics in particular are fundamentally critical to the generation and sustainment of the discharge via ionization and play an essential role in defining important plasma parameters such as the particle distribution functions at plasma-facing surfaces. Notably, most of the applied power from the voltage waveform is typically absorbed by the positive ions accelerated by the electric fields in each electrode sheath. However, due to the thermal non-equilibrium of electrons and heavier particles like ions, electrons are the primary particles in most RF-CCPs which can react to the applied frequencies on the appropriate timescales and thus are primarily responsible for the transfer of energy in excitation and ionization collisional processes to other particle species (e.g., neutral atoms or ions). Therefore, the plasma electrons are critical for the ionization in the discharge and the sustainment of the plasma itself. The exact mechanisms by which these electrons gain energy and thus the exact electron power absorption modes present in a discharge depend on the operating pressure, the characteristics of the driving voltage waveform [32, 45–53, 56–58, 60, 63–66, 77–81, 83–87, 103, 105, 107–120], the mixing ratio between gas components [69–71, 89–92], and occasionally the plasma-surface interactions such as secondary electron emission at plasma-facing surfaces (e.g., the electrodes) [35, 79, 121–123]. Several prominent heating mechanisms associated with electron power absorption are frequently observed in RF-CCPs, including those responsible for the α-mode [79, 80, 86, 108, 109, 111–113, 115, 116, 118, 124–132], the γ-mode [35, 79, 121–123], and the DA-mode [59, 72, 83–88, 104, 133, 134]. These different modes of electron power absorption have previously been examined in single- and dual-frequency RF-CCPs [20–23, 26–31]. For multi-frequency tailored voltage waveforms, though, these investigations had been primarily limited to electropositive gases operated in the α-heating mode [7, 8, 13, 32, 38–62, 65, 66, FJ15, SE15a, 77], but more recent works [BS16, 69–72] have examined electronegative gases operated in the DA-mode as well [59, 72, 83–88]. Additionally, the influence of a chosen gas mixing ratio on discharge operation and process control is strongly correlated to the specific spatio-temporal dynamics dictated by the electron power absorption modes occurring in the plasma, as demonstrated in section 6.2. Therefore, a complete fundamental understanding of the space and time resolved electron power absorption dynamics in each mode of operation on a nanosecond timescale within the RF period as a function of discharge conditions is necessary in multi-frequency discharges, and advanced methods for tailoring these dynamics are highly desired in most applications. In this section, the power absorption modes (α-, γ-, DA-) and their respective electron heating mechanisms which are utilized in the following chapters are discussed.

Traditionally, in single-frequency RF-CCPs, a strong coupling exists between the electron power absorption dynamics and the ionization and sustainment of the discharge. Thus, the plasma density, ion fluxes, and mean sheath voltages, which are crucial quantities for the mean ion energy at the electrodes, are intrinsically linked to these electron dynamics in applications. While both the ion fluxes and the ion energies can be controlled by changing the driving voltage amplitude or power, they cannot be controlled independently for single-frequency waveforms. This is due to the fact that an increase in the externally applied voltage or power will enhance both the electron heating and the mean sheath voltages [26]. In response to this limitation, classical dual-frequency discharges operated at substantially different frequencies (e.g., 1 and 100 MHz) attempt to separate this coupling by using the low frequency (lf) voltage amplitude to primarily control the sheath voltage and the high frequency (hf) voltage

amplitude to control the sheath dynamics and thus the electron heating. In such discharges, it is assumed that the lf component does not affect the electron heating and the hf component does not influence the mean sheath voltage significantly when the hf voltage amplitude is sufficiently small compared to the lf voltage amplitude [26, 27, 135–138]. Previous works demonstrate, however, that these assumptions are generally incorrect as significant coupling mechanisms still exist between both RF sources that again limit the control of the mean ion energy and ion flux due to effects of the lf voltage on the sheath dynamics and ionization due to secondary electrons [26–28, 35]. Furthermore, the ionization in the discharge has a strong, nonlinear dependence on the sheath dynamics and the specific electron heating mechanisms in the discharge. Therefore, control of process-relevant plasma parameters requires a means of finely controlling the sheath dynamics and sheath voltages separately but simultaneously. This is the basis for utilizing multi-frequency tailored voltage waveforms [7, 8, 13, 32, 37–66, FJ15, SE15a, 139–141] to control the electron power absorption dynamics by customizing the sheath dynamics, sheath voltages, and discharge symmetry (see sections 2.2 and 2.3) as needed. However, the influence of tailored voltage waveforms on the discharge heating strongly depends on the dominant electron heating mechanisms present in a given discharge.

The most prevalent electron power absorption modes observed in RF-CCPs are referred to as the α-mode, the γ-mode, and the DA-mode, each of which is dominant in different ranges of discharge conditions. In electropositive gases operated at low pressures (e.g., < 100 Pa), RF-CCPs are usually operated in the α-power absorption mode, where stochastic and ambipolar electron heating during sheath expansion [79, 80, 86, 108, 112, 113, 115, 116, 118, 124–129] and electron heating by electric field reversals during sheath collapse dominate [109, 111, 130–132]. At higher pressures and/or applied voltages, the γ-mode takes over, where the ionization is dominated by secondary electrons emitted from boundary surfaces which are accelerated and enhanced by collisions inside the boundary sheath during times of high sheath voltage [35, 79, 121–123]. For electronegative, dusty, and/or high pressure discharges, operation in the DA-mode is possible and significant electron heating can be observed in the plasma bulk due to reduced electrical conductivity and high electric drift fields. Additionally, strong ambipolar fields are created at the sheath edges under these conditions and cause significant electron heating and ionization during sheath collapse. Notably, the ionization maxima of the α- and γ-modes are usually located near the appropriate expanding sheath, but the maxima of the DA-mode is primarily in the bulk and near the opposite, collapsing sheath (see figure 2.4 below and chapters 6 and 7, for example). Therefore, the discharge symmetry is reversed in the DA-mode compared to the α- or γ-modes, and any mode transition to or from the DA-mode can potentially cause the discharge asymmetry to become reversed, as in the results presented in chapter 6.

In the case of the α-mode, the primary mechanism of electron heating is the acceleration of electrons in the electric field of each electrode sheath during their respective sheath expansion phases. When a given sheath collapses, bulk electrons are no longer repelled back into the bulk plasma by the sheath's electric field and can move into the sheath region and reach the electrode. This is necessary in order for the charged particle fluxes of ions and electrons to each electrode, and thus the currents to these electrodes, to be equal on time average, such that the electrodes do not build up excess charge and thus reach significant non-zero floating

potentials (e.g., see [2, p. 393]). Then, when the sheath expands again, these electrons are accelerated back into the bulk by the electric field of the expanding sheath, resulting in significant electron energy gain and subsequent ionization of the background gas via collisional processes. This process is referred to as being "stochastic" because the RF phases (i.e., values of t) when the electron enters the sheath electric field and over which the acceleration occurs, and thus the change in velocity from the acceleration during the electron's transit through the sheath region, is generally random. That said, it is apparent that the electrons which interact during the phases of sheath expansion gain significantly more energy due to the expanding motion of the sheath edge and the correspondingly longer duration of acceleration before exiting the sheath electric field. This phenomenon is most easily understood in the frame of the "hard wall" model where the initial electron velocity towards the electrode u is reversed to u_r upon undergoing an elastic collision with the expanding plasma sheath via the relation $u_\mathrm{r} = -u + 2u_\mathrm{es}(t)$, where $u_\mathrm{es}(t)$ is the time-varying velocity of the plasma sheath edge [2, p. 396]. Moreover, the particle velocities are then randomized after the acceleration by collisions with the background gas and other charged particles. These collisions are where the "electron heating" technically occurs as the accelerated velocity distribution is randomized.

The velocity of the resulting energetic electron beam generated by the sheath expansion is affected by how quickly the sheath expands and is therefore influenced by the shape of the driving voltage waveform via its relationship to the sheath dynamics (i.e., how $\widetilde{\phi}(t)$ relates to $\phi_\mathrm{sp}(t)$ for example, see section 2.2). Therefore, tailored voltage waveforms, which can tailor the sheath dynamics on a nanosecond timescale by choosing specific harmonic amplitudes and phases (see section 2.2 and chapter 3), are particularly useful for creating an asymmetric ionization profile. Notably, the collisionality of the discharge plays a significant role in the localization of the ionization, with lower pressures (lower collisionality) usually having ionization across the discharge bulk with the maximum ionization seen near the expanding sheath and higher pressures (higher collisionality) usually having ionization primarily near the edge of the expanding sheath (compare the high/low pressure results of chapter 4, i.e., [FJ15, BB15]). In the latter case, an asymmetric tailored voltage waveform allows for a large asymmetry in the discharge heating, where most of the electron power absorption is seen near only one electrode's sheath expansion and therefore the ion density near and ion flux to that electrode is increased [BB15]. This does not completely eliminate the electron heating from the other electrode's sheath expansion, but does significantly enhance the heating of one relative to the other. It should be noted, furthermore, that the emission of secondary electrons from the electrodes can influence the electron heating dynamics of the α-mode, particularly at low pressures [35, 121, 122].

Additionally, during the phases of sheath collapse, it is possible to induce electric field reversals which accelerate electrons towards the electrode (e.g., see [110]). When the sheath collapses faster than the electrons near the sheath edge can follow via diffusion, a locally reversed electric field begins to build up which accelerates electrons towards the electrode in order to maintain a constant current. This is often the case when the applied voltage waveform, and thus the sheath dynamics, operate on such a fast timescale, for example at a high enough applied frequency, that the electron inertia (related to the electron plasma frequency ω_pe, see section 2.5) prevents the electrons from fully responding. An electric field

is created near the sheath edge as a result because of the net charge ($n_i - n_e$) difference. Electrons are then accelerated by this field. Note that at higher pressures, a collisional drag force on the electrons that restricts their motion into the collapsing sheath can also be responsible [110]. In electronegative discharges, double layers caused by the presence of low mobility negative ions and a depleted density of electrons near the expanded sheath edge can also contribute to the generation of such fields [103, 142, 143].

The γ-power absorption mode, in contrast, is the result of an energetic electron avalanche in the expanded high voltage sheath seeded by the emission of secondary electrons from the associated plasma-facing surface [35, 79, 121–123]. In order for this electron avalanche to occur, several requirements need to be met. Firstly, emitted secondary electrons must be able to gain enough energy when accelerating inside the plasma sheath to ionize the background gas. Usually, this means that the most significant ionization from this mode occurs during the phases where the sheath voltage is largest, i.e., at times after sheath expansion but before sheath collapse. Secondly, the plasma sheath needs to be significantly collisional such that the secondary electrons can efficiently ionize the background gas inside the sheath, resulting in additional electrons which can then be accelerated in the sheath's electric field. This process, which is fairly similar to Townsend breakdown [34] occurring inside the sheath, is referred to as electron multiplication. Lastly, the SEEC (γ) of the plasma-facing surface, defined as the probability of emitting a secondary electron from the interaction of an incident particle of a given energy with the surface (e.g., see [2, p. 209-303] and [144]), must be sufficiently large enough that a significant number of secondary electrons seed this electron multiplication process. Traditionally, it is the incident ion flux to the electrodes with a mean ion energy defined by the sheath voltage (see subsection 3.2.3) which is responsible for the emission of the seeding secondary electrons, but other particles like plasma electrons, energetic "fast" neutral atoms/molecules, photons, and metastables can also cause secondary electron emission [121, 122]. Once such conditions are present, emitted secondary electrons are accelerated and collide repeatedly with the background gas, ionizing it and creating more electrons which are then accelerated. As the energetic electron avalanche reaches the bulk plasma, it causes significant ionization and excitation which is frequently located near the expanded sheath edge for the same reasons as the α-mode at high pressures, though typically the γ-mode is observed primarily at these high pressures. Additionally, the presence of the γ-mode is usually accompanied by a drastic increase in the plasma density compared to the α-mode [35, 83]. Therefore, the γ-mode is primarily dominant at high pressures and high applied voltages for most substrates and secondary electrons dominate the excitation and ionization dynamics [79, 103, 131, 145]. It should be noted, however, that this mechanism of electron heating is uniquely dependent on the SEEC of the plasma-facing surfaces discussed in more detail in section 2.6 and therefore any changes in the SEEC will likely affect the γ-mode excitation and ionization profiles. Notably, the γ-mode excitation could therefore also be used to study SEE as an in-situ diagnostic, as in subsection 3.2.4 based on the γ-CAST diagnostic [94] and in the discussions of chapter 7. It should also be noted, furthermore, that even in the case where the γ-mode is not the dominant electron heating mechanism, the incident ion flux and emitted secondary electrons can still play a major part in the ionization and sustainment of the discharge [35, 122].

In contrast to low pressure electropositive discharges (α-mode), a different heating mode caused by a significant electric field in the plasma bulk, known as the Drift-Ambipolar mode, has been observed in electronegative gases [59, 83–88]. Under these conditions, electrons are accelerated towards the electrode during sheath collapse by a drift electric field in the plasma bulk and by ambipolar fields at the sheath edges. The drift electric field is a consequence of the reduced bulk conductivity (see section 2.2), which itself is a result of the reduced electron density due to the attachment of electrons, forming negative ions with low mobility. These negative ions are confined within the bulk plasma by the electric fields of each sheath and do not generally reach the electrodes. The ambipolar field is the consequence of the peaked electron density at the sheath edges, which creates strong density gradients towards the bulk [59, 83, 118]. Significant electron acceleration occurs in the bulk for this heating mode, and strong local field reversals which also cause electron energy gain can be observed at the collapsing sheath edge [88, 109–111, 146]. If this heating during sheath collapse (field reversal heating) is dominant, the SAE can cause the discharge symmetry to be reversed compared to discharges operated in the α-mode [66]. This heating mode is highly relevant for the discussions of electronegative CF_4 and Ar-CF_4 RF-CCPs shown in chapter 6.

It should also be noted that each of these heating modes appears in specific regions in the spatio-temporal excitation rate plots obtained either via phase-resolved optical emission spectroscopy (PROES, see subsection 3.2.1) or as an output from the PIC/MCC simulations (see section 3.3). Figure 2.4 shows example spatio-temporal plots of the electron heating rate, ionization rate, electric field, and electron density under conditions typically characterized by each electron power absorption mode obtained from PIC simulations of a single-frequency (13.56 MHz) discharge performed by Schulze *et al.* [83]. Each row of figure 2.4 corresponds to operation in a different electron power absorption mode: the α-mode (figures 2.4(a)-(d)), the γ-mode (figures 2.4(e)-(h)), and the DA-mode (figures 2.4(i)-(l)). The electron heating rate and ionization rate plots (figures 2.4(a), 2.4(e), 2.4(i)) and figures 2.4(b), 2.4(f), 2.4(j), respectively) depict the general regions in which the maxima of each mode appears. For example, in the first row of figure 2.4, the electron heating near the powered (bottom) electrode at RF phases over which the powered electrode sheath expands (seen in approximately 5 ns $< t <$ 30 ns of figure 2.4(a)) corresponds to an ionization rate maxima at a similar location and time (figure 2.4(b)) associated with the α-heating mode for the powered RF sheath. Similar ionization can be observed near the grounded sheath later in the RF period by the same mechanism but for the grounded sheath expansion. In the second row, the γ-mode electron heating occurs in the expanded RF sheath during the RF phases where the sheath voltage is highest and corresponds to the ionization rate maxima associated with the γ-mode's energetic electron avalanche (figure 2.4(f)). The associated acceleration of secondary electrons and electrons generated by the electron multiplication process inside the RF sheath is typically not seen in electron heating plots which show the heating of bulk electrons (e.g., figure 2.4(e)). Notably, the ionization maxima of the γ-mode occurs significantly later in the RF period compared to the α-mode maxima (approximately 10 ns between the maxima of figures 2.4(b) and 2.4(f)). Lastly, in the third row, the electron heating in the bulk and at the collapsing grounded sheath edge at RF phases where the powered sheath is expanding (approximately 5 ns $< t <$ 28 ns in figure 2.4(i)) is the product of a drift electric field in the bulk and an ambipolar electric field near the sheath edge (figure 2.4(k)), i.e., the DA-mode, leading to the

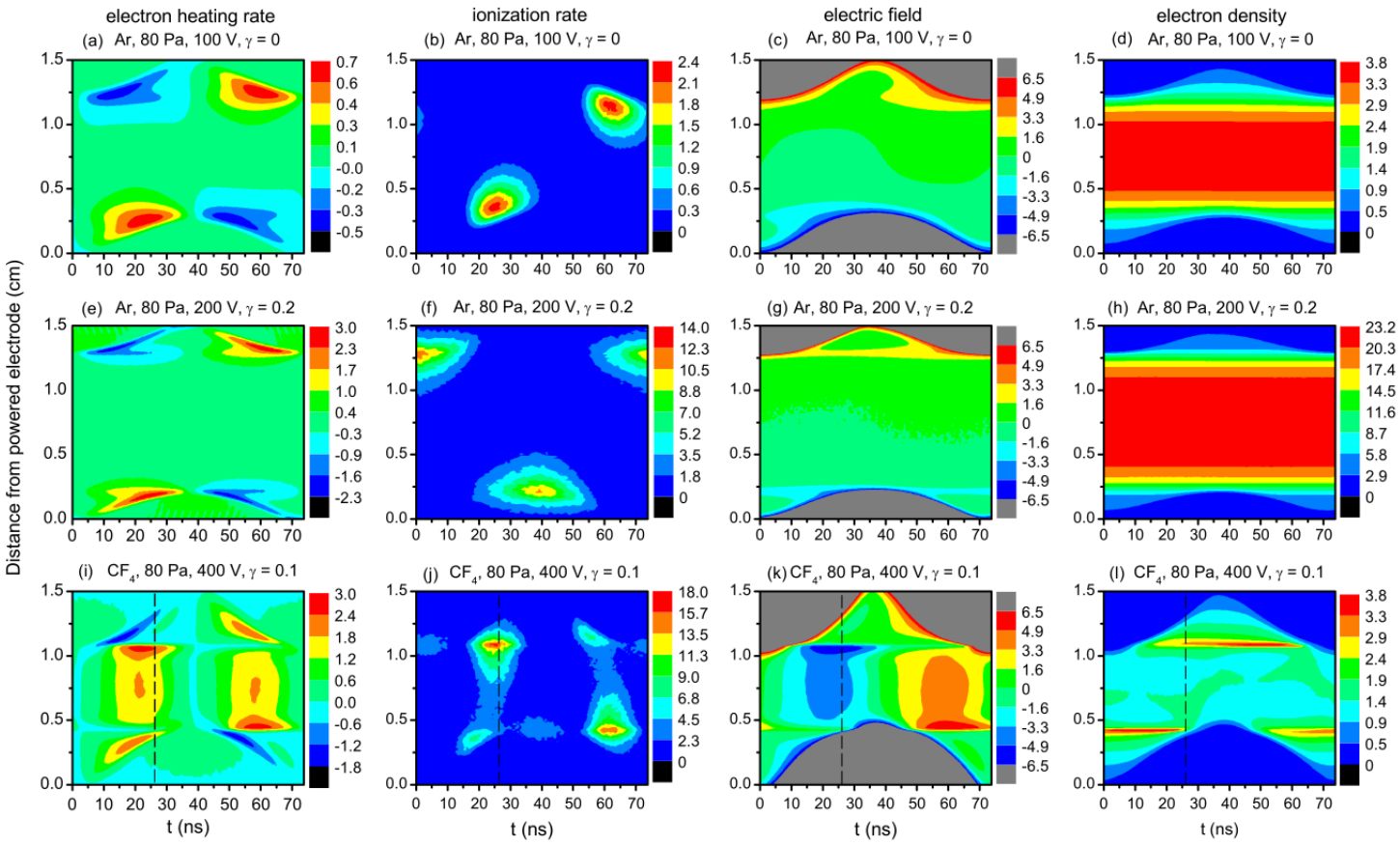

Figure 2.4: Example spatio-temporal plots of the electron heating rate (first column), ionization rate (second column), electric field in the bulk (third column), and electron density (fourth column) obtained from previous PIC simulations of argon and CF_4 discharges driven by a single-frequency 13.56 MHz waveform at 80 Pa and $d = 15$ mm. The powered electrode is located at $x = 0$ while the grounded electrode is located at a distance determined by the electrode gap separation (i.e., $x = d$). Simulation conditions are: (first row) Ar, $\phi_{\rm tot} = 100$ V, $\gamma = 0$; (second row) Ar, $\phi_{\rm tot} = 200$ V, $\gamma = 0.2$; (third row) CF_4, $\phi_{\rm tot} = 400$ V, $\gamma = 0.1$. The color scales have units of 10^5 W m^{-3} (electron heating rate), 10^{21} m^{-3} s^{-1} (ionization rate), 10^3 V m^{-1} (electric field), and 10^{15} m^{-3}, respectively. Figure reproduced from Schulze *et al.*, Phys. Rev. Lett. 107, 275001 (2011) [83] with the permission of APS Publishing.

dominant ionization maxima near the collapsing sheath edge (figure 2.4(j)). The DA-mode is also typically seen under conditions where the electron density in the bulk is depleted by the presence of negative ions, as in figure 2.4(l). The spatio-temporal separation of these heating mode maxima generally allows for the identification of each heating mechanism from ionization rate plots. Similarly, the chosen excitation rate in PROES measurements can also be used for identification of the dominant electron power absorption mode, as seen in the following chapters. However, it should be noted that the lifetimes of such measured excited states (see subsection 3.2.2) are non-negligible and can significantly affect the time resolution of such figures. Notably, in the perfectly symmetric discharge seen in figure 2.4, the localization of each mode's maxima during the powered sheath expansion is vertically mirrored later in the RF period during the grounded sheath expansion.

2.5 Self-excitation of the plasma series resonance in discharges driven by tailored voltage waveforms

Complex physical behaviors are frequently observed in RF-CCPs due to the nonlinear nature of the plasma. A particularly relevant example of such behavior is the self-excitation of higher harmonics in the discharge current of a discharge driven by a sinusoidal voltage (e.g., a single-frequency voltage waveform) via resonance phenomena. Such oscillations in the current at resonance frequencies above the applied frequency are possible as a product of the discharge's nonlinear electrical characteristics. An example perturbation to the current density induced by the plasma series resonance can be seen in figure 2.5. In the context of the circuit model established in section 2.2, the electron inertia and collisions correspond to an inductance and a resistance in the plasma bulk, respectively, which form a parallel circuit with the bulk capacitance, i.e., that associated with the bulk electric field, and a series circuit with the nonlinear sheath capacitances, associated with ϕ_{sp} and ϕ_{sg}, respectively (see figure 2.3). Parallel and series circuit resonances are then both possible [147–149]. Typically, the plasma series resonance is the more pronounced resonance feature in low pressure electropositive RF-CCPs, which are considered here and in chapter 5. The PSR can be self-excited in such discharges although the typical PSR resonance frequency is much higher than the driving frequency [96]. The resulting perturbed current waveform of the plasma has a direct impact on the electron heating dynamics [77, 150, 151], as implied in section 2.4 by the relationships between the voltage waveform, discharge current, and the sheath dynamics. This subsequently influences the densities, fluxes, and eventually process rates in industrial applications [152, 153]. Previous studies have demonstrated the electron heating associated with the self-excitation of the PSR significantly enhances the total electron heating [38, 77, 96, 147–168], even accounting for up to half the total electron energy gain as in Ziegler *et al.* [155]. Furthermore, in the kinetic description of heating mechanisms, Schulze *et al.* [77, 154, 156] experimentally confirmed the generation of multiple highly energetic electron beams during a single sheath expansion resulting from the stepwise sheath expansion caused by the PSR oscillations. PSR oscillations have been extensively investigated in geometrically asymmetric discharges, where the asymmetry is a product of the chamber geometry (see

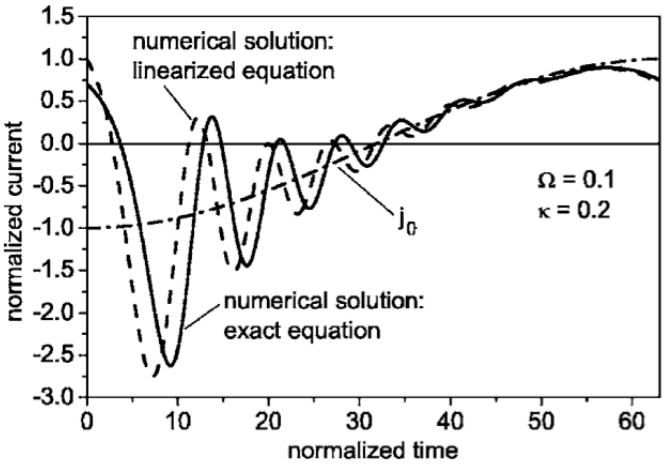

Figure 2.5: Example numerical solution of the normalized PSR current density for the application of a single-frequency voltage waveform. This corresponds to a solution of equation (2.17) for $\Omega = 0.1$ and $\kappa = 0.2$. Solid line is the exact solution; dashed line neglects the nonlinear q_1^2 term; dash-dotted line is the unperturbed current j_0. Figure reproduced from Czarnetzki *et al.*, Phys. Plasmas 13, 123503 (2006) [96] with the permission of AIP Publishing.

$A_p/A_g < 1$ in equation (2.15)), through many experiments, simulations, and theoretical models [44, 77, 96, 147, 150–153, 155–160, 162–167, 169].

As discussed in sections 2.2 and 2.3, however, the application of multiple applied frequencies, as with tailored voltage waveforms, allows a geometrically symmetric discharge to be made electrically asymmetric via the EAE. For example, Donkó *et al.* [162] demonstrated the possibility for PSR oscillations to be self-excited in geometrically symmetric discharges operated by asymmetric dual-frequency voltage waveforms. Therefore, a complete understanding of how the PSR is self-excited and how it affects the electron heating dynamics for geometrically symmetric discharges which use tailored voltage waveforms is necessary when seeking to utilize (or avoid, as may be the case) the PSR oscillations. In this section and in chapter 5, the circuit model described in section 2.2 is expanded upon and examined utilizing PIC/MCC simulations (see subsection 3.3.1) to describe the self-excitation of the PSR and its consequences on the electron power absorption dynamics. First, a traditional model for the self-excitation of the PSR in highly asymmetric discharges is discussed for context in subsection 2.5.1. The circuit model of section 2.2 is then expanded upon to examine the self-excitation of the PSR for other symmetries in subsection 2.5.2. Importantly, it is found that the requirement for the PSR is that the resonance circuit is nonlinear, which is possible in both asymmetric and symmetric multi-frequency discharges, whereas previous works attributed the self-excitation of the PSR to the presence of a discharge asymmetry. Here, the traditional single-frequency PSR is also briefly discussed first for context.

2.5.1 Self-excitation of the plasma series resonance in single-frequency, highly asymmetric discharges

The simplest analytical case for modeling the PSR consists of an electropositive, highly asymmetric ($\varepsilon \ll 1$) discharge operated by a single-frequency ($N = 1$) voltage waveform at low pressure, as demonstrated in Czarnetzki *et al.* [96]. The Debye length and maximum sheath thickness are both assumed to be small compared to the length-scale of the bulk plasma (L_{bulk}). The sheath voltages in this simplified model assume matrix sheaths, as seen in section 2.2, i.e., $\phi_{\mathrm{s}}(t) = -Q_{\mathrm{s}}^2(t)/(2eA^2\varepsilon_0 n_{\mathrm{i0}})$. The strong asymmetry of the discharge is traditionally assumed to be the result of a much higher grounded surface area in the chamber geometry such that $\varepsilon \ll 1$ due to $A_{\mathrm{p}} \ll A_{\mathrm{g}}$. Therefore, the grounded sheath voltage ϕ_{sg} under such conditions can be neglected in the voltage balance, for example in equation (2.5). For the application of a single-frequency waveform of the form $\widetilde{\phi}(t) = \frac{\phi_0}{2}\cos(\omega_{\mathrm{RF}}t)$, where $\omega_{\mathrm{RF}} = 2\pi f$ and $\phi_0 > 0$, this allows the DC self-bias to be analytically determined when $\phi_{sp}(t) = 0$, yielding $\eta = -\frac{\phi_0}{2}$. Therefore, the left-hand-side of the voltage balance can be written as

$$\eta + \widetilde{\phi}(t) = -\frac{\phi_0}{2}\left[1 - \cos(\omega_{\mathrm{RF}}t)\right] = -\phi_0 \sin^2\left(\frac{\omega_{\mathrm{RF}}}{2}t\right). \tag{2.16}$$

While the voltage balance of equation (2.5) neglects the bulk voltage, here it must be included for PSR perturbations to be observed. The determination of ϕ_{b} as described in equations (2.11) and (2.12) is applied here for simplicity. Then, by defining dimensionless quantities, the full voltage balance becomes

$$\sin^2\left(\frac{\Omega\tau}{2}\right) = q^2 - 2\left(\ddot{q} + \kappa_0\dot{q}\right), \tag{2.17}$$

where q is the same as in section 2.2, $\Omega = \frac{\omega_{\mathrm{RF}}}{\omega_0}$, $\tau = \omega_0 t$, and $\kappa_0 = \frac{\nu_{\mathrm{m}}}{\omega_0}$. The dot notation here denotes a derivative with respective to time (i.e., τ, here). The frequency ω_0 is used as a normalization factor here and corresponds to the plasma frequency ω_{pe} at a given plasma density $\bar{n}_{\mathrm{e}}$ reduced by a dimensionless geometric parameter $\chi < 1$:

$$\omega_0 = \chi\omega_{\mathrm{pe}} \text{ where } \chi = \sqrt{\frac{s_{\max}\bar{A}}{L_{\mathrm{bulk}}A_s}} \text{ and } s_{\max} = \sqrt{\frac{2\varepsilon_0\phi_0}{en_{\mathrm{s}}}}, \tag{2.18}$$

where $s_{\max}$ is the maximum sheath extension, $\bar{A}$ is the effective area of the discharge, A_{s} is the surface area of the sheath, n_{s} is the plasma density in the sheath, and $\omega_{\mathrm{pe}} = \sqrt{\frac{e^2\bar{n}_{\mathrm{e}}}{\varepsilon_0 m}}$ is determined as normal. Notably, χ is typically on the order of 10^{-1} as $s_{\max} \ll L_{\mathrm{bulk}}$ but $\bar{A} > A_{\mathrm{s}}$. The normalized current j in the discharge is then $j = \frac{2}{\Omega}\dot{q}$, as hinted at in section 2.2.

Numerical solutions of equation (2.17) for j can then be found (e.g., see figure 2.5) by introducing the ansatz $q = q_0 + q_1$ and $j = j_0 + j_1$, where q_0 and j_0 are from the solution without the bulk term $(\ddot{q} + \kappa_0\dot{q})$, i.e., with no PSR:

$$q_0 = \left|\sin\left(\frac{\Omega\tau}{2}\right)\right| \text{ and } j_0 = -\cos\left(\frac{\Omega\tau}{2}\right)\ \mathrm{sgn}\left(\sin\left(\frac{\Omega\tau}{2}\right)\right). \tag{2.19}$$

Here, sgn(x) is a sign function which is -1 for a negative argument and +1 otherwise, and thus the amplitude of this normalized current is also 1. This current j_0 is also described as the base current typically associated with the application of an RF voltage waveform. Inserting q_0 from equation (2.19) into equation (2.17) creates a non-linear differential equation for the perturbation q_1:

$$\ddot{q}_1 + \kappa_0 \dot{q}_1 - (q_0 + q_1)q_1 = -(\ddot{q}_0 + \kappa_0 \dot{q}_0). \tag{2.20}$$

This equation must be solved numerically (e.g., see figure 2.5). The perturbation from the bulk voltage term leads to high-frequency oscillations in the normalized current that are damped in time by collisions (i.e., the $\kappa_0 \dot{q}_1$ term).

However, determining the resonant frequency of the perturbation analytically is difficult in equation (2.20). To further simplify, equation (2.20) can be linearized by neglecting the q_1^2 term. This creates a damped, non-linear oscillation equation driven by an external force represented by the time derivatives of q_0 on the right-hand-side of equation (2.20). These terms contain a δ-function from the second derivative of q_0, which is further assumed to be the dominant contribution (i.e., $\Omega\delta(t)$ on the right-hand-side of equation 2.20) and thus other terms (e.g., $\kappa_0 \dot{q}_0$) are neglected. The excitation of the PSR oscillations in this case is the sudden change in the sign of the current, e.g., when the sheath transitions from an expanding sheath to a collapsing sheath or vice versa. Notably, this δ-function is closely related to the assumption of a highly asymmetric discharge where the DC self-bias is comparable to the applied voltage amplitude and the grounded sheath is neglected [96]. The inclusion of the grounded sheath voltage is therefore discussed later in this section. Furthermore, by integrating around $\tau = 0$ from -$\Delta\tau$ to + $\Delta\tau$ and noting $q_1(0) = 0$, equation (2.20) is limited by the boundary conditions and reduced to

$$\ddot{q}_1 + \kappa_0 \dot{q}_1 - q_0 q_1 = 0 \text{ with } q_1(0) = 0 \text{ and } \dot{q}_1(0) = \Omega. \tag{2.21}$$

These assumptions notably restrict these calculations to damped oscillations (i.e., $\kappa_0 \geqslant \Omega$). If the first derivative $\dot{q}_1$ in equation (2.21) is then neglected, an ansatz of the form:

$$q_1(\tau) = f_1(\tau) \exp(-\frac{\kappa_0}{2}\tau), \tag{2.22}$$

can be used. Applying this ansatz to equation (2.21) yields

$$\ddot{f}_1 + \widetilde{\Omega}_{\text{PSR}}^2 f_1 = 0 \text{ where } f_1(0) = 0 \text{ and } \dot{f}_1(0) = \Omega, \tag{2.23}$$

$$\widetilde{\Omega}_{\text{PSR}}^2 = -\left(q_0 + \frac{\kappa_0^2}{4}\right) \approx -q_0. \tag{2.24}$$

The oscillation frequency of this equation $\widetilde{\Omega}_{\text{PSR}}$ can thus be correlated to the observed frequency of PSR current oscillations and is notably a function of time via $q_0(\tau)$. The $\kappa_0/4$ term is also typically very small. From equations (2.19) and (2.24), the maximum possible frequency of PSR oscillations can be now be obtained as

$$\widetilde{\Omega}_{\text{PSR}} = \frac{\omega_{\text{PSR}}}{\omega_0} = \sqrt{\sin\left(\frac{\Omega\tau}{2}\right)}, \tag{2.25}$$

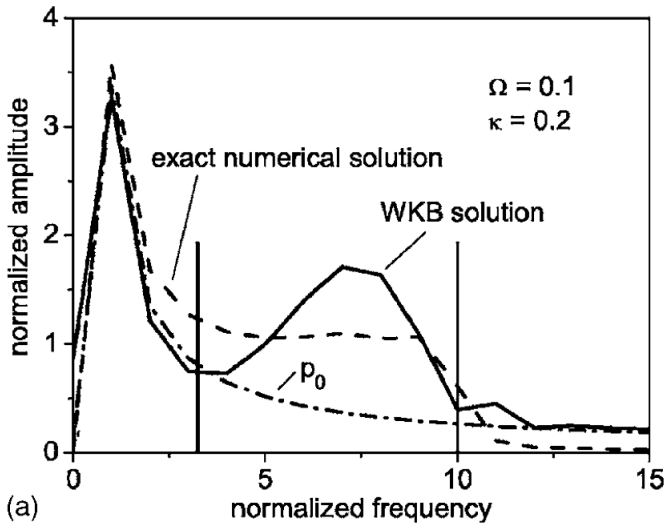

Figure 2.6: Example Fourier spectrum of the current from the self-excitation of the PSR for a single-frequency voltage waveform. Here, $\Omega = 0.1$ and $\kappa = 0.2$. The frequency scale is normalized by the fundamental RF frequency. The Fourier spectra technically exist at discrete intervals, but are shown as continuous lines here for better visibility. The solid line corresponds to a solution using the WKB approximation, while the dashed line is a numerical solution. The spectrum of the unperturbed current j_0 is also shown as a dash-dotted line. The vertical bars indicate the analytically calculated maximum and minimum frequencies for excited PSR oscillations. Figure reproduced from figure 9(a) of Czarnetzki *et al.*, Phys. Plasmas 13, 123503 (2006) [96] with the permission of AIP Publishing.

$$\omega_{\mathrm{PSR,max}} = \omega_0 = \chi\omega_{\mathrm{pe}} = \sqrt{\frac{s_{\mathrm{max}}}{L_{\mathrm{bulk}}}}\omega_{\mathrm{pe}}. \tag{2.26}$$

This implies the frequency of PSR oscillations is dependent on the plasma density through the maximum sheath width s_{max}. Furthermore, it is important to note that the use of applied MHz frequencies in most RF-CCPs, i.e., the criterion $\omega_{\mathrm{pe}} > \omega_{\mathrm{RF}} > \omega_{\mathrm{pi}}$, implies that the excited frequencies are typically much higher than the applied frequencies, i.e., $\omega_{\mathrm{PSR}} > \omega_{\mathrm{RF}}$. Further calculations can also be performed to determine the minimum possible frequency the PSR can be self-excited at. Notably, the current perturbation can be analytically modeled in this way using the first derivative of q_1 once the function $f_1(\tau)$ is determined, for example from applying a Wentzel-Kramers-Brillouin (WKB) approximation as in Czarnetzki *et al.* [96]. A more complete derivation of single-frequency PSR perturbations can also be found in that publication. The description of this simple model is used here to contextualize the model formulated in subsection 2.5.2.

The Fourier (i.e., frequency) spectrum of the discharge current generally reveals that a continuous, broad range of oscillation frequencies are induced by the self-excitation of the PSR, as suggested by figure 2.6. This can be interpreted as a consequence of the time-dependence of the oscillation frequency in equation (2.24). In the case of a single-frequency voltage waveform, however, the excited frequencies are restricted to being odd integer multiples of

the applied frequency due to the mandatory temporal symmetry of the discharge current waveform [169], i.e., the fact that the unperturbed current on time average is zero (e.g., consider integrating j_0 in time in figure 2.5). It should be noted that figure 2.6 is therefore actually a discrete spectra whose peaks have been connected for visibility of the overall spectrum.

However, if more than one frequency is applied to the system, i.e., for $N > 1$, j_0 may not be time-symmetric and this restriction then no longer applies, leading to a more continuous Fourier spectrum. In the case of a dual- or multi-frequency discharge, any of the applied harmonic frequencies may be able to induce PSR oscillations and therefore the frequency spectrum for dual- and multi-frequency ($N \neq 1$) discharges can be even broader than those seen for single-frequency waveforms. The application of higher frequency harmonics can also lead to increases in the plasma density (see chapters 4 and 5) and therefore alterations in the sheath widths. Furthermore, it should be noted that many assumptions in this subsection become untenable for the application of multi-frequency waveforms. In particular, subsection 2.5.2 demonstrates that the sheath dynamics, which have a role in determining the bulk length-scale and the calculation of the electron plasma frequency in the bulk (i.e., ω_{pe} above), are particularly relevant to the self-excitation of the PSR. Additionally, the assumption of a matrix sheath is demonstrated to be insufficient in the case of self-excitation of the PSR in symmetric discharges. Therefore, it is necessary to implement a more detailed model in order to properly investigate the effects of the plasma series resonance in discharges driven by tailored voltage waveforms, as discussed in subsection 2.5.2.

2.5.2 Model for self-excitation of the plasma series resonance in symmetric and asymmetric discharges

Utilizing the voltage balance model laid out in section 2.2, a more realistic representation of the charge voltage relation for each sheath as proposed by Czarnetzki [95] is necessary in order to examine the PSR, which is reliant on the non-linearity of the plasma sheaths to induce a circuit resonance [96]. In place of the quadratic relations of the form $\phi_{\mathrm{s}}(t) = -Q_{\mathrm{s}}^2(t)/(2eA^2\varepsilon_0 n_{\mathrm{i0}})$, this model includes an additional cubic relation to each sheath, yielding [95]

$$\bar{\phi}_{\mathrm{sp}}(t) = -q_{\mathrm{tot}}^2 q^2(t)\left[q(t)(1-a)+a\right], \tag{2.27}$$

$$\bar{\phi}_{\mathrm{sg}}(t) = \varepsilon q_{\mathrm{tot}}^2\left[1-q(t)\right]^2\left[\left[1-q(t)\right](1-b)+b\right], \tag{2.28}$$

where $\bar{\phi}_{\mathrm{sp,sg}}(t) = \phi_{\mathrm{sp,sg}}(t)/\phi_{\mathrm{tot}}$ are the normalized sheath voltage for the powered and grounded electrode sheaths, respectively. Again, the grounded electrode charge-voltage relation is derived using the assumption of a fixed total charge and $q_{\mathrm{sg}} = 1 - q$ (see section 2.2). This cubic ansatz, i.e., equations (2.27) and (2.28), is motivated by a power series approach [95]. As a result, however, two cubic term parameters, named a and b, must be specified in order to describe the behavior of the powered and grounded sheaths, respectively. These parameters depend on the ion density profile in each sheath region and thus the model used to describe the sheath. For example, taking $a, b = 1$ returns the quadratic charge-voltage relations

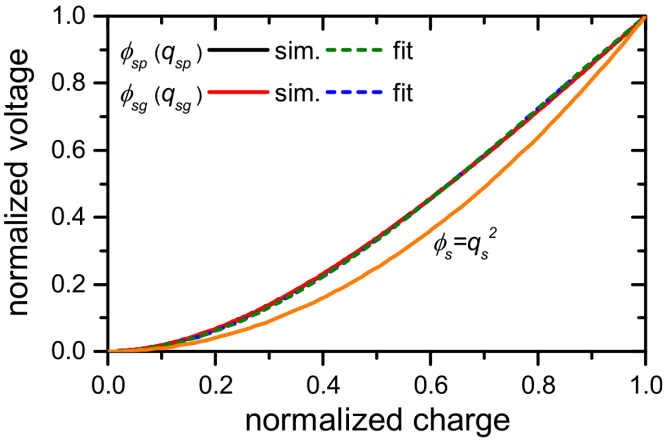

Figure 2.7: Voltage drop across the powered and grounded electrode sheaths, ϕ_{sp} and ϕ_{sg}, respectively, as a function of the charge within the respective sheath obtained in the PIC/MCC simulation (sim.) at 54.24 MHz and obtained from the model functions (equations (2.27) and (2.28)) fitted to the simulation data (fit). Here, $a \approx 1.66$ and $b \approx 1.66$, respectively. A simple quadratic relation is also shown. Figure reproduced from its original publication in Schüngel *et al.*, Physics of Plasmas 22, 043512 (2015) [SE15a] with the permission of AIP Publishing.

seen in section 2.2 and corresponds to assuming a matrix sheath at both electrodes. Cases with $a \neq 1$ and/or $b \neq 1$ allow for one or both of the electrode sheaths to have a cubic contribution. Notably, if both $a = 1$ and $b = 1$, the quadratic (i.e., $q^2(t)$) terms in equations (2.27) and (2.28) cancel one another when they are added together in the full voltage balance, as discussed later in this section.

The charge-voltage relation can therefore potentially strongly deviate from the quadratic relationship, as demonstrated in figure 2.7. Since the non-normalized sheath charges Q and $Q_{\mathrm{tot}} - Q$, for the powered and grounded electrode sheaths, respectively, are determined by the ion density profile $n_{\mathrm{i}}(x)$ and the time-dependent sheath edges $s_{\mathrm{p,g}}(t)$ (see equation (2.3)) and the sheath voltages are proportional to these charges (see equation (2.4)) via Poisson's equation [37], the individual sheath voltages and the charge inside each sheath varies as a function of the RF phase. Any significant deviation from the simple quadratic form can therefore significantly influence the time-dependence of the sheath voltages and must be accounted for to correctly represent the sheath voltages in the model. For example, when a matrix sheath model is used and the bulk voltage is neglected, e.g., equation (2.5), the quadratic terms in the voltage balance cancel one another in symmetric discharges ($\varepsilon = 1$) leaving only a constant term ($\phi_{\mathrm{tot}} q_{\mathrm{tot}}$) on the right hand side of the voltage balance. This effectively implies that the sheaths act linearly in the full voltage balance in a symmetric discharge and act non-linearly in asymmetric discharges, which is inconsistent with the individual charge-voltage relations obtained from simulations, e.g., figure 2.7. This is why the model of section 2.2 is insufficient for examining the PSR in symmetric RF-CCPs. Thus, clearly, $a \neq 1$ and $b \neq 1$.

These cubic parameters a and b for the cases discussed in chapter 5 are calculated from

fits of ϕ_{sp}/q_{tot}^2 as a function of q and ϕ_{sg}/q_{tot}^2 as a function of $q_{sg} = 1 - q$ (i.e., normalizing equations (2.27) and (2.28)) to the normalized charge-voltage relation resulting from the simulations presented in subsection 3.3.1. As seen in the example in figure 2.7, these fits are in excellent agreement with the simulated charge-voltage relation. The geometrically symmetric discharges of chapter 5 typically have cubic parameter values in the range $a \approx 1.5 - 1.7$ with $b \approx a$. The charge-voltage relations obtained from the simulations are found by i) taking the difference of the potential between the momentary plasma sheath edges defined by the criterion of [170] and the electrode surfaces and ii) adding up all net charges in these momentary sheath regions.

A discharge asymmetry determined by $\varepsilon \neq 1$ is often believed to be necessary for the self-excitation of the PSR in RF-CCPs [96, 159, 167, 169]. Most previous studies (before [SE15a, SE15b]) of the self-excitation of PSR oscillations involve strongly geometrically asymmetric chamber configurations, such that the grounded surface area is relatively large ($A_p \ll A_g$) and $\varepsilon < 1$. Studies assuming a quadratic charge-voltage relation for the RF sheaths, furthermore, only find PSR oscillations to be excited in asymmetric ($\varepsilon \neq 1$) discharges, as the quadratic nonlinearity with q in the voltage balance disappears, as in equation (2.5) for $\varepsilon = 1$. In cases utilizing multi-frequency voltage waveforms, however, the situation is more versatile. RF-CCPs driven by asymmetric voltage waveforms can be geometrically symmetric ($A_p = A_g$) but made electrically asymmetric ($\varepsilon \neq 1$) due to the application of the EAE (i.e., either the AAE or SAE, or both). Recent investigations, including the work shown here and in chapter 5, suggest that PSR oscillations are also possible in symmetric $\varepsilon = 1$ discharges [SE15a], but this appears to be reliant on retaining the nonlinearity with q in the voltage balance by including higher order terms like the cubic contribution used above and by including the time-dependent bulk voltage $\phi_b(t)$ from section 2.2.

The bulk voltage drop is traditionally necessary in the analysis of the self-excitation of PSR oscillations because the electron inertia (inductance) and electron momentum transfer collisions (resistance) in the bulk plasma play a key role. As demonstrated in chapter 5, the temporal variation of the bulk voltage terms must be taken into account to properly reproduce the observed current waveforms. The time-dependent, normalized bulk voltage drop $\bar{\phi}_b = \phi_b/\phi_{tot}$ utilizes the description of the bulk voltage discussed in section 2.2 alongside the electric field configuration from [96] to obtain

$$\bar{\phi}_b(t) = -2\beta^2(t)\left[\ddot{q}(t) + \kappa\dot{q}(t)\right]. \tag{2.29}$$

The dot notation of equation (2.29) refers to a derivative with respect to the RF phase (i.e., time t). The parameter $\kappa = \nu_m/\omega_{RF}$ is a characterization of the collisionality and therefore corresponds to a damping term in equation (2.29) for the PSR oscillations. The "bulk parameter" β is normally taken as a constant and is typically small for low pressure electropositive plasmas ($\beta \ll 1$) [96]. In this model, however, β is allowed to vary with time, such that it is defined as

$$\beta(t) = \frac{\omega_{RF}}{\bar{\omega}_{pe}(t)}\sqrt{\frac{L_{bulk}(t)}{s_{p,max}}}, \tag{2.30}$$

which depends on the ratio of the bulk length $L_{bulk}(t)$ to the maximum powered electrode sheath extension $s_{p,max}$ and the spatially averaged but temporally varying inverse electron

plasma frequency:

$$\bar{\omega}_{\mathrm{pe}}^{-1} = \sqrt{\frac{\varepsilon_0 m}{e^2 L_{\mathrm{bulk}}(t)} \int_{s_{\mathrm{p}}(t)}^{d-s_{\mathrm{g}}(t)} n_{\mathrm{e}}^{-1}(x,t)dx}. \tag{2.31}$$

Thus, the bulk parameter is calculated by integrating the inverse electron density profile over the bulk length $L_{\mathrm{bulk}}(t)$ between the momentary positions of the plasma sheath edges. The first term in equation (2.29) represents an inductance due to electron inertia, while the other represents a resistance from electron momentum transfer collisions. For the cases discussed in chapter 5 and in this section, $\beta(t)$ is determined explicitly from PIC/MCC simulation data as a function of t. The details of these simulations can found in subsection 3.3.1.

Figure 2.8 demonstrates the typical behavior of the electron density profile and the resulting bulk parameter $\beta(t)$ for the case of a single-frequency PIC/MCC simulation (subsection 3.3.1). In this section and in chapter 5, the RF phase variable ($\varphi = 2\pi f t$) is used in place of time t in the figures due to the differing RF periods between waveforms of differing applied frequencies (i.e., f). Notably, β varies significantly across the RF period and is maximum at times of complete sheath collapse at either the powered or grounded electrodes. The reason for this, as hinted at in section 2.2, is that the bulk region sweeps over one sheath's electron density profile. Since the electron density follows the ion density, which decreases towards the electrodes due to acceleration of ions in the sheath electric field at approximately constant flux, the electron density similarly decreases towards the electrodes. The local electron plasma frequency, therefore, also decreases and the effective inverse electron plasma frequency in equation (2.31) increases at times of sheath collapse. This leads to an oscillatory behavior with $\beta(t)$ increasing during times of either electrode's sheath collapse and decreasing at intermediate RF phases.

In the case of a single-frequency waveform, this oscillation of $\beta(t)$ is at approximately twice the applied frequency of the voltage waveform, as in figure 2.8, but this is not necessarily the case for time-asymmetric waveforms such as multi-frequency waveforms, as seen in figure 2.9. As the sheaths can remain fully expanded or collapsed for relatively large fractions of the RF period for some multi-frequency waveforms like the example in figure 2.9, β, correspondingly, will not vary much during these RF phases. However, the increase in β during the sheath collapse of such multi-frequency waveforms is much more significant due to the relatively short times of sheath collapse [25]. Additionally, when utilizing a higher frequency single-frequency waveform such as the 54.24 MHz case in figure 2.9, a reduced absolute value and variation of $\beta(t)$ is observed because the plasma density and therefore the effective electron plasma frequency are larger. Such waveforms also spend a comparably longer time, on RF period accumulated average, in the phases of sheath collapse when compared against lower applied frequencies.

The final model equation describing the self-excitation of PSR oscillations can now be constructed by combining equations (2.27), (2.28), and (2.29) into equation (2.1) after

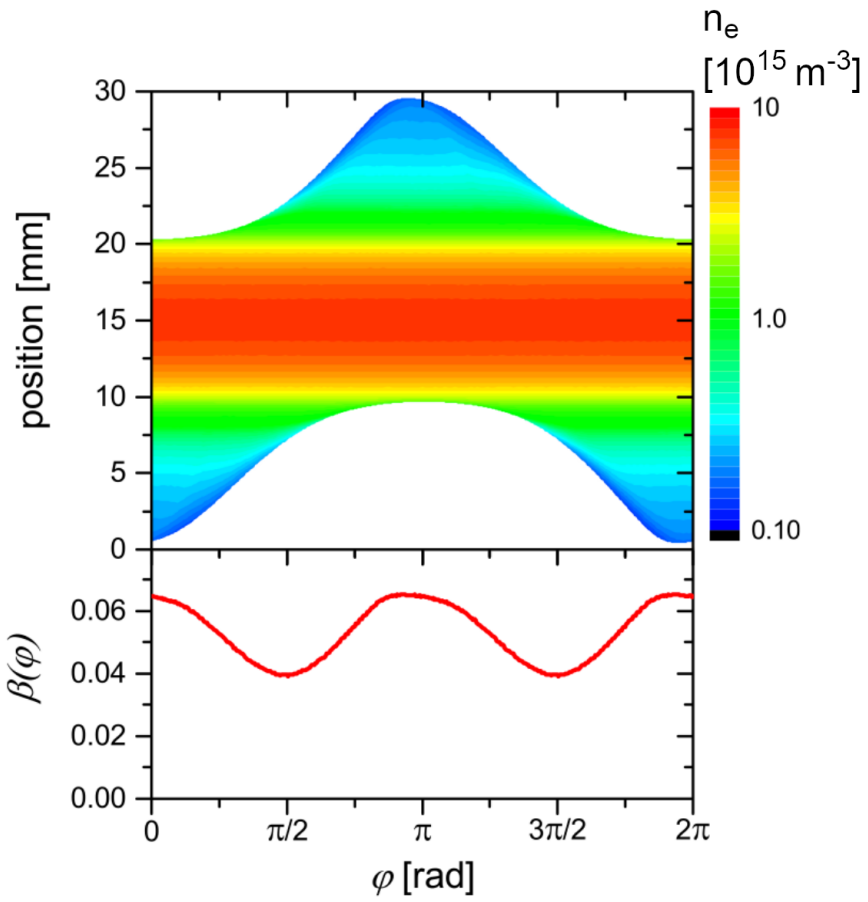

Figure 2.8: (Top) Spatio-temporal distribution of the electron density within the plasma bulk determined by the plasma sheath edges in the case of a single-frequency PIC/MCC simulation. The color scale is logarithmic. (Bottom) The bulk parameter β as a function of time in the RF period (represented by $\varphi = 2\pi ft$) calculated from the simulation data. The simulation conditions were: Ar, 3 Pa, $d = 30$ mm, 13.56 MHz, $\phi_{\mathrm{tot}} = 800$ V. Figure provided from its original publication in Schüngel *et al.*, Plasma Sources Sci. Technol. 24, 044009 (2015) [SE15a].

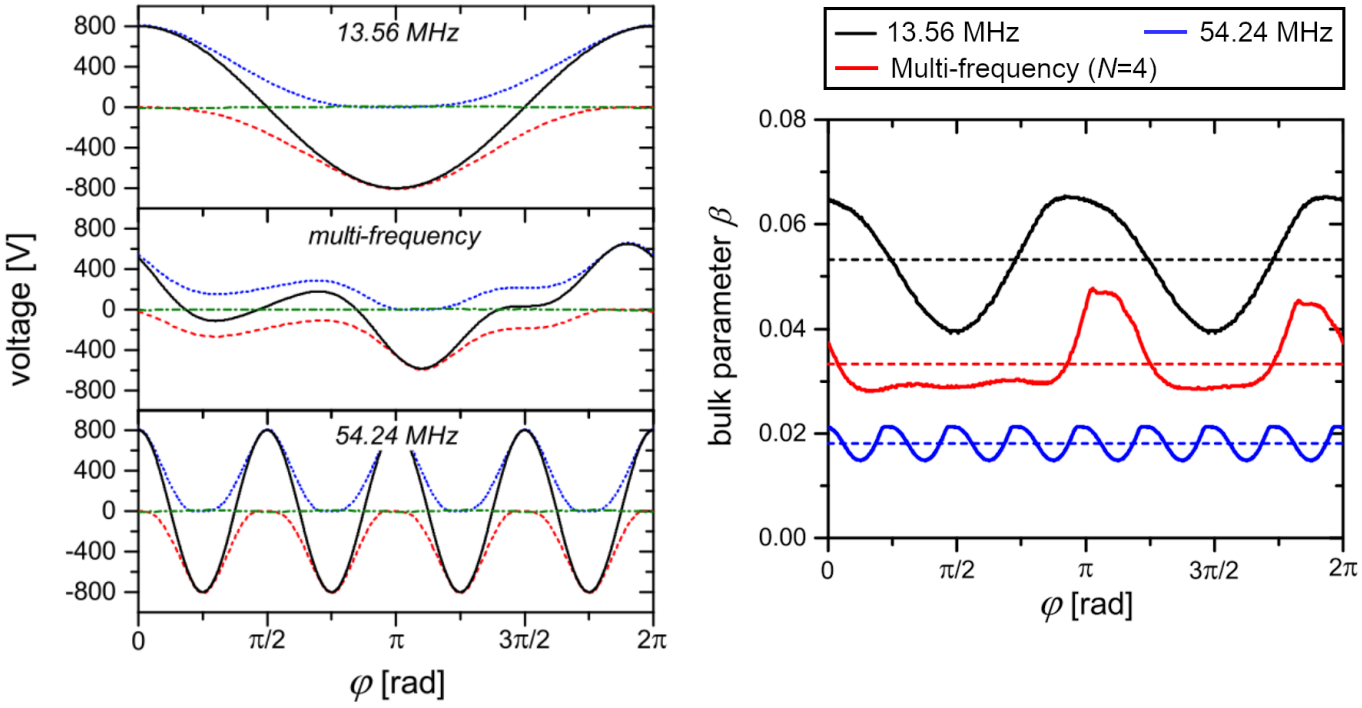

Figure 2.9: (Left) Total voltage drop between the electrodes, i.e., $\widetilde{\phi}(t) + \eta$ (black solid line), and the individual voltage drops across the powered electrode sheath (red dashed line), the grounded electrode sheath (blue dotted line), and the plasma bulk (green dash-dotted line), respectively as a function of time in the Rf period (represented by $\varphi = 2\pi f t$). The discharge is driven by a 13.56 MHz (top), a multi-frequency (equation (1.1)) with $N = 4$ harmonics (middle), and a 54.24 MHz (bottom) voltage waveform, respectively. (Right) Bulk parameter, β, as a function of the time in the RF period for the 13.56 MHz (black), multi-frequency (red), and 54.24 MHz (blue) waveforms specified above. The dashed lines correspond to RF period averaged values. The multi-frequency waveform is described by $N = 4$, $\theta_3 = 0°$, and $\theta_{2,4} = 90°$ in equation (1.1). For all waveforms, $\phi_{\text{tot}} = 800$ V and harmonic amplitudes are determined by equation (3.1). Published in Schüngel *et al.* [SE15a] as figures 1 (left) and 3 (right). Figure reproduced from its original publication as figures 1 (left) and 3 (right) in Schüngel *et al.*, Physics of Plasmas 22, 043512 (2015) [SE15a] with the permission of AIP Publishing.

normalization by ϕ_{tot}:

$$\begin{aligned}\bar{\eta} + \bar{\tilde{\phi}}(t) = &- q_{\text{tot}}^2 q^2(t)\left[q(t)(1-a)+a\right] \\ &- 2\beta^2(t)\left[\ddot{q}(t) + \kappa\dot{q}(t)\right] \\ &+ \varepsilon q_{\text{tot}}^2\left[1-q(t)\right]^2\left[\left[1-q(t)\right](1-b)+b\right].\end{aligned} \tag{2.32}$$

This resulting ordinary, nonlinear, second-order differential equation is unfortunately cumbersome to work with, as an analytical approximation for arbitrary values of a, b, ε, and $\beta(t)$ cannot be found. That said, it can be solved for $q(t)$ numerically [171].

The system described by equation 2.32 is effectively an oscillator driven by an external force ($\bar{\eta} + \bar{\tilde{\phi}}(t)$) with a restoring force caused by the inertia of the bulk electrons (the $\beta(t)\ddot{q}(t)$ term) and a damping term from the momentum loss of electrons due to collisions with the background gas (the $\kappa\dot{q}(t)$ term). Notably, the resonance frequency of this oscillator (ω_{PSR}) may potentially vary with time but will be significantly above the applied driving frequencies, recalling that $\bar{\tilde{\phi}}(t)$ has multiple harmonic terms in the case of multi-frequency waveforms, i.e., equation (1.1). Efficient coupling of energy from the external driver (i.e., the voltage waveform) to the series circuit is therefore possible, but only in the case where the oscillator is nonlinear. This explains the absence of observed PSR oscillations for models where $\varepsilon = 1$ (symmetric discharges) and $a, b = 1$ (the quadratic charge-voltage relation is assumed), as the q^2 nonlinearity cancels out in equation (2.32) and the oscillator becomes linear with q. The oscillator will be nonlinear for any other combination of a, b, and ε, even in the case where the variation in $\beta(t)$ is negligible. The nonlinearity of the right-hand-side of equation (2.32) is therefore an essential feature for the self-excitation of PSR oscillations. It should be noted that the bulk voltage drop ϕ_{b} must be included in equation (2.32) for this voltage balance to become a differential equation and thus an oscillator, such that the PSR can easily be turned on and off in this model by including or neglecting the ϕ_{b} terms.

The PSR oscillation features are often most visible in the current waveforms for discharges which undergo this self-excitation process, but the effects are also important for electron power absorption dynamics as pointed out in section 2.4. For example, figure 2.10 shows solutions of the normalized electron current density, $\bar{j}(t) = -\dot{q}$, to help visualize the effect of the different parameters on the self-excitation of the PSR. Here, q_{tot} is calculated from the symmetry parameter, ε, and the extrema of the applied voltage waveform, $\tilde{\phi}_{\text{max,min}}$, via equation (2.7) of this work, as performed in reference [37]. The normalized applied voltage waveform is taken to be a single-frequency case, such that $\bar{\tilde{\phi}}(t) = \cos(2\pi f t)$. The bulk parameter is set as a constant $\beta = 0.1$ in figures 2.10(a)-(d), and is assumed to vary as $\beta(t) = 0.1\left[1 + 0.5\cos(4\pi f t)\right]$ in figures 2.10(e)-(f). This variation of $\beta(t)$ is used here as it resembles $\beta(t)$ from the PIC/MCC simulation (e.g., figure 2.8). Figure 2.10 demonstrates the possibility for the PSR oscillations to be switched on and off by including and neglecting the bulk voltage drop ϕ_{b}, respectively. The other parameters used in figure 2.10 are listed in table 2.1. The cubic parameters a and b are set either to 1.0 (matrix sheath) or 1.5, since typically fits of equation (2.27) to normalized PIC/MCC simulation data yield $a \approx 1.5$ (see figure 2.7 also). The shape of each sheath's density profile $n_{\text{i}}(x)$ is assumed to not be drastically different such that a and b are equal, which is justified since the difference between a and b

Table 2.1: Values of the model parameters used for each solution of equation (2.32) shown in figure 2.10. Originally published in Schüngel *et al.*, Plasma Sources Sci. Technol. 24, 044009 (2015) [SE15b].

Figure	ε	$\bar{\eta}$	q_{tot}	a, b	β	κ
2.10(a)	1.00	0.00	1.00	1.5	0.10	1.0
2.10(b)	0.50	-1/3	1.15	1.0	0.10	1.0
2.10(c)	0.50	-1/3	1.15	1.5	0.10	1.0
2.10(d)	0.01	-0.98	1.41	1.0	0.10	1.0
2.10(e)	1.00	0.00	1.00	1.0	$\beta(t)$	1.0
2.10(f)	1.00	0.00	1.00	1.5	$\beta(t)$	1.0

$\beta(t) = 0.1\,[1 + 0.5\cos(4\pi f t)]$ for figures 2.10(e) and (f).

in the simulations is less than one percent. For the cases discussed here and in chapter 5, only geometrically symmetric ($A_{\mathrm{p}}/A_{\mathrm{g}} = 1$) discharges are considered, such that any deviation of ε from unity is due to the EAE from the applied voltage waveform. Notably, these are significant simplifications, as more complex discharges which are geometrically asymmetric, magnetized, or utilize electronegative gases may need to account for additional effects such as those mentioned in sections 2.2, 2.3, and 2.4. In particular, magnetized plasmas, such as those used in magnetron sputtering, will likely have differing charge-voltage relations for each sheath ($a \neq b$) if the magnetic field configuration/strength is not equal near both electrodes [172]. As mentioned in section 2.2, RF-CCPs operating in the DA-mode can also have significant drift electric fields in the bulk which affect $\phi_{\mathrm{b}}(t)$ and can constitute a significant displacement current (see section 2.4 and the results in chapter 6). These considerations are neglected for the work presented here and in chapter 5, but should reinforce the necessity of such investigations for the relevant discharges.

A number of key concepts can be drawn from the parameter variation in figure 2.10 and table 2.1. In the case of a symmetric discharge ($\varepsilon = 1$), the self-excitation of PSR oscillations cannot occur if β is constant even when including the cubic components of the charge-voltage relations (e.g., $a = b = 1.5$), as in figure 2.10(a). The shape of the unperturbed current waveform (the red dashed lines in figure 2.10) for $\varepsilon = 1$ is influenced by changing a and b, though, as in figures 2.10(e) and 2.10(f). Intermediate asymmetries, such as $\varepsilon = 0.5$, are also insufficient for the self-excitation of PSR oscillations if quadratic charge-voltage relations are used ($a = b = 1$), as in figure 2.10(b). PSR oscillations can be observed when the bulk voltage drop is included with a fixed β, the charge-voltage relation exhibits a cubic component, and the discharge is not symmetric, i.e., $\varepsilon \neq 1$ (figure 2.10(c)). This results from the linearity of $\bar{\phi}_{\mathrm{sp}} + \bar{\phi}_{\mathrm{sg}}$ with q becoming a nonlinear (cubic) relationship when $a = b \neq 1$ and $\varepsilon \neq 1$. Notably, this implies that the cubic nonlinearity from $a = b = 1.5$ is also insufficient on its own to cause self-excitation of PSR oscillations. This nonlinearity is crucial, however, for the correct modeling of the current waveform and PSR oscillations and is particularly relevant for weak and intermediate asymmetries (for example, $0.5 \geqslant |\varepsilon - 1| \geqslant 0$) where the quadratic nonlinearity in $\bar{\phi}_{\mathrm{sp}} + \bar{\phi}_{\mathrm{sg}}$ is small. For strongly asymmetric discharges, as in figure

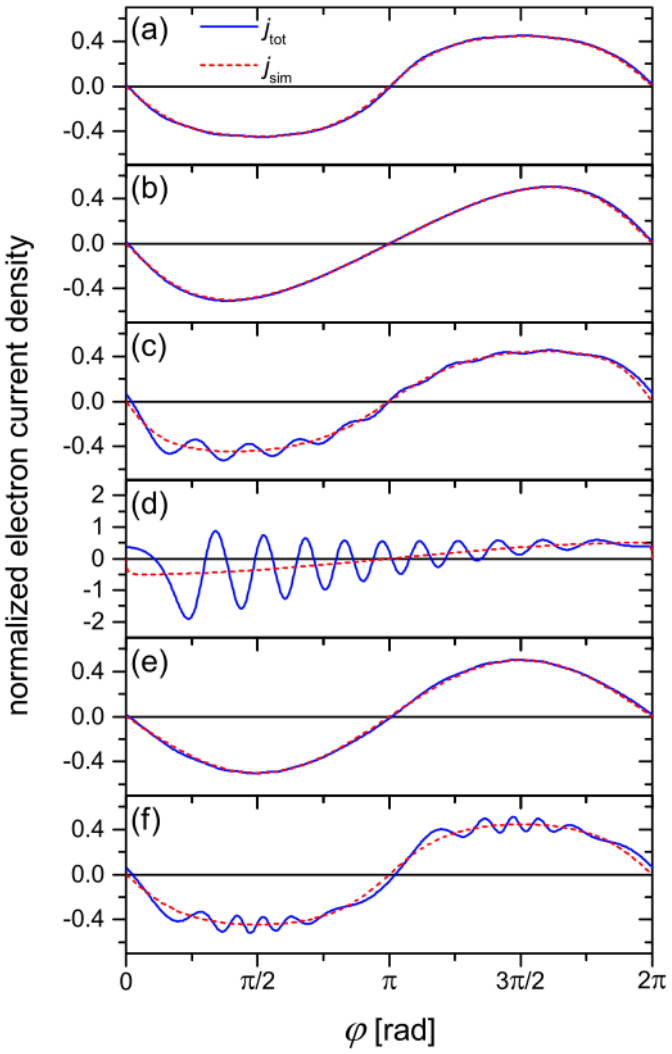

Figure 2.10: Normalized electron current density obtained using numerical solutions of the model PSR equation (2.32). In each plot the solution including (j_{tot}, blue solid line) and neglecting (j_{sim}, red dashed line) the voltage drop across the plasma bulk are shown. In all cases a single-frequency voltage waveform is applied. All other parameters are specified in table 2.1. Figure provided from its original publication in Schüngel *et al.*, Plasma Sources Sci. Technol. 24, 044009 (2015) [SE15b].

2.10(d) where $\varepsilon = 10^{-2}$ and $a = b = 1$, the amplitude of the PSR oscillations in the current waveform are significantly larger and $\bar{\phi}_{\mathrm{sp}} + \bar{\phi}_{\mathrm{sg}}$ is nonlinear regardless of the choice of a and b. This is effectively equivalent to neglecting ϕ_{sg} (equation 2.27) in the voltage balance as $\varepsilon \ll 1$ means that $\phi_{\mathrm{sg}} \ll \phi_{\mathrm{sp}}$, such that the quadratic nonlinearity in $\bar{\phi}_{\mathrm{sp}}$ does not cancel out. The unperturbed current waveforms also noticeably have a steep gradient at $t = 0$ in figure 2.10, shortly before PSR oscillations are observed in the perturbed current waveforms. Therefore, PSR oscillations are self-excited, or "driven" if the previous analogy of the PSR equation (eqn. 2.32) to an oscillator is used, when the absolute value of $\ddot{q} = \dot{\bar{j}}$ is largest. This corresponds to the time where the potential energy in the oscillator is largest and is associated with RF phases where one sheath is starting to expand (e.g., compare $t = 0$ for figures 2.10 and the $N = 1$ voltage waveform in figure 3.12 in section 3.4). The PSR can also be self-excited in symmetric discharges ($\varepsilon = 1$), but only when β exhibits a dependence on the RF phase and the charge-voltage relations deviate from quadratic behavior. Similarly to $a = b \neq 1$, $\beta(t)$ is an insufficient condition by itself for the self-excitation of PSR oscillations, as seen in figure 2.10(e). The cubic nonlinearity of $\bar{\phi}_{\mathrm{sp}} + \bar{\phi}_{\mathrm{sg}}$ is therefore a necessary condition for exciting the PSR in symmetric discharges. The self-excitation of PSR oscillations for symmetric discharges is then a product of the combination of these two effects [SE15a]. This situation is analogous to describing the discharge as a complicated RF-driven RLC circuit with nonlinear capacitance and a time modulated inductance which results in an electrical resonance, i.e., PSR oscillations.

For this model of the electron conduction current to be compared with that obtained from the output of the PIC/MCC simulations utilized in chapter 5 and presented in subsection 3.2.1, the ε, $\bar{\eta}$, and β parameters used in the model are obtained from the simulation data (see equations (2.30) and (2.31) for $\beta(t)$). The cubic parameters a and b are similarly obtained from fits of the normalized charge-voltage relations to the simulation results for each case, such as those seen in figure 2.7 of this section. The normalized collision frequency is estimated to be $\kappa \approx 2.4$ and corresponds to a relatively high momentum transfer collision frequency of $\nu_{\mathrm{m}} \approx 2.0 \times 10^8$ s^{-1} for an argon gas pressure of 3 Pa. This value is consistent with the findings of Lafleur *et al.* [173] under similar conditions and is in good agreement with the resulting damping with the attenuation of the PSR oscillations observed in the simulations. The amplitude of the non-normalized current density is determined in the model by multiplying the normalized current density $\bar{j}(t)$ with the value of $e\omega_{\mathrm{RF}} \int_0^{s_{\max}} n_{\mathrm{i}}(x)dx$ obtained from the simulations.

The effects that the PSR oscillations have on the electron power absorption dynamics are discussed here and in chapter 5 using only relative values. The dissipated electric power is generally proportional to the current squared (j^2). This model, however, allows for a distinction between electron heating caused by PSR oscillations referred to as nonlinear electron resonance heating (NERH), P_{PSR}, and electron heating without the presence of the PSR, P_{sim}, by neglecting any current perturbations:

$$\int_0^t P_{\mathrm{sim}}(t')dt' \propto \int_0^t j_{\mathrm{sim}}^2(t')dt' \tag{2.33}$$

$$\int_0^t P_{\mathrm{tot}}(t^{'})dt^{'} \propto \int_0^t j_{\mathrm{tot}}^2(t^{'})dt^{'} \tag{2.34}$$

$$\int_0^t P_{\mathrm{PSR}}(t^{'})dt^{'} \propto \int_0^t \left[j_{\mathrm{tot}}^2(t^{'}) - j_{\mathrm{sim}}^2(t^{'})\right] dt^{'} \tag{2.35}$$

The total current density $j_{\mathrm{tot}} = j_{\mathrm{sim}} + j_{\mathrm{PSR}}$ and the unperturbed current density j_{sim} can be obtained in the model by turning the bulk voltage term in the voltage balance (equation (2.32)) on and off, respectively. Similarly, $P_{\mathrm{tot}} = P_{\mathrm{sim}} + P_{\mathrm{PSR}}$ defines P_{PSR} in equation (2.35) and includes both terms of $j_{tot}^2 - j_{\mathrm{sim}}^2 = j_{PSR}^2 - 2j_{\mathrm{sim}}j_{\mathrm{PSR}}$ as they both depend on the PSR current density j_{PSR}.

The electron power absorption dynamics for the cases in chapter 5 is dominated by the α-mode (see section 2.4) and therefore the electron heating occurs primarily adjacent to each electrode during the sheath expansion phases of the respective sheath. As noted above in this section, the expansion phases of the powered electrode sheath are associated with an increase of the charge in that sheath, i.e., $\ddot{q} > 0$ is significant and $\dot{q} \geqslant 0$, and the acceleration of electrons towards the grounded electrode (i.e., in $+\hat{x}$) which is defined as a negative current density. Conversely, the expansion phases of the grounded electrode sheath cause a reduction in q, i.e., $\ddot{q}$ is again significant and $\dot{q} \leqslant 0$, and are related to a positive (i.e., electron acceleration in -$\hat{x}$) electron current density. The electron power absorption can then be separated into two spatial regions, i.e., the powered electrode half space ($0 \leqslant x \leqslant d/2$) and the grounded electrode half space ($d/2 \leqslant x \leqslant d$), by utilizing the sign of the current density in each region and the Heaviside function Θ:

$$\int_0^t P_{\mathrm{p}}(t^{'})dt^{'} = \int_0^t P(t^{'})\Theta[-j(t^{'})]dt^{'} \tag{2.36}$$

$$\int_0^t P_{\mathrm{g}}(t^{'})dt^{'} = \int_0^t P(t^{'})\Theta[j(t^{'})]dt^{'} \tag{2.37}$$

Furthermore, equations (2.36) and (2.37) are applicable to the total electron heating, P_{tot}, and the individual electron heating components, P_{PSR} and P_{sim}, by substituting the respective P and j from equations (2.33)-(2.35). The PIC/MCC simulations can also output the electron heating rate $P(x,t)$, where any electron cooling is neglected, which can be spatially integrated to obtain the accumulated electron heating in each half space region (see subsection 3.2.1). Comparisons of the simulations and the above model are used in chapter 5 to investigate the influence of PSR self-excitation on the symmetry of the electron heating in RF-CCPs.

2.6 Theory of secondary electron emission in capacitively coupled plasmas

Secondary electron emission (SEE) processes, where an electron is emitted due the interaction between the surface and a charged particle (usually a positive ion) [174], are an

essential plasma-surface interaction and a part of the electron power absorption dynamics which must be carefully considered and understood. Critically, SEE strongly depends on the electrical and physical properties of the surface material [175–182] and is, in particular, known to be significantly different for pure metals versus metals with deposited thin oxide films in certain incident particle energy ranges, as discussed by Phelps *et al.* [183]. These differences and their causes, alongside other possible dependencies such as with the shape of the surface profile, are further examined and hypothesized in chapter 7, while here the theoretical model behind the relevant SEE processes is described.

SEE can be categorized into kinetic or quantum processes depending on the incident particle energy. At high incident energies (> 100 eV), kinetic processes are the dominant method of secondary electron ejection from a surface [144, 184–187]; in particular, the release of bound electrons from the atoms of the surface or interior of the surface by transfer of kinetic energy to the surface appears to be the most probable kinetic ejection process for ions with energies between about 100 eV and 1000 eV [144]. It should also be noted that incident particles of such energies can also lose their kinetic energy to elastic vibrations in the solid (i.e., phonons) [188] or to sputtered atoms [189]. This kinetic ejection process is also well-known to have dependence on the angle of incidence, i.e., the angle an incident particle's velocity makes with the normal of the surface, with larger angles corresponding to higher SEEC values [184–187]. Notably, if the incident particle energy is very low, kinetic emission cannot occur due to the lack of kinetic energy. Therefore, at very low incident energies, like those seen in the results of chapter 7, SEE proceeds via quantum mechanical interactions between the potentials and quantum states of the surface material and the incident particle. Specifically, these interactions, known as resonance and Auger processes [144, 175, 190] cause a secondary electron to be emitted from the surface through one of two potential paths (see section 2 of [144]): i) Auger neutralization of an ion, or ii) resonance neutralization of an ion, creating a metastable atom, followed by Auger de-excitation of the metastable. Both here and in chapter 7, the theoretical model of quantum mechanical SEE for metals presented by Hagstrum [144] is considered for the case of low energy positive incident ions, as the incident ions in the experimental results of chapter 7 are assumed to have energies < 100 eV due to the high collisionality in the electrode sheaths at high pressures (100-200 Pa). The relevant parts of this complicated model are only briefly summarized here as the results of chapter 7 cannot be quantitatively correlated back to this model itself (see subsection 3.2.4). Instead, this model is used to provide conceptual context for the hypotheses postulated in chapter 7 in order to explain the observed changes in the measured γ-mode excitation across different aluminum (clean metal) and aluminum oxide (semiconductor) surfaces with varying surface roughness.

The incident angle dependence of kinetic SEE is, however, relevant to the discussions of chapter 7 in the context of the possibility for the quantum SEE process to also depend on the incident particle angle (here and in chapter 7). As mentioned above, the incident angle of an incoming particle, denoted as θ_{inc}, is measured relative to the normal of the surface, such that this angle is defined to be zero when the particle moves normal to the surface, i.e., directly towards it. The probability for a surface electron to escape via transfer of kinetic energy (i.e., the kinetic SEEC) is then maximized for "glancing" incident angles where a positive ion (e.g.,

He^+) is traveling nearly parallel to the surface interface, due to the reduced distance through the surface material an energized electron needs to travel to escape the surface. This can be thought of as a transfer of kinetic energy from the incident particle to an electron in the surface material, which must then escape the electric potential well created from the surface's density of states. Overcoming this potential well is easiest for surface electrons which are i) in a state located closer to the surface and ii) have velocity (after the transfer of kinetic energy) directly along the normal, away from the surface. In the case of a flat surface profile (i.e., $S(\vec{x})$ = constant in section 7.2), the incident angle dependence can be modeled as a secant function with a minimum SEEC value at normal incidence ($\gamma(\theta_{\text{inc}} = 0) = \gamma_0$) [184–187]:

$$\gamma(\theta_{\text{inc}}) = \gamma_0 \sec(\theta_{\text{inc}}). \tag{2.38}$$

The SEEC therefore has the highest probability of emitting one or more secondary electrons for an incident particle hitting the surface along the direction parallel to the surface (i.e., $\theta_{\text{inc}} = 90°$). The possibility of a similar incident angle dependence, where the SEEC increases for increasingly "glancing" angles, is considered for quantum SEE processes below and in chapter 7. It should be noted, however, that the reasons behind such incident angle dependence are very different for quantum SEE processes, where transition rates between the relevant states and the time an incident particle (ion) spends at a certain distance from the surface become the more significant factors.

The primary basis for Hagstrum's model [144] is Fermi's golden rule, which describes the transition rate (probability of transition per unit time) from an energy eigenstate of one quantum system to a group of energy eigenstates in a continuum as a weak perturbation. In the case of secondary electron emission from a single incident ion, this corresponds to a transition from a single eigenstate of the ion to the group of eigenstates described by the continuous density of states ($N(\epsilon)$, with ϵ being electron energy) of the surface material, or vice versa. As a result of this rule, only adiabatic processes are considered and thus energy conservation arguments are essential for explaining different electron ejection processes. These ejection processes occur in the framework presented in figure 2.11, where an initial electron configuration is described by the density of states in the surface's conduction band ($N_{\text{c}}(\epsilon)$) and the surface's potential profile. As an ion approaches the surface, notably bringing its own potential profile closer to that of the surface material, excitation of one of the SEE processes noted above occurs at a certain distance z between the surface and the ion. This produces an excited electron inside the surface material, which has not yet escaped the surface. The distribution of excited electrons from many of these interactions is described by $N_{\text{i}}(\epsilon_{\text{k}})$, which is notably different depending on the mechanism of electron ejection, as discussed below. The probability of such an excited electron escaping the surface, denoted by $P_{\text{e}}(\epsilon_{\text{k}})$, then depends on the direction of its escaping velocity vector relative the surface normal. Notably, Hagstrum demonstrates that emitted electron velocities are centered about the normal to the surface due to a loss of energy along the direction of the surface normal when the electron leaves the surface [144]. Effectively, this causes a refraction of escaping electrons towards a direction parallel to the surface, and thus only a limited range of angles below the associated critical angle (where the refracted electrons travel parallel to the surface), defined relative to the surface normal, will allow the electrons to leave the surface. $P_{\text{e}}(\epsilon_{\text{k}})$ is then determined by integrating the probability to escape at a specific angle $P_{e,\Omega}(\theta, \epsilon_{\text{k}})$ over all angles which allow

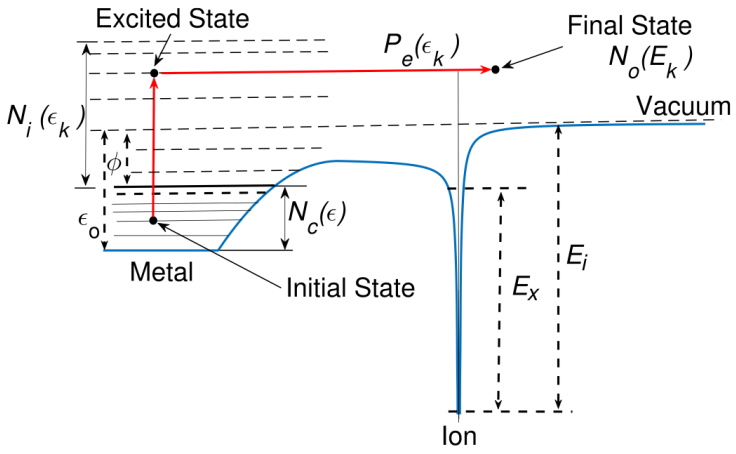

Figure 2.11: Visualization of Hagstrum's theorectical approach. Here, $\phi = \phi_{\mathrm{W}}$ is the work function, ϵ_0 is the metal potential well depth, E_{i} and E_{x} are the ionization and excitation energies of the ion, respectively. $N_{\mathrm{c}}(\epsilon)$ corresponds to the initial density of states of electrons in the conduction band while $N_{\mathrm{i}}(\epsilon_{\mathrm{k}})$ is the energy distribution of electrons that have been excited by a given process. $P_{\mathrm{e}}(\epsilon_{\mathrm{k}})$ is the probability that an excited electron escapes the metal. $N_0(E_{\mathrm{k}})$ is the energy distribution of the escaped electrons. In the text, ϵ corresponds to the initial electron energy and ϵ_{k} and E_{k} correspond to the energy of the excited and escaped electrons, respectively. Figure provided from Daksha *et al.*, Plasma Sources Sci. Technol. 28, 034002 (2019) [175]. ©IOP Publishing. Reproduced with permission. All rights reserved.

the electron to escape at a given energy (see section 6 of [144]). A distribution of escaped electrons, denoted by $N_0(E_{\mathrm{k}})$, can be obtained from this probability by applying [175]:

$$N_0(E_{\mathrm{k}}) = N_{\mathrm{i}}(\epsilon_{\mathrm{k}}) P_{\mathrm{e}}(\epsilon_{\mathrm{k}}), \tag{2.39}$$

$N_0(E_{\mathrm{k}})$ can then be integrated over all energies to obtain the secondary electron emission coefficient γ:

$$\gamma = \int_0^\infty N_0(E_{\mathrm{k}}) dE_{\mathrm{k}}. \tag{2.40}$$

Notably, this form of γ has an implicit dependence on the incident particle energy through the excited energy variable ϵ_{k}. However, the mechanisms for electron ejection must be specified in order to determine the distribution of excited electrons $N_{\mathrm{i}}(\epsilon_{\mathrm{k}})$ used in equation (2.39).

The two excitation processes specified above can also occur without any electron ejection, however, which becomes significant when considering the differences between a metal and a semiconductor surface. In the case of the latter, the electronic structure, i.e., the density of states of the surface $N(\epsilon)$, is significantly modified compared to a metal as the energy band gap is high and thus the conduction band, i.e., $N_{\mathrm{c}}(\epsilon)$, is primarily empty. The surface material's electrical properties, such as conductivity, can therefore be influenced by these processes as they may also excite electrons into the dielectric conduction band. Significantly more energy is then necessary for such an excitation to produce an ejected electron. This is likely the reason why semiconductors are observed to emit fewer secondary electrons for very

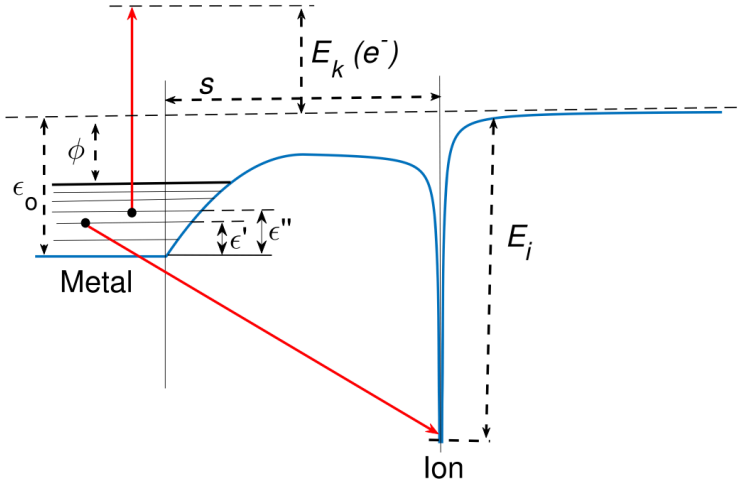

Figure 2.12: Visualization of Auger neutralization. The red arrows represent transition to the final state. Here, E_k is the kinetic energy of the escaped electron, $s = z$ is the distance between ion and metal surface, $\phi = \phi_\mathrm{W}$ is the work function, E_i is the ionization energy of the ion, ϵ_0 is the well depth, and $\epsilon^{'}$ and $\epsilon^{''}$ are the initial energies of the electrons undergoing Auger neutralization. Figure provided from Daksha *et al.*, Plasma Sources Sci. Technol. 28, 034002 (2019) [175]. ©IOP Publishing. Reproduced with permission. All rights reserved.

low incident particle energies, as in [183]. Notably, this also means that Hagstrum's model could likely be expanded upon to include semiconductors by incorporating a more complex density of states, but that is beyond the scope of this work. This concept is utilized when discussing the differences between metal and semiconductor SEE, however, as in section 7.1.

One mechanism for electron ejection from a surface material in this manner is Auger neutralization, which is depicted in figure 2.12. In this ejection process, two electrons, with energies $\epsilon^{'}$ and $\epsilon^{''}$, respectively (see section 3 of [144]), are initially present in the surface material's potential well. When the ion approaches at distance z, there is a chance for one of the surface electrons to neutralize the ion as a result of a perturbation from the Coulomb interaction between the participating electrons. The neutralizing electron (say the one with $\epsilon^{''}$) then rests in the ground state of the atom which has ionization energy E_i that is significantly larger than the depth of the surface's potential well ϵ_0, resulting in a significant net difference between its starting and ending energies. This extra energy is transferred to the second electron (with $\epsilon^{'}$ initially) in the surface material, causing it to become excited and potentially ejected from the surface, assuming that it gains sufficient energy to overcome the surface's work function ϕ_W and escape the surface. Thus, the conservation of energy produces the relation:

$$\epsilon_\mathrm{k} = \epsilon^{'} + \epsilon^{''} + (E_\mathrm{i} - \epsilon_0), \tag{2.41}$$

where ϵ_k is the energy of the excited electron. It is assumed that there are no energy level shifts resulting from the interaction of the potentials of the ion and surface material, and that the total energy of the system is zero. Since equation (2.41) is dependent on the initial energies of the electrons, every possible combination of starting energies needs to be accounted for. This requires the use of an Auger Transform (see section 3 of [144]) on the density of

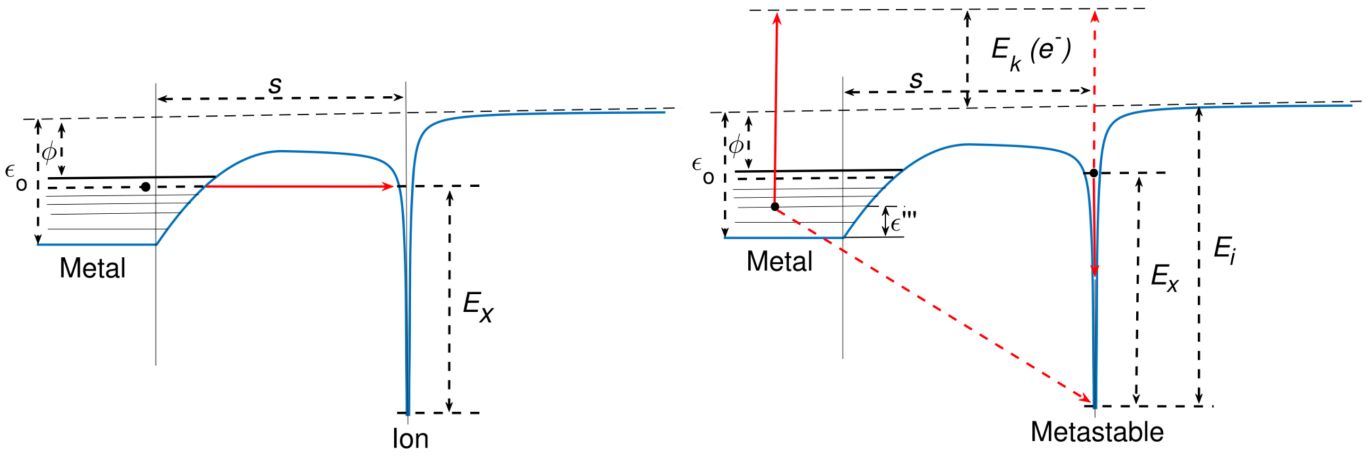

Figure 2.13: (Left) Visualization of resonance neutralization, where the dashed black lines represent the degenerate energy level shared between the ion and metal. (Right) Visualization of Auger de-excitation, where the dashed black lines represent de-excitation through the electron exchange pathway. The solid lines correspond to the non-exchange pathway. Here, E_i and E_x are the ionization and excitation energies, respectively, of the ion, $\phi = \phi_\mathrm{W}$ is the work function, ϵ_0 is the well depth, ϵ''' is the initial energy of the electrons undergoing Auger de-excitation, E_k is the kinetic energy of escaped electrons and $s = z$ is the distance between the ion and metal surface. Figures provided from Daksha *et al.*, Plasma Sources Sci. Technol. 28, 034002 (2019) [175].

states in the conduction band $N_\mathrm{c}(\epsilon)$ by assuming $\epsilon' = \epsilon + \Delta\epsilon$ and $\epsilon'' = \epsilon - \Delta\epsilon$. The transform notably depends on the temperature of the surface, which affects states near the Fermi energy ϵ_F. For ionization energies which are high enough to eject electrons with low initial electron energies, i.e., small ϵ', the SEEC associated with Auger neutralization becomes effectively independent of temperature as the only difference associated with a change in temperature would be in the high energy tail of the emitted distribution $N_0(E_\mathrm{k})$. This independence has been experimentally observed for argon and helium ions impinging on various atomically clean metals by Arifov [191]. The dependence on temperature in the case of semiconductor surfaces may also be relevant, especially if changes in temperature affect the conductivity of the surface. Once these factors are accounted for, the distribution of excited electrons $N_\mathrm{i}(\epsilon_\mathrm{k})$ can be found by shifting the distribution described by the Auger Transform by applying equation (2.41) and accounting for the available states for the excited electrons.

The second mechanism for electron ejection is actually a two-step process which entails the resonance neutralization of the ion, shown in left plot of figure 2.13, followed by Auger de-excitation, shown in the right plot of figure 2.13 (see section 4 of [144]). In resonance neutralization, an electron from the surface material tunnels into a degenerate state shared by the ion. In doing so, it neutralizes the ion and creates an excited atom or metastable. From here, two possible paths exist for Auger de-excitation to occur. In the first, known as the electron exchange pathway, another electron from the surface tunnels into the ground state of the atom and, similar to Auger neutralization, this energy difference is transferred to the excited electron. This causes the excited electron to escape the atom. Alternatively, in

the second "non-exchange" pathway, the excited electron de-excites to the ground state of the atom, transferring energy to an electron in the surface material and allowing it to escape. Energy conservation arguments similar in concept to that discussed for Auger neutralization can be made to perform Auger Transforms for these pathways. Lastly, the same ideology for obtaining the distribution of excited electrons applied to Auger neutralization can be applied here for both the Auger de-excitation pathways.

There are, however, some important caveats to consider with these electron ejection processes. Firstly, these processes are mutually exclusive, such that one ion cannot undergo both processes while near the surface. It should also be noted that Hagstrum's model assumes that the probability of either Auger neutralization or Auger de-excitation to occur is unity. Secondly, Hagstrum's model predicts that Auger neutralization occurs much further away from the surface (i.e., at a larger z) compared to the Auger de-excitation pathways. The reason for this is that resonance neutralization is a quantum tunneling process which requires the ion to be as close to the surface as possible, whereas Auger neutralization is the product of quantum Coulomb interactions. Thus, Auger neutralization is considered to be the dominant electron ejection process, accounting for up to 90% of the total SEEC, which is justified by Hagstrum using comparisons of the emitted electron distribution's energy range between experiments and the model (see sections 11 and 14 of [144]). This energy range is found to be within the range defined by Auger neutralization.

An additional consideration that needs to be made is that the distance z between the surface and the ion is not truly constant in time. The incident ion continues to approach the surface material as it transits from the plasma to the surface, causing z to decrease until the ion is neutralized by one of these processes. Note that this does not imply that a electron ejection must occur, as the incident ion's energy can also be used to excite surface states or structural vibrations (phonons) in the material. In some cases, the ion might also be reflected from the surface. Since the probability for the ion to excite one of these electron ejection processes depends on the interaction distance and the transit of the ion makes this interaction distance time dependent ($z(t)$) on the timescale of the ion transit near the surface, the motion of the ion near the surface becomes relevant (see sections 3 and 5 of [144]). In particular, as considered in chapter 7, if Auger neutralization resulting in an electron ejection from the surface has the highest probability to occur at a distance z_{AN}, then an ion which transits to the surface along the direction of the surface normal will spend comparably less time at distances close to z_{AN} (i.e., a "fast" or "direct" transit) than an ion which transits towards the surface in a direction nearly parallel to the surface (i.e., a "slow" transit). In the latter case, there is a much longer period of time over which Auger neutralization has the chance to occur. Notably, as a precedent shown in Hagstrum's model, the probability of one of the ejection processes to occur on the inward (towards surface) transit before collision with the surface is assumed to be unity. This is a result of taking the limit of the incident ion's velocity to zero, without which there is a non-zero probability (if small for low incident energies) for the ion to transit to the surface and not undergo one of these processes (see section 5 of [144]). Effectively, this limit is similar to taking the transit time of the motion from $z = \infty$ to the surface ($z \approx 0$) to infinity. Similarly, the transit time in the case of an ion moving perfectly parallel to the surface would also be infinite, and the probability of an

electron ejection event would also become unity if this transit was exactly at the position $z = z_{AN}$ where the interaction is most effective. This is therefore hypothesized here to be a quantum mechanical form of incident particle angle dependence thought to be responsible for the observed trend with increasing surface roughness in section 7.2, but this hypothesis requires additional research outside the scope of this work to be confirmed.

It should also be noted that there are several potentially significant effects which are not taken into account here, including shifts in energy levels, finite lifetimes, broadening of energy levels due to Heisenberg's uncertainty principle, etc. While Hagstrum attempted to implement such effects (see sections 8, 9, 10, and 12 of [144]), there are still many inaccuracies and disagreements between experiments and model results. Further research is necessary for the correct implementation of such effects, but accounting for these effects is also far beyond the scope of this discussion.

Furthermore, both kinetic and quantum SEE processes have been found to depend on a number of characteristics of the surface material and profile, such as the crystallinity, substrate thickness, electronic structure, and surface roughness [175–182, 184, 192, 193]. However, it should be noted that traditionally, say in the PIC/MCC simulations of RF-CCPs, these additional dependencies of the SEEC on numerous surface characteristics are neglected for simplicity (e.g., see section 3.3). This is unfortunately an inaccurate assumption for industrial applications, however, where changing substrate profiles (such as in sputtering or etching discharges) or substrate materials (as in the deposition of thin films or the etching of a mask layer) are very common. It is therefore crucial to develop a fundamental understanding of how changes in the surface properties affect both the secondary electron emission processes and plasma operation, i.e., the SEE plasma-surface interaction, and when these changes are significant enough that they cannot be neglected. The results and hypotheses presented here and in chapter 7 demonstrate, if only qualitatively, the necessity of such an understanding when attempting to model or optimize any low temperature plasma process in which a changing plasma-facing surface is present, including many important applications such as semiconductor etching, plasma chemical vapor deposition (PCVD), and sputtering.

Chapter 3

Experimental and computational methodology

The experimental setup and operating conditions for the following chapters are specified in section 3.1. The subsections under section 3.2 discuss the experimental methodology of the diagnostics utilized to obtain experimental data, including a high voltage probe (subsection 3.2.1), phase-resolved optical emission spectroscopy via an ICCD camera (subsection 3.2.2), a retarding field energy analyzer (RFEA, subsection 3.2.3), and an experimental implementation of the recent γ-CAST diagnostic [94] (subsection 3.2.4). The kinetic, particle-in-cell/Monte-Carlo-collision (PIC/MCC) simulations utilized in the following chapters are described in detail in section 3.3. In particular, the simulations operated solely in Ar associated with chapter 5 are discussed in subsection 3.3.1. The simulations operated in CF_4 or Ar-CF_4 gas mixtures utilized in chapter 6 are outlined in subsection 3.3.2. The specific experimental methodology and cases investigated are furthermore outlined in section 3.4.

3.1 Experimental plasma source and operation conditions

The experiments of subsequent chapters are performed in a modified Gaseous Electronics Conference (GEC) reference cell [194] at West Virginia University, shown in figure 3.1, consisting of a powered (driven) electrode at the bottom and a grounded counter-electrode at the top. The stainless steel electrodes both have a diameter of 10 cm and are separated by a variable gap length d. The grounded (top) electrode's position is adjustable such that the gap length d can be changed by raising or lowering the height of the grounded electrode while the powered electrode's position is fixed. The powered electrode is connected to a RF supply system designed to drive such a RF-CCP using three consecutive harmonics of the fundamental frequency 13.56 MHz with individually adjustable harmonic phases θ_k and voltage amplitudes

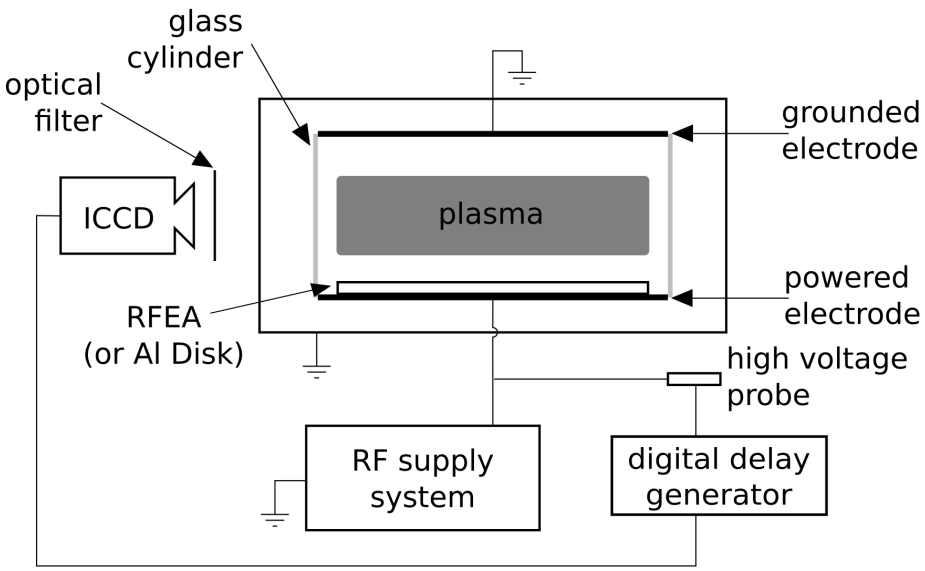

Figure 3.1: The experimental RF-CCP setup consisting of a capacitively coupled GEC reference cell monitored by diagnostics (phase-resolved optical emission spectroscopy (PROES) via ICCD camera, a high voltage probe, and a retarding field energy analyzer). The RFEA position also corresponds to the placement of aluminum disks in chapter 7.

ϕ_k [FJ15, 195]. The individual diagnostics seen in figure 3.1 are discussed in the subsections of section 3.2. Additionally, the walls of the chamber are also grounded. A glass cylinder is used in order to radially confine the plasma between the electrodes. This cylinder does increase the geometrical symmetry of the discharge when compared with confinement using the grounded chamber walls and allows for better comparison of the experimental results with the PIC/MCC simulations of section 3.3, which inherently simulate a geometrically symmetric reactor. A persisting capacitive coupling between this cylinder and these grounded walls effectively enlarges the area of the grounded electrode (A_g) and induces a geometrical asymmetry [39, 99, 100]. This geometric asymmetry is present throughout the experimental measurements of chapter 4, 6, and 7, and has influence over both the spatio-temporal heating dynamics and the DC self-bias of these chapters (see sections 2.2-2.4).

It should be noted that figure 3.1 does not accurately represent every case considered in he following chapters. In particular, the RFEA diagnostic (see subsection 3.2.3) shown to be placed on the powered electrode in figure 3.1, is utilized at both electrodes in chapter 4 by using a second grounded electrode with a recess into which the RFEA can be placed such that it is flush with the grounded electrode surface. This is notably not the case for when the RFEA rests on top of the powered electrode, which cannot be modified in this way. Additionally, the RFEA diagnostic is not used in the experiments of chapters 6 or of chapter 7 and subsection 4.2 due to concerns of fluorocarbon contamination and collisions of charged particles between the individual grids inside the RFEA due to the high background gas pressure, respectively. Furthermore, for the high pressure cases where the γ-heating mode is relevant in chapters 4 and 7, the glass cylinder is removed in order to increase the

geometrical asymmetry and thus enhance the voltage across the powered electrode sheath $\phi_{sp}(t)$. This is also utilized in chapter 7 for a cleaning process (see section 3.4). Lastly, the aluminum disks used in chapter 7 are identical in diameter to the powered electrode (10 cm) and are individually placed on top of the powered electrode; thus the position of the RFEA in figure 3.1 can also be used to identify the location of these aluminum disks in chapter 7.

In many previous experimental studies on driving RF-CCPs utilizing more than one driving frequency, there were severe limitations caused by the absence of an efficient multi-frequency RF power supply and impedance matching network for more than two consecutive harmonics. The first experimental confirmations of the EAE utilized classical dual-frequency impedance matching for two consecutive harmonics [39, 44, 97] but found that this matching was insufficient to experimentally test the EAE's full potential predicted by simulations and models [45, 46] to exist in the presence of multiple driving harmonics. Lafluer *et al.* [51] and Johnson *et al.* [7, 8, 61] later performed important initial investigations of the particle heating dynamics and the control of particle distribution functions for mutli-frequency waveforms without impedance matching, but obtained high reflected powers of about 90% as a result. The lack of impedance matching thus restricted this system's use to low voltage amplitudes and made practical implementations in industrial applications impossible.

In more recent works [FJ15, 67, 68], however, including the results of the following chapters, novel RF supply and matching systems are utilized to overcome these limitations. The experimental setup described in figure 3.1 uses one such system described in extensive detail in the owned publication of Franek *et al.* [FJ15], which also includes results presented in chapter 4. This multi-frequency RF supply and matching system, which can be seen in figure 3.2, consists of three independent matching branches used for each applied harmonic. The individual branches each consist of a single-frequency RF generator, an impedance matching circuit, and electrical filters for other frequencies. These band-pass filters are included in the generator and matchbox of a given branch for its particular frequency and are designed to transmit the corresponding frequency and prevent other frequencies, such as those from the other branches or those reflected by the plasma, from reaching the generator. The band-pass filters installed in the output of the matchboxes, for example, are used to block the signals from the other matching branches and thus minimize the parasitic coupling between each branch. The band-pass nature of the filters allows for this, as high- or low-pass filters would be insufficient to stop all other possible frequencies; e.g., a low-pass would likely not filter frequencies caused by the PSR, since these frequencies are typically much higher than the applied frequencies. Therefore, the first branch provides a 13.56 MHz signal, the second branch provides a 27.12 MHz signal, and the third branch provides a 40.68 MHz signal. In order to synchronize these individual signals and control the relative phases between them, an external signal generator sends phase-locked, low amplitude RF signals of the respective frequency to each generator. The phase control of the applied voltage waveform is thus realized by adjusting the relative phases between the RF generators. An additional phase-locked signal from this signal generator can be used to synchronize and trigger external equipment, but is not utilized in this work. The output signals from each branch are combined and directly applied to the powered electrode of the plasma reactor as the applied voltage waveform. This voltage waveform is monitored through use of a high-voltage probe located next to

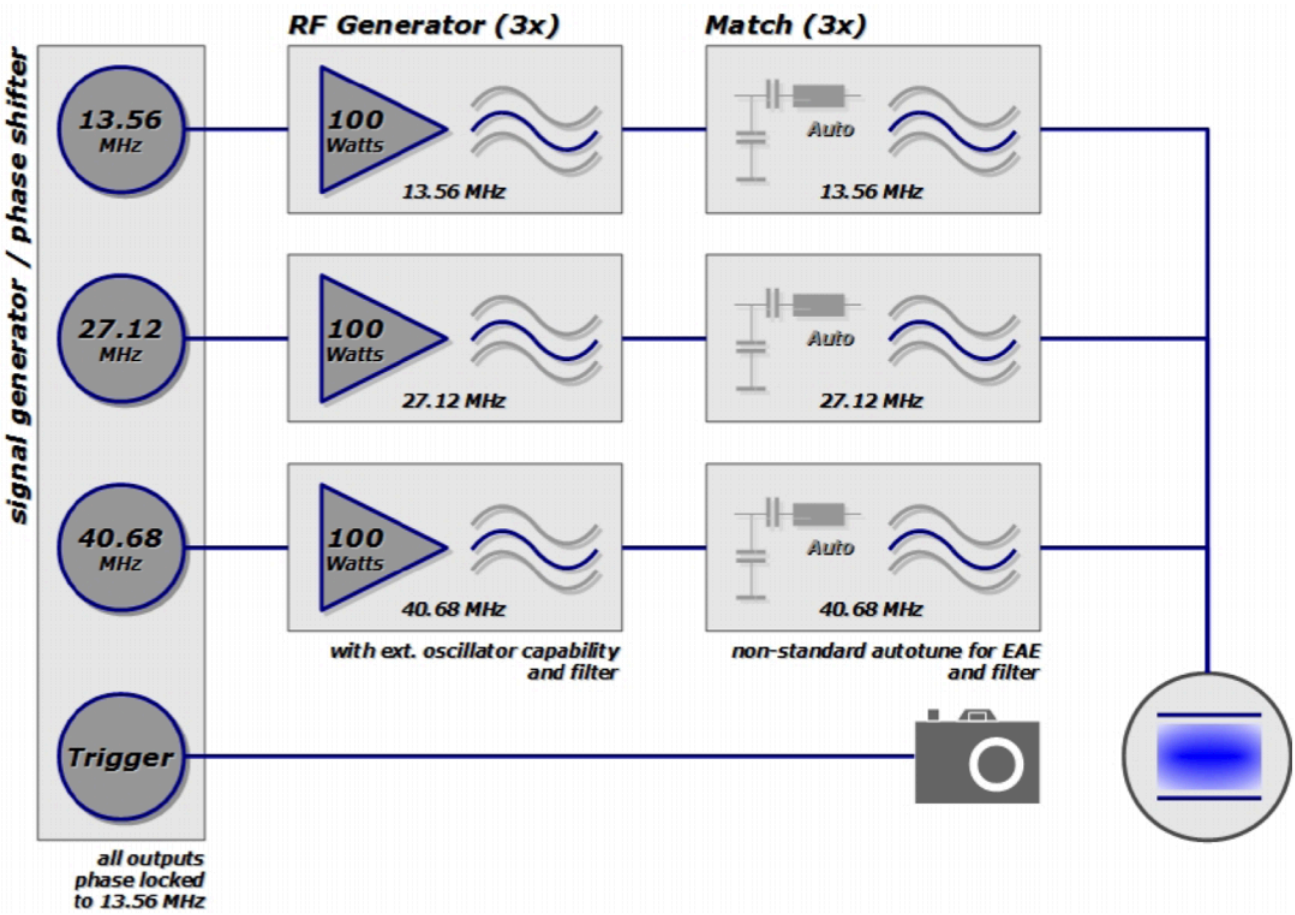

Figure 3.2: Schematic of the multi-frequency RF power supply and matching system used in the experimental RF-CCP setup, consisting of three consecutive harmonics of 13.56 MHz (up to 100 W per harmonic) and an additional phase-locked trigger output. Each harmonic frequency branch consists of an RF generator of the appropriate frequency and a matchbox. Each branch also has band-pass filters, represented by three stacked waves, for the other frequencies. Figure reproduced from its original publication in Franek *et al.*, Rev. Sci. Instrum. 86, 053504 (2015) [FJ15] with the permission of AIP Publishing.

the powered electrode (see subsection 3.2.1) and is controlled by a LabVIEW control panel connected to the external signal generator, the individual RF generators, and the individual matching units. Thus, each harmonic's amplitude and relative phase can be set independently and the matching network in each frequency branch can be controlled separately. It should be noted, however, that due to imperfect filters, there is still some interaction between the matching networks of each branch which is accounted for by systematically optimizing each matching branch and then the entire matching system for each specific tailored voltage waveform. The reflected power is thus minimized to approximately 5% of the total applied power, i.e., the sum over all applied frequencies, in most cases.

The applied voltage waveform can then be specified using equation (1.1) for each of the individual waveforms considered in the following chapters. Notably, the same equation is

used to specify the voltage waveform in the simulations as well as in the experiments. The specific harmonic amplitudes ϕ_k and relative phases θ_k chosen depend on the type of voltage waveform desired. Therefore, each relevant type of voltage waveform is discussed below in subsection 3.1.1. The specific conditions and voltage waveforms used in each chapter/section are then specified afterward in section 3.4.

3.1.1 Driving voltage waveforms

Different types of multi-frequency voltage waveforms are used to drive the RF-CCP in order to investigate the effects of voltage waveform tailoring, the EAE, and the control of plasma parameters as a function of discharge conditions. The "peaks-type" and "valleys-type" waveforms are applied to optimize the AAE (see figure 3.3(a)), while the Sawtooth waveforms are used to optimize and study the SAE separately from the AAE (see figure 3.3(c)). The intermediate waveforms shown in figure 3.3(b) isolate the SAE from the AAE, but do not optimize the SAE. It should be noted that there are any number of intermediate waveforms depending on the choice of the relative phases (see below), but the examples shown in figure 3.3(b) are of particular interest because they have equal magnitudes of maximum and minimum applied voltage when neglecting any DC self-bias present in the system, such that the AAE can be neglected and the SAE can be examined (see sections 2.2 and 2.3). However, as the SAE is most effective for waveforms with quick "rise" or "fall" times (see section 2.3), such as the Sawtooth waaveforms, the SAE is not optimized. All waveforms are generated as a superposition of multiple consecutive harmonics as outlined in equation (1.1) of section 2.2. Recall that N specifies the total number of applied harmonics and can vary from $N = 1$ (single-frequency) to $N = 3$ (generally referred to as the multi-frequency cases) in the experiments. Notably, in the simulations of chapter 5, $N = 4$ multi-frequency waveforms are also considered. The total possible amplitude of these multi-frequency waveforms is $\phi_{\text{tot}} = \sum_{k=1}^{N} \phi_k$, where k is again the harmonic index, but because of destructive interference between the harmonics, this amplitude is not reached for every set of phases. Also recall that the phase of the first harmonic (13.56 MHz), i.e., θ_1, is subtracted from all phases such that $\theta_1 = 0°$ for any waveform such that the other harmonics' phases (θ_k, $k \neq 1$) are relative to the phase of the fundamental 13.56 MHz component.

"Peaks-type" waveforms are generated by setting all phases to zero ($\theta_k = 0°$), while $\theta_k = 180°$ for even k and $\theta_k = 0°$ for odd k define the "valleys-type" waveforms. The intermediate waveforms shown in figure 3.3(b) are generated by choosing $\theta_k = 0°$ for odd k and either $\theta_k = 90°$ or $\theta_k = 270°$ for even k. The harmonics' amplitudes for all of these three waveform types are chosen according to the following criterion [45]:

$$\phi_k = \phi_{\text{tot}} \frac{2(N - k + 1)}{N(N + 1)}, \tag{3.1}$$

where ϕ_{tot} is specified in section 3.4 for each specific case examined in the following chapters. The harmonic voltage amplitudes of equation (3.1) are specifically chosen as they maximize the difference between the global extrema of the applied voltage waveform, i.e., $\widetilde{\phi}_{\text{max}}$ and

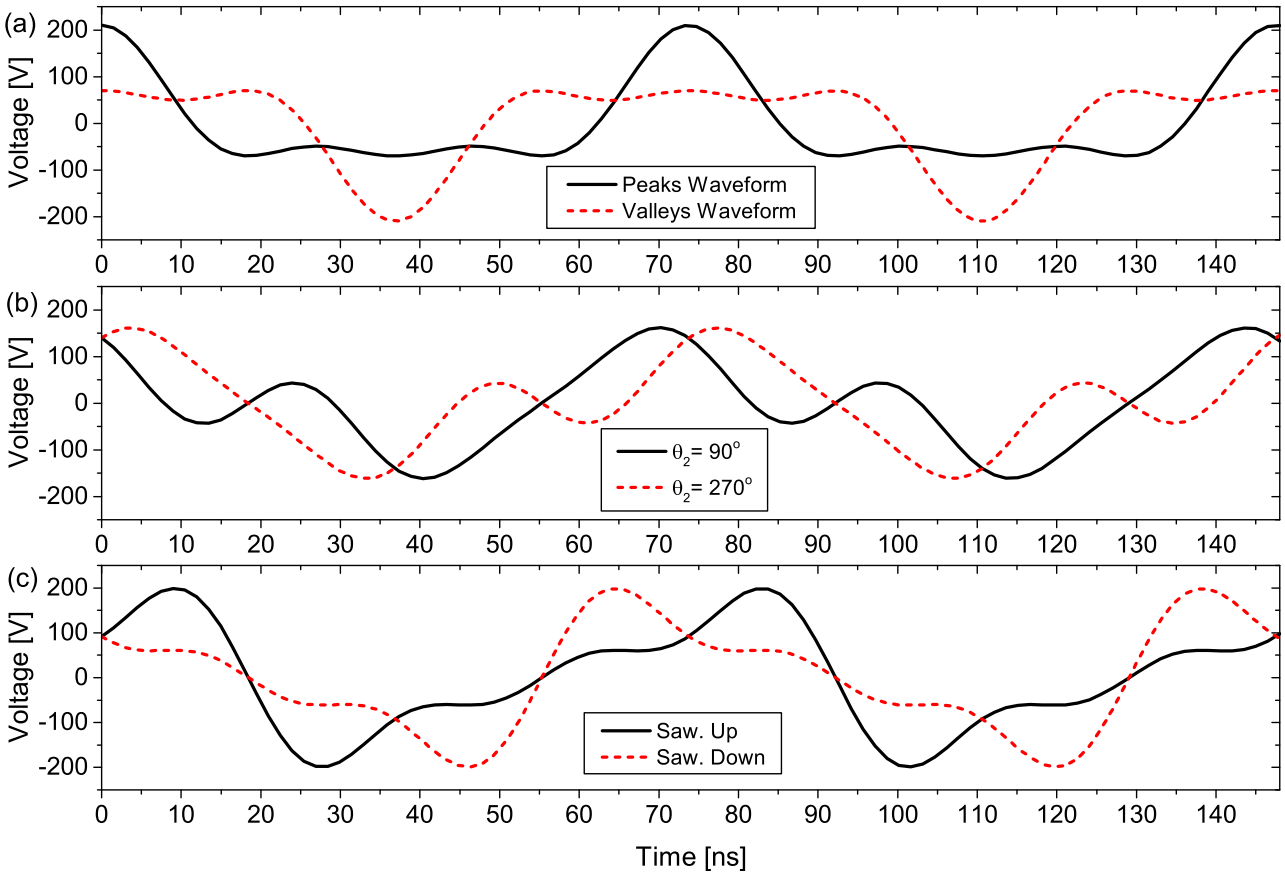

Figure 3.3: Examples of applied voltage waveforms over two consecutive RF periods for $N = 3$ harmonics: (a) "peaks-type" (solid) and "valleys-type" (dashed) waveforms (using equation (3.1)), (b) intermediate waveforms where $\theta_2 = 90°$ (solid) and $\theta_2 = 270°$ (dashed) and all other phases are zero (using equation (3.1)), and (c) Sawtooth Up (solid) and Down (dashed) waveforms (using equation (3.2)) [BS16]. All voltage waveforms utilize the general form of equation (1.1). Figure provided from its original publication in Brandt *et al.*, Plasma Sources Sci. Technol. 25, 045015 (2016) [BS16].

$\widetilde{\phi}_{\min}$. These kinds of voltage waveforms represent the extreme ends of the EAE, with the "peaks-type" waveforms inducing an asymmetry favoring the powered electrode's sheath voltage (i.e., $\varepsilon < 1$) and the "valleys-type" waveforms inducing an asymmetry favoring the grounded electrode's sheath voltage ($\varepsilon > 1$), as noted in section 2.2. As a result, these waveforms also generate a DC self-bias (see section 2.3) at either end of the self-bias control range for a given set of discharge conditions and are therefore very useful in examining the performance of the EAE under those conditions. These two types of waveforms are therefore utilized in chapters 4, 5, and 6 of this work.

For Sawtooth waveforms, the harmonic amplitudes are chosen according to the following criterion [63–66]:

$$\phi_k = \phi_N \frac{1}{k}, \tag{3.2}$$

where ϕ_N changes with the total number of applied harmonics (N). Notably, only $N = 3$ multi-frequency Sawtooth waveforms are considered in this work and are discussed only in chapter 6. For the Sawtooth Up waveform, the phases are set to $\theta_1 = 0°$, $\theta_2 = 270°$, and $\theta_3 = 180°$. The Sawtooth Down waveform has phases $\theta_1 = 0°$, $\theta_2 = 90°$, and $\theta_3 = 180°$. With this specific choice of individual harmonic amplitudes, these phases make the slope of the slowly rising/falling part of the waveform more linear and the fast drop/rise steeper (see figure 3.3(c)), thus enhancing the performance of the SAE under a given set of conditions. This type of waveform is thus quite useful for investigating the role of discharge asymmetry and the localization of electron power absorption dynamics from the SAE.

Single-frequency ($N = 1$) waveforms are utilized in chapters 4, 5, and 6 for comparison with the multi-frequency cases but are also used in chapters 5 and 7 to investigate phenomena which may be complicated by the more complex spatio-temporal dynamics of multi-frequency waveforms. In the simulations of section 5.1, both a low-frequency waveform (13.56 MHz) and a high-frequency waveform (54.24 MHz) are used for comparison with an intermediate-type $N = 4$ multi-frequency waveform with $\theta_k = 0°$ for odd k and $\theta_k = 90°$ for even k. The 13.56 MHz single-frequency waveform from section 5.1 is also utilized in section 5.2 for comparison with $N = 2$, $N = 3$, and $N = 4$ "peaks-type" waveforms. In chapters 4 and 6, similarly, the multi-frequency cases $N \geqslant 2$ are compared with the single-frequency case, but the single-frequency case is also utilized to measure the DC self-bias produced by the geometric asymmetry of the experimental reactor. For chapter 7, a single-frequency waveform is used in order to simplify the qualitative analysis from the changing plasma-facing surface properties to the changes in γ-mode heating observed via PROES (see sections 3.2.2 and 3.2.4) by avoiding the more complicated dynamics observed for multiple consecutive harmonics. The changes in the surface properties are attempted to be isolated from any change due to externally set factors, such as the background gas pressure and applied voltage waveform, by fixing these quantities for all variations of surface parameters. Therefore, this single-frequency waveform is fixed to have a total voltage amplitude of $\phi_{\text{tot}} = 200$ V. The relative phases between harmonics can be ignored for single-frequency waveforms, where only one harmonic is used, and thus are not necessary here. Lastly, dual-frequency ($N = 2$) waveforms are similarly utilized in chapters 4, 5, and 6 for comparison with the multi-frequency cases using higher numbers of harmonics, i.e., $N = 3$ or $N = 4$.

3.2 Experimental diagnostics

Several diagnostics are utilized in the following chapters to probe the discharge described in section 3.1, each of which is explained in one of the following subsections. The high voltage probe used to measure the harmonic voltage amplitudes and relative phases, as well as the DC self-bias is described in subsection 3.2.1. Phase-resolved optical emission spectroscopy via a synchronized external ICCD camera is utilized to investigate the electron impact excitation dynamics, and thus indirectly the electron power absorption, and is detailed in subsection 3.2.2. A retarding field energy analyzer is used for low pressure electropositive cases to measure the ion flux energy distribution function (FEDF) at one or both of the electrode surfaces and is discussed in subsection 3.2.3. Lastly, in order to qualitatively consider changes in an electrode's/substrate's SEEC, the experimental methodology of the γ-CAST diagnostic, which heavily utilizes PROES measurements, is applied without complementary simulations. The relevant parts of the γ-CAST diagnostic can be found in subsection 3.2.4.

3.2.1 Voltage waveform and DC self-bias measurements

The voltage waveform $\widetilde{\phi}(t)$ and the DC self-bias η are essential to the study of the EAE and the voltage waveform tailoring technique, as discussed in chapter 2 and above in subsection 3.1.1. Therefore, a LeCroy high voltage probe is attached to the cable connecting the combined matching branches (see section 3.1) to the powered electrode in order to measure both of these voltages. This location on the cable, which is approximately 0.33 m below the powered electrode surface, is chosen due to limited mechanical access for placing the probe directly at the powered electrode. A Fourier series analysis of the measured voltage waveform from this probe, performed using a simple analysis code on the associated oscilloscope, provides the amplitudes ϕ_k and relative phases θ_k of each applied harmonic, as well as the DC self-bias, which is calculated as the RF period average of the measured waveform. These quantities are necessary to know at the powered electrode surface in order to determine the exact conditions the discharge is operating under. However, the voltage amplitudes and phases of each harmonic measured at this point on the cable during plasma operation are different than those existing at the powered electrode due to reflection on the cable.

It is therefore necessary to perform a calibration procedure in order to consistently determine the voltage amplitudes and phases at the powered electrode surface (i.e., $\widetilde{\phi}(t) + \eta$) from the measured quantities at the measurement point on the cable. This calibration is accomplished in the vented vacuum chamber (i.e., no plasma, exposed to air) by measuring the voltage directly at the powered electrode surface ($\widetilde{\phi}_{\mathrm{el}}$) and then at the position on the cable where the voltage is measured during plasma operation ($\widetilde{\phi}_{\mathrm{m}}$). These measurements are performed for each individual frequency at several increasing applied powers. A comparison of the measurements at the electrode and at the measurement point provide calibration factors for both the harmonic voltage amplitudes (i.e., $\phi_{k,\mathrm{el}}/\phi_{k,\mathrm{m}}$) and the harmonic phases (i.e., $\theta_{k,\mathrm{el}}/\theta_{k,\mathrm{m}}$). These calibration factors are system dependent and are different for each frequency.

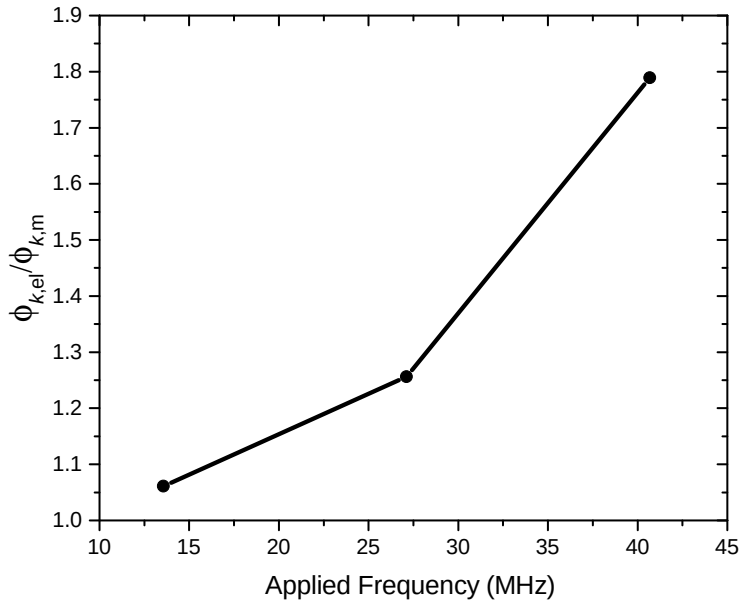

Figure 3.4: Example calibration factors ($\phi_{k,\mathrm{el}}/\phi_{k,\mathrm{m}}$) for each harmonic voltage ϕ_k as a function of the harmonic's applied frequency in MHz. Thus, each data point corresponds to the calibration factor for the 13.56 MHz ($k = 1$), the 27.12 MHz ($k = 2$), and the 40.68 MHz ($k = 3$) harmonics. This calibration corresponds to that for the uncontaminated, stainless steel electrodes, i.e., the RFEA and any aluminum disks are absent, and follows the procedure in Schulze *et al.* [39].

The appropriate voltages and phases at the electrode during plasma operation can then be easily determined using these calibration factors and the measured values. Notably, the powered electrode acts like an open end when there is no plasma. The calibration is therefore accurate and reliable only if the electrode similarly acts like an open end when the plasma is ignited. This can be checked by estimating the capacitive impedance of the cable to ground and the plasma impedance to calculate a reflection factor for operation with and without the plasma. In a previous work [39], calibration measurements were performed in 15° increments in the harmonic phases. The difference in the harmonic phases between the measurement point on the cable and the electrode surface was found to be smaller than the increment in these phases between measurements ($\approx 6°$ vs. 15°). This error is then due to the fact that the powered electrode does not exactly correspond to an open end, but can be assumed as one to a fairly good approximation. In the following chapters, similarly, the increment between the measured harmonic phases is assumed to be significantly larger than the potential error in the calibration procedure, such that the phase calibration factors are effectively close to one. This calibration procedure has been previously applied to dual-frequency discharges [39]. The voltage calibration factors of each harmonic for the uncontaminated, stainless steel electrodes can be seen in figure 3.4, as an example. Disturbances due to reflected power are minimized during both the calibration procedure and during actual measurements by systematically

tuning the matching branches and system for each given frequency and voltage waveform. The harmonic phases are also tuned systematically during this process to account for any potential phase shifts resulting from changes in the matching network.

It should be noted that changes to the powered electrode surface, such as those due to a change in the surface material, i.e., from the stainless steel electrode to the aluminum disks utilized in chapter 7, can affect this calibration. Therefore, for the conditions considered in chapter 7, this calibration is performed again for each new aluminum disk and the respective calibration factors for a disk are used in order to determine the voltage amplitudes and phases during the associated measurements involving that disk. It is assumed here that the development of an aluminum oxide (Al_2O_3) film on the surface of these disks does not significantly change the calibration factors, but as the calibration is performed with exposure to air, it was not possible to check this by performing the calibration for a clean metal surface because of the quick oxidation of the surface [196]. A similar situation exists for contamination of the powered electrode by a fluorocarbon film in chapter 6, but a calibration performed after the measurements of this chapter demonstrated that the change in the calibration factors was minimal.

3.2.2 Phase-resolved optical emission spectroscopy

Phase-resolved optical emission spectroscopy is an optical diagnostic with high spatial and temporal resolution within the RF period which measures the electron impact excitation rate from the ground state into a specific excited state associated with the optical emission from a given atomic transition in order to probe the spatio-temporal electron power absorption dynamics [BS16, 86, 108, 109, 197–199]. A nano-second gated, high repetition rate ICCD camera (Andor IStar) with an optical filter is synchronized with the applied voltage waveform through an external digital delay generator (DDG) and views the plasma through a window in the vacuum chamber, as shown in figure 3.1. The optical filter (Edmund Optics bandpass filter) helps ensure that the light reaching the ICCD camera is primarily from the specifically desired atomic transition, and therefore depends on the chosen gases in the discharge and the chosen wavelength of the associated optical emission. The optical filters used for each chosen gas and gas admixture in this work is therefore specified later in this subsection. The high voltage probe of subsection 3.2.1 is connected as a trigger signal to the DDG. The DDG effectively reduces the high frequency MHz-signal to a kHz-signal to which the camera is able to be triggered from and enables a delay between the trigger and the camera gate, i.e., when the ICCD takes optical data. The experimental methodology for PROES is visualized in figure 3.5. The ICCD camera is then set to trigger at a specific phase in the voltage waveform, at which it accumulates emission over a brief camera gate width (2 ns) at the same RF phase (represented in such plots by time t) over many RF periods (typically several thousand). Once the measurement accumulates sufficient counts, the image, which at this point includes both the inter-electrode direction (i.e., $\hat{x}$) and the horizontal direction (i.e., radial direction of the plasma), is saved and the delay is increased by one gate width (2 ns) to accumulate another image (seen as the small increment between the delay and gate width in figure 3.5(a)). Thus,

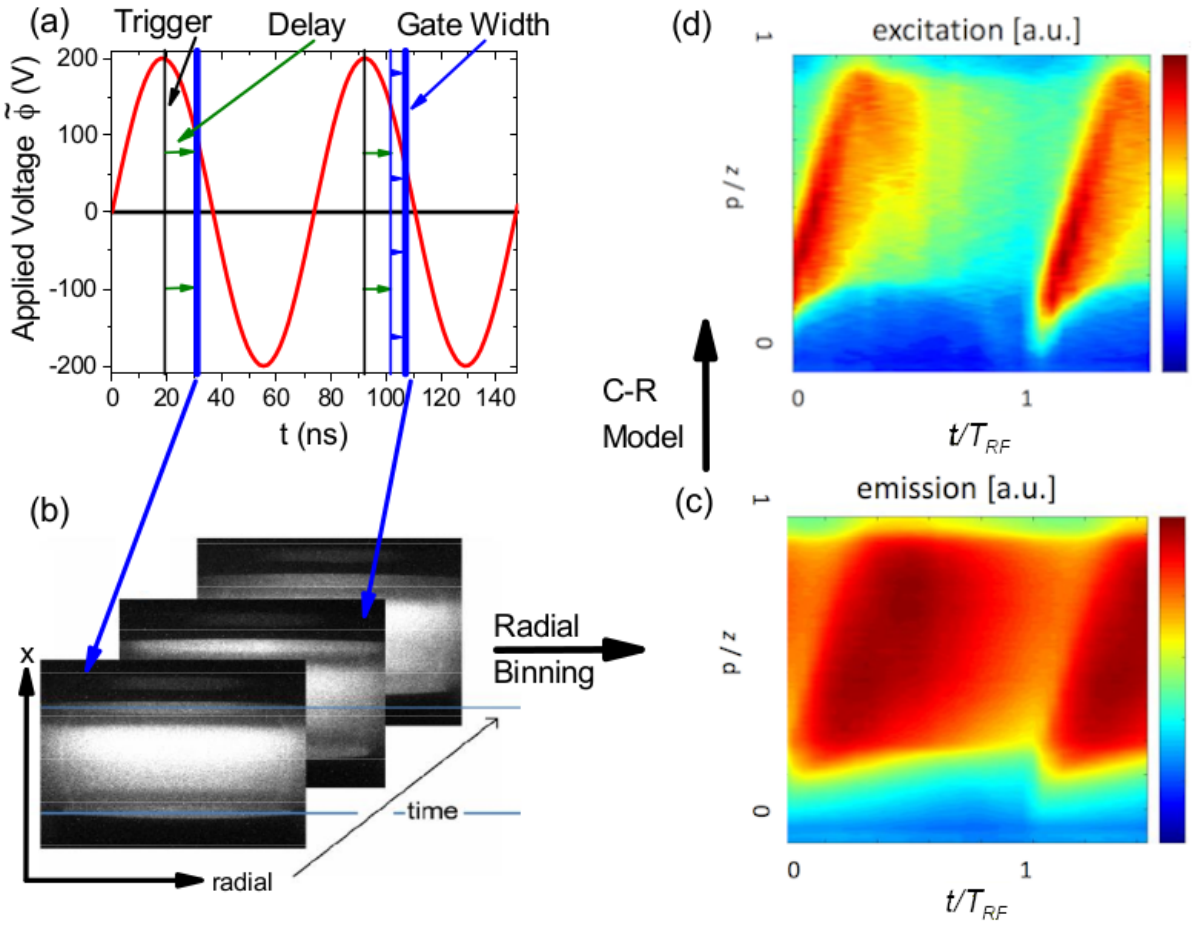

Figure 3.5: Schematic of the experimental methodology for phase-resolved optical emission spectroscopy comprised of (a) taking optical emission data at specific times in the applied voltage waveform, yielding two-dimensional images (b) which are then binned in the horizontal (radial) direction to create a spatio-temporal emission plot (c). The spatio-temporal excitation rate (d) can then be calculated from the emission data using the collisional-radiative (C-R) model for the appropriate states. Here, z in plots (c) and (d) is the same as the inter-electrode distance x in plot (b). A similar plot to (a) can be seen in Schulze *et al.*, J. Phys. D 43, 124016 (2010) [197]. Plots (b), (c), and (d) are provided from a private communication with Birk Berger and Julian Schulze.

this first image accumulates data for t = 0-2 ns and the second accumulates data for t = 2-4 ns, and so on. This process is repeated by increasing the delay (green arrows in figure 3.5(a)) until the entire RF period has been imaged [197]. These optical emission images, visualized by figure 3.5(b) are then binned in the horizontal direction, such that each image is averaged in the horizontal (radial) direction. This leaves each image as a single column of emission data which depends on the inter-electrode distance x at a specific RF phase (i.e., t). Once this process is applied to all images over the RF period, the columns can be combined into a spatio-temporal image of the emission (e.g., figure 3.5(c)) where the left axis is position x between the electrodes and the bottom axis is time t in the RF period. A collisional-radiative

model can then be used to calculate the excitation rate from the emission data (e.g., figure 3.5(d)). These measurements are performed with a spatial resolution of about 1 mm in the vertical direction ($\hat{x}$), limited by the ICCD camera resolution, and a time resolution of about 2 ns, limited by the camera gate width used and the effective lifetime of the observed energy level. If the gate width is changed this resolution will also change appropriately (e.g., 3 ns gate width means 3 ns resolution); this is noted in the appropriate figures.

A collisional-radiative model outlined in Schulze *et al.* [197] can then be used to calculate the excitation rate from the spatio-temporal emission data. This model is based on a simplified rate equation for electron impact excitation $\hat{E}_{0,i}(t)$ from a ground state to the observed excitation state responsible for the atomic transition associated with the measured optical emission. The population of a given excited state i with a population density $n_{i,\mathrm{exc}}$ is then described by the rate equation:

$$\frac{dn_{i,\mathrm{exc}}}{dt} = n_{E0}\hat{E}_{0,i}(t) + \sum_{M} n_M \hat{E}_{M,i}(t) + \sum_{c} R_{ci} n_c(t) - R_i n_{i,\mathrm{exc}}(t). \tag{3.3}$$

where n_{E0} is the population density of the ground state. The $n_M\hat{E}_{M,i}(t)$ terms correspond to excitation to the excited state (i) from metastable levels M with population densities n_M. Similarly, the $R_{ci}n_c(t)$ terms describe additional population of the excited state by cascades from high energy levels c with respective population densities n_c, where R_{ci} is the decay rate for a given cascade. When the excited state i undergoes de-excitation, a photon of the appropriate emission wavelength is emitted. However, this photon can be partially or fully re-adsorbed by other particles in the plasma. Furthermore, an atom in excited state can also undergo radiationless collisional de-excitation, in which case no photon is emitted. Thus, an effective decay rate $R_i = 1/T_i = \sum_h R_{ih}G_{ih} + \sum_q K_q n_q$ is included in this rate equation in order to account for the re-adsorption of radiation and radiationless collisional de-excitation, which is also referred to as "quenching." Here, T_i here is the lifetime of the excited state i, R_{ih} is the transition probability of spontaneous emission from level i to h, G_{ih} are escape factors which reflect the probability of single photon from the i to h transition to leave the plasma without re-adsorption, and K_q and n_q are the quenching coefficients and densities of each collision partner. This effective decay rate is therefore dictated by the probability of emitted photons leaving the plasma without being re-adsorbed, which is key in cases where the ground sate is overpopulated, and the likelihood of undergoing quenching with any potential collision partners. Increases in re-adsorption generally reduce R_i and increase the corresponding lifetime T_i of the excited state, while increases in quenching increases R_i and decreases T_i. Both of these factors can also reduce the observed emission, since this energy is transferred between particles in the plasma and/or not emitted as a photon of the desired wavelength.

However, equation (3.3) is part of a highly complicated system of coupled differential equations that describes the rate equations for all cascade and metastable levels and the quenching coefficients and decay rates must be known. Therefore, the determination of the excitation $\hat{E}_{0,i}(t)$ is frequently difficult. Thus, specific transitions which satisfy several qualifications must be identified to be readily useful in PROES. These criteria include [197]:

i) A unique optical emission line (no superposition with other emission lines) of significant intensity with known optical transition rates.

ii) A short lifetime in order to temporally resolve the RF period (typically on or below the order of tens of ns for the MHz waveforms used in this work).

iii) Low population of the associated excited state from both cascades from higher energy levels and excitation from metastable levels, i.e., the state is primarily excited via electron impact excitation from the ground state.

iv) Quenching does not significantly influence the associated excited state, such that it primarily de-excites by emission of the relevant optical photon to be measured.

v) The excitation threshold energy for the associated excited state should be close to an energy (or energies) of interest, such as the ionization energy (or energies) of the primary background gas(es). Typically, threshold energies close to that of ionization are chosen in order to observe the excitation dynamics of highly energetic electrons which are responsible for sustaining the discharge via ionization.

An atomic transition which satisfies all these criteria may not necessarily be present in any given gas or gas admixture. Therefore, it is common to include a small admixture of a gas with such an atomic transition in order to utilize this diagnostic. The diagnostic is generally otherwise non-invasive to the discharge itself. since it is an optical diagnostic.

Once an atomic transition that satisfies these criteria is identified, the metastable and cascade contributions in equation (3.3) can be neglected. The electron impact excitation from the ground state to the excited state can then be calculated from the measured emission without needing to specify the shape of the electron energy distribution function (EEDF):

$$\hat{E}_{0,i}(t) = \frac{1}{R_{ih} n_{E0}} \left(\frac{d\dot{n}_{ph,i}(t)}{dt} + R_i \dot{n}_{ph,i} \right) \tag{3.4}$$

where $\dot{n}_{ph,i}(t) = R_{ih} n_{i,exc}(t)$ is the number of photons (counts) per unit volume measured at the ICCD over a unit time, i.e., the measured emission from the specified transition. It should be noted that since n_{E0} is generally unknown, only relative values of the excitation rate can be calculated using equation (3.4). This equation can then be used to calculate the spatio-temporal (x, t) excitation rate matrix from the measured emission matrix. Therefore, the same space and time resolutions from the emission data also apply to the spatio-temporal excitation rate calculated by the collisional-radiative model. However, for emission whose associated transition has a long lifetime (i.e., low R_i), the ICCD camera may measure a photon significantly later in the RF period than the time at which it was excited. This causes the ensemble emission to appear "smeared" in time as the population of the excited state gradually decays. However, this is accounted for by the inclusion of the R_i term in equation (3.4) and any overall shift in time of the excitation produced by the long lifetime can be fixed by appropriately shifting the spatio-temporal excitation data in time by the lifetime. Furthermore, as PROES excitation rate measurements are frequently compared with the applied voltage waveform to discuss sheath and electron power absorption dynamics (see

section 2.4), the spatio-temporal excitation rate can also be qualitatively matched against the applied voltage waveform (e.g., see the PROES measurements in chapters 4 and 6). A more comprehensive overview of the diagnostic is available in Schulze *et al.* [197].

The ICCD camera also requires an alignment and calibration procedure in order to properly define the region of interest (ROI) in which the plasma is located. This procedure entails positioning the camera such that it views the discharge horizontally through the chamber window; thus, the height and angle of the camera is fixed such that the camera sees approximately the same amount of the powered (bottom) and grounded (top) electrodes. To do so, the camera settings are changed significantly compared to the actual PROES measurements in order for standard lighting in the room to be utilized to see the interior of the vacuum chamber with the camera; furthermore the optical filter is removed during this process. The camera is then focused to the center point between the electrodes using an optical camera lens (Nikon AF NIKKOR 50 mm adjustable camera lens), which remains attached to the ICCD during actual PROES measurements. Once aligned and focused, a region of interest in the emission images spanning from the powered electrode surface to the grounded electrode surface (i.e., the x direction) and the entire horizontal width of the observed plasma (i.e., in the radial direction, approximately to where emission from the plasma disappears) is determined. This ROI remains fixed for all further PROES measurements and dictates the spatio-temporal emission data that is utilized to generate the spatio-temporal excitation rate plots, as outside of this region of interest no plasma and thus no emission is observed. Furthermore, the ROI can change between different operating conditions, particularly if the electrode gap separation (i.e., d) is changed or if the glass containment cylinder is removed. The inter-electrode distance (i.e., x) in the excitation rate plots is therefore mapped from the vertical direction of this ROI to the gap separation for each set of conditions, with the bottom of the ROI corresponding to the surface of the powered electrode at $x = 0$ and the top of the ROI corresponding to the surface of the grounded electrode at $x = d$.

PROES is used in chapter 4 to investigate the spatio-temporal excitation dynamics of highly energetic electrons in order to examine the electron heating dynamics responsible for the sustainment of the discharge as a function of different applied waveforms and conditions in Ar gas. However, most atomic Ar transitions either do not meet the criteria listed above or are inefficient [197], so a small amount of Neon is admixed (see section 3.4) in order to utilize the emission line at 585.2 nm originating from the Ne $2p_1$ state [200–202]. This transition is used because the Ne $2p_1$ state has a relatively short lifetime of 15 ns [201] as compared to the RF period (approximately 74 ns for all waveforms with $f = 13.56$ MHz) and yields a more accurate calculation of the excitation rate as a result [197]. Furthermore, this line has an excitation energy of around 19 eV and thus resembles the excitation threshold energy of argon ionization. This means that the measured spatio-temporal excitation rate provides information about the dynamics of electrons which can cause ionization and therefore on the electron power absorption dynamics/mechanisms present in the discharge. Therefore, a bandpass optical filter (Edmund Optics TECHSPEC fluorescence bandpass filter) with a central wavelength of 586 nm, a bandwidth of 20 nm, and a full-width half-maximum of 26 nm is placed in between the ICCD camera and the optical lens in order to perform the PROES measurements for this chapter.

For the cases considered in chapter 7, PROES is utilized in the experimental half of the γ-CAST diagnostic, discussed in subsection 3.2.4, in order to qualitatively probe changes in the γ-heating mode excitation rate as a function of changing plasma-facing surface properties. Therefore, a similar gas admixture of Ar-Ne (see section 3.4) and the same neon line (585.2 nm with 15 ns lifetime) and optical filter is utilized in chapter 7 as in chapter 4. Subsection 3.2.4 details how these PROES measurements are used in order to qualitatively hypothesize about the surface's secondary electron emission coefficient γ.

In chapter 6, similarly, PROES measurements are performed in order to probe the spatio-temporal excitation dynamics of highly energetic electrons responsible for sustainment of the discharge. For the CF_4 gas and Ar-CF_4 gas mixtures discussed in chapter 6, PROES measures emission from a specifically chosen Flourine atomic transition (F $2s^2 2p^4 3p^1 \rightarrow 3s^1$) at 703.7 nm with a lifetime of 26.3 ns [203]. A different optical filter (Edmund Optics TECHSPEC bandpass filter), with a central wavelength of 700 nm and a bandwidth and a full-width half-maximum of 25 nm, is therefore utilized in the same position when performing the PROES measurements in chapter 6. Notably, this Fluorine line has a relatively long lifetime compared to the RF period (≈ 74 ns). The collisional-radiative model [197] is then used to calculate the spatio-temporal excitation rate of this transition between the electrodes and over the RF period. The measured excitation dynamics are indicative of electrons with energies above the excitation threshold of the above level of 14.5 eV. As this line cannot be used in the pure (100%) argon content case, PROES measurements in section 6.2 are executed for argon content values between 0% and 90%.

Notably, PROES can be replicated in PIC/MCC simulations by directly accumulating excitation rate data using collisional cross-sections for the appropriate excitation process [197]. This technique is particularly utilized in chapter 6 to allow for qualitative comparison of the electron power absorption dynamics between the experiments and the simulations. Since the experiment is geometrically asymmetric (see section 3.1 and sections 2.2 and 2.3) and simulations are traditionally run in geometrically symmetric configurations, this may also provide a useful contrast when the simulations differ from the experiments, as in section 6.2. However, this also means that cases which strongly deviate from geometrical symmetry (e.g., $A_p/A_g \ll 1$), such as the low pressure measurements of section 6.1, may not be comparable with the spatio-temporal excitation rate obtained from the simulation. As chapter 5 is based solely on simulation results and is not compared with experiments, it should also be noted that the spatio-temporal electron power absorption dynamics can also be investigated more directly in the simulations. The spatio-temporal ionization rate and spatio-temporal electron heating (i.e., power density in W m^{-3}), for example, can also be outputs of the simulation, as seen in section 5.2.

3.2.3 Retarding field energy analyzer

A retarding field energy analyzer (Impedans Semion) [204–207] is used to measure the ion flux-energy distribution function of positive ions incident on either the powered or grounded

electrode. The RFEA essentially consists of three grids and a collector plate, as seen in figure 3.6. The first grid, situated at the top of the RFEA, is kept at the same potential as the RFEA's housing and thus has the oscillating potential of the electrode on which it is located. This is done to prevent any disturbance to the plasma itself, such that any ions enter the RFEA with similar energies to those which are normally incident on the electrodes themselves. A second grid, located inside the RFEA below the first, is set at a potential of about -60 V with respect to the first grid in order to repel any negative particles, particularly electrons, which pass the first grid. The potential of the third grid, located below the second, is varied from zero to a large positive voltage during measurement, such that the minimum kinetic energy at which the ions enter the RFEA and can pass this grid is varied. As the third grid's voltage is increased, only ions with increasing high kinetic energies can pass through the grid and reach the collector plate. Therefore, the energy of ions which are collected as positive ion current at the collector plate is varied as a function of the third grid's voltage. A voltage of about -60 V is applied to the collector plate to ensure all ions which overcome the third grid are collected. The positive ion current is then measured at each voltage applied to the third grid. It should be noted that the additional acceleration of the ions through the RFEA by the collector voltage is accounted for in the calculation of the ion FEDF by shifting the starting voltage of the current-voltage trace. The first derivative of this ion current as a function of the discriminating voltage (the third grid) yields the ion flux-velocity distribution function, which can be plotted easily in energy units with a resolution of approximately 1-2 eV [205]. This current is sent along a wire which is covered in thick ceramic plating through one of the vacuum chambers ports to be amplified and measured by the Impedans RFEA software. The ceramic coverings minimize the impact the wire has on the discharge as well as any stray currents to this wire from it.

For measurements of the ion FEDF at the bottom (powered) electrode, the RFEA is simply placed on top of the powered electrode. Measurements at the top (grounded) electrode require the use of a modified grounded electrode, however, into which a slot with the dimensions of the disk-shaped RFEA housing (approximately 7 cm in diameter and 5 mm in height), as well as a slot for the ceramic covered wire, has been made. Notably, the probe itself is significantly smaller (about 3 cm in diameter) and is located in the center of the surface of the housing. The RFEA itself can then be placed into this slot and held in place using a small spring-loaded pin, with the surface of the RFEA being flush with the rest of the grounded electrode. Notably, this is distinct from the method at the powered electrode, where it simply rests on top of it, such that the surface of the RFEA is slightly higher than the electrode surface. Therefore, in the case where the RFEA is placed on the powered electrode, the grounded electrode is also raised by the RFEA housing's height to keep the electrode gap distance (d) the same as that without the RFEA. This generally does not negatively impact the measurement of the FEDF. Therefore, the ion distribution function (FEDF) at either electrode can be measured, as demonstrated in chapter 4. This diagnostic is more comprehensively covered in [204–207].

The measured ion FEDF, denoted $F(\epsilon_\mathrm{i})$ where ϵ_i is the incident ion energy, can then be further analyzed to obtain the total ion flux Γ_i and the mean ion energy $\langle\epsilon_\mathrm{i}\rangle$, which are key parameters in many processing applications. To obtain the total ion flux and mean ion

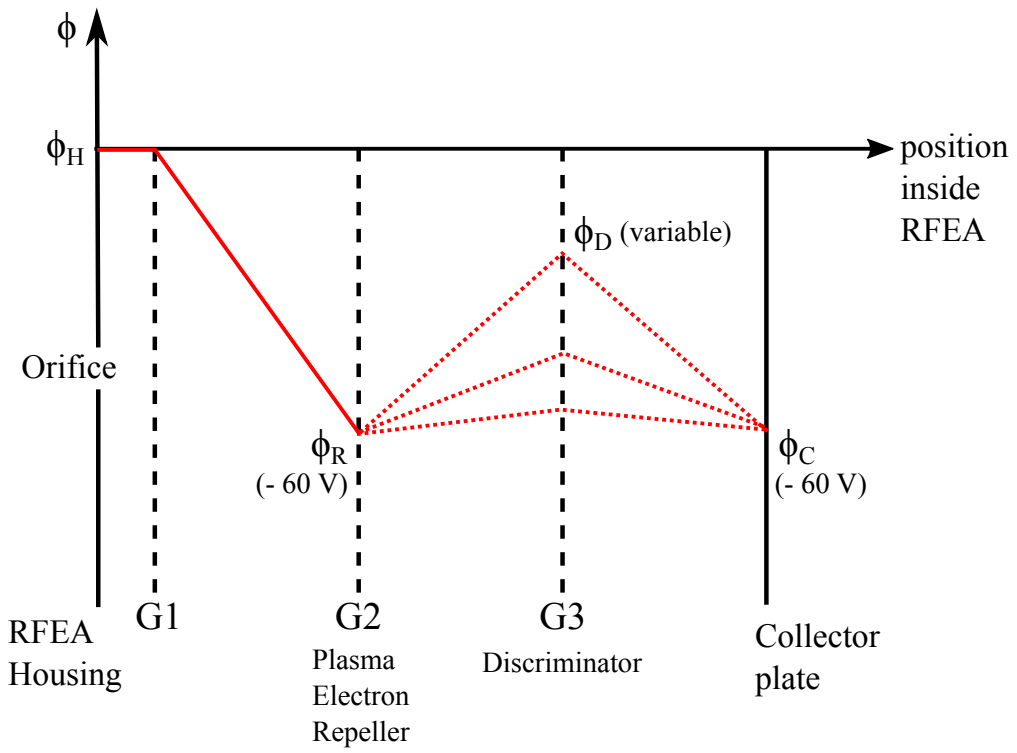

Figure 3.6: Internal schematic of the retarding field energy analyzer comprised of three metal grids and a collector plate. Positive ions enter through orifices in the RFEA housing such as the one depicted here. Each grid is biased at a specific voltage (or set of voltages) for a specific purpose, with the first grid (G1) at the same potential of the RFEA housing (ϕ_{H}), the second (G2) biased negatively (ϕ_{R}), and the third (G3) acting as a discriminating voltage (ϕ_{D}). The collector plate is also biased negatively (ϕ_{C}). The dotted red lines represent the changing potential profile for different discriminating voltages. This schematic is similar in concept to those seen in Gahan *et al.* [204], Bohm *et al.* [206], and Baloniak *et al.* [207].

energy, the FEDF is integrated across all energies [39, 44, 208], yielding

$$\Gamma_{\mathrm{i}} = \int_0^{\epsilon_{\mathrm{i,max}}} F(\epsilon_{\mathrm{i}}) d\epsilon_{\mathrm{i}} \tag{3.5}$$

$$\langle \epsilon_{\mathrm{i}} \rangle = \Gamma_{\mathrm{i}}^{-1} \int_0^{\epsilon_{\mathrm{i,max}}} \epsilon_{\mathrm{i}} F(\epsilon_{\mathrm{i}}) d\epsilon_{\mathrm{i}} \tag{3.6}$$

where $\epsilon_{\mathrm{i,max}}$ is the maximum possible energy of the incident ions. Furthermore, these parameters can be obtained as a function of the discharge conditions or the applied voltage waveform, as seen throughout chapter 4.

It should be noted, however, that this diagnostic is limited to lower background gas pressures. At higher gas pressures, the collisionality increases [2, p. 80] and thus the probability of a collision occurring during the transit of an ion across the grids of the RFEA also increases. An ion which undergoes such a collision may have its velocity and thus energy changed, such that the current received at the collector plate is no longer consistently correlated to the discriminating voltage. Thus, measurements of the FEDF cannot be performed once the collision length-scale(s) become similar to the dimensions of the RFEA. The high pressure cases of chapter 4 (at 200 Pa), for example, do not use this diagnostic for this reason. Additionally, it should be mentioned that the RFEA housing is made of aluminum as compared to the stainless steel of the electrodes. Measurements performed in the γ-heating mode or in which secondary electron emission significantly alters the discharge may be affected by the change in the surface material of a large fraction of the electrode, but since RFEA measurements are traditionally not utilized at higher pressures, this is generally not a concern for the results seen in chapter 4. In reactive gases, contamination of the collector plate could potentially affect the measured current. This can be accounted for with regular replacement of the RFEA grids. To prevent contamination of the RFEA by CF_4, this diagnostic was not used for the results presented in chapter 6.

3.2.4 Experimental implementation of the γ-CAST diagnostic

Recently, a new computationally assisted diagnostic technique developed by Daksha *et al.* [94] has been implemented in order to estimate a plasma-facing surface's secondary electron emission coefficient (see section 2.6) using non-intrusive and *in-situ* phase-resolved optical spectroscopic measurements (i.e., PROES). This diagnostic technique, referred to as γ-CAST, is highly relevant for industrial discharges where the surface conditions may not be at all similar to the particle-beam experiments typically used to determine SEEC values and conducted in the absence of a plasma and for ultra-clean surfaces [183, 209, 210]. The γ-CAST technique is based on utilizing the excitation rate maxima of the γ-heating mode and the α-heating mode associated with a given plasma sheath of a plasma-facing electrode/substrate (see section 2.4) obtained via PROES measurements (see subsection 3.2.2), as well as the fact that the γ-mode heating mechanism is directly associated with secondary electron emission, in order to obtain an estimation of a plasma-facing surface's γ. Recall that the intensity of the γ-heating mode's excitation rate maximum is a product of

the electron multiplication process occurring in the collisional sheath during times of high RF sheath voltage as well as the distribution of secondary electrons which seed this multiplication process. However, a method to separate these two dependencies experimentally does not currently exist due to the complicated nature of the SEE plasma-surface interaction and the coupling between the sheath properties and the SEE processes (see section 2.4). Therefore, in order to correlate a specific γ value to the measured excitation rate maxima of the γ-heating mode excitation, PIC/MCC simulations using a benchmarked code [211, 212] are performed for a sequence of different γ values under identical conditions to the experiment in [94]. The excitation rate maxima obtained from these simulations are then compared to those observed in the experiment. If good agreement is found between a simulation with a specific γ and the experiment, then the SEEC of the associated surface in the experiment can be estimated to be the SEEC of that surface set in the simulation. Typically, multiple measurements and sets of simulations are performed at conditions where the discharge transitions from the α-heating mode to the γ-heating mode as a function of increasing background gas pressure (usually 50-250 Pa) in order to accurately determine the SEEC value of a given surface [94].

Notably, in order to achieve the comparison between the simulations and the experimental PROES measurements, the average intensity of the excitation maxima caused by secondary electron heating I_γ, which is found by integrating the excitation rate over a region of interest corresponding to the observed γ-mode excitation rate maxima, is normalized relative to the average intensity of the excitation maxima corresponding to the α-mode, I_α, similarly determined by integrating the excitation rate over a region of interest corresponding to the observed α-mode maxima. An example definition of these ROIs given in Daksha *et al.* [94] is shown in figure 3.7 as black rectangles. This can be done for both the experimental PROES measurements at each pressure as well as the simulated excitation (or ionization) rate, but care must be taken to ensure that the intensity ratio I_γ/I_α in the experiment and in the simulations is comparable for each set of conditions. Therefore, the aforementioned regions of interest must remain identical for each PROES measurement for a given surface in the experiment; the same condition applies to the simulations as well. The exact regions of interest used in the measurements of chapter 7 are noted at the end of this section.

These intensity ratios can then be plotted as function of increasing background gas pressure across the conditions where the α-to-γ-mode transition occurs. The electron multiplication process typically yields higher excitation rates at higher pressures where the collisionality in the sheath is higher (see section 2.4). The intensity ratio I_γ/I_α thus typically increases with increasing pressure across this mode transition. However, the slope of the increasing trend must also depend on the choice of SEEC, since different surfaces with different γ will seed the electron multiplication process differently. If the same pressures and discharge conditions (e.g., applied waveform, gas mixture, etc.) are used across all measurements/simulations, the differences in the excitation rate intensities and thus I_γ/I_α should primarily be caused by difference in SEEC values between different surfaces or due to changes in the SEEC of a given surface. Therefore, the slope of such plots (I_γ/I_α vs pressure) are indicative of the SEEC of a given surface, with higher slope values corresponding to a qualitatively higher SEEC values. The slopes obtained from the experiment, again, cannot be directly correlated to a SEEC value, but those from the simulations can be. For example, figure 3.8 shows example intensity

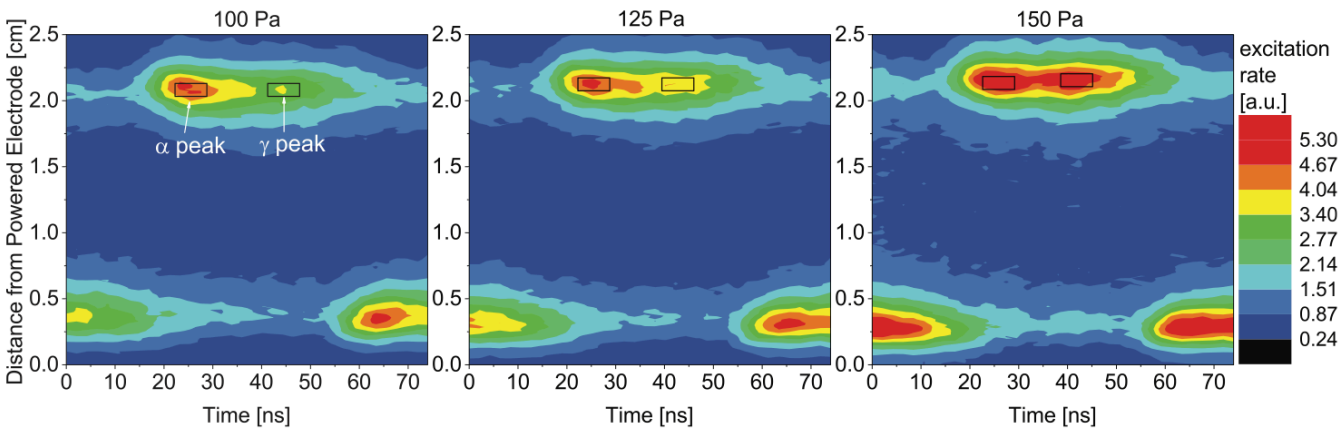

Figure 3.7: Example spatio-temporal plots of the electron impact excitation rate from the ground state into the Ne2p$_1$-state obtained by experimental PROES measurements in the description of the γ-CAST diagnostic for a single-frequency 13.56 MHz argon discharge at different pressures. The black boxed regions correspond to that publication's definitions of the regions of interest for the α- and γ-mode excitation rate intensities. Here, the power is kept constant with increasing pressure, such that the driving voltage is different at each pressure ($\phi_{\text{tot}} = 266$ V at 100 Pa, $\phi_{\text{tot}} = 256$ V at 125 Pa, and $\phi_{\text{tot}} = 244$ V at 150 Pa). Discharge conditions are: Ar + 10% Ne, $d = 25$ mm. Figure provided from Daksha *et al.*, J. Phys. D: Appl. Phys. 49, 234001 (2016) [94].

ratios as a function of increasing pressure from both PROES measurements and simulations under identical conditions but with various γ values obtained in Daksha *et al.* [94]. It can seen from this figure that the trend in the experimental measurements can be matched to that for a specific SEEC value in the simulations, and thus the SEEC of surfaces in the experiment can be estimated from this diagnostic. In this work, complementary simulations are not performed for the measurements of chapter 7. However, qualitative comparisons are still possible between different experiments, although these are limited only to concluding one surface's SEEC is relatively higher or lower than another surface's SEEC. Furthermore, more complicated SEEC models, such as an energy-dependent or incident-angle dependent γ, could be implemented into these simulations for comparison with experiments, but that is outside the scope of the discussion here.

In chapter 7, the experimental methodology in Daksha *et al.* [94] used to obtain I_γ/I_α measurements via PROES is applied as a function of different surface parameters, such as surface material, film thickness, and surface roughness (i.e., surface profile), in order to qualitatively demonstrate the dependence of the SEEC, and thus the discharge heating associated with secondary electrons, on these surface parameters. These measurements, as stated in section 3.4, are performed in Ar with a trace admixture of Neon in order to utilize the optical emission line discussed in subsection 3.2.2. A single-frequency 13.56 MHz waveform with an RF period of ≈ 74 ns is utilized for simplicity at 100, 150, and 200 Pa. From these PROES measurements, I_γ/I_α is calculated for each surface and pressure by integrating the

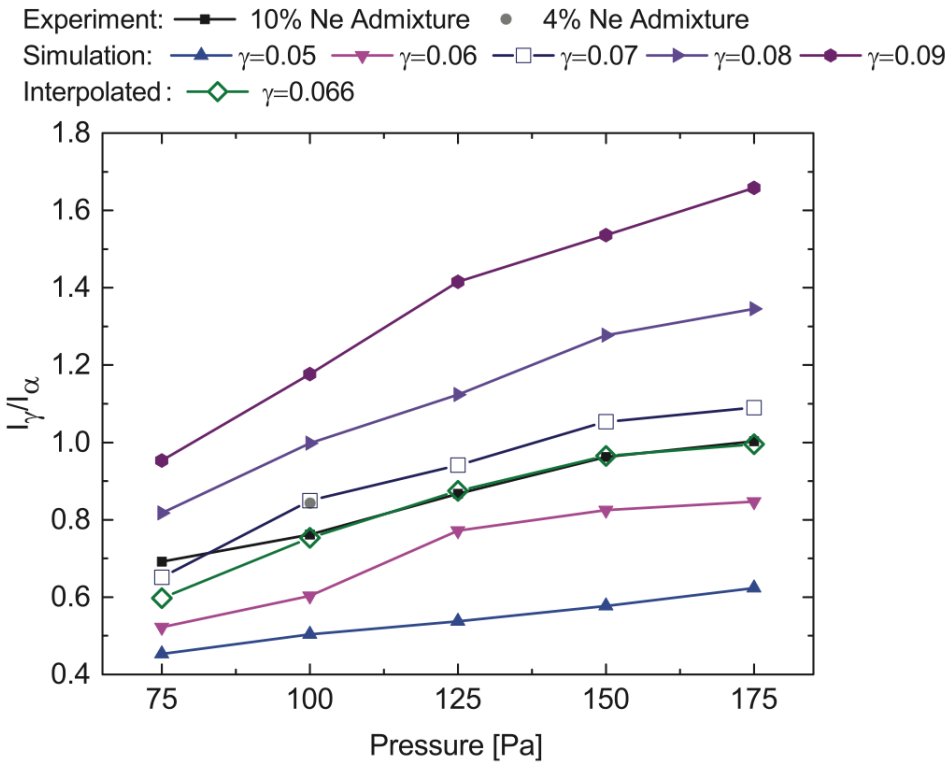

Figure 3.8: Example ratios of the averaged intensities of the excitation rate maxima caused by secondary electrons, I_γ, and by sheath expansion heating, I_α, obtained in the description of the γ-CAST diagnostic from PROES measurements in argon with 10% neon admixture and from simulations with various γ values at identical conditions as a function of increasing neutral gas pressure. Discharge conditions are: Ar + 10% Ne, $d = 25$ mm, single-frequency waveform at a fixed power of 20 W. The neon admixture is neglected in the simulations. Figure provided from Daksha *et al.*, J. Phys. D: Appl. Phys. 49, 234001 (2016) [94].

appropriate excitation rate data (see subsection 3.2.2) over the spatio-temporal regions of interest. The γ-mode intensity I_γ corresponds to integration over a region of interest in the spatio-temporal PROES plots in chapter 7 spanning approximately $x \approx 2.5$ mm to $x \approx 4.5$ mm for the RF phases $\varphi \approx 0.57\pi$ ($t = 21$ ns) to $\varphi \approx 0.97\pi$ ($t = 36$ ns). The α-mode intensity I_α corresponds to integration over a region of interest spanning $x \approx 2.5$ mm to $x \approx 4.5$ mm for the RF phases $\varphi \approx 0.3\pi$ ($t = 11$ ns) to $\varphi \approx 0.54\pi$ ($t = 20$ ns). The I_γ/I_α values calculated for each surface at different conditions is then qualitatively compared and hypotheses are made about the dependence of the SEEC on the surface parameters. Since these surface properties frequently change during plasma operation in many RF-CCP applications, such as semiconductor etching or PECVD, and the SEEC is highly sensitive to the surface's electrical properties (see section 2.6 and chapter 7), the application of the experimental part of the γ-CAST diagnostic to industrial discharges in this way may be a useful qualitative tool for probing how SEE changes during industrial processing.

3.3 Kinetic particle-in-cell/Monte-Carlo-collision simulations

Kinetic simulations of RF-CCPs, implemented and performed by the group of Aranka Derzsi, Ihor Korolov, and Zoltan Donkó of the Institute for Solid State Physics and Optics at the Wigner Research Centre for Physics in Hungary, are analyzed in chapters 5 and 6 in order to obtain a fundamental understanding of the physical origins behind experimentally observed phenomena. In the case of chapter 5, these simulations are used to computationally investigate the self-excitation of the PSR and its effects on electron heating. The simulations used to investigate the self-excitation of the PSR in argon gas for chapter 5 are described in subsection 3.3.1. The effects of electronegativity on the voltage waveform tailoring technique and the EAE are investigated in chapter 6 by performing experimental measurements and comparing these to the results of simulations under the same conditions. The simulations in CF_4 gas and Ar-CF_4 gas mixtures are described in detail in subsection 3.3.2. The specific cases investigated are listed in section 3.4.

3.3.1 Particle-in-cell simulations in argon

Numerical simulations are analyzed in chapter 5 in order to investigate the self-excitation of PSR and its subsequent effect on electron power absorption. These simulations are the result of a 1D3V (one-dimensional in space, three-dimensional in velocity space) particle-in-cell simulation code complemented by a Monte-Carlo treatment of collision processes (PIC/MCC) implemented and performed by the group of Zoltan Donkó [SE15a, SE15b]. The PIC/MCC code describes a geometrically symmetric discharge where the electrodes are assumed to be infinite, planar, and parallel. The bottom electrode is driven by one of the voltage waveforms described in section 3.4 (see also sections 2.2 and 3.1.1) and the other, top electrode is kept

Table 3.1: List of electron-argon collision processes considered in the argon simulations. E_0 is the threshold energy in eV. The analytical functions and E_0 values used in the argon simulations are taken from Phelps and Petrović [183].

Collision partners	Description	Product	E_0
$e^- + Ar$	Elastic momentum transfer		0
$e^- + Ar$	Electronic excitation	Ar^*	11.5
$e^- + Ar$	Electron impact ionization	Ar^+	15.8

grounded at a gap separation of $d = 30$ mm. Thus, the powered electrode is located at $x = 0$ and the grounded electrode is located at $x = 30$ mm.

Simulations are performed in argon gas with a fixed $\phi_{tot} = 800$ V and voltage amplitudes according to equation (3.1). A fundamental frequency of 13.56 MHz is used for most cases, but a 54.24 MHz frequency waveform is also considered in section 5.1. Different voltage waveforms are achieved by changing the number of applied harmonics (N) and the relative phases between the harmonics (see section 3.4). A DC self-bias generally builds up for a given driving voltage waveform (see section 2.1) in order to equalize the time-averaged fluxes of electrons and positive ions to each electrode. The DC self-bias in these simulations is therefore adjusted in an iterative manner in order to satisfy this current (i.e., flux) balance requirement [38]. The neutral gas pressure and temperature are set to 3 Pa and 400 K, respectively. Secondary electron emission from and electron reflection at the electrodes are both included by taking each to be a fixed value of 0.2 (20%) at both electrodes. It should be noted that this is a strong simplification of secondary electron emission (e.g., see section 2.6), but including a more complicated SEEC is outside the scope of the discussions on the PSR in chapter 5.

Cross-section data for elastic, excitation, and ionization collisions of electrons with Ar atoms is included in the simulations for the collision processes tabulated in table 3.1. The analytical description of these cross-sections in the simulation is taken from the appendix B of Phelps and Petrović [183], where a more complete description can be found. Cross-sections for isotropic and backward elastic scattering of Ar^+ ions from Ar atoms presented by Phelps [213] are also included in the simulations and can be seen in figure 3.9.

Each type of charged particle species (electrons, ions) is traced in the simulation through representation by approximately 10^5 superparticles. The number of superparticles for each species are monitored as a function of time in order to ensure convergence of the simulation. Convergence is then considered to be achieved when the drift of any of these numbers becomes less than the statistical fluctuation of these quantities (at the level of a few %). Convergence is reached on time-scales much longer than the RF period such that the simulation runs for at least a few thousand RF cycles before sufficient convergence is obtained. Once convergence is achieved, the simulation data is averaged over 2,400 consecutive RF periods to obtain the results shown in chapter 5 [SE15a, SE15b]. Therefore, highly reliable data can be produced

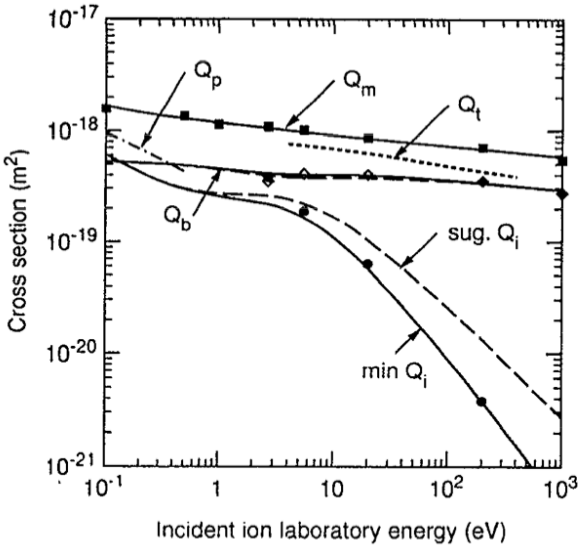

Figure 3.9: Cross-sections of Ar^+-Ar collision processes used in the argon simulations. Q_m, Q_i, Q_p, and Q_b here refer the momentum transfer, isotropic, polarization spiraling, and backward scattering cross section components of elastic scattering. Q_t is the total cross section from Cramer [214]. Solid curves indicate the minimum values of Q_i and the maximum values of Q_b, while the suggested values (sug.) of Q_t and Q_b for Monte Carlo calculations are shown by dashed curves. The argon simulations of chapter 5 use the Q_i and Q_b cross-sections shown here. Figure reproduced from Phelps, J. Appl. Phys. 76, 747 (1994) [213] with the permission of AIP Publishing.

in this way.

In section 5.2, the electron current density and electron heating rate from the simulation are considered. The electron current density is calculated from the spatially and temporally resolved electron current (e.g., see section 2.5) by averaging over a region within the plasma bulk. Recall that the bulk remains quasineutral throughout the RF period. As noted in section 2.5, this current, j , can be associated with electron power absorption via j^2 and is used to calculate the electron heating in the model. Notably, the model does not include any cooling of electrons because of this. The spatial-temporal electron heating rate, denoted by $P(x,t)$, obtained from the simulation itself is found by adding up the local gain and loss of energy of electrons at all positions and RF phases, and therefore also includes electron cooling. Thus, for comparison, the simulation output considers only positive (heating) values by defining

$$P_e^+(x,t) = P(x,t)\Theta[P(x,t)] \tag{3.7}$$

where Θ is the Heaviside step function. The total electron heating within the RF period is then calculated by integration over t. Similar to section 2.5, the electron heating in each half of the discharge can also be considered by splitting the discharge in two spatial halves adjacent to either the powered electrode ($x = 0$ mm to $x = d/2 = 15$ mm) or the grounded electrode ($x = d/2 = 15$ mm to $x = d = 30$ mm). Integration over each spatial region and

over the RF phase then yields the accumulated electron heating for each half:

$$\int_0^t P_{\mathrm{e,p}}^{+}(x,t')dt' = \int_0^{d/2}\int_0^t P_{\mathrm{e}}^{+}(x,t')dt'dx \tag{3.8}$$

$$\int_0^t P_{\mathrm{e,g}}^{+}(x,t')dt' = \int_{d/2}^{d}\int_0^t P_{\mathrm{e}}^{+}(x,t')dt'dx \tag{3.9}$$

3.3.2 Particle-in-cell simulations in CF_4 and argon-CF_4 gas mixtures

The numerical studies of CF_4 plasmas in chapter 6 are based on a bounded 1D3V particle-in-cell simulation code, complemented with a Monte Carlo treatment of collision processes (PIC/MCC) [215–217] implemented and performed by the group of Zoltan Donkó [BS16, BS19]. The output of these simulations are analyzed in chapter 6 in comparison with the experimental measurements. The electrodes are assumed to be planar and parallel with a fixed gap separation of $d = 25$ mm. To further simplify, the large aspect ratio (electrode diameter over electrode separation) of the experimental device justifies neglecting the radial losses. The discharge modeled by the code is assumed to be perfectly geometrically symmetric, in potential contrast to the experimental setup (section 3.1). The (bottom) powered electrode is driven by the same voltage waveforms specified in the experiment in section 3.4 (see also sections 2.2 and 3.1.1), while the other (top) electrode is grounded.

The charged species taken into account in the model are CF_3^+, CF_3^-, F^- ions, and electrons. For the Ar-CF_4 mixtures of section 6.2, Ar^+ ions are also included. The cross-sections of electron-CF_4 collision processes (see table 3.2) are adopted from Kurihara *et al.* [101], with the exception of electron attachment processes (producing CF_3^- and F^- ions), which are adopted from Bonham [102]. Cross-sections for electron-Ar and Ar^+-Ar collision processes are taken from Phelps [183, 213]. The electron-impact collision processes associated with CF_4 that are considered in the model are listed in table 3.2 and their energy dependent cross-sections are displayed in figure 3.10. As a simplification, the electron-induced processes that create radicals, or charged species other than CF_3^+, CF_3^-, Ar^+ and F^-, are allowed to affect only the electron kinetics. The products of these radicals are not otherwise accounted for.

The simulations include ion-molecule reactive reactions between CF_3^+, CF_3^-, F^- and CF_4 molecules, as well as elastic scattering of these ions from Ar atoms and elastic scattering of Ar^+ ions from CF_4 molecules [218–221]. Ar^+ + Ar collisions have a contribution with isotropic scattering and a contribution with backward scattering (charge transfer) [218–220]. For the elastic collisions of ions with buffer gas molecules, the model adopts Langevin type cross-sections:

$$\sigma_L = \left(\frac{\pi\alpha_p e^2}{\epsilon_0\mu}\right)^{1/2}\beta_\infty^2 g^{-1}, \tag{3.10}$$

Table 3.2: List of electron-CF_4 molecule collision processes considered in the model. E_0 is the threshold energy in eV [101, 102]. Originally published in Brandt *et al.*, Plasma Sources Sci. Technol. 25, 045015 (2016) [BS16].

Collision partners	Description	Product	E_0
$e^- + CF_4$	Elastic momentum transfer		0
$e^- + CF_4$	Vibrational excitation		0.108
$e^- + CF_4$	Vibrational excitation		0.168
$e^- + CF_4$	Vibrational excitation		0.077
$e^- + CF_4$	Electronic excitation	CF_4^*	7.54
$e^- + CF_4$	Dissociative ionization	CF_3^{++}	41
$e^- + CF_4$	Dissociative ionization	CF_3^+	16
$e^- + CF_4$	Dissociative ionization	CF_2^{++}	42
$e^- + CF_4$	Dissociative ionization	CF_2^+	21
$e^- + CF_4$	Dissociative ionization	CF^+	26
$e^- + CF_4$	Dissociative ionization	C^+	34
$e^- + CF_4$	Dissociative ionization	F^+	34
$e^- + CF_4$	Attachment	F^-	0
$e^- + CF_4$	Attachment	CF_3^-	0
$e^- + CF_4$	Neutral dissociation	CF_3	12
$e^- + CF_4$	Neutral dissociation	CF_2	17
$e^- + CF_4$	Neutral dissociation	CF	18

where μ is the reduced mass, α_p is the polarizability, g is the relative velocity of the colliding partners, and β_∞ is the dimensionless impact parameter for which the deflection angle is negligible [218–220] (notably unrelated to the β of section 2.5). The ion-molecule reaction processes considered in our model are listed in table 3.3 and their cross-sections are shown in figure 3.11.

The ion-molecule reactions produce the charged species considered in the model (CF_3^+, CF_3^-, F^-, and e^-), with the exception of the first reaction in table 3.3 that results in the formation of CF_2^+ ions. CF_2^+ and CF_3^+ ions react similarly with CF_4 and the recombination rate of CF_2^+ with electrons is only slighter higher than the recombination rate of CF_3^+ [222]. The model assumes, as a simplification, that the above CF_2^+ generation process does not convert CF_3^+ ions to CF_2^+ ions. This is further justified by the high rates for CF^+-neutral and CF_2^+-neutral reactions, which convert these lighter ions into CF_3^+ ions [223]. This assumption makes it unnecessary to introduce an additional type of charged species of minor importance into the computations and improves the balance of positive ion density.

Recombination processes between positive and negative ions as well as between electrons and CF_3^+ ions are simulated according to the procedure outlined in the work of Nanbu and Denpoh [224]. In section 6.1, the ion-ion recombination rate coefficients are adopted from

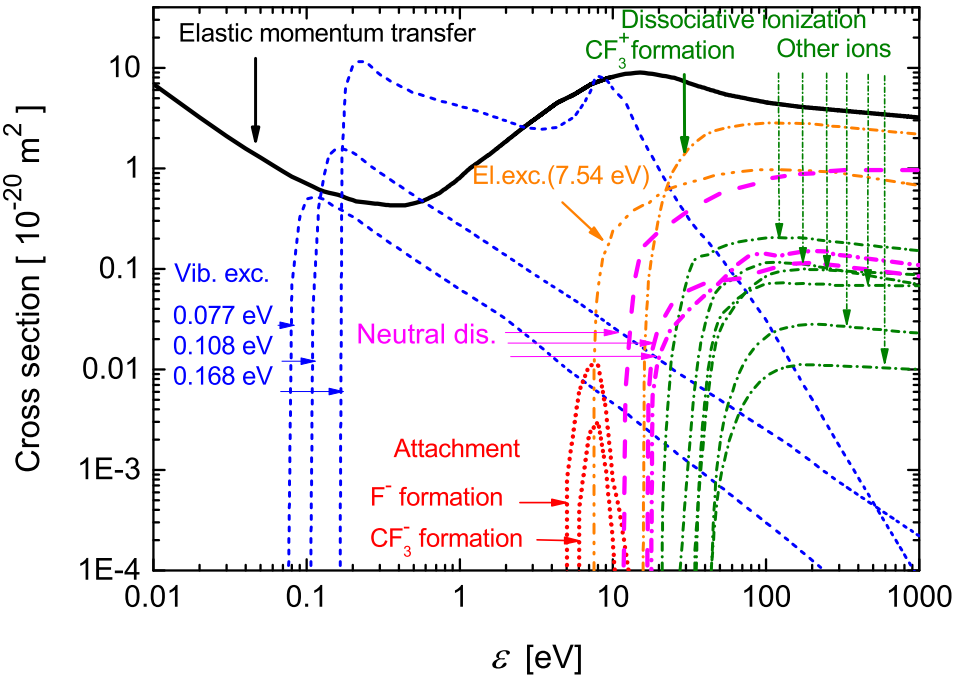

Figure 3.10: Cross-sections of electron-impact collision processes for CF_4 [101, 102]. Figure provided from its original publication in Brandt *et al.*, Plasma Sources Sci. Technol. 25, 045015 (2016) [BS16].

Table 3.3: Ion-CF_4 molecule collision processes considered in the model. E_0 is the threshold energy in eV [218–221]. Originally published in Brandt *et al.*, Plasma Sources Sci. Technol. 25, 045015 (2016) [BS16].

Projectile	Reaction	E_0
CF_3^+	$CF_3^+ + CF_4 \rightarrow CF_2^+ + CF_4 + F$	5.843
CF_3^+	$CF_3^+ + CF_4 \rightarrow CF_3^+ + CF_3 + F$	5.621
CF_3^+	$CF_3^+ + CF_4 \rightarrow CF_3^+ + CF_4$	0
CF_3^-	$CF_3^- + CF_4 \rightarrow CF_4 + CF_3 + e^-$	1.871
CF_3^-	$CF_3^- + CF_4 \rightarrow CF_3^- + CF_3 + F$	5.621
CF_3^-	$CF_3^- + CF_4 \rightarrow CF_2 + CF_4 + F^-$	1.927
CF_3^-	$CF_3^- + CF_4 \rightarrow CF_3^- + CF_4$	0
F^-	$F^- + CF_4 \rightarrow CF_4 + F + e^-$	3.521
F^-	$F^- + CF_4 \rightarrow CF_3 + F^- + F$	5.621
F^-	$F^- + CF_4 \rightarrow F^- + CF_4$	0

Table 3.4: Recombination processes considered in the model for section 6.1. Note that the ion-ion recombination rates are set at 10^{-13} m^{-3} s^{-1} for section 6.2. The ion and electron temperatures, T_i and T_e, respectively, are given in electronvolts [89, 102, 224, 225]. Originally published in Brandt *et al.*, Plasma Sources Sci. Technol. 25, 045015 (2016) [BS16].

Reaction	Rate coefficient (m^3s^{-1})
$CF_3^+ + e^-$	$3.95 \times 10^{-15} T_i^{-1} T_e^{-0.5}$
$CF_3^+ + F^-$	5.5×10^{-13}
$CF_3^+ + CF_3^-$	5.5×10^{-13}

Proshina *et al.* [89], while the rate for the electron-CF_3^+ recombination process is from Denpoh and Nanbu [225]. For section 6.2, the ion-ion recombination rates are set instead at 10^{-13} m^{-3} s^{-1} [219, 226] but the electron-CF_3^+ recombination rate is again taken from [225]. The recombination processes are listed in table 3.4 for section 6.1.

The gas temperature is assumed to be 350 K in the simulations. The emission of secondary electrons from the electrodes due to ion impact is included via the secondary electron emission coefficient, γ, which is set at $\gamma = 0.4$ (i.e., 40%) for the best agreement with experimental results. In the experiment, the plasma is reactive and operates at a relatively high pressure. Consequently, a thin fluorocarbon film with unknown properties is deposited on the electrodes. This high secondary electron coefficient in the simulations is required to reproduce the experimentally measured DC self-bias. In section 6.2, this secondary electron emission yield also corresponds to an effective value that includes secondary electron emission processes due to incident particle species other than ions (e.g., photons) as well. However, it should be mentioned that this choice of γ is still a strong simplification, as demonstrated

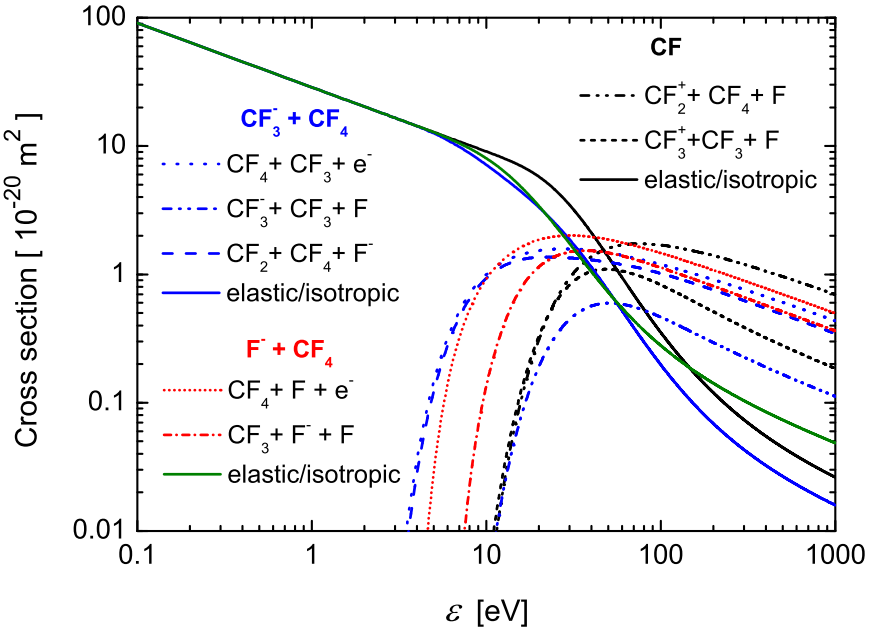

Figure 3.11: Cross-sections of ion-impact collision processes associated with CF_4 [218–221]. Figure provided from its original publication in Brandt *et al.*, Plasma Sources Sci. Technol. 25, 045015 (2016) [BS16]. ©IOP Publishing. Reproduced with permission. All rights reserved.

in section 2.6 and chapter 7. The excitation rate from energetic secondary electrons is smaller in pure CF_4 compared to pure Argon due to the lower positive ion flux in CF_4. The secondary electrons also cause more ionization than excitation due to their differing cross sections and can strongly affect the discharge symmetry via ionization in the sheaths. The (elastic) reflection of electrons from the electrodes is also considered by adopting a reflection probability value of 0.2 (i.e., 20%) [227].

For a given driving voltage waveform, a DC self-bias generally builds up in order to equalize the time-averaged electron and positive-ion fluxes to each of the electrodes, like the simulations of subsection 3.3.1. Negative ions are confined within the bulk and do not reach the electrodes. This DC self-bias is adjusted in the simulation in an iterative way to satisfy the current (i.e., flux) balance requirement mentioned in the previous subsection. The same voltage waveforms used in the experiments of chapter 6 are applied to the simulations (see section 3.4).

The electron-impact excitation rate from ground-state F atoms to the excited F-level responsible for the 703.7 nm emission measured experimentally by PROES (see subsection 3.2.2) is approximated in the simulation using the cross-section for the electronic excitation process (i.e., $e^- + CF_4 \rightarrow CF_4^*$, where CF_4^* is an excited state) having an energy threshold of 7.54 eV (see the El. exc. line in figure 3.10; also see table 3.2) by specifically accumulating excitation data for electrons with energies equal to or higher than 14.5 eV. This calculation is used exclusively for diagnostic purposes and does not affect the total electronic excitation calculated in the code. The F atom density is also assumed to be uniform in space and does

not vary over time. In this way, comparisons of the simulated spatio-temporal excitation dynamics of electrons to the experimental PROES measurements are possible without explicitly including F atoms in the simulation.

In order to ensure convergence of the simulation the superparticle number of each charged particle species traced in the simulation (electrons, CF_3^+, CF_3^-, F^-, Ar^+) is monitored as a function of time. Convergence is considered to be achieved, when the drift of any of these numbers becomes less than the statistical fluctuation of these quantities (which is at the few % level). Notably, convergence is reached on time scales that are significantly longer than those corresponding to electropositive discharges. While in the latter case typically a few thousand RF cycles are known to be sufficient for convergence, in the CF_4-Ar mixtures studied in chapter 6, up to 150,000 cycles are simulated before data collection starts. After convergence the data are averaged over 2,400 consecutive RF periods to obtain the results shown in chapter 6. In this way highly reliable data are obtained in the same way as in previous simulations performed in pure CF_4. This data shows excellent agreement with experiments, as seen in chapter 6 [BS16, BS19].

3.4 Methodology and Conditions

In this section, the exact operating conditions and diagnostics used for the experimental measurements of the following chapters are laid out. As some simulations are performed alongside these measurements for comparison, the appropriate methodology and conditions for the simulations will also be noted below, but further simulation details can be found in subsections 3.3.1 and 3.3.2. It should also be noted that chapter 5, on the PSR, is based solely from simulation results while chapters 4 and 7 contain only experimental measurements. All measurements performed in the setup of section 3.1 use a fundamental frequency of $f = 13.56$ MHz and generally contain the plasma with the glass confinement cylinder, unless noted otherwise. Table 3.5 lists the conditions described more extensively throughout this section, for quick reference.

In section 4.1, the effects of tailored voltage waveforms (i.e., of subsection 3.1.1 and sections 2.2 and 2.3) on the control of the EAE in the setup outlined in section 3.1 is studied in argon at low pressures (3 and 5 Pa). The effects of tailored voltage waveforms on the electron heating dynamics (see section 2.4) in argon are explored in section 4.1 using PROES measurements at low pressure (3 Pa), representing a collisionless regime, for a variety of voltage waveforms dictated by the number of harmonics and their relative phases at fixed voltage amplitudes. Neon gas is admixed to the argon (75% Ar, 25% Ne) in order to utilize the Neon line listed in subsection 3.2.2 for PROES. Both triple- ($N = 3$) and dual-frequency ($N = 2$) voltage waveforms are considered and use voltage amplitudes according to equation 3.1 with a total voltage amplitude of $\phi_{tot} = 210$ V. Therefore, $\phi_1 = 105$ V, $\phi_2 = 70$ V, and $\phi_3 = 35$ V for $N = 3$ and $\phi_1 = 140$ V, $\phi_2 = 70$ V, and $\phi_3 = 0$ V for $N = 2$. In the collisionless regime (subsection 4.1.1), PROES measurements, RFEA measurements at both electrodes, and voltage measurements are performed at 3 Pa in the α-mode with a gap separation of

Table 3.5: List of discharge conditions and applied voltage waveforms investigated in chapters 4-7. The 200 Pa measurements of chapter 4 and the measurements of chapter 7 are notably performed without the glass confinement cylinder. Furthermore, the results of chapter 5 are co-authored alongside Edmund Schüngel and are based purely on analysis of the kinetic simulations implemented and performed by the group of Zoltan Donkó. Additionally, chapter 7 utilizes various aluminum disks of varying surface roughness (8, 24, 75, and 150 Ra, measured in μm) and aluminum oxide film thickness.

Chapter	Gas(es)	Pressures	d	Voltage Waveforms	ϕ_{tot}	Sims.
Chapter 4 [FJ15, BB15]	Ar + 25% Ne	3 Pa	30 mm	$N = 2, 3$	210 V	[46]
		5 Pa	40 mm	$N = 2, 3$	120 V	N/A
		200 Pa	150 mm	$N = 2, 3$	210 V	[46]
Chapter 5 [SE15a, SE15b]	Ar	3 Pa	30 mm	N = 1-4, f = 13.56, 54.24 MHz	800 V	Only
Chapter 6 [BS16, BS19]	CF_4	10-100 Pa	25 mm	N = 1-3, $N = 3$ Sawtooth	210 V, ϕ_N = 138 V	Yes
	CF_4-Ar (varied)	20, 60 Pa	25 mm	$N = 1, 3$ "Peaks-/Valleys-type"	150 V	Yes
Chapter 7	Ar + 10% Ne	100-200 Pa	32 mm	$N = 1$	200 V	N/A

$d = 30$ mm for the various waveforms above. The DC self-bias is measured as a function of the second (θ_2) and third (θ_3) harmonic phases for $N = 3$. Recall that $\theta_1 = 0°$ is fixed by definition. The DC self-bias is also measured for $N = 2$, $N = 3$ with the third harmonic phase-unlocked relative to the other, as well as calculating another case by averaging the results over θ_3, in order to compare these cases as a function of θ_2. PROES measurements are performed for both $N = 2$ and $N = 3$ at low pressure for the "peaks-type" ($\theta_2 = 0°$), "valleys-type" ($\theta_2 = 180°$), and intermediate-type ($\theta_2 = 90°$) waveforms discussed in subsection 3.1.1 by setting $\theta_{1,3} = 0°$ and changing θ_2 in 90° increments. The spatially and temporally averaged mean excitation rate in each half of the discharge (powered, grounded sides) is also measured by integrating the calculated excitation rate data from PROES over the appropriate spatio-temporal region of interest for each case as a function of θ_2. RFEA measurements of the ion FEDF at each electrode (powered, grounded), and thus also the mean ion energy and total ion flux, are similarly performed for $N = 2, 3$ with $\theta_{1,3} = 0°$ as a function of θ_2 in increments of 45°. This work is also published in Berger *et al.*, J. Appl. Phys. 118, 223302 (2015) [BB15] and is reproduced here with the permission of AIP Publishing.

Further measurements at low pressure (5 Pa) are also included in subsection 4.1.2. These comprise the first measurements performed with the experimental setup and utilize the high voltage probe to measure the DC self-bias η generated by a $N = 3$ (triple-frequency) waveform

as a function of the second (θ_2) and third (θ_3) harmonic phases. These measurements are experimentally performed at 5 Pa with an electrode gap separation of $d = 4$ cm and $\phi_{\text{tot}} = 120$ V with individual harmonic amplitudes according to equation (3.1). These measurements are compared with the results of the model outlined in sections 2.2 and 2.3 for the DC self-bias using equation (2.14) in its reduced form excluding the bulk and floating voltages. An assumed constant value of $\varepsilon = 0.63$ is used in the model for equation (2.14), determined by averaging over the ε obtained in the experiment for each choice of θ_2 and θ_3 based on equation (2.6) from the measured, phase-resolved DC self-bias values and the global extrema of the driving waveform. Measurements of the DC self-bias are also performed for two ($N = 2$) applied harmonics as a function of θ_2 under otherwise identical conditions. RFEA measurements are also performed at the powered electrode as a function of the θ_2 for both $N = 2, 3$. From these RFEA measurements, the mean ion energy and total ion flux at the powered electrodes is calculated as a function of θ_2. In the comparisons of the $N = 2, 3$, $\theta_3 = 0°$ is set for $N = 3$. This work is also published in Franek *et al.*, Rev. Sci. Instrum. 86, 053504 (2015) [FJ15] and is reproduced here with the permission of AIP Publishing.

A collisional regime at high pressure (200 Pa) is also considered in section 4.2, where PROES and voltage measurements are performed under conditions where the discharge operates in the range of the γ- to α- mode transition as a function of N, with the grounded electrode moved to the maximum gap separation ($d = 15$ cm) and the glass cylinder removed in order to maximize the geometrical asymmetry of the discharge. PROES measurements are performed at this high pressure for "peaks-type" waveforms ($\theta_k = 0°$) as a function of the number of applied harmonics ($N = 1, 2, 3$), as well as for dual- ($N = 2$) and triple-frequency ($N = 3$) intermediate-type ($\theta_2 = 90°$, $\theta_{1,3} = 0°$) and "valleys-type" ($\theta_2 = 180°$, $\theta_{1,3} = 0°$) waveforms. The effects of changing the shape of the driving voltage waveform on the electron impact excitation dynamics are therefore studied as a function of space and time on a nanosecond timescale within the RF period using PROES and voltage measurements alongside the model used to determine the sheath voltage waveforms at each electrode (see section 2.2). This work is also published in Berger *et al.*, J. Appl. Phys. 118, 223302 (2015) [BB15] and is reproduced here with the permission of AIP Publishing.

The examination of the self-excitation of the PSR and its effects on spatio-temporal electron heating is performed entirely by analyzing the results of the model outlined in sections 2.2, 2.3, and 2.5 and the PIC/MCC simulation results. Therefore, no experimental measurements are performed for the discussions detailed in section 2.5 and in chapter 5. While the finer details of these simulations can be found in subsection 3.3.1, the specific conditions examined by these simulations in chapter 5 are stated here. In the discussions on the generation of the PSR in section 5.1, a geometrically symmetric discharge operated in argon with an electrode gap separation of $d = 30$ mm is simulated at a neutral gas pressure and temperature of 3 Pa and 400 K, respectively. Two single-frequency voltage waveforms of fundamental frequencies 13.56 MHz and 54.24 MHz are considered alongside a quadruple-frequency ($N = 4$) intermediate-type waveform with $\theta_{1,3} = 0°$ and $\theta_{2,4} = 90°$, as seen in figure 2.9. These waveforms are chosen such that the absolute values of the maximum and minimum applied voltages are equal and the resulting density and potential profiles are approximately symmetric around the discharge center when averaged over the RF

period such that the disturbance to the symmetry of the discharge from applying a weakly asymmetric multi-frequency waveform is small [63, 64]. Each waveform utilizes equation (3.1) and $\phi_{\text{tot}} = 800$ V to determine its voltage amplitudes. Various simulations are then performed for a variety of ε, a, b, and $\beta(t)$ choices to examine the generation of the PSR in geometrically symmetric RF-CCPs. This work is also published in Schüngel *et al.*, Physics of Plasmas 22, 043512 (2015) [SE15a] and is reproduced here with the permission of AIP Publishing.

The spatio-temporal excitation dynamics that occur in geometrically symmetric RF-CCPs as a consequence of the results of section 5.1 are considered in section 5.2. Here, a wider variety of applied voltage waveforms are considered, as seen in figure 3.12, but for identical gap separation, neutral gas pressure and temperature, and voltage amplitudes via equation (3.1) and ϕ_{tot} as in section 5.1. Single- and multi-frequency voltage waveforms with $N = 1, 2, 3, 4$ and $\theta_k = 0° \; \forall \; k$ are considered in order to compare changes between temporally symmetric but electrically (amplitude) asymmetric waveforms with differing number of applied harmonics (see top of figure 3.12). Additionally, $N = 4$ waveforms with different phase shifts, which have $\theta_{1,3} = 0°$ and either $\theta_{2,4} = 0°$, $\theta_{2,4} = 90°$, or $\theta_{2,4} = 180°$ are also compared to examine the effect of a temporally asymmetric waveform (see bottom of figure 3.12). For each number of applied harmonics N, the simulation current is compared to that obtained in the model for a variety of chosen ε, a, b, and $\beta(t)$ to examine the generation of the PSR. The current waveform and thus the generation of the PSR, as well as the DC self-bias, is also extracted from the simulations as a function of $\theta_2 = \theta_4$ between 0° and 180°. The electron power absorption is also calculated from the simulation data (see section 2.5) and examined in detail, including investigations of the EEDFs of each electron beam created by the PSR and the time-accumulated electron heating across the whole and in each half of the discharge. The ionization rate for the $N = 4$, $\theta_k = 0° \; \forall \; k$ waveform and the ion flux for the $N = 4$ waveforms as a function of $\theta_2 = \theta_4$ is also extracted. This work is also published in Schüngel *et al.*, Plasma Sources Sci. Technol. 24, 044009 (2015) [SE15b].

The effects of using an electronegative gas (CF_4) on VWT, the control range of the EAE, and the spatio-temporal electron power absorption dynamics are investigated in section 6.1. Experimental DC self-bias and PROES measurements of a fluorine line (see subsection 3.2.2) are combined with PIC/MCC simulations (see subsection 3.3.2) to obtain a complete understanding of the electron power absorption dynamics as a function of gas pressure (representative of changing global electronegativity and collisionality, see section 2.2), the number of applied harmonics N, and the harmonics' phases. The experimental discharge is operated for pressures between 10 Pa and 100 Pa with an electrode gap separation of $d = 25$ mm. The subsections of section 6.1 utilize different types of waveforms to isolate and examine the AAE (subsection 6.1.1) and the SAE (subsection 6.1.2), respectively. These can be seen in figure 3.3 in subsection 3.1.1. For the AAE, "peaks-type" ($\theta_k = 0°$), "valleys-type" ($\theta_2 = 180°$), and intermediate-type ($\theta_2 = 90°$ or $\theta_2 = 270°$) waveforms with amplitudes chosen by equation (3.1) and $\phi_{\text{tot}} = 210$ V are utilized. Dual- ($\phi_1 = 140$ V, $\phi_2 = 70$ V) and triple- ($\phi_1 = 105$ V, $\phi_2 = 70$ V, $\phi_3 = 35$ V) frequency cases are studied. DC self-bias measurements are then performed as a function of θ_2 at 20 Pa and 80 Pa for $N = 1, 2, 3$ waveforms with

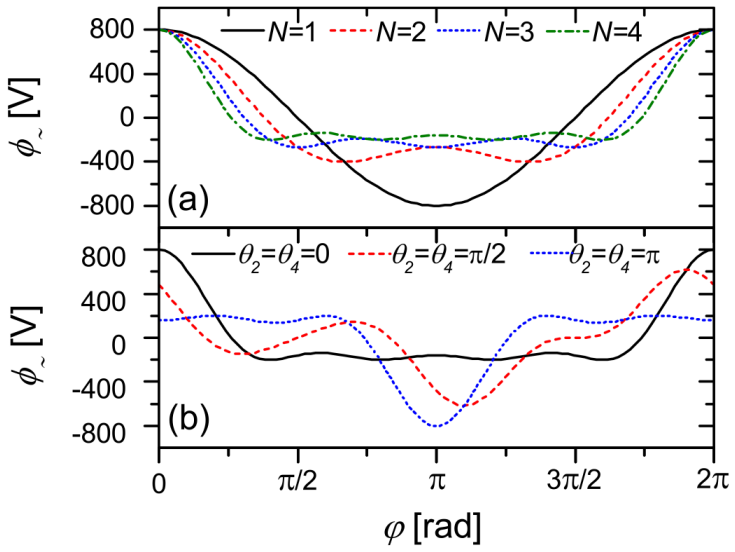

Figure 3.12: Applied voltage waveform as a function of time in the RF period (represented by $\varphi = 2\pi ft$). (a) Voltage waveforms for different total number of applied harmonics with all phases set to zero: $N = 1$ (black solid line), $N = 2$ (red dashed line), $N = 3$ (blue dotted line), and $N = 4$ (green dash-dotted line). (b) $N = 4$ voltage waveforms at different phase shifts where $\theta_{1,3} = 0°$: $\theta_{2,4} = 0°$ (black solid line), $\theta_{2,4} = \pi/2 = 90°$ (red dashed line), and $\theta_{2,4} = \pi = 180°$ (blue dotted line). Figure provided from its original publication in Schüngel *et al.*, Plasma Sources Sci. Technol. 24, 044009 (2015) [SE15b]. ©IOP Publishing. Reproduced with permission. All rights reserved.

$\theta_{1,3} = 0°$. PROES measurements are taken at both 20 Pa and 80 Pa for the $N = 3$ waveforms listed above and are compared to simulations only in the 80 Pa case due to a large geometric asymmetry at 20 Pa in the experiment (see subsection 3.3.2 and section 6.1). The spatio-temporal electric field, mean electron energy, electron attachment rate, CF_3^+ creation rate, and the time-averaged particle densities are taken from the simulation to further explain the spatio-temporal electron dynamics, including a unique localized DA-mode observed at 80 Pa in the simulation resulting from the formation of a potential well between the sheath electric field and an ambipolar electric field near the maximum sheath edge. Additionally, PROES is performed at both $N = 2, 3$ for the intermediate $\theta_2 = 270°$ waveform at 80 Pa for comparison between dual-frequency ($N = 2$) and triple-frequency ($N = 3$) operation. For the SAE, triple-frequency ($N = 3$) sawtooth waveforms are utilized with voltage amplitudes dictated by equation (3.2) and $\phi_N = 138$ V. This value of ϕ_N, and thus the total possible voltage amplitude $\phi_{\text{tot}} = 253$ V, is chosen so that the absolute possible positive and negative voltages are approximately the same as those reached by the aforementioned AAE waveforms. The DC self-bias as a function of pressure from 10 Pa to 100 Pa is measured for both sawtooth up ($\theta_1 = 0°$, $\theta_2 = 270°$, $\theta_1 = 180°$) and sawtooth down ($\theta_1 = 0°$, $\theta_2 = 90°$, $\theta_1 = 180°$) waveforms. PROES measurements of both sawtooth waveforms are performed at 20 Pa, 50 Pa, and 80 Pa, but are not compared to simulation results. This work is also published in Brandt *et al.*, Plasma Sources Sci. Technol. 25, 045015 (2016) [BS16]. ©IOP Publishing. Reproduced here with permission. All rights reserved.

The effect of a changing electronegative gas admixture of argon (Ar) and CF_4, representative of a changing global electronegativity (see section 2.2), on the EAE and the spatio-temporal electron power absorption dynamics is investigated in section 6.2. Experimental PROES (subsection 6.2.1) and DC self-bias (subsection 6.2.2) measurements of the fluorine line used in section 6.1 are performed at both 20 Pa and 60 Pa with a fixed gap separation $d = 25$ mm as a function of the argon gas admixture and are compared to PIC/MCC simulation results (see subsection 3.3.2). At each pressure and applied waveform, the mixing ratio of Ar to CF_4 is varied between pure CF_4 to pure Ar by incrementally increasing the ratio of the argon gas flow rate to the total (Ar + CF_4) gas flow rate. The total gas flow rate is set to 20 sccm at 20 Pa and 40 sccm at 60 Pa. The relationship between the flow rates and the gas concentrations in the chamber is assumed to be monotonic. DC self-bias measurements are performed at both pressures as a function of the argon content for both single- ($N = 1$) and triple-frequency ($N = 3$) "peaks-type" ($\theta_k = 0°$) and "valleys-type" ($\theta_{k\neq 2} = 0°$ with $\theta_2 = 180°$) waveforms with a fixed total voltage amplitude of $\phi_{\text{tot}} = 150$ V. For $N = 3$, these waveforms have $\phi_1 = 75$ V, $\phi_2 = 50$ V, and $\phi_3 = 25$ V. PROES measurements are performed at both pressures for argon content values between 0% and 90% but are limited to "peaks-type" $N = 3$ waveform described above as a detailed example. These measurements are carefully compared to the PIC/MCC simulation results, including the simulated spatio-temporal attachment rates, time-averaged particle densities, spatio-temporal bulk electric fields, and spatio-temporal mean electron energies, in order to fully explain the effects of the changing electro-negativity on the spatio-temporal electron power absorption dynamics in subsection 6.2.1. The changes in these quantities are then correlated to the discharge's electrical symmetry and DC self-bias to determine the effects of a changing electronegativity on the EAE. This work is also published in Brandt *et al.*, Plasma Sources Sci. Technol. 28, 095021 (2019) [BS19].

In chapter 7, the experimental methodology outlined in the γ-CAST diagnostic (subsection 3.2.4) is utilized to qualitatively examine changes in the SEEC of plasma-facing aluminum and aluminum oxide disk surfaces of varying surface roughness provided by the Lam Research corporation [228]. Changes in the SEEC from a change in surface material (Al or Al_2O_3 films) and from changes in film thickness are considered in section 7.1, while changes in the SEEC as a result of a changing surface profile, i.e., changing surface roughness, is considered in section 7.2. Each aluminum disk of a given surface roughness (8 Ra, 24 Ra, 75 Ra, and 150 Ra, respectively) is exposed to air in order to form an aluminum oxide film [196] and is then placed on the powered electrode. Notably, each surface roughness is measured in Ra, i.e., the absolute mean deviation from a surface's average height in μm; each surface roughness is thus defined by averaging over the entire surface in chapter 7. The discharge is operated in argon with a trace admixture of neon (10%) for using the neon PROES line (see subsection 3.2.2) at pressures in the 100 Pa to 200 Pa range with the glass cylinder removed and the gap separation fixed to $d = 32$ mm, in order to span the α- to γ-mode transition and help increase the geometric asymmetry of the setup to enhance the powered sheath voltage waveform $\phi_{\text{sp}}(t)$ and its associated electron power absorption dynamics. A single-frequency (13.56 MHz) waveform with $\phi_{\text{tot}} = 200$ V is utilized for simplicity in the spatio-temporal excitation dynamics, which approximately yields a -100 V DC self-bias under these conditions. PROES

measurements are then performed at 100 Pa, 150 Pa, and 200 Pa for the aluminum oxide film case of a given disk (surface roughness). The aluminum oxide film is then sputtered off using a "peaks-type" triple-frequency waveform at 1 Pa with $\phi_{\text{tot}} = 500$ V (and thus $\phi_1 = 250$ V, $\phi_2 = 166.66$ V, and $\phi_3 = 83.33$ V) and the grounded electrode moved to its maximum gap separation of $d = 15$ cm. DC self-biases around approximately -415 V are generated by this waveform, with an increase in the DC self-bias magnitude of about 25-30 V starting from near -400 V occurring over the duration of the sputtering process. This increase is likely produced by the change in the surface material from an aluminum oxide to clean aluminum metal, as suggested by the PROES measurements in chapter 7. The sputtering process is monitored by an Ocean Optics atomic spectrometer connected to a fiber optic aimed at the plasma through one of the chamber windows. Specifically, the 394.4 nm emission line associated with an atomic transition of sputtered aluminum atoms (Al $3s^2 4s \rightarrow 3s^2 3p$) [229] is observed to increase during the sputtering process until it reaches a plateaued value at the end of the sputtering process (i.e., for a clean disk) after approximately 40 minutes. The sputtering procedure itself does not appear to affect the PROES measurements unless a large number of additional cleanings are performed and only seems to affect the clean metal case, as confirmed by additional cleanings and PROES measurements for the 24 Ra disks. This may be a product of sputtering significantly changing the surface profile (see the hypotheses in chapter 7), but due to lack of surface profilometry measurements this is not confirmed in this work. All measurements shown in chapter 7 are performed many cleanings before this deviation from the cleaning process appears. PROES measurements for the clean metal surface are then performed at identical conditions to the oxide film counterpart. The other aluminum disks of differing surface roughness undergo the same procedure. An additional set of measurements is also performed for a 24 Ra disk which had developed a much thicker oxide film due to long term exposure to air [196]. The methodology outlined in subsection 3.2.4 is then utilized to compare the individual cases using the optical excitation rate intensity ratio I_γ / I_α as a function of the changing surface parameters.

Chapter 4

Effects of voltage waveform tailoring and the Electrical Asymmetry Effect on charged particle dynamics in argon

The consequences of using various highly customized voltage waveforms in electropositive RF-CCPs are investigated at both low (3 Pa and 5 Pa) and high (200 Pa) neutral gas pressures in this chapter. The effects of the voltage waveform tailoring technique on the electrical asymmetry effect when using more than two consecutive voltage harmonics, the possibility of controlling the electron power absorption dynamics through the shape of the applied voltage waveform, and the resulting impact these effects have on relevant process parameters such as plasma density, ion flux, mean ion energy are all discussed in the following sections. In section 4.1, experimental voltage and RFEA measurements (see section 3.2) are performed for a variety of dual- and triple-frequency waveforms at low pressure. These measurements demonstrate that the control range of the EAE is enhanced by adding the third harmonic component at a fixed total voltage amplitude, increasing the range of potential mean ion energies at a given electrode while also enhancing the sheath expansion heating and therefore the total ion flux. The spatio-temporal excitation dynamics of discharges driven by customized voltage waveforms are also investigated experimentally at low pressure in subsection 4.1.1. Further voltage and RFEA measurements at low pressure are presented in subsection 4.1.2. The spatio-temporal excitation dynamics are also examined at high pressure using PROES (see subsection 3.2.2) in section 4.2. From this data, important conclusions are drawn on how customized driving voltage waveforms dictate the spatio-temporal electron power absorption dynamics of the discharge and therefore control the subsequent ionization and plasma density localization in the discharge. Additional findings on the control of the ion FEDFs at both electrodes as a result of these changes in electron heating further expand the documentation of the low pressure discharge.

4.1 Charged particle dynamics and ion flux-energy distributions in multi-frequency low pressure argon discharges

In this section, the experimental setup of section 3.1 is operated in argon gas at low pressures (3 Pa and 5 Pa) for a variety of multi-frequency waveforms (see subsection 3.1.1 and section 3.4) at a fixed voltage amplitude ($\phi_{\mathrm{tot}} = 210$ V) in order to demonstrate the enhanced control over the electron power absorption dynamics and highly relevant plasma parameters (e.g., plasma densities, ion FEDFs at the electrodes) when using voltage waveforms with more than two consecutive applied harmonics. The spatio-temporal excitation rate obtained via PROES (see subsection 3.2.2), and thus the associated electron heating and ionization, are discussed in conjunction with voltage measurements and circuit model results for each pressure as a function of the number of applied harmonics N and the chosen harmonic phases. For the low pressure (3 Pa) discharge presented in subsection 4.1.1, these results are complemented by RFEA measurements of the ion FEDFs at both electrodes to establish a fundamental understanding of both the electron heating dynamics and its effects on ion FEDF control. Additional ion FEDF and DC self-bias results at 5 Pa are presented in subsection 4.1.2. The work in sections 4.1.1 and 4.1.2 are also published in Berger *et al.* [BB15] and Franek *et al.* [FJ15], respectively.

4.1.1 Electron power absorption and the Electrical Asymmetry Effect in multi-frequency low pressure argon discharges

The control of the electron heating dynamics and the ion flux-energy distribution functions through the use of voltage waveform tailoring, i.e., by changing the number of applied harmonics and their relative phases, is considered in this section for a low-pressure argon discharge. As stated in section 3.4, the gap distance and gas pressure are fixed to $d = 30$ mm and 3 Pa, respectively. Measurements for both dual- ($N = 2$) and triple-frequency ($N = 3$) discharges are performed and compared with one another.

The experimentally measured DC self-bias normalized by the total applied voltage amplitude ($\phi_{\mathrm{tot}} = 210$ V), again denoted $\bar{\eta}$, for the $N = 3$ waveforms is plotted as a function of the second and third harmonic phases (θ_2, θ_3, respectively) in figure 4.1(a). The minimum DC self-bias value is found at $\theta_{2,3} = 0°$, while the maximum value is found at $\theta_2 = 180°$ and $\theta_3 = 0°$, corresponding to the "peaks-type" and "valley-type" waveforms, respectively, where these extrema are usually found (see subsection 4.1.2 [FJ15]). DC self-bias values between these extrema are easily achieved by fixing the third harmonic's phase to zero ($\theta_3 = 0°$) and varying θ_2, as in subsection 4.1.2. Thus, θ_2 is again utilized throughout the following measurements in order to control the DC self-bias and the mean ion energy at the electrodes.

A comparison of the normalized DC self-bias for $N = 3$ with $\theta_3 = 0°$ (squares), $N = 3$

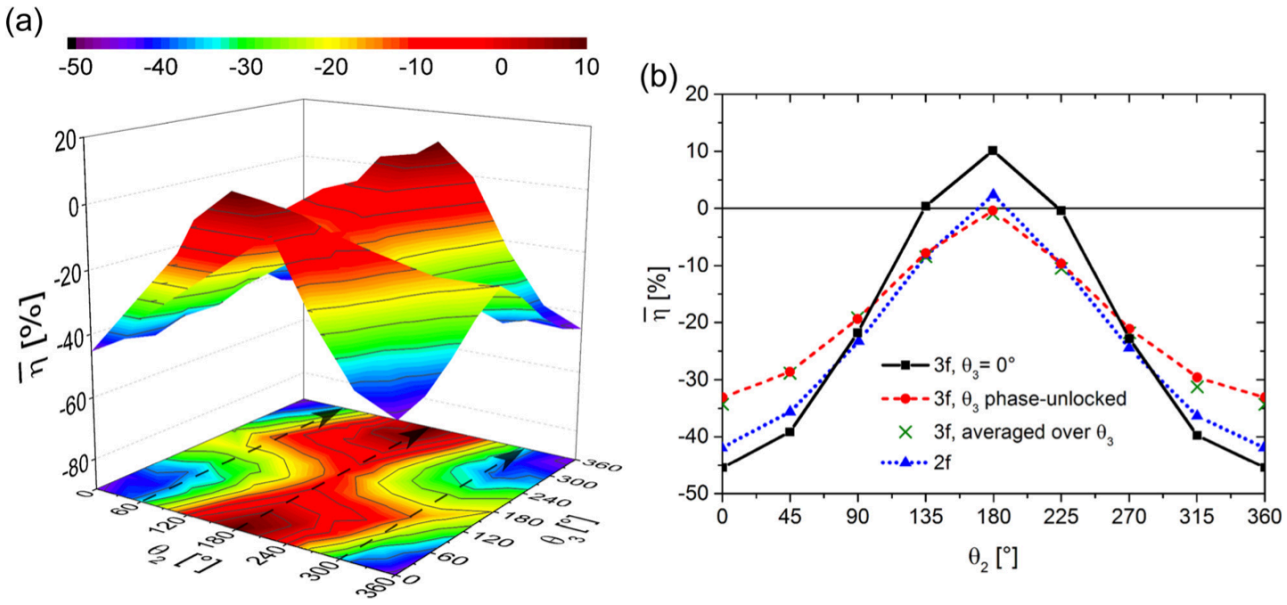

Figure 4.1: (a) The normalized DC self-bias, $\bar{\eta}$, in the $N = 3$ discharge as a function of the second (θ_2) and third (θ_3) harmonic phases. (b) A comparison of the normalized DC self-bias for three ($\theta_3 = 0°$, solid line) and two (dotted line) consecutive harmonics as a function of the second harmonic phase. Additional $N = 3$ measurements including a phase-unlocked third harmonic (dashed line) and $\bar{\eta}$ values (crosses) calculated by averaging over θ_3 for each θ_2 in the phase-locked discharge, i.e., from (a), are also shown. The arrows in (a) are indicative of the calculation of the phase-averaged DC self-bias values in (b). Discharge conditions are: Ar, 3 Pa, $d = 30$ mm, $\phi_{\mathrm{tot}} = 210$ V. Figure reproduced from its original publication in Berger *et al.*, J. Appl. Phys. 118, 223302 (2015) [BB15] with the permission of AIP Publishing.

with the third harmonic phase-unlocked (circles), and for $N = 2$ is shown in figure 4.1(b). For the phase-unlocked case, which was performed and analyzed by Birk Berger [BB15], the trigger signal from the synchronization unit in the setup (see section 3.1), which ensures each harmonic is synchronized and thus phase-locked, is removed for the third harmonic's generator. Therefore, this generator applies a slightly higher frequency of 40.685 MHz to the discharge, which is slightly different from the expected integer harmonic frequency for the third harmonic (40.680 MHz). Thus, in the phase-unlocked case, it is not possible to measure the third harmonic's voltage amplitude and phase from the Fourier transform using the high voltage probe (see subsection 3.2.1), as the voltage waveform changes for each RF cycle and no stable signal can be obtained. Instead, a temporal mean voltage waveform is measured over a sufficient number of RF cycles to obtain information on the first and second harmonic amplitudes and phases. The third harmonic voltage amplitude is then estimated using the following procedure. In the phase-locked $N = 3$ discharge, the power delivered by the third harmonic (40.68 MHz) generator needs to be altered by approximately 10% for different values of θ_2 and θ_3 in order to maintain a constant third harmonic voltage at the electrode surface. When the third harmonic is phase-unlocked, the third harmonic's phase (θ_3) evolves in time, such that the temporal mean waveform measured is effectively averaging over the entire range of θ_3 values. Therefore, a mean value for the third harmonic's amplitude is calculated and the 40.68 MHz generator is set to the corresponding applied power value. Again, the DC self-bias is normalized by the sum of all applied harmonics' voltage amplitudes. Instabilities produced by phase-unlocking the high frequency component of the voltage waveform were not observed in the discharge during this process. For comparison with the phase-unlocked case, the measured $N = 3$ DC self-bias values in figure 4.1(a) were averaged over θ_3 for each θ_2, as indicated by the dashed arrows in figure 4.1(a) and the X marks in figure 4.1(b). Excellent agreement is found between the phase-unlocked and θ_3 averaged DC self-bias values, which justifies the procedure explained above.

The normalized DC self-bias $\bar{\eta}$ in figure 4.1 is shifted towards negative values in all measurements due to the presence of the setup's geometrical asymmetry. For example, there is a non-negligible negative DC self-bias at $\theta_2 = 90°$ in figure 4.1(b) despite the extrema of the driving voltage waveform being equal in magnitude ($\widetilde{\phi}_{\max} = -\widetilde{\phi}_{\min}$). As in subsection 4.1.2, this geometric asymmetry is reduced but not eliminated by the presence of the glass confinement cylinder [FJ15]. The DC self-bias for the $N = 2$ waveforms, therefore, varies from $\bar{\eta} = -42\%$ at $\theta_2 = 0°$ to $\bar{\eta} = 3\%$ at $\theta_2 = 180°$, enabling a control range for the DC self-bias of 45%. The inclusion of a third harmonic for the $N = 3$ waveforms increases this control range to 55% and thus constitutes a substantial increase of 20% in the control range compared to the $N = 2$ discharge. However, if the third harmonic is phase-unlocked, the control range decreases to 33% because the DC self-bias is averaged over all θ_3 phases, which is generally undesirable when attempting to maximize this control range (e.g., see figure 4.1(a)). This is a substantial decrease of 40% compared to the phase-locked $N = 3$ discharge. Figure 4.1 therefore demonstrates that including higher harmonics in the voltage waveform tailoring technique requires all harmonics to be phase-locked with one another in order to optimize the control range of the DC self-bias and the EAE. Notably, the inclusion of phase-unlocked high frequency harmonics may generally improve the electron heating and the plasma properties, such as plasma density (see chapter 2), but will not improve control over the mean ion energy

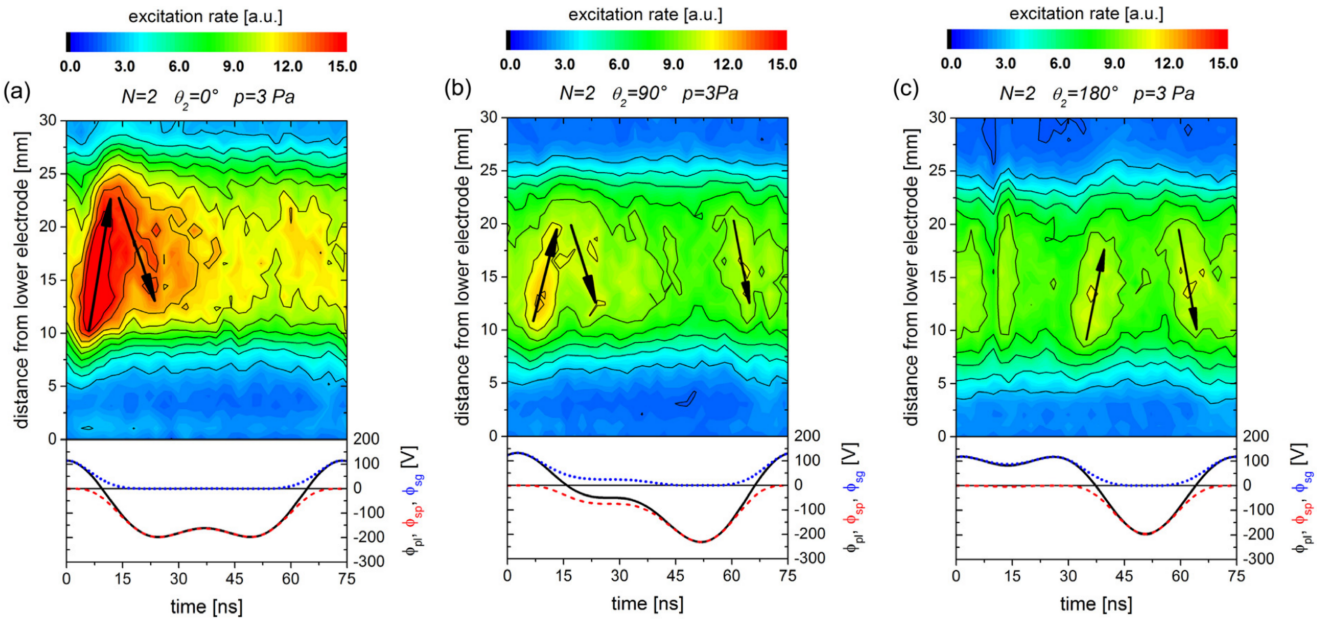

Figure 4.2: Spatio-temporally resolved plots of the Ne $2p_1$ excitation rate in the $N = 2$ discharge ($\theta_{1,3} = 0°$) at (a) $\theta_2 = 0°$, (b) $\theta_2 = 90°$, and (c) $\theta_2 = 180°$. The arrows in each plot represent the estimated trajectories of the electron beams. The appropriate voltage drop across the plasma, ϕ_{pl} (solid line), and across each electrode sheath, ϕ_{sp} (dashed line), ϕ_{sg} (dotted line), are shown below each spatio-temporal plot as a function of time across one RF period of the fundamental frequency. Discharge conditions are: Ar, 3 Pa, $d = 30$ mm, $N = 2$, $\phi_{\mathrm{tot}} = 210$ V. Figure reproduced from its original publication in Berger *et al.*, J. Appl. Phys. 118, 223302 (2015) [BB15] with the permission of AIP Publishing.

because of the time-averaged effects on the DC self-bias explained above. The phase-unlocked $N = 3$ discharge is therefore not considered in the following measurements, such that $\theta_3 = 0°$ for $N = 3$ waveforms in this chapter.

The experimentally measured electron-impact excitation rate for the Neon line discussed in subsection 3.2.1 obtained via PROES is shown in figure 4.2 for several $N = 2$ waveforms with different θ_2 values. The total voltage waveform ($\phi_{\mathrm{pl}} = \eta + \widetilde{\phi}(t)$, black solid line), as well as the voltage drops across the powered electrode's sheath (ϕ_{sp}, red dashed line) and the grounded electrode's sheath (ϕ_{sg}, blue dotted line) obtained from the model in section 2.2, is plotted underneath the spatio-temporal excitation rate in each case. The time axes of the voltage and spatio-temporal excitation rate plots are shifted such that the excitation maximum caused by sheath expansion heating (see section 2.4) at the powered electrode occurs at the same time in the RF period as observed in previous PIC/MCC simulations [46] in order to replicate the correct temporal dependence between the excitation rate and the sheath dynamics. The maximum sheath voltage at the grounded electrode is significantly lower at all phase shifts compared to that of the powered electrode, again due to the presence of the geometric asymmetry and thus $\varepsilon < 1$. A similar effect is observed in subsection 4.1.2.

The electron heating under these conditions is observed in figure 4.2 to be primarily from

the α-heating mode at all phase shifts. Recall that the α-mode is characterized by sheath expansion heating (see section 2.4), which is the dominant cause of electron excitation here. For the $N = 2$ "peaks-type" waveform at $\theta_2 = 0°$ (figure 4.2(a)), the grounded sheath expands in the time interval 60 ns $\leqslant t \leqslant$ 74 ns and accelerates electrons towards the powered electrode. Notably, the grounded electrode sheath expands relatively slowly compared to the sheath expansion at the powered electrode sheath as a result of the overall reduced grounded sheath voltage and the shape of the voltage waveform (e.g., see the slope of ϕ_{sg} in figure 4.2(a)). The discharge electrons, furthermore, have not been significantly heated prior to this grounded sheath expansion for a significant part of the RF period. The electron beam generated by this expansion gains comparably less energy as a result, such that these electrons are not accelerated to energies above the excitation threshold (19 eV) of the Neon line observed in PROES. This explains why the excitation from the grounded sheath expansion is hardly visible in figure 4.2(a). These warm electrons do, however, propagate towards the powered electrode and are subsequently reflected by the powered electrode's sheath expansion. The powered sheath expands quickly (e.g., see the slope of ϕ_{sp}) in the time interval 0 ns $\leqslant t \leqslant$ 20 ns as a product of the high maximum sheath voltage at the powered electrode. The warm electron beam generated at the grounded electrode is again accelerated by the powered sheath expansion and reaches sufficient energy to exceed the excitation threshold and thus cause the beam to become visible. This new electron beam propagates towards the grounded electrode and hits the local collapsing sheath and undergoes yet another reflection back into the bulk plasma. These beams are scattered by electron-neutral collisions as they cross the bulk plasma. Significant excitation is observed from these two reflected beams in figure 4.2(a), with the second reflection at the collapsing grounded sheath causing notably less excitation compared to that from the powered sheath expansion. The $N = 2$ intermediate-type waveform with $\theta_2 = 90°$ (figure 4.2(b)), by comparison, causes the sheath at the powered electrode to expand much slower during the time where beam electrons from a prior grounded sheath expansion arrive (0 ns $\leqslant t \leqslant$ 20 ns). The energy gained during this reflection and thus excitation rate caused by this reflected beam are both reduced as a result. Since the excitation threshold for the observed line is close to the ionization energy of neutral argon atoms (see subsection 3.2.2), this can also be assumed to be a reduction in the ion flux and plasma density, as seen later in this section. This also causes a reduction of the excitation rate at different times in the same RF period. A "valley-type" waveform with $\theta_2 = 180°$ (figure 4.2(c)) further reduces the excitation rate produced by the electron beam from the powered electrode sheath expansion (30 ns $\leqslant t \leqslant$ 50 ns) relative to that caused by the beam generated by the grounded electrode sheath expansion (60 ns$\leqslant t \leqslant$ 74 ns). The powered electrode sheath does, however, expand more quickly than the intermediate waveform at $\theta_2 = 90°$. This reduction in the powered sheath expansion heating can be explained by the fact that the powered sheath expands shortly before the grounded sheath expansion for $\theta_2 = 180°$, whereas the opposite was observed for 0° and 90°. Therefore, cold electrons are accelerated by the powered (bottom) sheath for 180° while warm electrons originating from this expansion then undergo reflection at the grounded sheath expansion, resulting in comparably weaker excitation from the powered sheath expansion. Notably, this is the reverse of the situation seen in figure 4.2(a) ($\theta_2 = 0°$), where cold electrons are accelerated by the grounded electrode sheath. The velocity u_{B} of these beams generated at the powered electrode, determined by the arrows indicating their trajectories in figure 4.2, may therefore be lower at 90° ($u_{\mathrm{B}} \approx 1.38 \times 10^6$

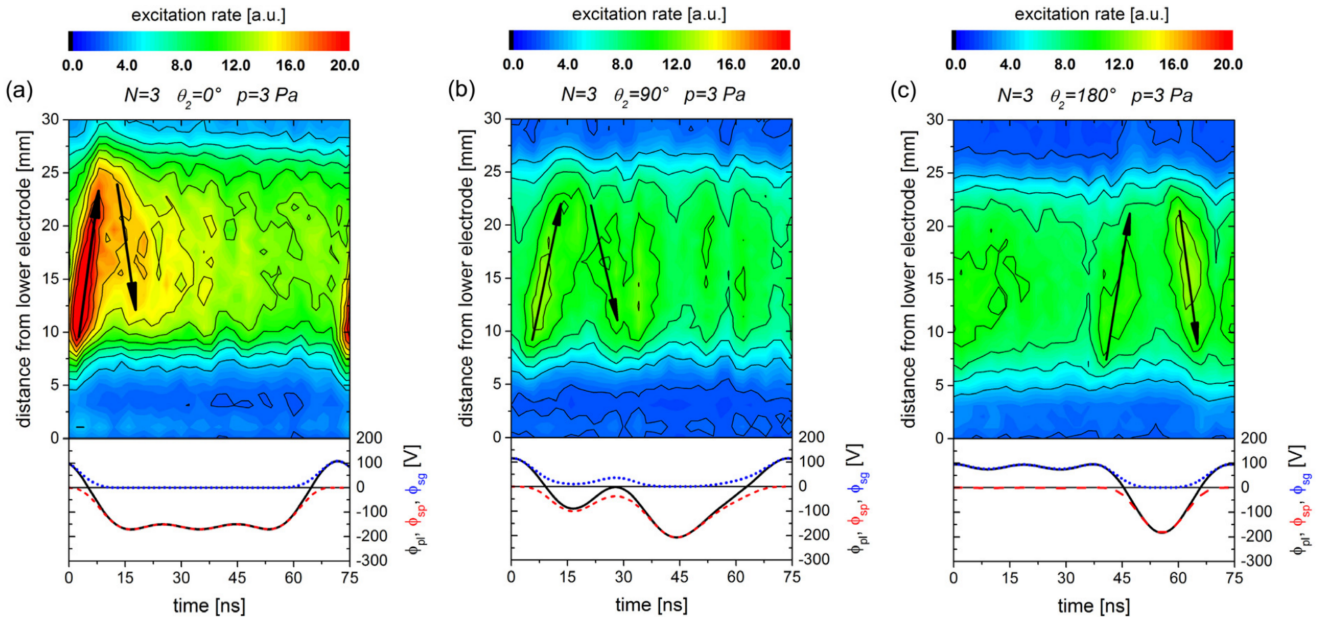

Figure 4.3: Spatio-temporally resolved plots of the Ne $2p_1$ excitation rate in the $N = 3$ discharge ($\theta_{1,3} = 0°$) at (a) $\theta_2 = 0°$, (b) $\theta_2 = 90°$, and (c) $\theta_2 = 180°$. The arrows in each plot represent the estimated trajectories of the electron beams. The appropriate voltage drop across the plasma, ϕ_{pl} (solid line), and across each electrode sheath, ϕ_{sp} (dashed line), ϕ_{sg} (dotted line), are shown below each spatio-temporal plot as a function of time across one RF period of the fundamental frequency. Discharge conditions are: Ar, 3 Pa, $d = 30$ mm, $N = 3$, $\phi_{\mathrm{tot}} = 210$ V. Figure reproduced from its original publication in Berger *et al.*, J. Appl. Phys. 118, 223302 (2015) [BB15] with the permission of AIP Publishing.

m/s) and 180° ($u_{\mathrm{B}} \approx 1.80 \times 10^6$ m/s) compared to 0° ($u_{\mathrm{B}} \approx 2.20 \times 10^6$ m/s). These beam velocities can only be roughly estimated from the excitation profiles, however.

The measured spatio-temporal excitation rate for the $N = 3$ waveforms is shown in figure 4.3 for various values of θ_2. The excitation rate exhibits similar effects due to changing θ_2 to those seen for the $N = 2$ waveforms (figure 4.2). The inclusion of the third, high frequency harmonic (40.68 MHz) while keeping a fixed total voltage amplitude causes each sheath expansion velocity to increase as the slopes in the voltage waveform become steeper. Therefore, the velocity of the electron beams generated by each sheath expansion in the triple-frequency discharge for a given θ_2, again determined by the trajectories seen in figure 4.3, may always be higher than those in the dual-frequency discharge and as a result, the excitation rate from sheath expansion heating is generally enhanced for $N = 3$ waveforms compared to the $N = 2$ waveforms. Electron beam velocities for the $N = 3$ waveforms of $u_{\mathrm{B}} \approx 2.62 \times 10^6$ m/s at $\theta_2 = 0°$, $u_{\mathrm{B}} \approx 1.69 \times 10^6$ m/s at $\theta_2 = 90°$, and $u_{\mathrm{B}} \approx 2.19 \times 10^6$ m/s at $\theta_2 = 180°$ are calculated from these trajectories. As with the $N = 2$ waveforms, the sheath expansion heating at one side is observed to be enhanced by the reflection of the warm electron beam generated by the previous expansion of the opposite sheath at $\theta_2 = 0°, 180°$, i.e., the "peaks-type" and "valleys-type" waveforms. In the intermediate waveform case (90°), the sheath expansion velocities are again reduced due to the shape of the voltage

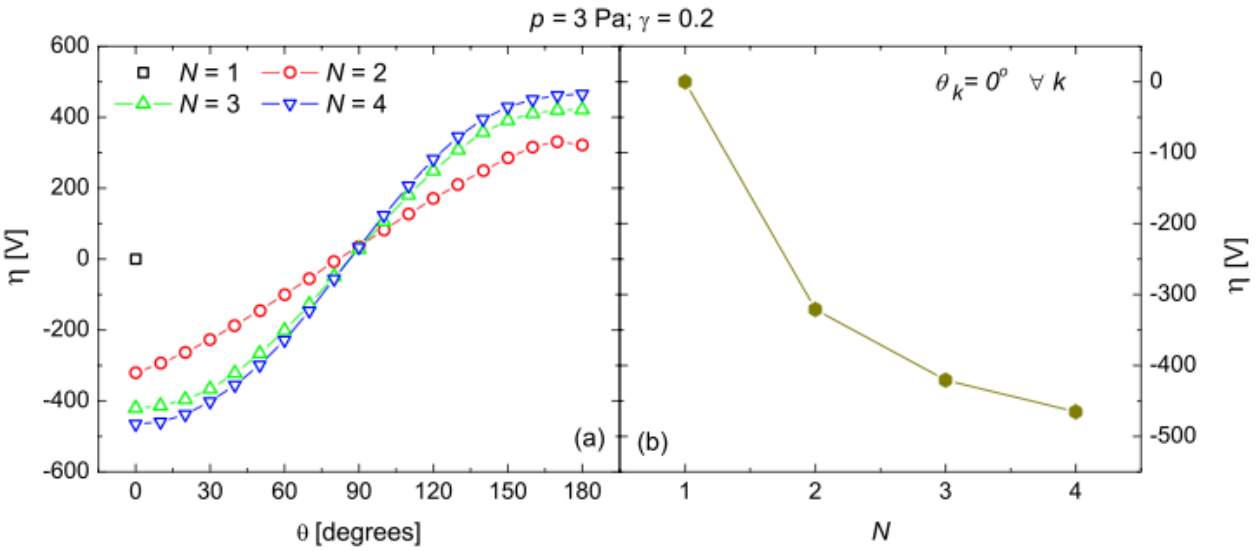

Figure 4.4: (a) DC self-bias η obtained in previous simulations as a function of the even harmonic phases $\theta_2 = \theta_4$ (referred to as θ) and the number of applied harmonics N. (b) DC self-bias for different numbers of applied harmonics for $\theta_k = 0° \ \forall \ k$. Simulation conditions are: Ar, 3 Pa, $d = 30$ mm, $\gamma = 0.2$, $\phi_{\text{tot}} = 800$ V, $\theta_{1,3} = 0°$. Figure provided from Derzsi *et al.*, Plasma Sources Sci. Technol. 22, 065009 (2013) [46]. ©IOP Publishing. Reproduced with permission. All rights reserved.

waveform, resulting in reduced electron heating and observed excitation rate. Furthermore, the geometric asymmetry of the setup once again increases the excitation rate for the $\theta_2 = 0°$ and limits the electron heating caused by the grounded (top) sheath expansion. The enhanced excitation rate for the $N = 3$ waveforms overall compared to the $N = 2$ waveforms, though, indicates that the ion flux and plasma density are increased by the addition of the high frequency third harmonic despite keeping a fixed total voltage amplitude.

The experimental spatio-temporal excitation dynamics measured in this subsection qualitatively agree with previous kinetic simulations performed for similar conditions [46] and correspond to their original experimental verification [BB15]. For comparison with the results presented here, some of these simulation results are provided in figures 4.4-4.6. Figure 4.4 shows the DC self-bias from these simulations as a function of $\theta_2 = \theta_4$ and as a function of increasing N. Figures 4.5 and 4.6 show the spatio-temporal ionization in these simulations for increasing N and as a function of $\theta_2 = \theta_4$ for $N = 4$ waveforms, respectively. The primary difference between the experiment and the simulations is again the presence of the geometric asymmetry in the experimental setup, which is not included in these simulations. This geometric asymmetry, as noted in the discussions of figure 4.2 and figure 4.3, causes a reduction in all excitation rates adjacent to the effectively larger grounded electrode in comparison to those adjacent to the powered electrode. This is again due to the inherently altered symmetry parameter ε limiting the maximum possible grounded sheath voltage $\phi_{\text{sg,max}}$ at all phase shifts.

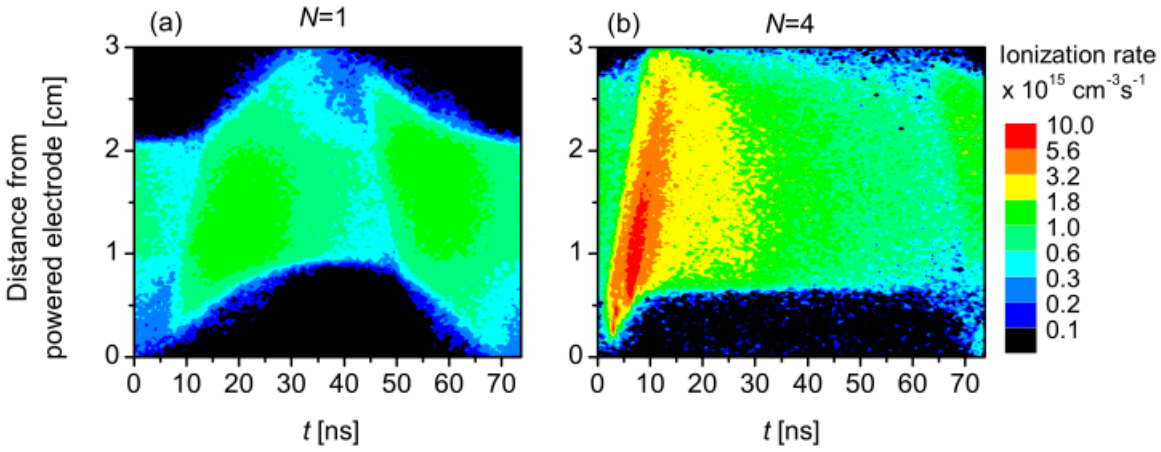

Figure 4.5: Spatio-temporal plots of the ionization rate for different numbers of applied harmonics (N) obtained in previous simulations using logarithmic color scales. Simulation conditions are: Ar, 3 Pa, $d = 30$ mm, $\gamma = 0.2$, $\phi_{\mathrm{tot}} = 800$ V, $\theta_k = 0° \; \forall \; k$. Figure provided from Derzsi *et al.*, Plasma Sources Sci. Technol. 22, 065009 (2013) [46].

Figure 4.7 shows the measured ion flux-energy distributions (using the RFEA diagnostic, see subsection 3.2.3) at the powered (figure 4.7(a),(c)) and grounded (figure 4.7(b),(d)) electrodes as a function of θ_2 for both the $N = 2$ (figure 4.7(a),(b)) and $N = 3$ (figure 4.7(c),(d)) discharges. These measurements are performed under identical conditions ($d = 30$ mm, 3 Pa, $\phi_{\mathrm{tot}} = 210$ V) to the previous measurements in this section but for a purely argon gas discharge to avoid any contribution from positive neon ions. The ion mean free path at these conditions is shorter than the maximum thickness of the RF sheaths adjacent to the electrodes, and therefore the probability of an ion undergoing collisions inside the sheath is relatively high (similar to subsection 4.1.2). This allows for the broad shape of the ion FEDF between $\epsilon_{\mathrm{i}} = 0$ and $\epsilon_{\mathrm{i,max}}$, as the collisions randomize the energies of ions as they transit through the sheath. The FEDF becomes increasingly narrow at the powered electrode with increasing θ_2, like in subsection 4.1.2, due to the increasing DC self-bias and therefore decreasing mean powered sheath voltage (e.g., see ϕ_{sp} in figure 4.3). This effect is further enhanced by including the third harmonic, as the control range of the DC self-bias is larger in the $N = 3$ discharge. The reverse trend can be seen at the grounded electrode, where increasing θ_2 leads to a higher mean grounded sheath voltage and thus a broader distribution of ion energies. The total ion flux, additionally, can be seen to be significantly increased in the $N = 3$ discharge compared to the $N = 2$ discharge.

Furthermore, a flux peak at high energies is observed in most of the measured IEDFs at both electrodes, which is associated with ions which traverse the sheath without undergoing a collision. Notably, the ion transit time across the RF sheath is much longer than one RF cycle (74 ns). The energy gap of a possible bi-modal structure in the FEDF at a given electrode due to such collisionless transit of ions can be estimated using equation (9) from [230]. The energy gap for the applied frequencies considered here typically only reaches energies of a few eV (e.g., consider figures 4.2 and 4.3) because the ions take many RF periods to traverse the

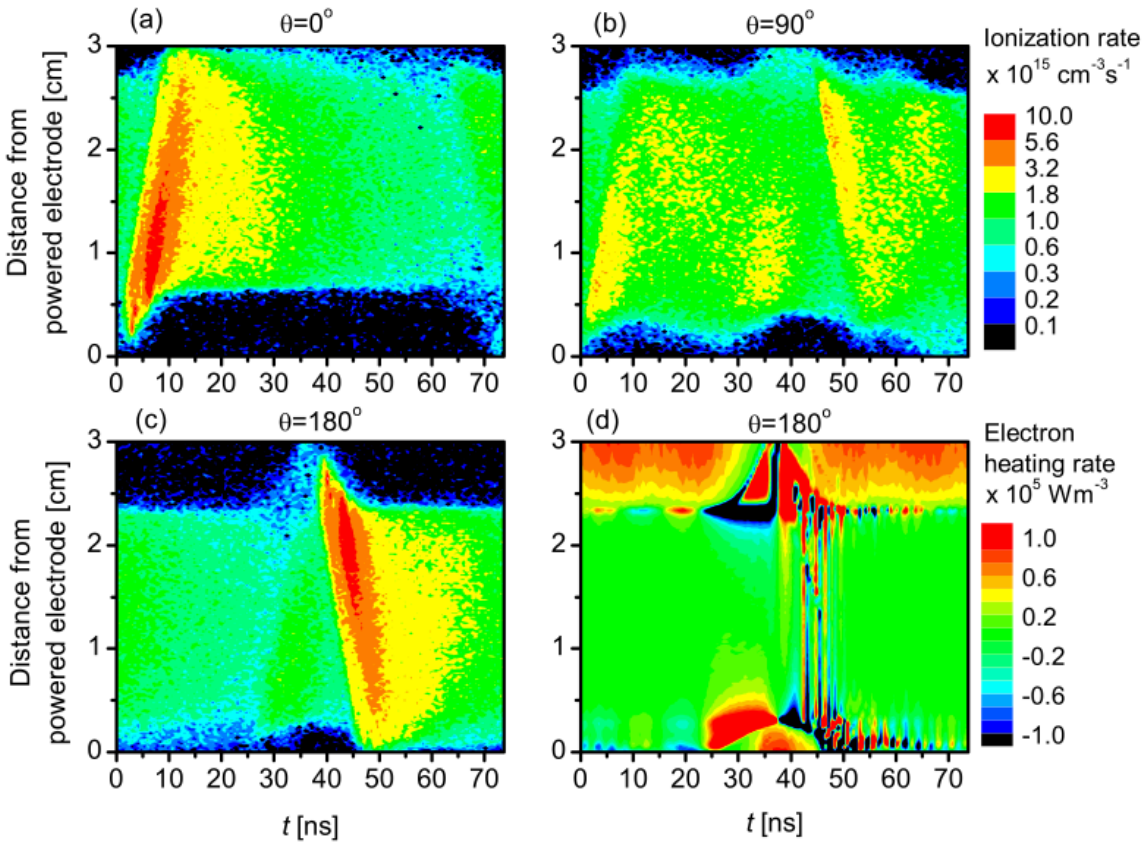

Figure 4.6: (a)-(c) Spatio-temporal plots of the ionization rate obtained in previous simulations for different values of $\theta_2 = \theta_4$ (referred to as θ) for $N = 4$ waveforms and (d) the electron heating rate for $\theta_2 = \theta_4 = 180°$. Simulation conditions are: Ar, 3 Pa, $d = 30$ mm, $\gamma = 0.2$, $\phi_{\text{tot}} = 800$ V, $\theta_{1,3} = 0°$. The color scales in (a)-(c) are logarithmic. Figure provided from Derzsi *et al.*, Plasma Sources Sci. Technol. 22, 065009 (2013) [46].

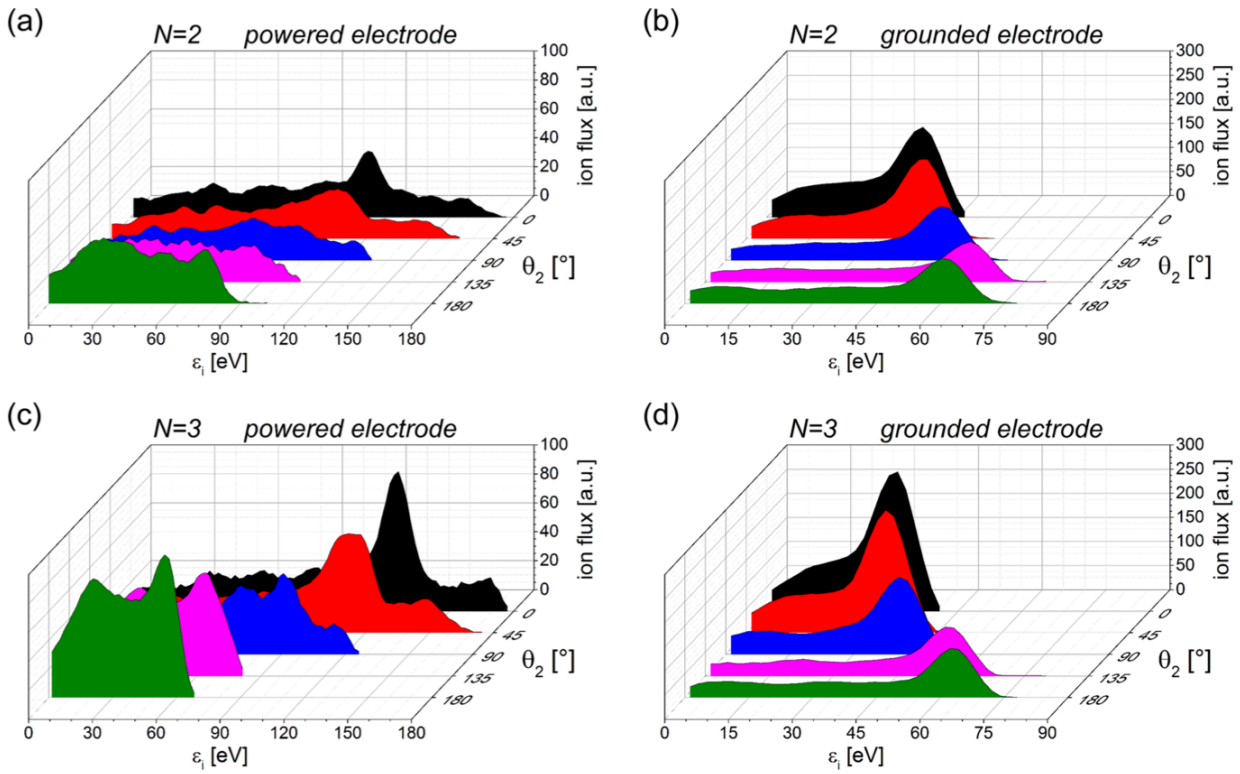

Figure 4.7: Measured ion flux-energy distribution functions as a function of the second harmonic's phase θ_2 in the $N = 2$ ((a) and (b)) and $N = 3$ ((c) and (d)) discharges at the powered ((a) and (c)) and grounded ((b) and (d)) electrode. The ion energy is denoted as ϵ_i. Discharge conditions are: Ar, 3 Pa, $d = 30$ mm, $\phi_\mathrm{tot} = 210$ V, $\theta_{1,3} = 0°$. Figure reproduced from its original publication in Berger *et al.*, J. Appl. Phys. 118, 223302 (2015) [BB15] with the permission of AIP Publishing.

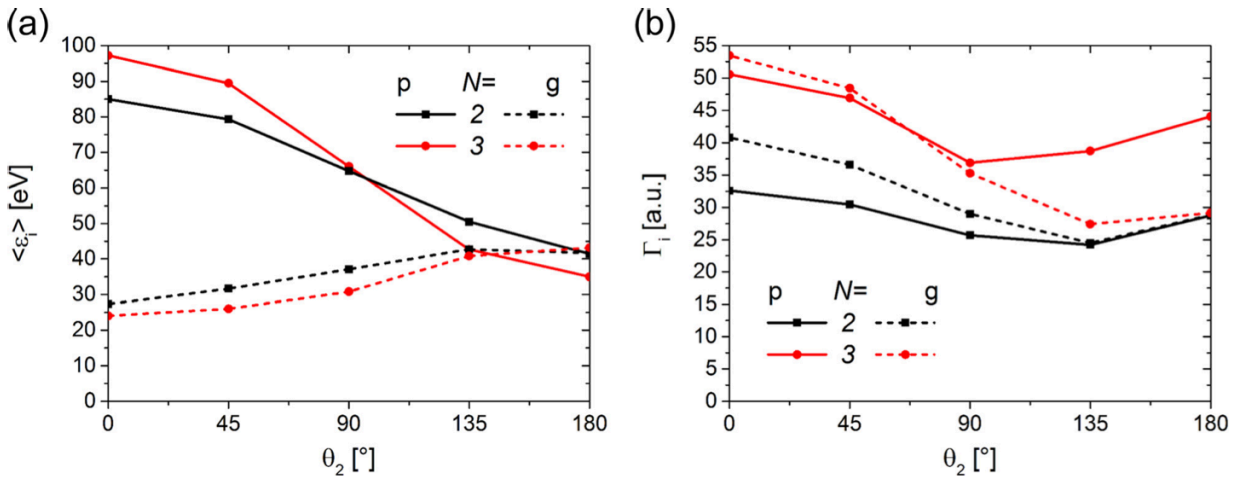

Figure 4.8: (a) The mean ion energy and (b) total ion flux as a function of the second harmonic's phase θ_2 calculated from the measured ion FEDF (equations (3.5) and (3.6)) in the $N = 2$ (squares) and $N = 3$ (circles) discharges at the powered (p, solid lines) and grounded (g, dashed lines) electrodes. The ion energy is denoted as ϵ_i. Discharge conditions: Ar, 3 Pa, $d = 30$ mm, $\phi_{tot} = 210$ V, $\theta_{1,3} = 0°$. Figure reproduced from its original publication in Berger *et al.*, J. Appl. Phys. 118, 223302 (2015) [BB15] with the permission of AIP Publishing.

sheath and cannot respond to the high frequency RF signal due to their low mobility. The energy gap is generally below the resolution of the RFEA (1-2 eV) as a result such that any possible bi-modal structures cannot be resolved in figure 4.7. The maximum possible energy a transiting ion can reach then corresponds approximately to the mean sheath voltage for the respective sheath [205]. Collisions within the sheath redistribute the energy of ions and produce ion flux at energies below the high energy flux peak. Ion flux with energies above this value corresponds to an artifact from the RFEA's imperfect filtering of the RF signal from the RFEA data, which can be seen as this feature is not present in the measurements at the grounded electrode. The error this artifact produces in the mean ion energy and ion flux at the electrode in later analysis of the FEDFs is negligible.

Recall that the total ion flux and the mean ion energy can be calculated from the measured FEDF using equations (3.5) and (3.6) from subsection 3.2.3, respectively. The resulting mean ion energy and total ion flux from the data in figure 4.7 is plotted as a function of θ_2 for both the $N = 2$ (squares) and $N = 3$ (circles) discharges in figure 4.8. Solid lines are used to depict values for measurements at powered electrode (p) while dashed lines are used for measurements at the grounded electrode (g). Figure 4.8 demonstrates that the mean ion energy at the powered electrode decreases as a function of increasing θ_2, as predicted by the increasing DC self-bias and the decreasing mean powered sheath voltage implied from the previous PROES measurements. The opposite trend occurs at the grounded electrode for the same reasons as the previous measurements. The total ion flux increases significantly at both electrodes in the $N = 3$ discharge due to the aforementioned enhancement of the electron heating and thus higher ionization rates and plasma densities implied by the observed

excitation rate in PROES (figure 4.2 and figure 4.3). The sheath widths are also reduced by the increased plasma density, as also seen in subsection 4.1.2, and thus the probability for collisions inside the sheaths is also reduced. Thus, more ions hit the electrode at higher energies and the ion flux fraction at high energies, i.e., the flux peak near the mean sheath voltage, is enhanced. The shape of the FEDF in figure 4.7 therefore depends on the number of applied harmonics N, with higher ion fluxes at specific energies, which is usually desirable in applications, being seen much more dominantly in the $N = 3$ discharge.

The total ion flux in figure 4.8(b) is also affected by the choice of θ_2 for both the $N = 2$ and $N = 3$ discharges. In both discharges, the total ion flux is observed to decrease at both electrodes with θ_2 but eventually begins to increase with θ_2 after a certain phase, depending on the chosen N and the electrode. Again, the changes in the $N = 3$ discharge are notably larger than those seen in the $N = 2$ discharge. These changes, furthermore, are relatively large compared to the simulation results of Derzsi *et al.* [46], and can be attributed to the geometric asymmetry present in the experiment which is absent from the simulations [44]. The mean ion energy and ion flux of these previous simulations can be seen in figures 4.9 and 4.10, respectively. The changes in ion flux to each electrode are related to the specific ionization profiles in the discharge, and thus the electron heating and the excitation rate profiles observed in PROES, occurring for each waveform.

The excitation rate profile measured by PROES, denoted here by $\hat{E}(x,t)$, can therefore be qualitatively correlated to the ion flux by examining the mean excitation rates adjacent to each electrode. Recall that the measured emission line of PROES utilized here is chosen such that the measured excitation rate probes the dynamics of electrons with energies near the ionization threshold of argon atoms (see subsection 3.2.2). The excitation rate measured by PROES is therefore assumed to be qualitatively indicative of the ionization rate as well. The ionization rate in the halves of the discharge adjacent to each electrode can therefore be qualitatively considered using the excitation rate in each discharge half. Effectively, this splits the discharge into two spatial regions of interest (ROI) defined by the center of the bulk plasma, i.e., the position x_c, for a given phase θ_2. Notably, this position does not need to be located at the middle of the electrode gap for an electrically and geometrically asymmetric discharge and may change for different conditions. To remove any concern of dependence on the RF phase (i.e., time t), the mean excitation profile over one RF period $\left\langle \hat{E}(x) \right\rangle = \int_0^T \hat{E}(x,t)dt$, where $T = 74$ ns is the RF period, is considered. Two spatial positions at which the mean excitation profile in the regions adjacent to the powered and grounded electrodes, respectively, decreases to 1/e (i.e., the exponential e^{-1}) of its maximum value are then identified to estimate the maximum sheath width at each electrode. The bulk center x_c is calculated as the midpoint between these two maximum sheath width positions. Thus, x_c corresponds to the location of maximum ion density, where the electric field is nearly zero, to a fairly good approximation [63]. The ion motion in the region surrounding x_c is primarily caused by diffusion, such that ions located closer to the grounded electrode ($> x_c$) diffuse towards the grounded electrode and ions located closer to the powered electrode ($< x_c$) diffuse towards the powered electrode. The excitation above and below x_c, therefore, is associated with the ionization occurring in these regions which produces ions

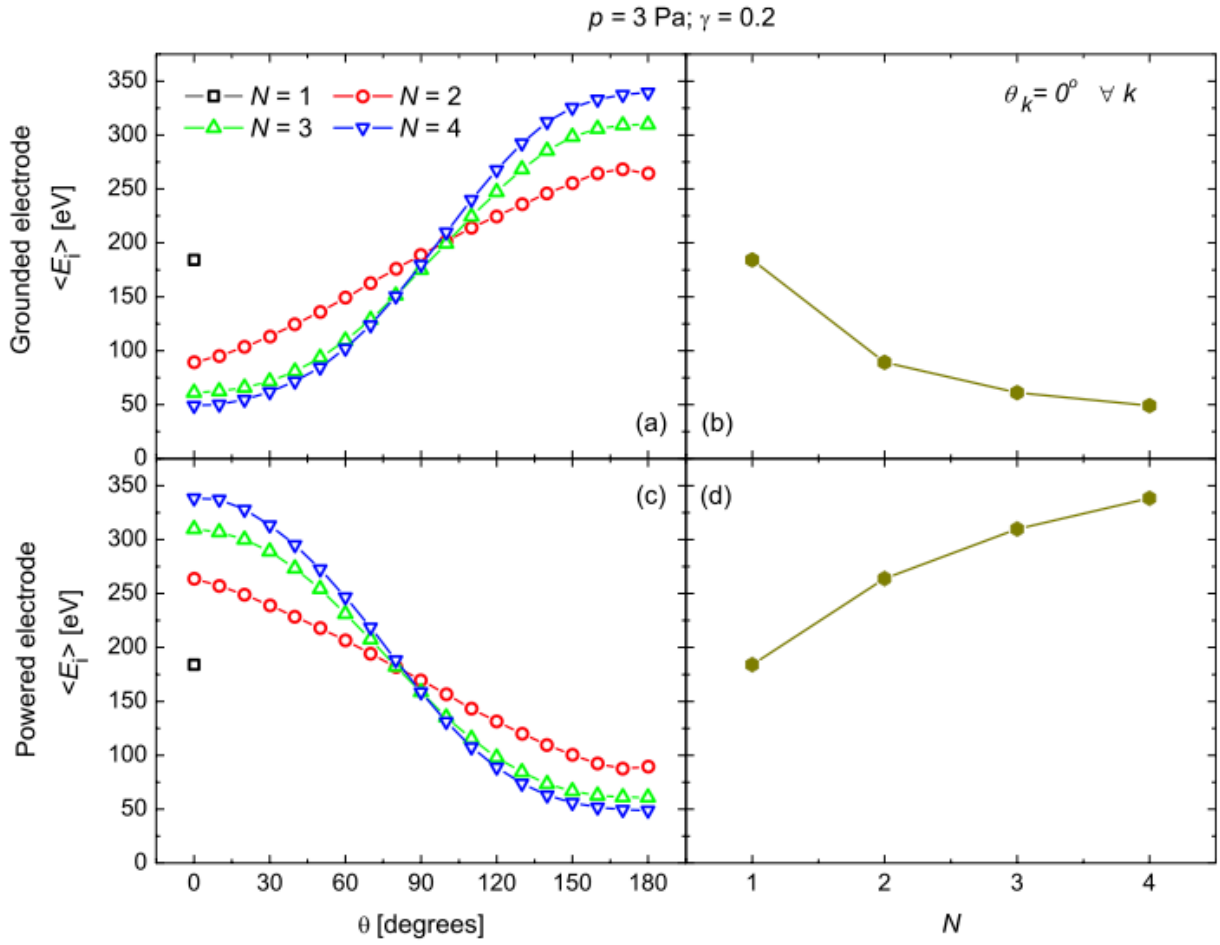

Figure 4.9: Mean ion energy $\langle E_\mathrm{i} \rangle$ at the grounded (top row) and powered (bottom row) electrodes obtained in previous simulations as a function of (left column) the even harmonic phases $\theta_2 = \theta_4$ (referred to as θ) and the number of applied harmonics N, and (right column) as a function of N for $\theta_k = 0° \ \forall \ k$. Simulation conditions are: Ar, 3 Pa, $d = 30$ mm, $\gamma = 0.2$, $\phi_\mathrm{tot} = 800$ V, $\theta_{1,3} = 0°$. Figure provided from Derzsi *et al.*, Plasma Sources Sci. Technol. 22, 065009 (2013) [46]. ©IOP Publishing. Reproduced with permission. All rights reserved.

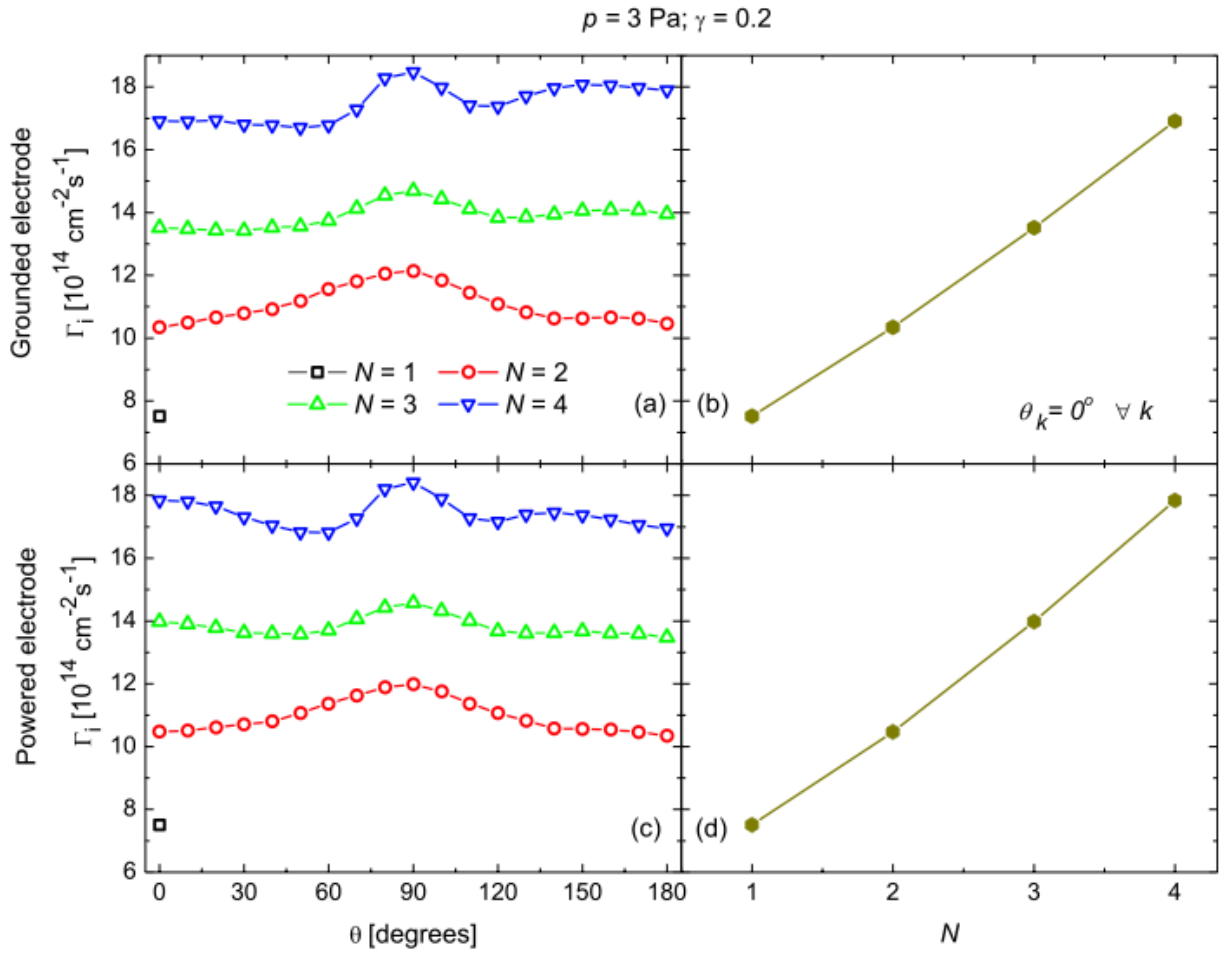

Figure 4.10: Ion flux Γ_i at the grounded (top row) and powered (bottom row) electrodes obtained in previous simulations as a function of (left column) the even harmonic phases $\theta_2 = \theta_4$ (referred to as θ) and the number of applied harmonics N and (right column) as a function of N for $\theta_k = 0° \ \forall \ k$. Simulation conditions are: Ar, 3 Pa, $d = 30$ mm, $\gamma = 0.2$, $\phi_{tot} = 800$ V, $\theta_{1,3} = 0°$. Figure provided from Derzsi *et al.*, Plasma Sources Sci. Technol. 22, 065009 (2013) [46].

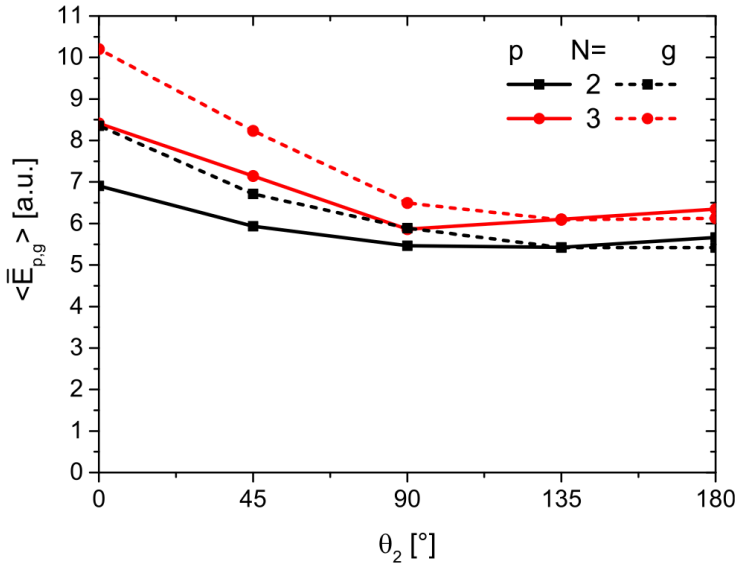

Figure 4.11: The temporally and spatially averaged mean excitation rate in two spatial regions of interest (ROI) adjacent to the powered (p) and grounded (g) electrode, $\langle \bar{E}_{\mathrm{p,g}} \rangle$, as a function of the second harmonic's phase θ_2 in the $N = 2$ (squares) and $N = 3$ (circles) discharges. The ROIs are defined by $0 \leqslant x \leqslant x_{\mathrm{c}}$ and $x_{\mathrm{c}} \leqslant x \leqslant d$ for the powered and grounded electrode, respectively, where x_{c} is the center of the plasma bulk. Discharge conditions are: Ar, 3 Pa, $d = 30$ mm, $\phi_{\mathrm{tot}} = 210$ V, $\theta_{1,3} = 0°$. Figure reproduced from its original publication in Berger *et al.*, J. Appl. Phys. 118, 223302 (2015) [BB15] with the permission of AIP Publishing.

that diffuse towards the respective electrode surface and thus is also associated with the number of ions propagating towards each electrode, i.e., the ion flux. The spatially averaged excitation rate value in each region can then be calculated as $\langle \bar{E}_{\mathrm{p}} \rangle = \int_0^{x_{\mathrm{c}}} \left\langle \hat{E}(x) \right\rangle dx$ and $\langle \bar{E}_{\mathrm{g}} \rangle = \int_{x_{\mathrm{c}}}^{d} \left\langle \hat{E}(x) \right\rangle dx$ for the powered-adjacent and grounded-adjacent regions, respectively.

The spatially and temporally averaged excitation rate for each region of interest ($\langle \bar{E}_{\mathrm{p}} \rangle$ and $\langle \bar{E}_{\mathrm{g}} \rangle$) calculated from this approach is shown in figure 4.11. Notably, the mean excitation rate follows an identical trend with increasing θ_2 to that observed for the ion flux measured by the RFEA (figure 4.8(b)). The changing ion flux with θ_2 can thus be explained by the different excitation dynamics in the each corresponding half of the plasma bulk. Furthermore, this demonstrates that the non-intrusive PROES diagnostic could be utilized to qualitatively monitor and detect changes in the ion flux to the electrodes.

The RFEA measurements in this subsection and in subsection 4.1.2 demonstrate that the ion FEDF at each electrode can be controlled using RF-CCPs driven by customized voltage waveforms produced by the voltage waveform tailoring technique outlined in chapters 2 and 3. This control is particularly important for many applications [33, 231–233]. The mean ion energy at a surface can be controlled in such discharges by tuning the second harmonic's phase θ_2. Here, the average value of the mean ion energy when applying two consecutive harmonics ($N = 2$) is found to be 64 eV, which can be varied through the choice of θ_2 by

35%. At the same time, the ion flux varies only by ±15%. For the $N = 3$ discharge, the average value for the mean ion energy is similar at 60 eV, but has an increased control range with θ_2 of 47%. Additionally, the ion flux variation for $N = 3$ of ±16% is almost the same as in the $N = 2$ discharge. The triple-frequency discharge therefore has several advantages over the dual-frequency discharge as it extends the control range of the mean ion energy, increases the total ion flux (associated with processing rates in applications), and retains the desired separate control of the mean ion energy and ion flux.

4.1.2 Control of the DC self-bias and ion flux-energy distributions in multi-frequency, low pressure argon discharges

The application of the voltage waveform tailoring technique to indirectly control relevant process parameters in both industrial and fundamental multi-frequency discharges through the EAE is experimentally investigated in this section. The experimental setup of section 3.1 is operated in argon gas at 5 Pa with $d = 4$ cm for a variety of dual-frequency ($N = 2$) and triple-frequency ($N = 3$) waveforms (see section 3.4) at a fixed total applied voltage amplitude ($\phi_{\text{tot}} = 120$ V). Voltage measurements (see subsection 3.2.1) demonstrate that the control range of the DC self-bias via the EAE is enhanced in the $N = 3$ discharge. RFEA measurements at the powered electrode (see subsection 3.2.3) are also performed at these conditions. The resulting ion FEDF measurements demonstrate that the mean ion energy control range is also increased due to the extended control of the DC self-bias in the $N = 3$ discharge. The total ion flux is also found to be increased due to an enhancement of the sheath expansion heating (i.e., the α-mode) for the $N = 3$ waveforms. This work is also published alongside a complete description of the experimental setup in [FJ15].

The DC self-bias normalized by the total applied voltage amplitude (ϕ_{tot}), denoted by $\bar{\eta}$, is shown to be controlled at fixed harmonic amplitudes as a function of the phases of the second (θ_2) and third (θ_3) harmonics in figure 4.12 for both the experiment and the circuit model outlined in sections 2.2 and 2.3. The symmetry parameter in the model is taken to be constant for all phases at a value of $\varepsilon = 0.63$. This value is determined by averaging over the ε values obtained in the experiment for each combination of θ_2 and θ_3 by solving for ε in equation (2.14), neglecting the floating and bulk terms due to operation in a low pressure electropositive discharge, and using the measured value of the DC self-bias η and the extrema of the driving voltage waveform. Notably, this choice of ε in the model is a simplification, as significant changes in symmetry can be observed as a function of the relative harmonic phases, primarily due to enhancement of ionization and the plasma density near one sheath (e.g., see subsection 4.1.1 and section 6.2). Thus, ε varies significantly (±40%) as a function of the harmonics' phases around this averaged value in actuality. Good agreement can none-the-less be seen between the experiment (figure 4.12(a)) and the model (figure 4.12(b)). The overall shape of each is very similar and resembles the results of a previous simulation on geometrically symmetric triple-frequency discharges [45]. However, in contrast to this study, the measured and modeled DC self-bias here are shifted towards negative

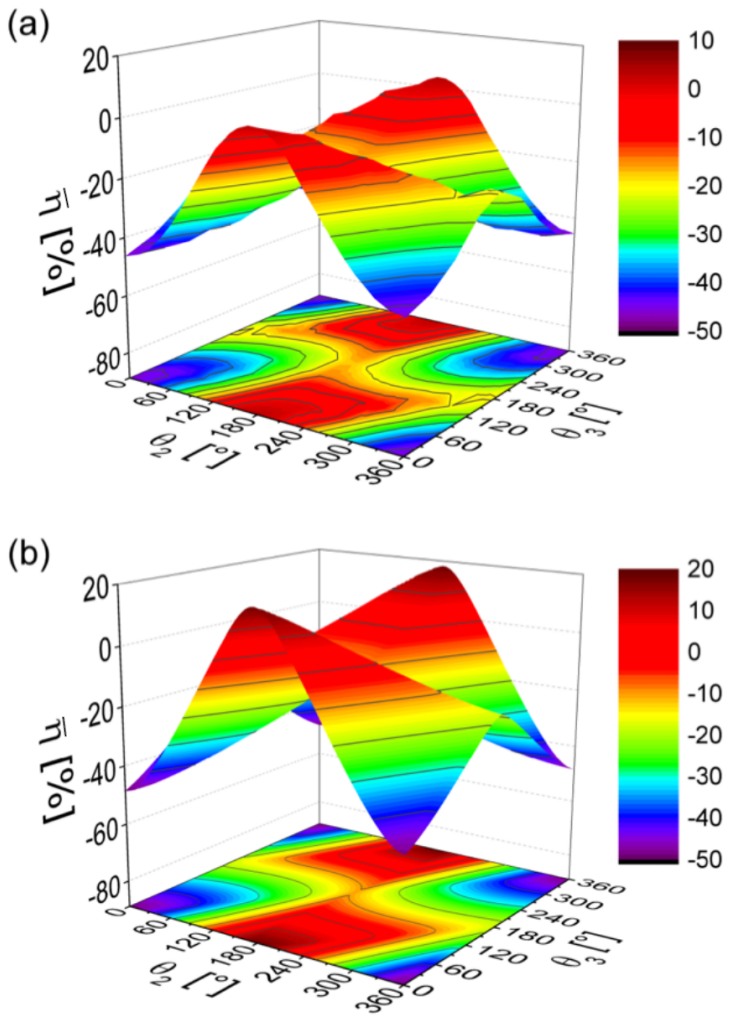

Figure 4.12: Normalized DC self-bias $\bar{\eta}$ as a function of the second and third harmonic phases from (a) the experiment and (b) the circuit model outlined in sections 2.2 and 2.3. In the model, $\varepsilon = 0.63$ is used. Discharge conditions are: Ar, 5 Pa, $d = 4$ cm, $\phi_{\mathrm{tot}} = 120$ V with harmonic amplitudes according to equation (3.1). Figure reproduced from its original publication in Franek *et al.*, Rev. Sci. Instrum. 86, 053504 (2015) [FJ15] with the permission of AIP Publishing.

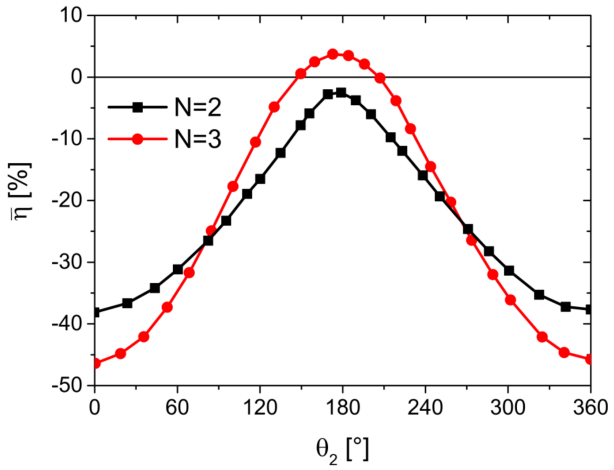

Figure 4.13: Normalized DC self-bias as a function of the second harmonic phase for two ($N = 2$) and three ($N = 3$) applied consecutive harmonics in the experiment ($\theta_1 = \theta_3 = 0°$). Discharge conditions are: Ar, 5 Pa, $d = 4$ cm, $\phi_{\mathrm{tot}} = 120$ V with harmonic amplitudes according to equation (3.1). Figure reproduced from its original publication in Franek *et al.*, Rev. Sci. Instrum. 86, 053504 (2015) [FJ15] with the permission of AIP Publishing.

values as a result of the experimental discharge's geometric asymmetry ($A_{\mathrm{p}}/A_{\mathrm{g}} < 1$) which is excluded from that work. This geometric asymmetry is the result of capacitive coupling from the glass containment cylinder to the grounded chamber walls [39, 99, 100] and causes the symmetry parameter to deviate from unity for any voltage waveform, as in equation (2.15). The control range of the DC self-bias is also slightly smaller in the experiment compared to that of the model with constant ε. This is the result of the mean ion density ratio ($\frac{\bar{n}_{\mathrm{sp}}}{\bar{n}_{\mathrm{sg}}}$) in equation (2.15), and therefore the symmetry parameter, varying as a function of θ_2 and θ_3 in the experiment. Again, this is not the case for the model (figure 4.12(b)), where ε is taken to be independent of the harmonic phases. The minimum and maximum DC self-bias are obtained for $\theta_{2,3} = 0°$, and $\theta_2 = 180°$ with $\theta_3 = 0°$, respectively, in both the experiment and the model.

Figure 4.12 therefore demonstrates that there are multiple ways to tune $\bar{\eta}$ between its extrema via phase control by choosing specific values of θ_2 and θ_3. Notably, in the model, this is equivalent to modifying $\widetilde{\phi}_{\mathrm{max,min}}$ by changing the shape of the driving voltage waveform while keeping ε the same, while both $\widetilde{\phi}_{\mathrm{max,min}}$ and ε vary in the experiment to achieve this control. However, the simplest control method which also maximizes the control range over $\bar{\eta}$ is to fix $\theta_3 = 0°$ and vary θ_2 [45, 46]. This allows access to the full range of DC self-bias values and is utilized throughout the following sections/chapters to control the DC self-bias and therefore the mean ion energy at the electrodes.

Furthermore, figure 4.13 shows that the control of the DC self-bias via θ_2 is enhanced by applying additional consecutive harmonics under otherwise identical discharge conditions. The values of η are again normalized by ϕ_{tot}. The electrically asymmetric triple-frequency discharge ($N = 3$), as compared to the dual-frequency case ($N = 2$), spans a significantly

larger set of $\bar{\eta}$ values. This is, again, a result of a changing ion density ratio, and thus a changing symmetry parameter (see subsection 4.1.1 and section 6.2), due to ionization from the α-mode, which is typically dominant under these conditions, being enhanced near the more quickly expanding sheath edge, i.e., by an enhancement of the SAE (see section 2.4). Notably, it should be mentioned that the difference between the absolute values of the global extrema of the voltage waveform changes for the same $\phi_{\text{tot}} = 120$ V for the $N = 3$ waveforms compared to the $N = 2$ waveforms (e.g., for "peaks-type" waveforms, see figure 3.12) as a result of destructive interference by the additional harmonic for θ_2 values near 0° ("peaks-type" waveform) and 180° ("valleys-type" waveform). Therefore, the spatial asymmetry in the ion density, i.e., the changes in ε, are also due to an enhancement of the AAE (see section 2.3). The control parameter in both cases ($N = 2, 3$) is the second harmonic's phase θ_2, since $\theta_1 = \theta_3 = 0°$. The DC self-bias in the dual-frequency discharge ($N = 2$) is negative for all phases due to the geometrical asymmetry and the control range is approximately 35% of the total driving voltage amplitude, between $\bar{\eta} = -38\%$ at $\theta_2 = 0°$ to $\bar{\eta} = -3\%$ at $\theta_2 = 180°$. When the third frequency is included ($N = 3$), this control range increases to approximately 50%, from $\bar{\eta} = -46\%$ at $\theta_2 = 0°$ to $\bar{\eta} = 4\%$ at $\theta_2 = 180°$. Importantly, small positive DC self-bias values, in addition to $\bar{\eta} = 0$, can be accessed in the $N = 3$ discharge, which is not possible in the dual-frequency case under these conditions. The electrical control range is therefore significantly extended by approximately 43% by increasing the number of applied harmonics from $N = 2$ to $N = 3$. This extended control range is particularly important since the DC self-bias largely determines the mean sheath voltages (see section 2.3) and thus the range of ion energy control at the electrodes produced by the EAE, as seen in subsection 4.1.2.

The ion FEDFs measured at the powered electrode are shown in figure 4.14 as a function of θ_2 in both the dual- and triple-frequency discharge. The ion mean free path under these experimental conditions is smaller than the width of the powered electrode sheath, and therefore the probability of ions undergoing collisions within the sheath is relatively high [44, 204–207]. The resulting ion FEDFs exhibit a broad shape between $\epsilon_{\text{i}} = 0$ and $\epsilon_{\text{i,max}}$ as a result. Furthermore, the shape of the FEDF can be controlled by tuning θ_2. The DC self-bias is most negative at $\theta_2 = 0°$ and, appropriately, the time averaged voltage drop across the powered sheath is largest. Conversely, the DC self-bias is maximum at $\theta_2 = 180°$ such that the time averaged voltage drop across the powered sheath is smallest. Ions thus gain significantly more energy in the $\theta_2 = 0°$ case, but due to collisions as they traverse the sheath region, a broad distribution across a large range of energies is observed instead of a peak at the high mean sheath voltage. As θ_2 is increased, the maximum powered sheath voltage decreases, resulting in a reduced range of observed energies in the FEDF. Thus, the distribution becomes narrower in energy space and the maximum ion energy decreases as θ_2 increases. For example, in the $N = 2$ discharge (figure 4.14(a)), the maximum ion energy decreases from 108 eV to 58 eV. The addition of a third harmonic ($N = 3$), in agreement with figure 4.13, causes a larger change in the ion FEDF as a function of θ_2 at the same fixed ϕ_{tot} as the $N = 2$ case. Thus, for $N = 3$, the maximum possible ion energy is increased to $\epsilon_{\text{i,max}} = 118$ eV and the minimum width of the FEDF is decreased to $\epsilon_{\text{i,max}} = 50$ eV. The ion flux also becomes larger in the $N = 3$ case due to the enhanced electron heating (e.g., see section 4.1) compared to the $N = 2$ discharge [45, 46]. The fraction of the ion flux

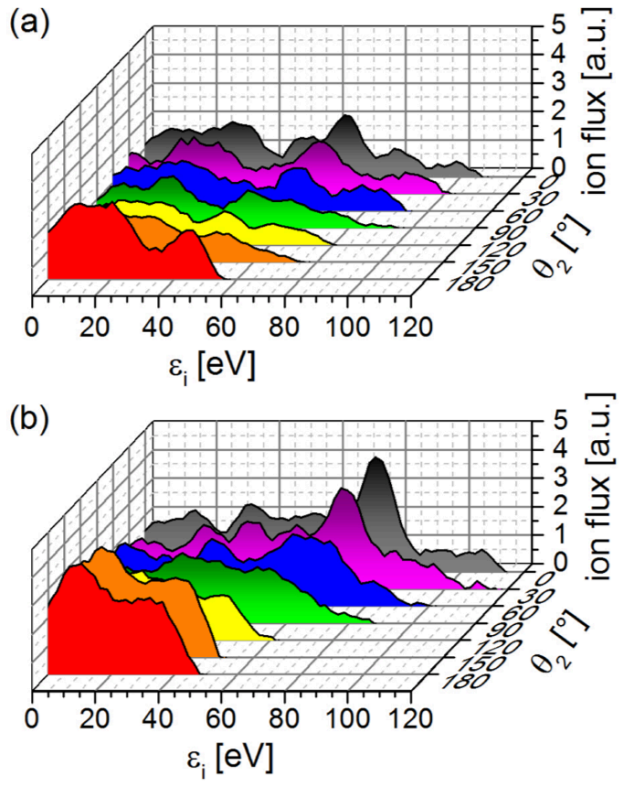

Figure 4.14: Ion flux-energy distribution functions measured at the powered electrode using an RFEA as a function of the second harmonic phase for (a) two ($N = 2$) and (b) three ($N = 3$) applied consecutive harmonics in the experiment ($\theta_2 = \theta_3 = 0°$). The ion energy is denoted as ϵ_i. Discharge conditions: Ar, 5 Pa, $d = 4$ cm, $\phi_\mathrm{tot} = 120$ V with harmonic amplitudes according to equation (3.1). Figure reproduced from its original publication in Franek *et al.*, Rev. Sci. Instrum. 86, 053504 (2015) [FJ15] with the permission of AIP Publishing.

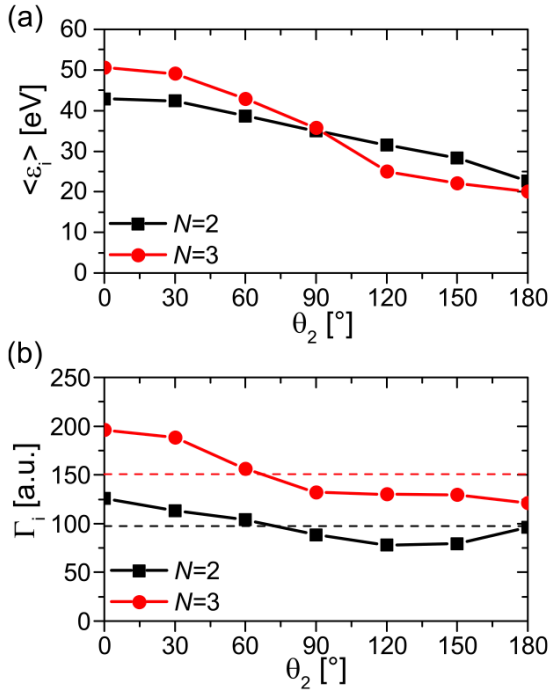

Figure 4.15: (a) The mean ion energy, $\langle\epsilon_\mathrm{i}\rangle$, and (b) total ion flux, Γ_i, calculated from the measured ion FEDF via equations (3.5) and (3.6) as a function of θ_2 for the electrically asymmetric dual- ($N = 2$) and triple-frequency ($N = 3$) discharges with fixed $\theta_{1,3} = 0°$. The phase averaged ion flux, $\Gamma_{\mathrm{i},\theta_2}$, for each N is shown as a dashed line. Note $\Gamma_{\mathrm{i},\theta_2} = 1/n \sum_{i=1}^{n} \Gamma(\theta_2 = (i-1) \times 30°)$, where $n = 7$ is the number of measured Γ_i for different θ_2 values taken in 30°-steps. The ion energy is denoted as ϵ_i. Discharge conditions are: Ar, 5 Pa, $d = 4$ cm, $\phi_\mathrm{tot} = 120$ V with harmonic amplitudes according to equation (3.1). Figure reproduced from its original publication in Franek *et al.*, Rev. Sci. Instrum. 86, 053504 (2015) [FJ15] with the permission of AIP Publishing.

at relatively high energies is also increased for the triple-frequency discharge because the sheath width is reduced due to the increased plasma density as a function of N resulting from enhanced electron heating for higher applied frequencies [45, 46, 140, 141]. The sheath therefore becomes less collisional, i.e., s_p is reduced but is still larger than the ion mean free path, and therefore more ions reach the electrode at higher energies. Thus, this mechanism changes the shape of the ion FEDF between $N = 2$ and $N = 3$, with significantly more ion flux overall and particularly, more highly energetic ion flux at small θ_2 values. This implies the mean ion bombardment energy at the substrate in applications can be controlled over a large range of energies with higher ion flux (and thus process rate) by including a third harmonic without increasing the total driving voltage. It should be noted that the inclusion of higher frequency harmonics while keeping ϕ_tot constant typically corresponds to an increase in the applied power since the discharge current will also be higher.

The control of ion properties at the powered electrode surface is therefore significantly improved by utilizing advanced customized voltage waveforms. The mean ion energy $\langle\epsilon_\mathrm{i}\rangle$

and the total ion flux Γ_i, in particular, quantify this enhanced control and are essential parameters in many applications. Figure 4.15 shows these quantities, using the definitions for each in subsection 3.2.3, as a function of θ_2 for the $N = 2, 3$ cases considered in this section. The mean ion energy (figure 4.15(a)) can be tuned from approximately 43 eV (51 eV) to 23 eV (20 eV) by varying θ_2 from 0° to 180° for $N = 2$ (and $N = 3$), respectively. Notably, this corresponds to a control range for $\langle \epsilon_i \rangle$ which is extended by more than 50% for $N = 3$ compared to $N = 2$. This difference between $N = 2$ and $N = 3$ is also larger at $\theta_2 = 0°$ than at $\theta_2 = 180°$ due to the reduced sheath width and thus the reduced collisionality in the sheath for the triple-frequency discharge. Therefore, for $N = 3$, the mean ion energy is increased for all values of θ_2 compared to those obtained for $N = 2$, i.e., the $\langle \epsilon_i \rangle$ curve for $N = 3$ appears slightly shifted upwards compared to the $N = 2$ curve in figure 4.15(a). Furthermore, the electrical control range of $\langle \epsilon_i \rangle$ is enlarged for $N = 3$ as a result of the increased control range for η as seen in figure 4.13 and figure 4.14. This larger control interval of the DC self-bias is thus associated with a larger control interval for $\langle \epsilon_i \rangle$, as suggested by the voltage balance (see equation (2.1)). This enhanced control range of η and the reduced collisionality in the sheath are thus the mechanisms responsible for the enhanced ion energy control as a function of increasing number of applied harmonics.

The ion flux is also generally larger for $N = 3$ compared to $N = 2$ due to the enhancement of the electron power absorption dynamics from adding the higher frequency component [45, 46, 140], as seen in figure 4.15(b). In both types of discharges, the ion flux varies by approximately ±23% as a function of θ_2, as determined by a relative deviation from the averaged value (see each respective dashed line in figure 4.15(b)). Furthermore, Γ_i tends to decrease as θ_2 increases. This is the result of a reduced ion density near the powered electrode sheath which is due to the decreasing powered sheath voltage as θ_2 is increased, similar to the results of subsection 4.1.1. As θ_2 is increased, the discharge's electrical asymmetry is reduced, the DC self-bias becomes less negative, the powered electrode sheath voltage also decreases, and thus this electron power absorption and ionization rate near the powered electrode are also reduced. Notably, the reverse occurs at the grounded electrode sheath, such that the grounded sheath voltage and ionization rate near the grounded electrode increases, but due to the geometric asymmetry, this only partially compensates the decrease in electron power absorption and ionization. Thus, the overall electron power absorption, ionization, and subsequently the plasma density and particle fluxes, are reduced at $\theta_2 \neq 0°$, with a minimum generally observed at 180°. Similar behavior has been previously observed in a geometrically and electrically asymmetric discharge [44]. Recall, however, that the ionization rate has a strong, non-linear dependence on the electron power absorption which itself strongly depends on the sheath dynamics (see section 2.4). Furthermore, this effect occurs only for the total ion flux at the powered electrode in electrically asymmetric discharges which also exhibit an additional geometrical asymmetry due to the electrode configuration [39, 44, 208]. This effect vanishes for electrically asymmetric but geometrically symmetric discharges, where variations in $\Gamma_i(\theta_2)$ of less than ±10% have been achieved in both experimental dual-frequency plasmas and simulations of multi-frequency RF-CCPs. This is most easily visualized as an innate shift in discharge symmetry, i.e., ε, caused by the geometric asymmetry ($A_p/A_g < 1$) which somewhat resists attempts to increase the grounded sheath voltage. This is a product of the ionization rate's non-linear dependence on the sheath dynamics, and the fact that the

geometrical asymmetry in the experiment enhances the powered electrode's sheath voltage for any set of relative harmonic phases. Thus, for these conditions, the grounded sheath voltage can never be enhanced enough relative to that of the powered electrode, i.e., η cannot reach significantly large positive values (see figure 4.13), to counteract the loss of ionization rate from the powered electrode's sheath as θ_2 is varied. Section 4.1.1 also demonstrates this effect. A similar kind of phenomenon is observed between the simulated DC self-bias and symmetry parameter values and the experimentally measured DC self-bias of section 6.2, where the experiment's geometric asymmetry dramatically reduces changes in the symmetry parameter due to a DA- to α-mode transition.

4.2 Electron power absorption dynamics in high pressure argon discharges

In this section, the high pressure (200 Pa) argon discharge is experimentally investigated using PROES (see section 3.2.2). The results presented here further demonstrate the essential influence of the shape of the driving voltage waveform over the relative importance of each electron power absorption mechanisms, and therefore its control of electron heating dynamics and excitation/ionization in the discharge. This work can also be found in Berger *et al.* [BB15].

The spatio-temporal electron-impact excitation rate measured via PROES at high pressure (200 Pa) is shown in figure 4.16 for an increasing number of applied harmonics ($N = 1, 2, 3$) with fixed harmonic phases ($\theta_2 = 0°$, i.e., "peaks-type" waveforms). The applied voltage amplitude is kept the same as in subsection 4.1.1, i.e., $\phi_{\text{tot}} = 210$ V, and the individual harmonic amplitudes are again dictated by equation (3.1) for each N. The glass containment cylinder is removed and the grounded electrode is set to its maximum gap separation ($d = 15$ cm) for measurements at this high pressure in order to maximize the geometric asymmetry of the discharge (see sections 2.3 and 3.4). With the glass cylinder removed, the entire grounded chamber wall acts as the grounded electrode, such that $A_{\text{p}} \ll A_{\text{g}}$. A large, negative DC self-bias is generated and the grounded sheath voltage is minimized while the powered sheath voltage drop is maximized (e.g., see subsections 4.1.1 and 4.1.2). However, the increased pressure results in significantly increased probability for collisions in the discharge, including inside each sheath. Thus, the discharge under these conditions, without accounting for the specific voltage waveform and sheath dynamics, facilitates operation in the γ-heating mode, as the high voltage drop across the powered sheath and high collisionality are ideal for the acceleration and multiplication of secondary electrons emitted from the powered electrode (see sections 2.4 and 2.6). It should be noted that the measured data in figure 4.16 shows only the region near the powered electrode (0 mm $< x <$ 15 mm), i.e., the region of interest for PROES is not identical to previous measurements in this chapter (subsection 4.1.1). This region is the only one which has significant excitation, however.

The single-frequency discharge ($N = 1$, figure 4.16(a)) at 200 Pa exhibits significant

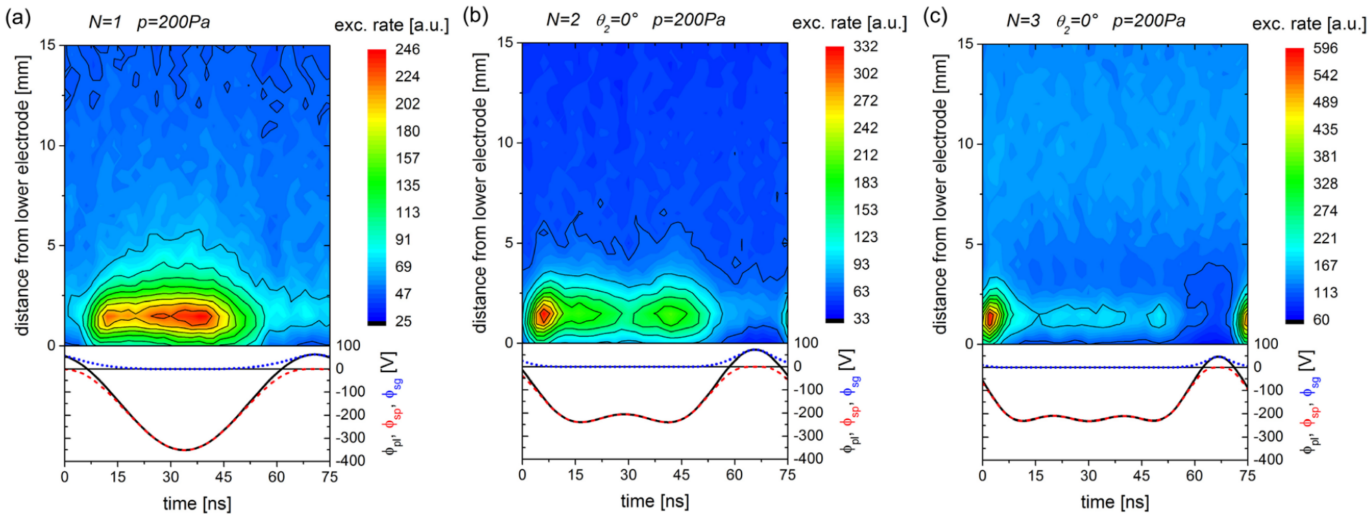

Figure 4.16: Spatio-temporally resolved plots of the Ne $2p_1$ excitation rate for (a) $N = 1$, (b) $N = 2$, and (c) $N = 3$ consecutive harmonics. The appropriate voltage drop across the plasma, ϕ_{pl} (solid line), and across each electrode sheath, ϕ_{sp} (dashed line), ϕ_{sg} (dotted line), are shown below each spatio-temporal plot as a function of time across one RF period of the fundamental frequency. Discharge conditions are: Ar, 200 Pa, $d = 30$ mm, $N = 3$, $\phi_{\mathrm{tot}} = 210$ V, $\theta_{1,2,3} = 0°$. Figure reproduced from its original publication in Berger *et al.*, J. Appl. Phys. 118, 223302 (2015) [BB15] with the permission of AIP Publishing.

excitation produced from electrons accelerated by the powered sheath expansion (i.e., the α-mode) in the interval 10 ns $\leqslant t \leqslant$ 20 ns similar to that observed at lower pressures (subsection 4.1.1). In comparison to the 3 Pa discharge, though, the excitation is strongly localized near the powered sheath edge because of the reduced mean free path of electrons resulting from the increased collisionality of the discharge. A second excitation maximum is also observed near the time the driving voltage is most negative (23 ns $\leqslant t \leqslant$ 45 ns), such that the powered sheath voltage drop is maximum. This new excitation maximum is significantly stronger than that from the α-mode and is associated with secondary electrons emitted from the powered electrode surface. Thus, the highest excitation rate is observed when the sheath potential is highest and thus acceleration and multiplication of these secondary electrons is also most efficient. The discharge therefore operates primarily in the γ-heating mode (see section 2.4) for $N = 1$. If the number of applied harmonics is increased ($N = 2, 3$, figures 4.16(b) and 4.16(c)), the sheath expansion velocity for the powered electrode is enhanced for $\theta_2 = 0°$, as in subsection 4.1.1, but the peak-to-peak voltage of the voltage waveform (i.e., ϕ_{pl}) is reduced slightly for a constant ϕ_{tot} due to destructive interference between the harmonics at some RF phases. These changes can also be seen in the voltage waveforms and the sheath voltage drops shown in figure 4.16. The excitation rate maximum produced by the powered sheath expansion (α-mode) thus increases in strength relative to that produced by secondary electrons (γ-mode) as N is increased. In the dual-frequency discharge ($N = 2$), the α-mode excitation is already much stronger than the γ-mode excitation. The γ-mode excitation becomes relatively small in the triple-frequency discharge, and thus the $N = 3$ discharge primarily operates in the α-heating mode. A mode transition from the γ-mode to

the α-mode can thus be induced at fixed applied voltage and pressure by increasing N, as the sheath expansion heating is enhanced by the steeper slopes of multi-frequency voltage waveforms.

These results support the critical conclusion that the shape of the driving voltage waveform, and thus the specific sheath dynamics associated with each specific waveform, has a determining influence on the relative strength of individual electron heating mechanisms within one fundamental RF period. The electron heating modes and their associated excitation and ionization are therefore also affected by the shape of the voltage waveform. This shape can also be significantly altered by changing θ_2 for a fixed N, as seen in figure 4.17. In a comparison between $\theta_2 = 0°$ (figures 4.16(b) and 4.16(c)) and $\theta_2 = 90°$ (figures 4.17(a) and 4.17(c)), the excitation rate maximum produced by secondary electrons is increased relative to that from sheath expansion heating for both $N = 2$ and $N = 3$ discharges at 90°. For intermediate-type waveforms (e.g., $\theta_2 = 90°$), the slopes of the voltage waveform become less steep compared to those observed at other phases. The sheath expansion velocity, and therefore its associated α-mode heating and excitation maximum, is then comparably reduced for such waveforms. Thus, at 90°, both the $N = 2$ and $N = 3$ discharges operate in a hybrid of the α- and γ-heating modes. For $\theta_2 = 180°$ (i.e., "valleys-type" waveforms, figures 4.17(b) and 4.17(d)), the slope of the voltage waveform once again increases and thus increases the α-mode heating and associated excitation rate. However, the excitation maximum from secondary electrons partially merges with that from sheath expansion heating for these waveforms as the time interval of the powered sheath expansion (approximately 15 ns $\leqslant t \leqslant$ 30 ns) and the time interval of near-maximum sheath voltage (approximately 25 ns $\leqslant t \leqslant$ 45 ns) occur almost immediately after one another. This does make identifying the source of the excitation in PROES slightly more difficult, as the maxima for each mode are no longer temporally separated enough for PROES to resolve each. It can be estimated, though, that the excitation occurring after 30 ns is primarily due to secondary electrons. A second heating mode transition from a typically α-mode dominant regime to a hybrid of the α- and γ-heating modes is therefore possible by changing θ_2 for multi-frequency ($N = 2, 3$) waveforms. Again, the triple-frequency discharge ($N = 3$ waveforms) is seen to have relatively enhanced α-mode excitation compared to the dual-frequency discharge ($N = 2$ waveforms).

When compared against the low pressure discharge of subsection 4.1.1, the maximum excitation rate in the high pressure discharge is almost constant as a function of θ_2 despite such the changing importance of each heating mode. This is due to the high pressure discharge operating in a strongly localized regime where the excitation is not modulated by the confinement of accelerated electron beams or sheath-to-sheath interaction effects (see subsection 4.1.1). That is, the excitation and ionization caused by electron heating near the powered electrode occurs almost entirely in the region very close to the powered sheath edge. Again, the excitation rate elsewhere, i.e., near the grounded electrode or the chamber walls, is insignificant due to the extreme geometric asymmetry of the setup at this electrode gap. This localization is primarily a product of the high collisionality of the discharge (see section 2.4).

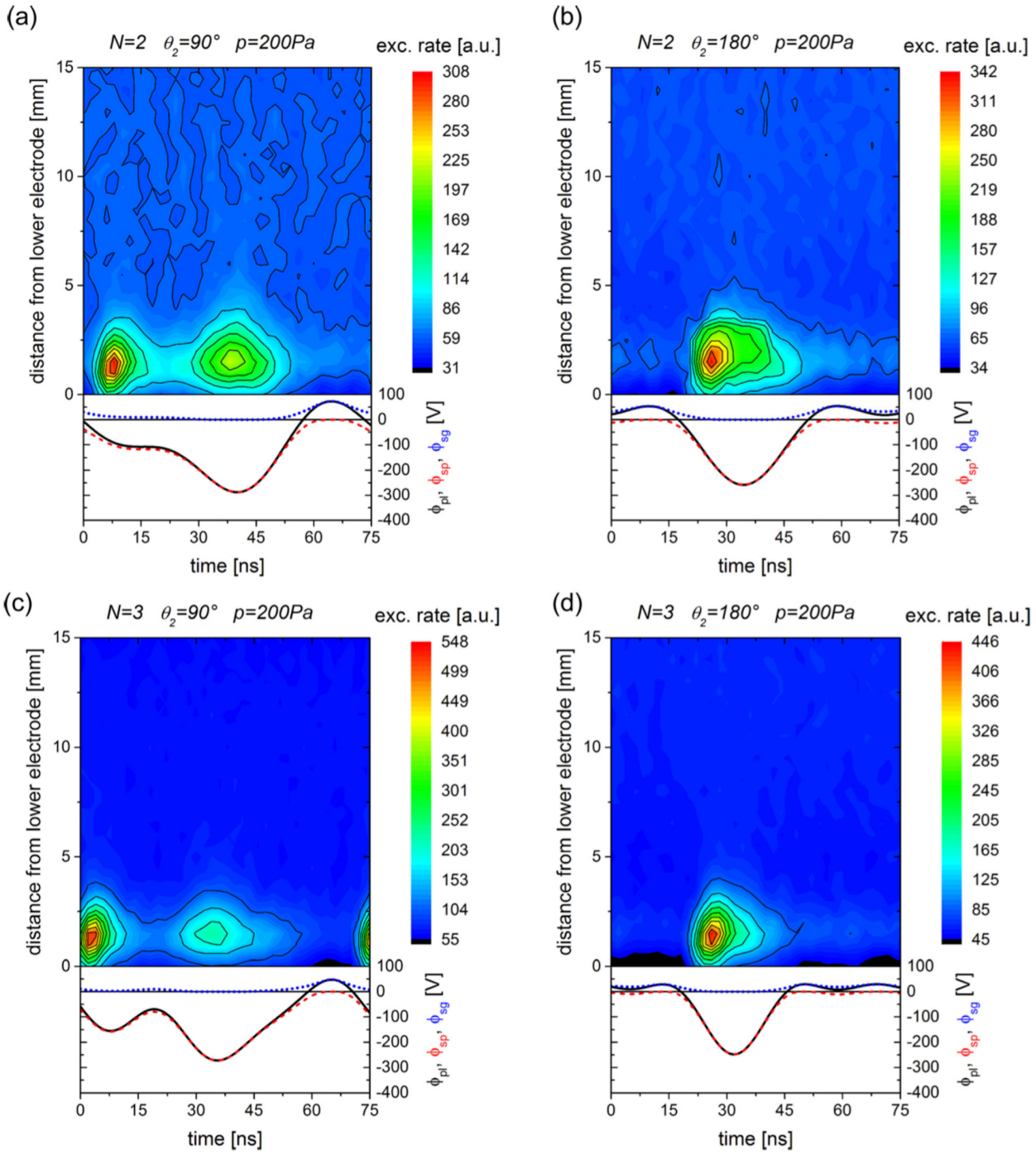

Figure 4.17: Spatio-temporally resolved plots of the Ne $2p_1$ excitation rate in the $N = 2$ ((a) and (b)) and $N = 3$ ((c) and (d)) discharges at $\theta_2 = 90°$ ((a) and (c)) and $\theta_2 = 180°$ ((b) and (d)). The appropriate voltage drop across the plasma, ϕ_{pl} (solid line), and across each electrode sheath, ϕ_{sp} (dashed line), ϕ_{sg} (dotted line), are shown below each spatio-temporal plot as a function of time across one RF period of the fundamental frequency. Discharge conditions are: Ar, 200 Pa, $d = 30$ mm, $N = 3$, $\phi_{\mathrm{tot}} = 210$ V, $\theta_{1,3} = 0°$. Figure reproduced from its original publication in Berger *et al.*, J. Appl. Phys. 118, 223302 (2015) [BB15] with the permission of AIP Publishing.

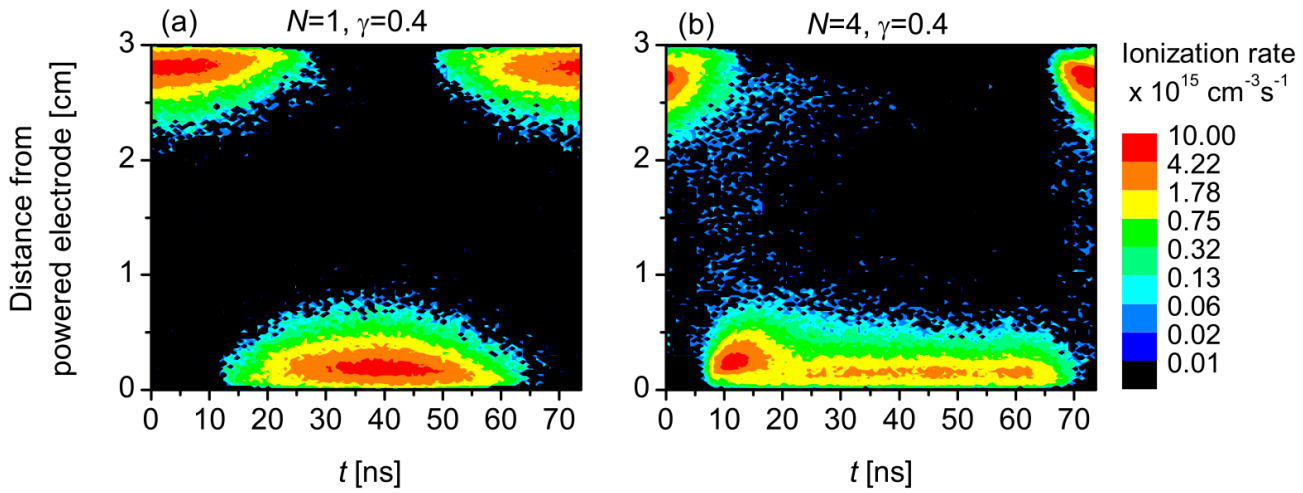

Figure 4.18: Spatio-temporal plots of the ionization rate obtained in previous simulations for different numbers of applied harmonics (N) using logarithmic color scales. Simulation conditions are: Ar, 100 Pa, $d = 30$ mm, $\gamma = 0.4$, $\phi_{\mathrm{tot}} = 120$ V, $\theta_k = 0° \; \forall \; k$. Figure provided from Derzsi *et al.*, Plasma Sources Sci. Technol. 22, 065009 (2013) [46]. ©IOP Publishing. Reproduced with permission. All rights reserved.

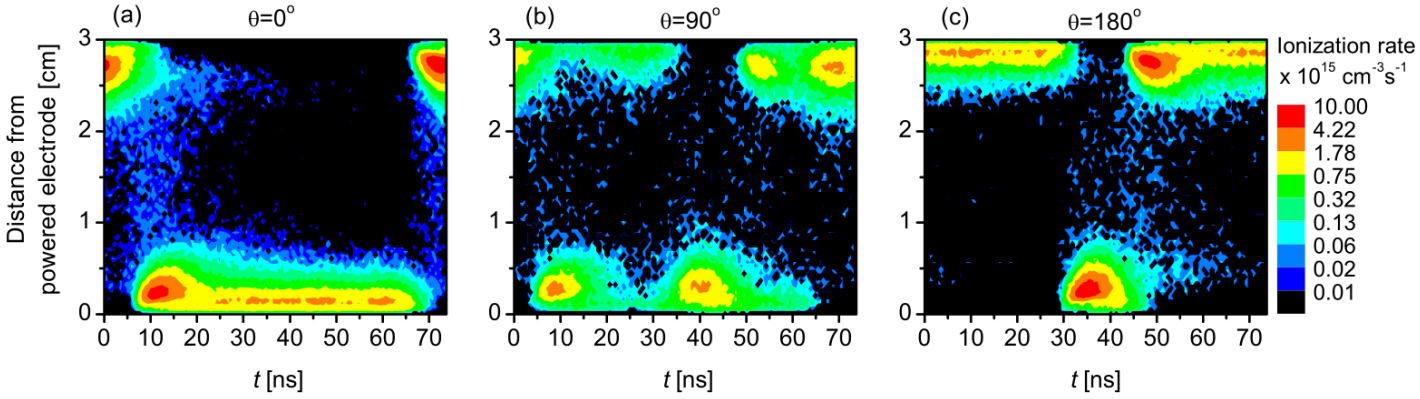

Figure 4.19: Spatio-temporal plots of the ionization rate obtained in previous simulations for different values of $\theta_2 = \theta_4$ (referred to as θ) for $N = 4$ waveforms using logarithmic color scales. Simulation conditions are: Ar, 100 Pa, $d = 30$ mm, $\gamma = 0.4$, $\phi_{\mathrm{tot}} = 120$ V, $\theta_{1,3} = 0°$. Figure provided from Derzsi *et al.*, Plasma Sources Sci. Technol. 22, 065009 (2013) [46]. ©IOP Publishing. Reproduced with permission. All rights reserved.

The results presented in this subsection are in good qualitative agreement with previous kinetic simulations performed by Derzsi *et al.* [46]. This includes the γ- to α-mode transition as a function of increasing N as well as the dependence of the spatio-temporal excitation on θ_2 at fixed N resulting in a α- to hybrid (α- and γ-) mode transition. Furthermore, this work corresponds to their first experimental verification [BB15]. Plots of the spatio-temporal ionization rate obtained at high pressure (100 Pa) in these previous simulations can also be seen in figures 4.18 and 4.19 as a function of increasing N and as a function of $\theta_2 = \theta_4$ for

$N = 4$ waveforms, respectively.

Chapter 5

Self-excitation of the plasma series resonance in electropositive, geometrically symmetric capacitively coupled plasmas and its influence on electron heating

The 1d3V Particle in Cell simulation code, complemented by a Monte Carlo treatment of collision processes (PIC/MCC) outlined in subsection 3.3.1 describes an electropositive, geometrically symmetric argon RF-CCP. Simulations are implemented and performed by the group of Ihor Korolov, Aranka Derzsi, and Zoltan Donkó [SE15a, SE15b] for the prescribed voltage waveforms and conditions in each section below to investigate the generation and electron heating effects of the plasma series resonance in RF-CCPs operated in argon. The results of these simulations were then thoroughly analyzed in the following work presented here. Parts of this analysis are jointly co-authored with Edmund Schüngel and are noted appropriately in the following sections.

The mechanisms behind the generation of the plasma series resonance in geometrically symmetric RF-CCPs are, in section 5.1, demonstrated to be the non-linearities in the charge-voltage relations in the plasma sheaths near the electrodes and a temporally modulated bulk voltage through the bulk parameter $\beta(t)$ (see section 2.5) by using self-consistent PIC/MCC simulations (discussed in subsection 3.3.1) and an appropriate model (outlined in section 2.5) for cases driven by either a 13.56 MHz waveform, a 54.24 MHz waveform, or a multi-frequency waveform of fundamental frequency 13.56 MHz. The discharge is driven in argon gas by applying the given waveform at one electrode while keeping the other grounded, using an inter-electrode gap distance of $d = 30$ mm and a total voltage amplitude of $\phi_{\mathrm{tot}} = 800$ V. The neutral gas pressure and temperature are 3 Pa and 400 K, respectively. Both the ion induced secondary electron emission coefficient and the electron reflection coefficient are

set to be 0.2 at both electrodes. The non-linearity of the sheath capacitances is due to the presence of quadratic and cubic components in the sheath charge-voltage relation, i.e., $q^2(t)$ and $q^3(t)$, that are caused by the inhomogeneity of the static ion sheath density profile [95] which does not cancel out in geometrically symmetric discharges, as discussed in section 2.5. The time-dependent bulk parameter $\beta(t)$ is representative of an inductance and a resistance due to electron inertia and electron momentum transfer collisions in the bulk, which increases during the collapse of either sheath due to the sweep of the plasma bulk region across the strongly varying electron density profile in the sheath (see section 2.5). In this section, it is shown that the model current replicates the current waveforms of the simulations only where both the temporally modulated $\beta(t)$ and the cubic contribution of the charge-voltage relations are taken into account.

The changes in electron power absorption dynamics caused by the self-excitation of the PSR in geometrically symmetric argon RF-CCPs is considered in section 5.2 as a function of both the increasing number of applied harmonics N and harmonic phases θ_k. In subsection 5.2.1, the self-excitation of the PSR discussed in sections 2.5 and 5.1 is extended to a variety of multi-frequency (i.e., $N > 1$) voltage waveforms. The consequences of the PSR perturbations observed for the $N = 4$ multi-frequency waveforms on the electron heating are then determined in subsection 5.2.2. Importantly, it is found that the self-excitation of the PSR increases the overall discharge heating and can introduce a spatial asymmetry in the electron heating. The discharge conditions, excluding the choice of applied voltage waveform, are otherwise the same as the simulations in section 5.1.

5.1 Self-excitation of the plasma series resonance in single- and multi-frequency capacitively coupled plasmas

The temporal dependence of the bulk parameter $\beta(t)$ within the RF period is calculated for the 13.56 MHz, multi-frequency ($N = 4$, $\theta_3 = 0°$, $\theta_{2,4} = 90°$), and 54.24 MHz discharge simulations by using the time dependent bulk integration discussed in section 2.5. The results are plotted in figure 2.9. The bulk parameter β varies significantly in all cases. As noted in section 2.5, the modulation of β is the result of the sweeping of the plasma bulk region across the strongly varying electron density profile in the sheath, leading to a decrease in the effective electron plasma frequency and a strong increase in β during phases of either sheath collapse. This change in β is much stronger for the multi-frequency waveform case due to the relatively short times for sheath collapse [234] (see voltage waveforms in figure 2.9).

Figure 5.1, created jointly with Edmund Schüngel using the PSR model (see section 2.5) and parameters taken from the analysis of simulation data, shows the electron current flowing through the center of the discharge obtained from the PIC/MCC simulations and the PSR model for the three different applied waveforms. For the 13.56 MHz single-frequency waveform in figure 5.1, the plasma series resonance is not self-excited. The perturbation to

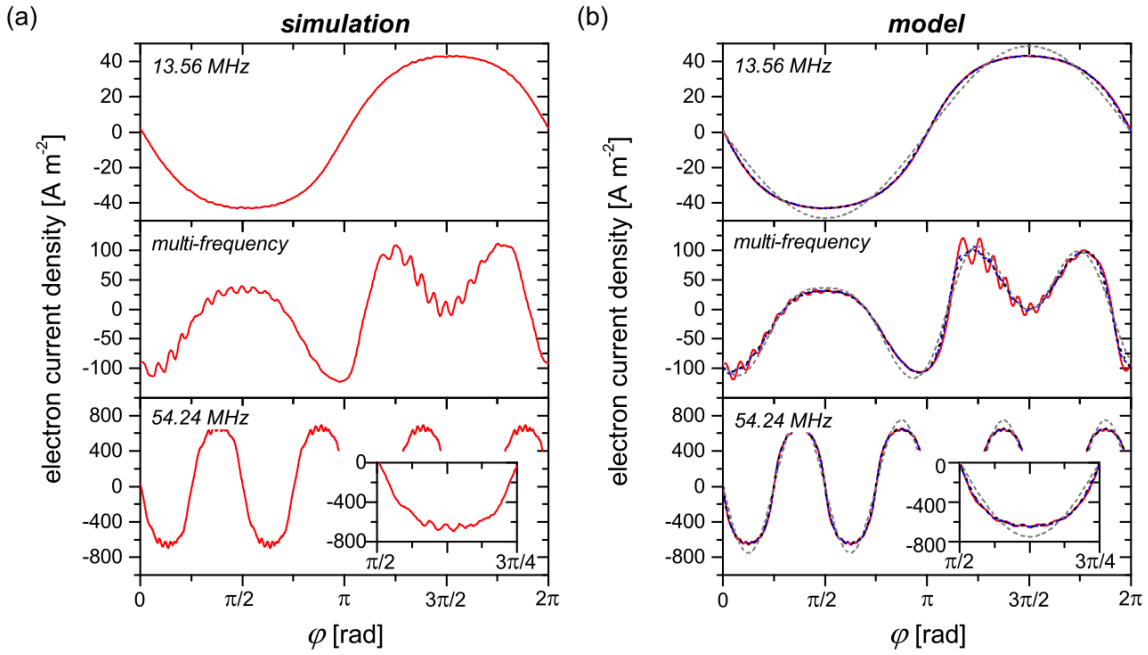

Figure 5.1: Electron current in the plasma bulk obtained from (a) the PIC/MCC simulations and (b) the PSR model. The discharge is driven by a 13.56 MHz (top), a multi-frequency (middle), and a 54.24 MHz (bottom) voltage waveform, respectively. The model plots show the current obtained using $\beta(t)$, a, and b obtained from fits (red solid line), $\beta(t)$ with $a = 1$ and $b = 1$ (dashed gray line), or the RF period averaged β, a, and b (blue dashed line) from the PIC/MCC simulations. The black dotted lines correspond to solutions neglecting the bulk voltage. The multi-frequency waveform is described by $N = 4$, $\theta_3 = 0°$, and $\theta_{2,4} = 90°$ in equation (1.1). Simulation conditions are: Ar, 3 Pa, $d = 30$ mm, $\phi_{\mathrm{tot}} = 800$ V. Figure reproduced from its original publication in Schüngel *et al.*, Physics of Plasmas 22, 043512 (2015) [SE15a] with the permission of AIP Publishing.

the PSR between the model current which includes the time-resolved $\beta(t)$ and the model current which neglects the bullk voltage, i.e., without the PSR (black dotted line), is less than 1% for this case. The model curves are nearly identical as a result. There is a notable deviation in the shape of the model current from the other model curves for the case where $\beta(t)$ is included but the cubic charge-voltage contribution is dropped ($a = 1$ and $b = 1$, dashed gray line), which can also be seen for the other waveforms. This further emphasizes the importance of both mechanisms in accurately replicating the simulated current waveform.

The excitation of the PSR is relatively strong in the multi-frequency case using the $N = 4$ voltage waveform seen in figure 2.9 of section 2.5. The model current matches the simulated current if and only if the temporal variation of $\beta(t)$ obtained from the simulations is included in the model alongside the cubic contribution of the charge-voltage relations (red solid line in model). This offers a possible explanation for the discrepancy between the theoretical and measured current waveforms observed in previous studies [155, 235, 236]. Figure 5.1 also shows that the PSR is self-excited at the times of sheath collapse at both the powered and the grounded electrode sheaths for geometrically symmetric discharges, in contrast to the geometrically asymmetric discharges of these studies.

The single-frequency 54.24 MHz voltage waveform also exhibits a plasma series resonance, but the excitation and amplitude of the higher harmonics are much smaller compared to the multi-frequency waveform. The reduced absolute value and the reduced variation of the bulk parameter $\beta(t)$ (see figure 2.9) are primarily responsible for this, as the plasma density and therefore the effective electron plasma frequency are higher and the RF period accumulated time of sheath collapse is longer. The total current amplitude is also notably much larger for this waveform because of the increased plasma density. For a symmetric discharge, only the odd harmonics of the applied frequency are allowed to be self-excited in the perturbed current waveform due to the temporal symmetry of the applied voltage waveform and thus the discharge's unperturbed current [169], as discussed in subsection 2.5.1. This restriction is removed when applying multi-frequency waveforms using consecutive harmonics, such that a much broader Fourier spectrum in the discharge current is allowed in the multi-frequency discharge. A weak resonance is nevertheless present for the 54.24 MHz discharge, as seen in the zoomed-in inlay of a minimum in the current within the RF period shown in figure 5.1. The model curves further demonstrate that no high frequency oscillations are observed if a simple quadratic sheath charge-voltage relation is assumed. The temporal variation of $\beta(t)$ and the deviation of the charge-voltage relations away from the quadratic assumption are therefore found to be critical in the self-excitation of the PSR and are required to correctly describe the effect. The shape of the current waveform is furthermore essential to the description of the electron heating and power dissipation in such RF-CCPs [150, 151, 237] (see section 5.2), meaning that these parameters are also particularly important to accurately replicating the discharge heating.

Figure 5.2, also created jointly with Edmund Schüngel, depicts the Fourier amplitude spectrum of the electron current density (using a logarithmic scale) obtained from PIC/MCC simulations. The harmonic number k_{FT} is defined with respect to the lowest applied frequency such that $k_{\mathrm{FT}} = 1$ corresponds to the 13.56 MHz component in the analysis of the 13.56

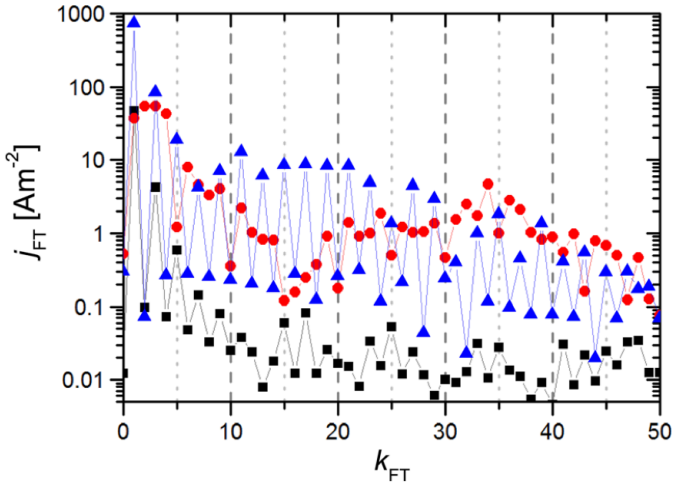

Figure 5.2: Fourier amplitude spectrum, j_{FT}, of the electron current density obtained from PIC/MCC simulations of discharges operated by a 13.56 MHz (black squares) waveform, a multi-frequency waveform (red dots), and a 54.24 MHz waveform (blue triangles). Simulation conditions are: Ar, 3 Pa, $d = 30$ mm, $\phi_{\mathrm{tot}} = 800$ V. Figure reproduced from its original publication in Schüngel *et al.*, Physics of Plasmas 22, 043512 (2015) [SE15a] with the permission of AIP Publishing.

MHz waveform and the multi-frequency waveform cases and corresponds to the 54.24 MHz component in the analysis of the 54.24 MHz waveform case. The 13.56 MHz waveform, which notably does not self-excite the PSR (see figure 5.1), has a rapid decrease in the contribution of higher harmonics with increasing k_{FT}. The odd harmonics are again more pronounced in this case due to the symmetry constraints of the current waveform [169]. The 54.24 MHz waveform experiences similar symmetry constraints but the contribution of the odd harmonics remains significant for a large range of k_{FT} due to the weak PSR for this case. The PSR oscillations observed in the bottom panel of figure 5.1 primarily correspond to the plateau of odd harmonics in the range $k_{\mathrm{FT}} = 13 - 23$. The multi-frequency waveform conversely uses multiple consecutive harmonics and makes the discharge electrically asymmetric. This case is thus not bound by these symmetry constraints and a broad spectrum of higher harmonics is generated by the self-excitation of the PSR [150, 238–241].

5.2 The effects of the plasma series resonance in geometrically symmetric multi-frequency capacitively coupled plasmas

The influence of self-exciting PSR perturbations on the electron heating dynamics in geometrically symmetric argon RF-CCPs driven by both symmetric and asymmetric multi-frequency voltage waveforms is investigated in this chapter by analysis of numerical simulations

(see subsection 3.3.1) and an expanded global circuit model (see section 2.5). In subsection 5.2.1, the self-excitation of the PSR is further examined as a function of increasing number of applied harmonics N and chosen harmonic phases θ_k, i.e., as a function of the shape of the applied voltage waveform. The consequences of this resonance on the electron heating dynamics are then examined for $N = 4$ voltage waveforms in subsection 5.2.2.

5.2.1 Self-excitation of plasma series resonance oscillations in capacitive discharges driven by customized voltage waveforms

Figure 5.3, created jointly with Edmund Schüngel, shows the electron current density obtained from PIC/MCC simulations and the model for different numbers of applied harmonics. Here, all harmonic phase shifts are set to zero (see figure 3.12 in section 3.4) and thus only single-frequency (13.56 MHz) waveforms and multi-frequency "peaks-type" waveforms are considered. The input parameters used in the model (section 2.5) are taken from the PIC/MCC simjulation results. Good agreement is seen in the general shape of the current waveform and the current density amplitude between that obtained from the simulations and that obtained from the model if the bulk voltage is modeled realistically, i.e., a time-dependent $\beta(t)$ is included. In the $N = 1$ simulation, the current density is approximately sinusoidal, as might be expected in such a traditionally symmetric discharge [SE15a, 95]. The unperturbed current density at increasing numbers of harmonics ($N \neq 1$) exhibits multiple local maxima and minima due to the inclusion of all applied frequencies. The current density's global maximum and minimum obtained from the model neglecting the PSR, i.e., neglecting the bulk voltage drop ϕ_b, have the same absolute value. This symmetry in the current waveform is a product of the phase shift of about $90° = \pi/2$ between all harmonics in the current waveform and the applied voltage waveform. [40, 42, 44, 59, 60, 242].

The PSR oscillations are self-excited in all multi-frequency cases with $N \geqslant 2$ (see figure 5.3) but the amplitude of these high-frequency oscillations increases as a function of N. Importantly, this excitation amplitude observed in the PIC/MCC simulations can only be reproduced with the model when the temporal variation of the bulk parameter $\beta(t)$ is included. When using only the value of β averaged over the RF period $(T)^{-1} \int_0^T \beta(t)dt$, the PSR oscillation amplitude is significantly underestimated. It is therefore critically important that the bulk inductance must be treated realistically, i.e., as varying in time, in order to realistically model the self-excitation of PSR. As noted in section 2.5, the sheath charge-voltage relations (equations (2.27) and (2.28)) must similarly be modeled realistically, i.e., not as a simplified matrix sheath. A constant bulk parameter and a quadratic sheath charge-voltage relation are strongly simplifying assumptions and are thus insufficient to properly replicate experimentally observed PSR oscillations. These are likely the main reasons for the discrepancy between the current densities obtained in theoretical models and in simulations/experiments of previous works [40, 44, 154, 155, 235, 237, 240, 243].

The temporal dependence of the bulk parameter $\beta(t)$ is shown in figure 5.4. For the

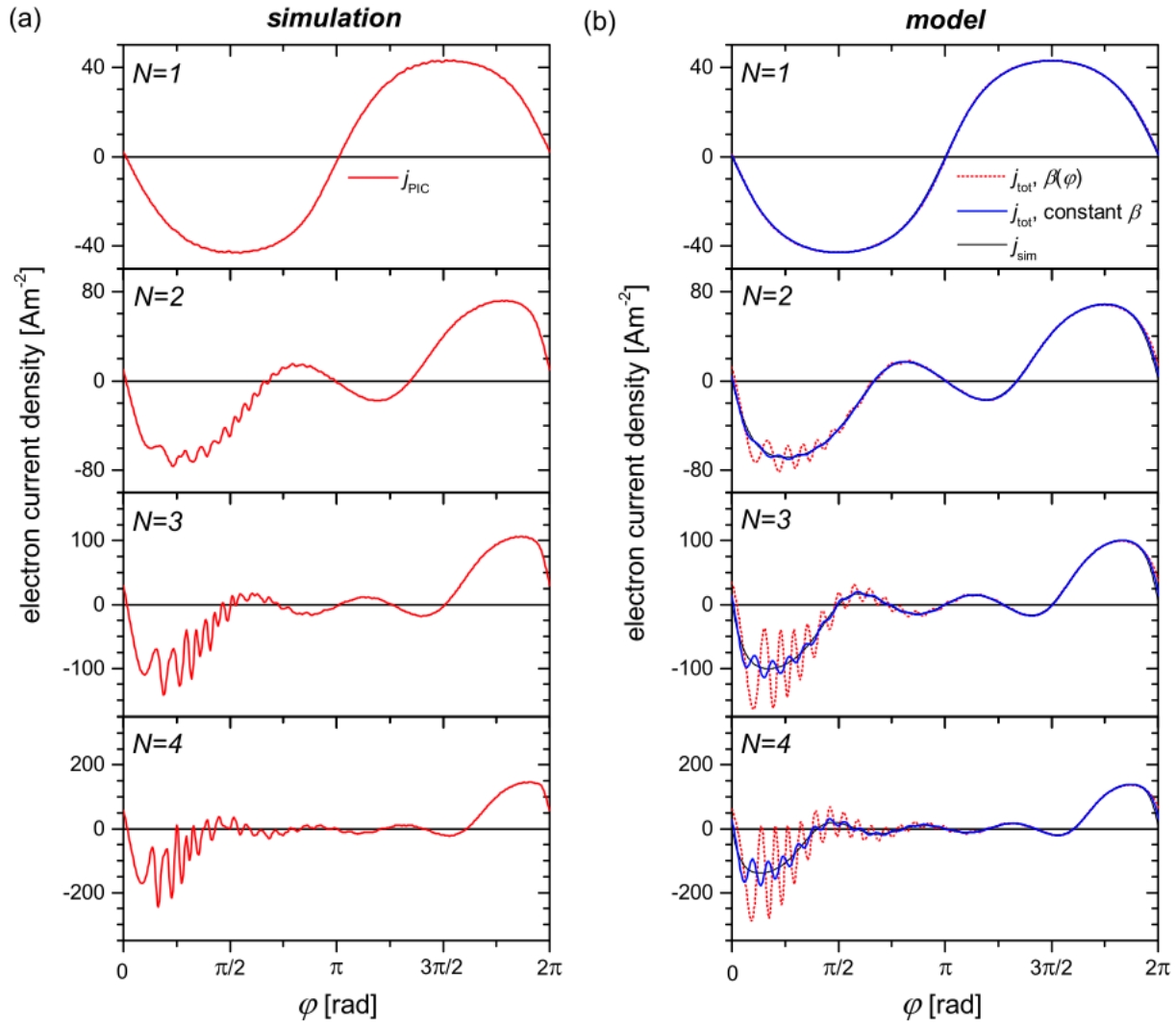

Figure 5.3: Electron current density within one RF period for different numbers of applied harmonics, N, produced by (a) the PIC/MCC simulations of subsection 3.3.1, and (b) the model outlined in section 2.5. The time in the RF period is represented here by $\varphi = 2\pi ft$. The model curves are obtained by using all parameters taken from the simulation (red dotted lines), using the temporally averaged value of β (blue solid lines), and using only the unperturbed current waveform without the bulk voltage (black thin solid lines). Simulated conditions are: Ar, 3 Pa, $d = 30$ mm, $\phi_{\mathrm{tot}} = 800$ V, $\theta_k = 0° \ \forall \ k$. Figure provided from its original publication in Schüngel *et al.*, Plasma Sources Sci. Technol. 24, 044009 (2015) [SE15b].

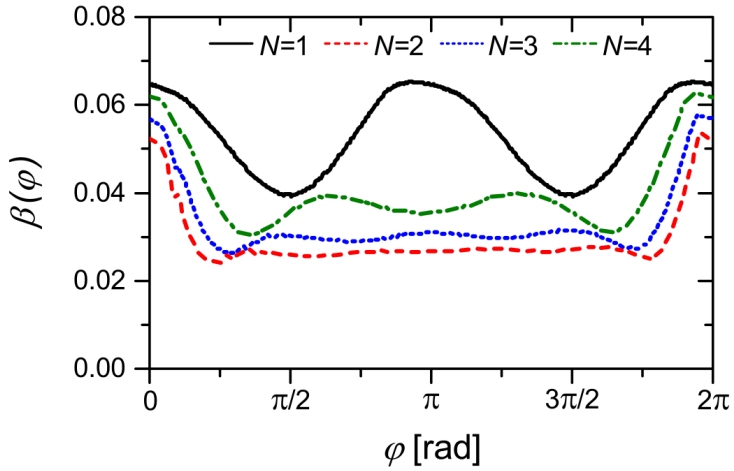

Figure 5.4: The bulk parameter β as a function of time within one RF period (represented by $\varphi = 2\pi ft$) resulting from the $N = 1$ (black solid line), $N = 2$ (green dash-dotted line), $N = 3$ (blue dotted line), and $N = 4$ (red dashed line) PIC/MCC simulations. Simulation conditions are: Ar, 3 Pa, $d = 30$ mm, $\phi_{\mathrm{tot}} = 800$ V, $\theta_k = 0° \ \forall \ k$. Figure provided from its original publication in Schüngel *et al.*, Plasma Sources Sci. Technol. 24, 044009 (2015) [SE15b]. ©IOP Publishing. Reproduced with permission. All rights reserved.

conditions in this section, $\beta(t)$ typically varies by almost a factor of two. The maximum value of β is observed at times when either electrode sheath (powered or grounded) is fully collapsed. The effective electron plasma frequency, $\bar{\omega}_{pe}$ (equation (2.31)), is also at its smallest values at these times as the electron density is depleted in the sheath regions compared to the bulk, where it approximately equals the ion density for quasi-neutrality. When one of the sheaths is fully collapsed, the electron density profile is able to follow the decrease in the ion density towards the electrode as these electrons are no longer repelled by a strong electric field inside the sheath region. As the bulk region sweeps over this part of the electron density profile, the inductance of the plasma bulk is effectively increased due to the locally reduced electron density. Thus, from equations (2.31) and (2.29), this reduction in the effective electron plasma frequency is the main reason for the temporal dependence of $\beta(t)$. The density profiles for the "peaks-type" multi-frequency waveforms are generally asymmetric (e.g., as discussed in chapter 4 since these waveforms apply an electrical asymmetry). The bulk parameter $\beta(t)$ is then maximal for such voltage waveforms only during the powered electrode sheath collapse, i.e., around $t = 0$. Notably, the powered sheath collapse takes place around $7\pi/4 < \varphi < 2\pi$ (i.e., 64 ns $< t <$ 74 ns, see figure 3.12 of section 3.4), where β dramatically increases. The mean ion energy is typically higher at the powered electrode than at the grounded electrode for these conditions (e.g., see section 4.1), such that the ion density decreases more across the powered electrode sheath [38]. The smallest spatio-temporal electron density in the plasma bulk region is therefore located at the powered electrode surface ($x = 0$) at the time of local sheath collapse ($t = 0$). Furthermore, it should be noted for these multi-frequency waveforms that during the grounded sheath collapse (approximately $0 < \varphi < \pi/4$ or 0 ns $< t <$ 10 ns in figure 3.12), $\beta(t)$ actually decreases. This is a result of the aforementioned asymmetry of these waveforms, as the increase in β from the grounded sheath collapse is

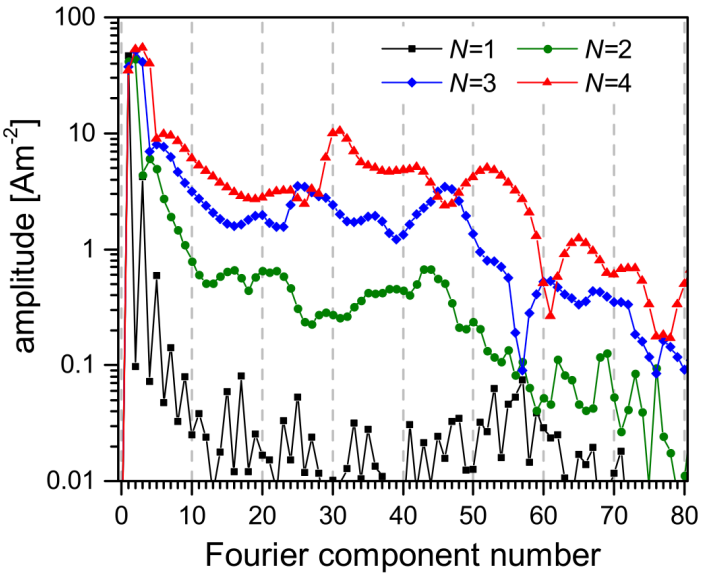

Figure 5.5: Fourier spectrum of the electron current density in the PIC/MCC simulations for $N = 1$ (black squares), $N = 2$ (green circles), $N = 3$ (blue diamonds), and $N = 4$ (red triangles), respectively. Simulation conditions are: Ar, 3 Pa, $d = 30$ mm, $\phi_{\mathrm{tot}} = 800$ V, $\theta_k = 0° \; \forall \; k$. Figure provided from its original publication in Schüngel *et al.*, Plasma Sources Sci. Technol. 24, 044009 (2015) [SE15b].

relatively small compared to that produced by the powered sheath collapse, and thus only one global maximum of β is observed in each of the multi-frequency simulations. As an aside, the discharge is typically asymmetric, either from a geometrical asymmetry in the setup or an electrical asymmetry from the applied waveform, in many experimental or industrial RF-CCPs. Often, $\varepsilon < 1$ for such discharges and therefore the grounded sheath voltage is reduced (e.g., see chapter 4). The increase in β from the grounded sheath collapse would therefore also be reduced as the density profile drop across this sheath is relatively small compared to that at the powered electrode.

The current density in the simulations is further analyzed via a Fourier transform jointly performed with Edmund Schüngel [SE15b] and shown in figure 5.5 as a function of the Fourier component number, i.e., in integer multiples of the fundamental applied frequency (13.56 MHz). Therefore, the current amplitude is naturally highest for the Fourier components at the applied harmonic frequencies (i.e., 1-4 in figure 5.5), and higher Fourier components (i.e., higher frequencies) are produced by interactions in the plasma. The simulations reveal that the PSR oscillations result in a broad frequency spectrum [150, 155, 158, 161, 238–241, 244]. In the single-frequency $N = 1$ discharge, the symmetry of the current waveform (see section 2.5 and figure 5.5) prevents the excitation of even Fourier components [169]. As PSR oscillations are not excited in the $N = 1$ simulation, the current amplitude decreases substantially at higher frequencies. When applying an electrically asymmetric voltage waveform ($N \geqslant 2$), however, this symmetry constraint is removed and all higher harmonics of the fundamental

frequency can potentially be excited in the discharge current. The main PSR frequencies that also dominate the current perturbations seen in figure 5.3 correspond to the peaks around the 25th ($N = 3$) and 30th ($N = 4$) harmonics of the fundamental applied frequency (figure 5.5), such that these frequencies are seen to be in the 311-407 MHz range. The current amplitudes of these higher PSR frequencies and thus the strength of the self-excitation of the PSR is observed to increase as a function of N. This is primarily caused by two effects. Firstly, the voltage waveform becomes increasingly asymmetric as a function of N (see the discussion above). Therefore, the discharge itself also becomes increasingly asymmetric due to the enhanced asymmetry of the plasma density profile and the self-amplification of the EAE at low pressures [37, 38, 45, 46, 162]. For example, $\epsilon \approx 1.00$, 0.68, 0.57, and 0.52 for the $N = 1$, 2, 3, and 4 simulations, respectively. Secondly, the bulk parameter $\beta(t)$ changes quickly for waveforms with high N due to a decreasing time interval between the collapsing and expanding phases of the powered electrode sheath, which is the dominant source of changing β (see figure 5.4 and figure 3.12). Notably, the application of higher harmonics, i.e., increasing N, can also increase the overall plasma density (e.g., see chapter 4). Therefore, the PSR frequency ω_{PSR}, which is related to the plasma frequency (i.e., $\omega_{\mathrm{PSR}} \approx \sqrt{\frac{s_{\max}}{L_{\mathrm{bulk}}}}\omega_{\mathrm{pe}}$; see subsections 2.5.1 and 2.5.2) and thus the plasma density, can also increase as a result of increasing N. It should be noted, though, that increases in the plasma density like those seen in chapter 4 may also reduce the sheath widths (i.e., $s_{\max}$) and thus reduce this PSR frequency. Here, the PSR spectrum is observed to broaden as a function of N in figure 5.5. As an aside, this broad frequency spectrum also influences the spatial electric potential in the discharge and results in enhanced power density at high frequencies up to the local electron plasma frequency (see figure 8 of the full publication of Schüngel *et al.* [SE15b], where the work presented here is also included). This effect is only seen in the simulations, however, meaning that the global model does not capture this additional, kinetic effect.

The asymmetry of the applied voltage waveform (see figure 3.12) and thus the discharge's asymmetry can be controlled simply by changing the relative phases of the applied voltage harmonics. Similar to the waveforms in chapter 4, it is possible to span the maximum possible control range of this asymmetry using only one ($N = 2, 3$) or two ($N = 4$) harmonic phases while keeping the other phases fixed. Here, the minimum negative and maximum positive DC self-bias values are achieved by setting $\theta_k = 0°$ for all harmonics or $\theta_k = 0°$ for the odd harmonics (e.g., $k = 1, 3$) and 180° for even harmonics (e.g., $k = 2, 4$), respectively [45]. This is demonstrated for the $N = 4$ simulation in figure 5.6, corresponding to the largest control range of the cases considered in this section. Recall that the model of section 2.5 predicts the PSR to be self-excited in symmetric discharges ($\epsilon = 1$) but only if the plasma bulk inductance changes in time and the charge-voltage relation for the plasma sheaths includes a cubic component. For the $N = 4$ waveforms, these two conditions appear to be fulfilled such that PSR oscillations are self-excited in the current density at all phase shifts $\theta_{2,4}$ (see figure 5.7). The PSR is therefore excited for all values of the symmetry parameter seen in figure 5.7 corresponding to $\epsilon \approx 1/2$ at $\theta_2 = \theta_4 = 0°$ through $\epsilon \approx 1$ at $\theta_2 = \theta_4 = 90°$ to $\epsilon \approx 2$ at $\theta_2 = \theta_4 = 180°$ (see figure 5.6). The excited amplitude of the PSR current perturbations are significantly smaller for phases around $\theta_{2,4} = 90°$, i.e., for less asymmetric discharges, however. Furthermore, figure 5.7 demonstrates that the RF phase where the PSR perturbations begin

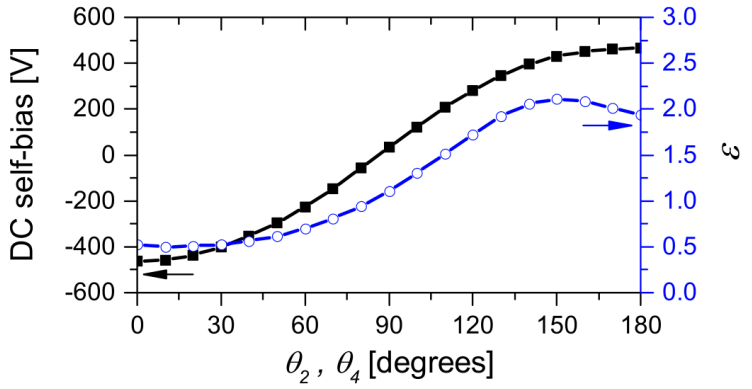

Figure 5.6: DC self-bias (black squares) and the symmetry parameter ε (blue circles) obtained from the $N = 4$ PIC/MCC simulations as a function of the second and fourth harmonic phases $\theta_2 = \theta_4$. Simulation conditions are: Ar, 3 Pa, $d = 30$ mm, $\phi_{\mathrm{tot}} = 800$ V, $\theta_{1,3} = 0°$. Figure provided from its original publication in Schüngel *et al.*, Plasma Sources Sci. Technol. 24, 044009 (2015) [SE15b].

moves from $\varphi \approx 0$ ($t = 0$ ns) at $\theta_2 = \theta_4 = 0°$ to $\varphi \approx \pi$ ($t = 37$ ns) at $\theta_2 = \theta_4 = 180°$. As discussed above, the PSR is self-excited during the time of either the powered sheath collapse or the grounded sheath collapse for $\theta_{2,4} = 0°$, i.e., "peaks-type" waveforms, and $\theta_{2,4} = 180°$, i.e., "valleys-type" waveforms, respectively (see figure 3.12). For each of these types, one sheath causes a relatively enhanced increase in β during its collapse compared to that from the other sheath (see figure 5.4 for high N). Thus, for intermediate-type waveforms (e.g., $\theta_{2,4} = 90°$) where the induced electrical asymmetry is small and thus the density profiles in each sheath behave similarly, both sheath collapses result in comparable increases in β. The PSR can then be excited twice in the RF period, i.e., once per each sheath collapse, but the amplitude of each individual PSR excitation is significantly reduced compared to the strongly asymmetric waveforms (e.g., 0° and 180°).

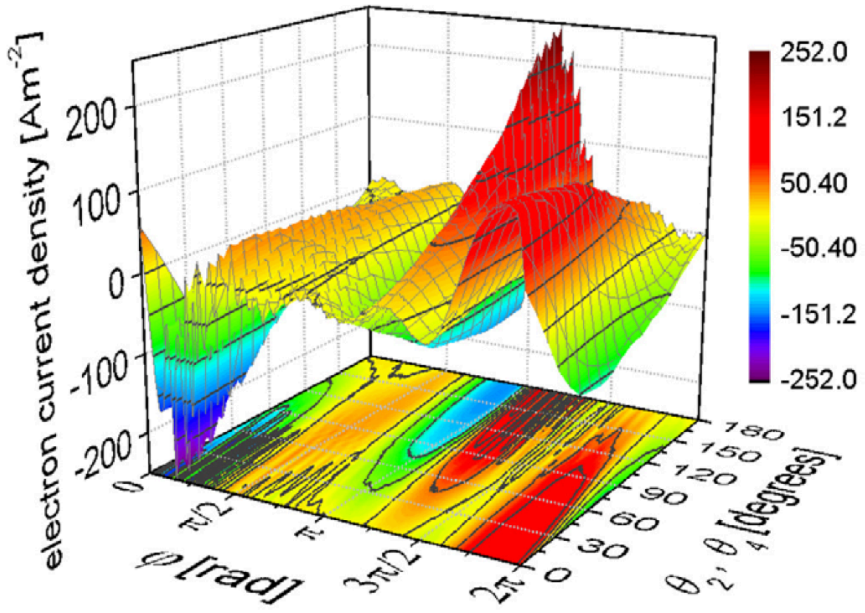

Figure 5.7: Electron current density in the $N = 4$ simulations as a function of time in the RF period (represented by $\varphi = 2\pi ft$) and the phase shifts of the second and fourth harmonics $\theta_2 = \theta_4$ within one RF period. Simulation conditions are: Ar, 3 Pa, $d = 30$ mm, $\phi_{\mathrm{tot}} = 800$ V, $\theta_{1,3} = 0°$. Figure provided from its original publication in Schüngel *et al.*, Plasma Sources Sci. Technol. 24, 044009 (2015) [SE15b].

5.2.2 Role of the plasma series resonance in electron heating dynamics

The electron heating dynamics in low pressure RF-CCPs are traditionally very complex [59, 78–80, 83, 84, 86, 87, 103, 104, 107–115, 118, 154, 198, 237, 245, 246] and there is not yet a fully complete understanding how resonance effects influence the electron heating. The spatio-temporal electron heating rate observed in the PIC/MCC simulation for the $N = 4$ "peaks-type" waveform used in subsection 5.2.1 is depicted in figure 5.8, created jointly with Edmund Schüngel. The discharge operates in the α-heating mode since the strongest electron heating occurs during the phases of sheath expansion in the regions near the momentary plasma sheath edge. As noted in section 4.1 and subsection 5.2.1, this kind of temporally asymmetric multi-frequency waveform causes the powered sheath voltage, the powered sheath expansion velocity, and thus any electron heating from the α-mode near the powered electrode sheath (see $x \approx 7$ mm in figure 5.8) to be enhanced. The contribution to the electron heating rate from secondary electrons inside the sheath (i.e., the γ-mode) is very small under these conditions compared to that observed in section 4.2 for high pressures discharges due to the comparably reduced ion flux to the electrodes generating less seeding secondary electrons and the low collisionality which prevents efficient multiplication of these electrons inside the sheath. This comparably reduced ion flux is due to generally lower plasma densities being observed for the α-mode compared to the γ-mode. It should be noted, though, that the contribution of secondary electrons to the overall electron heating can still be significant at low pressures [35, 190]. The maximum electron heating is thus observed close to the powered electrode during the powered sheath expansion ($0 \leqslant \varphi \leqslant \pi/4$ or approximately 0 ns $< t <$ 10 ns). However, the PSR is self-excited in the simulation, resulting in a high frequency modulation of the sheath expansion velocity (i.e the sheath potential, see [SE15b]) which is traditionally not observed in the α-mode (e.g., see chapter 4). This modulation causes a step-wise-like expansion of the powered sheath which generates multiple distinct energetic electron beams that propagate into the plasma bulk [78, 84, 86, 87, 108–111, 115, 118, 154, 237, 246]. Furthermore, these electron beams gain energy as they cross the ambipolar electric field present near the position of maximum sheath extension [118]. Notably, during times between the rapid partial sheath expansions, the PSR perturbations drive electron cooling (i.e., electron deceleration) near the momentary sheath edge, such that the electron heating near the powered electrode is negative at these times in figure 5.8. This electron cooling appears to be less than the overall heating at the powered electrode, however. The associated grounded sheath collapse, in comparison, is dominated by a pattern of electron cooling again modulated by the presence of the PSR oscillations. The electron heating from the grounded sheath expansion during $7\pi/4 \leqslant \varphi \leqslant 2\pi$ (i.e., approximately 65 ns $< t <$ 74 ns) is relatively small due to the electrical asymmetry, similar to the results of chapter 4. Additionally, this asymmetry causes the maximum sheath width and sheath expansion velocity to become reduced; the increase in β during this expansion is therefore comparably small (see figure 5.4), and thus a series resonance is not excited by the grounded sheath expansion. The spatio-temporal electron heating profile of figure 5.8 furthermore motivates the approach used in the model of section 2.5, where the electron heating associated with the expansion of a given electrode sheath is correlated to the sign of the electron current density.

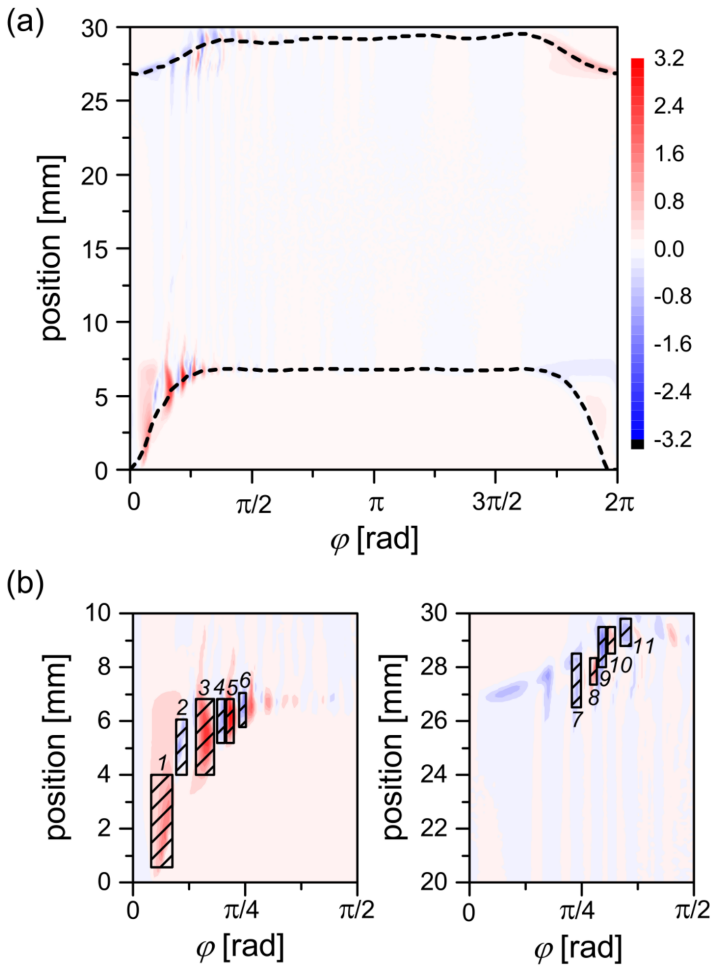

Figure 5.8: (a) The spatially and temporally resolved electron heating rate within one RF period between the powered (at 0 mm) and grounded (at 30 mm) electrodes obtained in the PIC/MCC simulation for the $N = 4$ "peaks-type" waveform. The color scale provides the heating rate in 10^6 W m^{-3}. The dashed lines indicate the positions of the plasma sheath edges. (b) Zoom-ins of the regions close to the powered (left) and grounded (right) sheath during the initial phases of the RF period where the PSR is self-excited. The hatched boxes indicate regions of interest in which the EEDFs are analyzed in the full publication (see figure 12 of [SE15b]). The time in the RF period is represented by φ here. Simulation conditions are: Ar, 3 Pa, $d = 30$ mm, $\phi_{\mathrm{tot}} = 800$ V, $\theta_k = 0° \; \forall \; k$. Figure provided from its original publication in Schüngel *et al.*, Plasma Sources Sci. Technol. 24, 044009 (2015) [SE15b].

The regions of interest shown in figure 5.8(b) are utilized in the full publication (figure 12 of Schüngel *et al.* [SE15b]) to examine the perturbations to the electron energy distribution functions of the produced electron beams at the powered sheath expansion and the electron cooling observed at the grounded sheath collapse as a result of self-exciting the PSR. Notably, the electron beams produced from the powered sheath expansion have a substantially enhanced high-energy tail compared to the bulk electron distribution, as expected, but the alternating electron heating and cooling leads to an alternating gain and loss of energy in each region near the powered electrode sheath expansion. The high-energy tails of these distributions (i.e., > 15 eV) are again responsible for ionization and sustainment of the plasma. The largest gain in electron energy occurs in region 3, where the sheath expansion velocity is highest. Therefore, the multiple electron beams are found to have a range of mean electron energies from 5.1 eV to 8.5 eV, as compared to the 3.2 eV of bulk electrons [SE15b]. Perturbations like this in the discharge's EEDF as a result of self-excitation of the PSR can potentially affect the plasma chemistry and collisional dynamics of the discharge. Furthermore, these electron beams can traverse the entire plasma bulk at low pressures and reflect multiple times between the two sheaths [128], as seen in section 4.1.

The accumulated electron heating within one RF period is calculated from the PIC/MCC simulations and the model for different numbers of applied harmonics N using the technique outlined in section 2.5. The results from this technique are produced jointly with Edmund Schüngel and are shown in figure 5.9, where only the positive contributions (heating) are considered, i.e., negative heating rates (cooling) are neglected. This is necessary in order to compare the simulation results with the model, which only includes electron heating. Notably, the model exhibits a plateau in the accumulated electron heating during the interval between each sheath expansion, such that no significant electron heating between $\varphi \approx \pi/2$ ($t \approx 74$ ns) and $\varphi \approx 3\pi/2$ ($t \approx 55$ ns) at $N = 4$ is observed. The plateau feature is absent from the simulations, though, where the accumulated electron heating rate continues to increase during this interval albeit at a slower pace than during the intervals of intense sheath expansion heating. Electron heating produced by secondary electrons, which are implemented in the simulations but are absent in the model, is the primary cause of this difference. As in section 2.4, the electron heating by secondary electrons is strongest during the time interval where one sheath is fully expanded and the corresponding sheath voltage is maximum. Since the discharge is made electrically asymmetric at higher N, however, the dominant heating from secondary electrons is produced by the powered electrode sheath for the $N = 2, 3, 4$ simulations. Furthermore, the powered sheath remains fully expanded, i.e., near the same sheath voltage, for a large fraction of the RF period for such waveforms, resulting in a nearly linear gain in the accumulated electron heating in the simulation (see figure 5.9). The simulated electron heating is, however, well reproduced by the model during the initial phases ($0 \leqslant \varphi \leqslant \pi/4$ or approximately 0 ns $< t <$ 10 ns) of sheath expansion. Large PSR oscillations are also present for $N \neq 1$ during these phases that modulate the electron heating (figure 5.8). Here, cooling is neglected and therefore a step-wise increase in the accumulated electron heating can be seen for each partial sheath expansion. This step-wise behavior is typical of electron heating produced by such PSR oscillations, also called non-linear electron resonance heating (NERH) [150, 151, 153, 155, 157, 158, 160–162, 165, 235, 237, 240, 241, 243, 247]). The PSR self-excitation, furthermore, can be turned on and off in the model by neglecting the

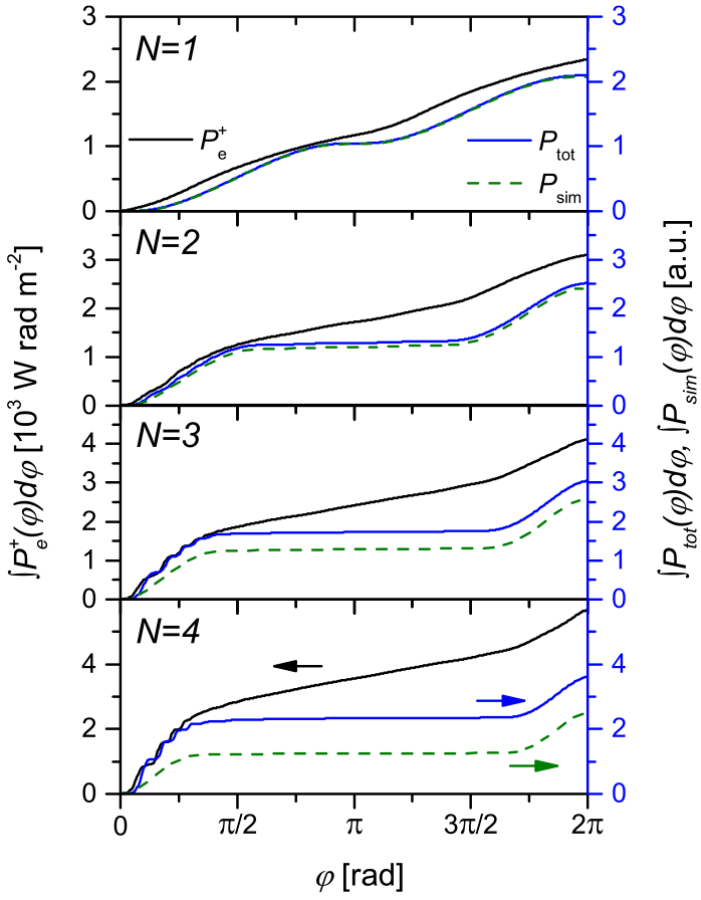

Figure 5.9: Accumulated electron heating within one fundamental RF period for increasing numbers of applied harmonics, N, obtained from the PIC/MCC simulations (P_e^+, black line, left scale) and the model of section 2.5 including (P_{tot}, blue line, right scale) and excluding (P_{sim}, green dashed line, right scale) the PSR self-excitation. Simulation conditions are: Ar, 3 Pa, $d = 30$ mm, $\phi_{tot} = 800$ V, $\theta_k = 0° \; \forall \; k$. Figure provided from its original publication in Schüngel *et al.*, Plasma Sources Sci. Technol. 24, 044009 (2015) [SE15b].

bulk voltage term (see section 2.5). The difference in accumulated electron heating between the model including (P_{tot} of equation (2.34)) and excluding (P_{sim} of equation (2.33)) the PSR perturbations increases as a function of increasing N since the strength of the self-excitation of the PSR and thus the resulting oscillation amplitudes also increases. The associated electron heating from the PSR therefore becomes increasingly relevant for multi-frequency waveforms with high N. Notably, this effect on the discharge's electron heating is partially due to the increasingly quick changes in $\beta(t)$ for voltage waveforms which produce fast sheath expansions at one electrode (see the discussion surrounding figure 5.4). Furthermore, the step-wise behavior produced by the partial sheath expansions at the beginning of the RF period is absent in the model when the PSR is excluded. The model curves for the $N = 4$ waveform in figure 5.9 suggest that approximately one-third of the total electron heating in the RF period is directly associated with the enhancement of electron heating produced by the PSR oscillations.

The accumulated electron heating for the $N = 1$ and $N = 4$ waveforms is divided into two half-space regions adjacent to the powered ($0 \leqslant x \leqslant d/2$, $P^{+}_{\text{e,p}}$) and grounded ($d/2 \leqslant x \leqslant d$, $P^{+}_{\text{e,g}}$) electrodes according to the technique outlined by equations (2.36) and (2.37) in section 2.5, respectively, and is depicted in figure 5.10. The single-frequency ($N = 1$) waveform produces identical sheath voltages and sheath expansions in both the simulation and the model; thus, the discharge is perfectly symmetric and no PSR oscillations are present such that the total electron heating in each discharge half is identical within one RF period (see top plots of figures 5.10(a) and 5.10(b)). Notably, the electron heating produced by one sheath expansion is $180^{\circ} = \pi$ out of phase compared to the other, as may be expected from the voltage waveform (see figure 3.12). This description changes completely when driving the discharge with an asymmetric multi-frequency waveform, however. For such waveforms, a strong spatial asymmetry in the electron heating rate is produced, as discussed previously (see figure 5.8). This dramatically enhances the electron heating produced near the powered electrode relative to that near the grounded electrode and therefore the accumulated electron heating in the discharge half adjacent to the powered electrode consistently dominates the overall electron heating in both the simulation and the model (see the middle plots of figure 5.10). The model fails to capture small details, however, such as the heating of electrons near the grounded sheath collapse which is visible in figure 5.8, as they are based on kinetic effects not included in the model, although $P_{tot,g} > 0$ for $\varphi \geqslant \pi/2$ (approximately $t \geqslant 19$ ns) is observed. The heating on each side differs by almost a factor of two in the model for the multi-frequency waveform. This difference is further enhanced by the presence of electron heating due to secondary electrons in the simulations, which is strongest for the powered sheath that remains fully expanded for a large fraction of the fundamental RF period.

The model also provides the option for switching on and off the self-excitation of PSR oscillations, as seen in the middle and bottom plots of figure 5.10(b), respectively. Therefore, figure 5.10(b) demonstrates that the spatial asymmetry in the electron heating obtained from the model is produced solely by the contribution of the series resonance oscillations to the electron heating (i.e., NERH) as this asymmetry vanishes when this resonance is neglected (bottom plot of figure 5.10(b)). In contrast, the asymmetry seen in the simulations is due to both this effect and the unequal heating in each discharge half caused by the

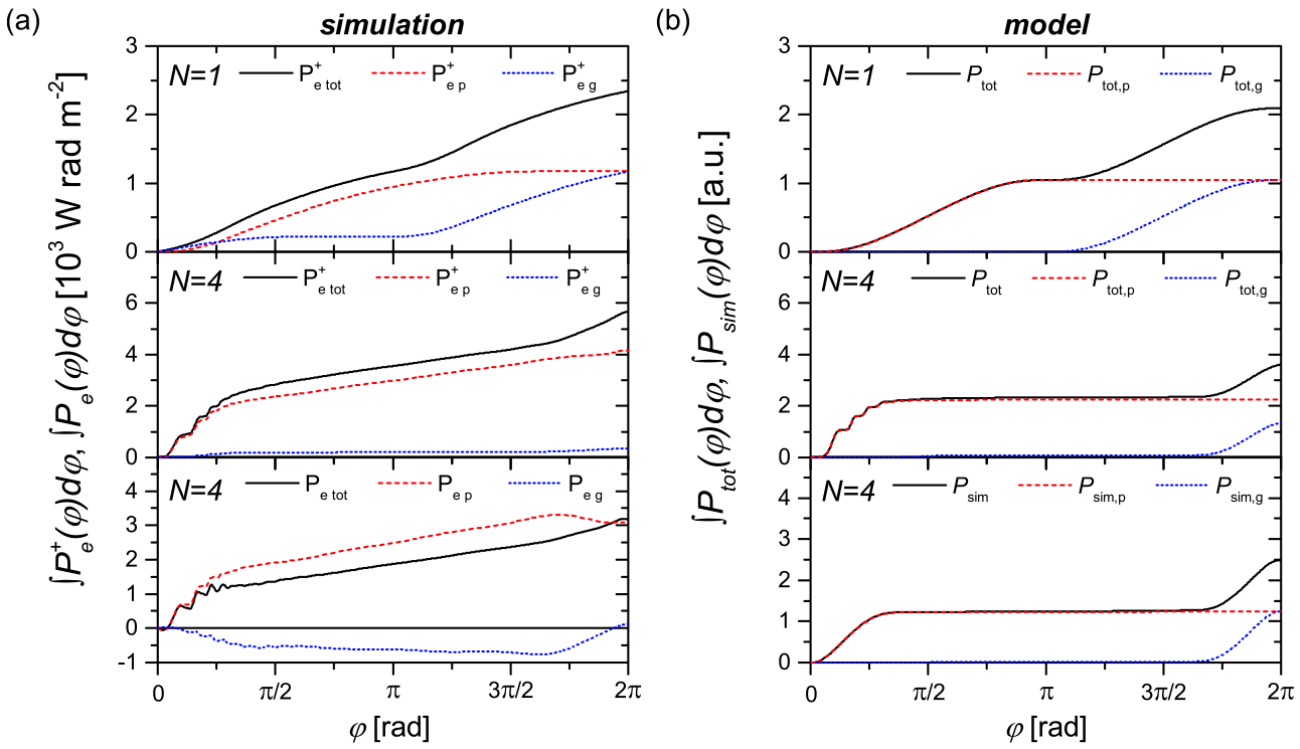

Figure 5.10: Accumulated electron heating within one RF period calculated from (a) the PIC/MCC simulations and (b) the model of section 2.5. The total heating in the entire discharge ($P_{\mathrm{e,tot}}$, black solid line) is split into the components for two discharge halves adjacent to either the powered ($P_{\mathrm{e,p}}$ for $0 \leqslant x \leqslant d/2$, red dashed line) or grounded ($P_{\mathrm{e,g}}$ for $d/2 \leqslant x \leqslant d$, green dotted line) electrodes. A single-frequency voltage waveform ($N = 1$) is applied in the top plots, while a $N = 4$ multi-frequency waveform is applied for the center and bottom plots, respectively. Electron cooling observed in the simulation is included in the bottom plot of (a), while the PSR self-excitation is excluded in the model in the bottom plot of (b). Simulation conditions are: Ar, 3 Pa, $d = 30$ mm, $\phi_{\mathrm{tot}} = 800$ V, $\theta_k = 0° \; \forall \; k$. Figure provided from its original publication in Schüngel *et al.*, Plasma Sources Sci. Technol. 24, 044009 (2015) [SE15b].

secondary electrons in the powered and grounded electrode sheaths, and therefore cannot reach perfect electrical asymmetry for such multi-frequency waveforms. Thus, by excluding the self-excitation of the PSR in the model, i.e., neglecting the bulk term in the voltage balance (equation (2.1)), the step-wise increase in the accumulated electron heating at the powered electrode vanishes and the electron heating becomes symmetric. The asymmetry in the simulations is further enhanced by including electron cooling (i.e., negative electron heating rate) in the analysis, as seen in the bottom plot of figure 5.10(a). Notably, no net heating is produced in the discharge half adjacent to the grounded electrode over the course of the RF period as a result of significant cooling occurring during the phases of grounded sheath collapse (approximately $0 < \varphi < \pi/4$ or 0 ns $< t <$ 10 ns). Additional cooling is observed between the phases of rapid sheath expansion (see figure 5.8) at the powered electrode which causes a repetitive change in the slope of the accumulated electron heating during the same initial phase interval. The inclusion of electron cooling therefore reduces the observed total electron heating of the whole discharge and increases the discharge asymmetry compared to cases where electron cooling is neglected (see figure 5.10(a)). The nearly linear increase of the accumulated electron heating at intermediate RF phases ($\pi/2 \leqslant \varphi \leqslant 3\pi/2$, approximately 19 ns $< t <$ 56 ns) is once again caused by secondary electrons and should not be neglected.

A comparison of the bottom panels of figures 5.10(a) and 5.10(b), furthermore, indicates an enhancement of the net discharge heating produced by the self-excitation of the PSR. The total accumulated electron heating and cooling (i.e., P_{tot} in bottom plot of figure 5.10(a)) after the initial phases dominated by heating close to the powered electrode in the simulation is similar to the accumulated electron heating obtained from the model which neglects the PSR perturbations (ignoring the contribution from secondary electrons in the simulation). This implies that the NERH caused by the PSR self-excitation largely compensates for the cooling that would be present in the absence of the PSR. The net discharge heating, i.e., the sum of all additional heating and cooling, resulting from PSR self-excitation is therefore positive and the self-excitation of the PSR is thus generally associated with a net gain in electron heating, despite its complicated details. However, proper implementation of this enhancement of electron heating via NERH in applications requires careful consideration of discharge conditions which affect the discharge symmetry (i.e., ε), the sheath properties (i.e., the sheath charge-voltage parameters a and b), the bulk inductance (i.e., $\beta(t)$), or the bulk voltage (e.g., ϕ_{b} is primarily determined by the DA-heating mode in chapter 6), and would be problematic for discharge conditions where the PSR is typically not self-excited. Notably, the opposite of this, i.e., the self-excitation of the PSR without user knowledge, may alter plasma properties. Thus, a complete understanding of when PSR perturbations are excited and how much they influence plasma operation is particularly necessary when driving RF-CCPs using customized voltage waveforms.

The enhancement of the electron heating suggested by the previous figures also indicates an enhancement of the ionization in the discharge and therefore the ion flux to the electrodes in a similar fashion to that observed in chapter 4. It is demonstrated in figure 15 of the full publication (Schüngel *et al.* [SE15b]) that while the dominant electron heating is highly localized to near the powered electrode, the resulting electron beams propagate through the entire discharge bulk and can reflect at the collapsing grounded sheath edge. These electron

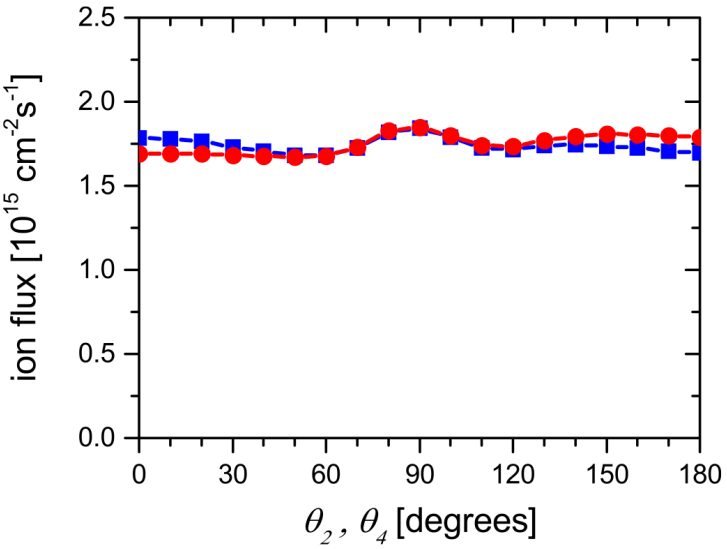

Figure 5.11: Ion flux onto the powered (blue squares) and grounded (red circles) electrodes within one fundamental RF period as a function of the second and fourth harmonic phases $\theta_2 = \theta_4$ obtained from the $N = 4$ PIC/MCC simulations. Simulation conditions are: Ar, 3 Pa, $d = 30$ mm, $\phi_{\mathrm{tot}} = 800$ V, $\theta_{1,3} = 0°$. Figure provided from its original publication in Schüngel *et al.*, Plasma Sources Sci. Technol. 24, 044009 (2015) [SE15b]. ©IOP Publishing. Reproduced with permission. All rights reserved.

beams therefore cause subsequent ionization over a much larger region in the discharge bulk which exhibits only a slight spatial asymmetry. That is, the ionization rate in the discharge half adjacent to the grounded electrode is only slightly enhanced compared to that for the half adjacent to the powered electrode. The resulting ion density profile is then likely significantly more symmetric than may be expected from the electron heating in figure 5.8.

The non-local relationship between the electron heating and ionization under these conditions therefore helps to maintain constant ion fluxes to each electrode surface, as shown in figure 5.11 for $N = 4$ waveforms. The mean ion energy is traditionally controlled independently from the ion flux via the EAE as a function of the even harmonic phase shifts (θ_2 and θ_4) for such multi-frequency waveforms, as shown in chapter 4 and numerous previous works [37–39, 44–46, 162, 208]. Figure 5.11 demonstrates that this separate control is not heavily disturbed by the the PSR oscillations due to two effects. Firstly, these PSR oscillations are self-excited at all values of harmonic phase shifts (see figure 5.7) and therefore are not solely self-excited for phase shifts where the waveform causes the discharge to become asymmetric. That is, PSR oscillations in the current waveform can be observed for all discharge asymmetries (see figures 5.7 and figure 5.6) such that an enhancement of electron heating is found for all applied $N = 4$ multi-frequency waveforms and therefore only minimal changes due to the PSR enhancement as a function of harmonic phases is observed. This should not be confused with the results of a previous work [162] where this enhancement was only seen for asymmetric voltage waveforms in dual-frequency ($N = 2$) discharges. Secondly, the non-local relationship between the electron heating and the ionization prevents any

significant asymmetry in the ion fluxes to each electrode. This is a product of the large energy relaxation length under these conditions which causes ionization by electron-neutral collisions to be broadly distributed across the entire plasma bulk region. It should be noted, however, that this non-local behavior likely does not extend to higher pressure regimes, where the electron energy relaxation length is much smaller (e.g., see section 4.2). The PSR, furthermore, is increasingly dampened at higher pressures (i.e, κ increases with pressure), such that the application of NERH to high pressure industrial discharges (e.g., deposition discharges) may be much more limited.

Chapter 6

Charged particle dynamics in an electronegative CF_4 capacitive radio-frequency plasma and in argon-CF_4 gas mixtures

The charged particle dynamics of a given low-temperature plasma are often the controlling force of many process-relevant plasma parameters, like plasma density, radical densities, and ion energy distributions at the surface of a substrate. Therefore, a fundamental understanding of these charged particle dynamics provides significant insight into how to control these process-relevant plasma parameters. However, while electropositive gases such as argon have been studied extensively in previous works, the effects of electronegative gases on these charged particle dynamics and discharge operation are currently not fully understood. Furthermore, in many industries, it is commonplace to use complicated gas mixtures of electropositive and electronegative gases, with one or more molecular gases resulting in highly complex plasma chemistry. Thus, it is critical to these industries that a full understanding of how these more complicated gases and gas mixtures affect the charged particle dynamics and the resulting discharge operation is obtained. In this chapter, the major results of the owned publications [BS16] and [BS19] will be presented in section 6.1 and section 6.2, respectively. Section 6.1 focuses on the effects of applying various tailored voltage waveforms and the electrical asymmetry effect (EAE) in the electronegative molecular gas CF_4. The modified effects of voltage waveform tailoring and the EAE are investigated in gas mixtures of argon and CF_4 gases in section 6.2. The experimental setup and diagnostics used in the experimental studies in these sections, as well as the kinetic simulations used here, are described in previous chapters.

In section 6.1, the dependence of the electron power absorption dynamics and the DC self-bias of a CF_4 plasma on the applied tailored voltage waveform is investigated by combined experimental studies and kinetic simulations as a function of the number of applied harmonics

of the fundamental frequency 13.56 MHz and the relative phases of these harmonics. Phase-resolved optical emission spectroscopy is used for a fluorine line discussed in subsection 3.2.2 to experimentally examine the spatio-temporal excitation dynamics of the experimental setup. "Peaks/valleys-type" and sawtooth-type waveforms are used to study the effects of the amplitude asymmetry effect (AAE) and slope asymmetry effect (SAE), respectively, on the electron power absorption dynamics and the generation of the DC self-bias in an electronegative plasma at different pressures (20 Pa and 80 Pa) and a fixed electrode gap of 25 mm. For the AAE cases, the total possible applied voltage is set to $\phi_{\mathrm{tot}} = 210$V while for the SAE cases, $\phi_{\mathrm{tot}} = 253$ V such that the absolute positive and negative voltages of all waveforms are similar. Compared to electropositive discharges, strongly different effects and unique power absorption dynamics are observed. At high pressures and high electronegativities, the discharge is found to operate in the drift-ambipolar heating mode. A dominant excitation/ionization maximum is observed during sheath collapse at the edge of the sheath region where high negative ion densities are observed and electrons are confined for part of the RF period in a potential well formed by the ambipolar electric field at this sheath edge and the collapsed (floating potential) sheath at the electrode. For specific driving voltage waveforms the plasma becomes divided spatially into two different halves of strongly different electronegativity. This asymmetry can be reversed electrically by inverting the driving waveform. For sawtooth waveforms, the discharge asymmetry and the sign of the DC self-bias are found to reverse as the pressure increased from 10 Pa to 100 Pa, due to a transition of the electron heating mode from the α-mode to the DA-mode. These effects are interpreted with the aid of the simulation results. In subsection 6.1.1, the results for the "peaks/valleys-type" waveforms and the AAE are presented, while in subsection 6.1.2, the results for the sawtooth waveforms and the SAE are presented.

The charged particle dynamics of capacitively coupled plasmas operated in different Ar-CF_4 gas mixtures driven by tailored voltage waveforms are investigated in section 6.2 using experimental phase-resolved optical emission spectroscopy measurements in conjunction with the kinetic simulations and the analytic model described in previous chapters. Single- and triple-frequency "peaks-type" and "valleys-type" waveforms (generated as a superposition of multiple consecutive harmonics of 13.56 MHz) are studied at pressures of 20 Pa and 60 Pa with 25 mm electrode gap and 150 V total driving voltage amplitude to determine the effects of the tailored driving voltage waveform in different gas mixtures on the density profiles of the particle species, the electronegativity, the DC self-bias, and the excitation/ionization dynamics. As the argon content in the buffer gas is increased, the discharge switches from the drift-ambipolar (DA) power absorption mode to the α-mode. This transition occurs due to the disappearance of the bulk and ambipolar electric fields as the electronegativity of the plasma decreases with increasing argon content. This effect is more pronounced at higher pressures, where the negative ion density is higher. Significant changes in the plasma's asymmetry, DC self-bias, and mean electron energy are observed as a result of the DA- to α-mode transition. The generation of the DC self-bias as a function of the argon content is understood by the analytical model based on these fundamental insights into the plasma physics. The spatio-temporal charged particle dynamics as a function of the argon content is presented in subsection 6.2.1, while the generation of the DC self-bias as a function of the argon content is presented in subsection 6.2.2.

6.1 Electron power absorption dynamics in CF_4 capacitively coupled plasmas driven by tailored voltage waveforms

This section is divided into two parts according to the different shapes of the driving voltage waveform used to operate the CCP. First, tailored voltage waveforms are used based on harmonics' amplitudes chosen according to equation (3.1) and a systematic variation of θ_2 ($\theta_1 = \theta_3 = 0°$). Such waveforms generate a pure AAE ("peaks-type"/"valleys-type" waveforms), or a non-optimized SAE ($\theta_2 = 90°, 270°$ waveforms). Second, Sawtooth waveforms are used to isolate the SAE from the AAE, while also optimizing the SAE. The harmonics' amplitudes are chosen according to equation (3.2) with $\theta_1 = 0°$, $\theta_2 = 270°$, $\theta_3 = 180°$ for Sawtooth Up waveforms and $\theta_1 = 0°$, $\theta_2 = 90°$, $\theta_3 = 180°$ for Sawtooth Down waveforms.

The effects of each voltage waveform on the spatio-temporal electron power absorption dynamics and the generation of a DC self-bias are studied by a synergistic combination of experiments and simulations to obtain a complete interpretation of the effect of using a reactive electronegative gas such as CF_4 on the EAE in CCPs driven by customized voltage waveforms.

6.1.1 Amplitude asymmetry in CF_4

A driving voltage waveform according to equation (1.1), with amplitudes according to equation (3.1), is used. Single- ($N = 1$), dual- ($N = 2$), and triple- ($N = 3$) frequency scenarios are investigated. Here, $\phi_{tot} = 210$ V is kept constant while θ_2 is varied. Two different pressures of 20 Pa and 80 Pa are used to study a weakly electronegative (20 Pa) and a strongly electronegative (80 Pa) scenario.

The measured and simulated DC self-bias voltages are shown in figure 6.1 as a function of the second harmonic's phase (the 27 MHz signal's phase, θ_2) for both 20 Pa and 80 Pa. The other harmonics' phases are fixed at zero throughout these variations. In the experiment, the discharge is always geometrically asymmetric at 20 Pa, as indicated by the $\eta \approx -29$ V value obtained for $N = 1$ (see figure 6.1(a)). Therefore, the experimental measurements at 20 Pa are not compared to the results of the (geometrically symmetric) simulation. At 20 Pa, the control range of η is increased by using more harmonics for the same total voltage, due to an enhanced Amplitude Asymmetry Effect (AAE) similar to the AAE in electropositive argon discharges [39–44, 51, 52, 58]. For 80 Pa, the control range of η is larger for $N = 2$ compared to $N = 3$ and the functional dependence of the bias on the phase is significantly different. This is caused by the presence of a different electron heating mode which enhances the Slope Asymmetry Effect (SAE) for $N = 2$ at phases around 90° and 270°. This heating mode will be discussed later in this subsection. The $N = 2$ DC self-bias caused by the SAE at $\theta_2 = 90°$ is almost the same as the one caused by the AAE at $\theta_2 = 180°$. Such an effect is

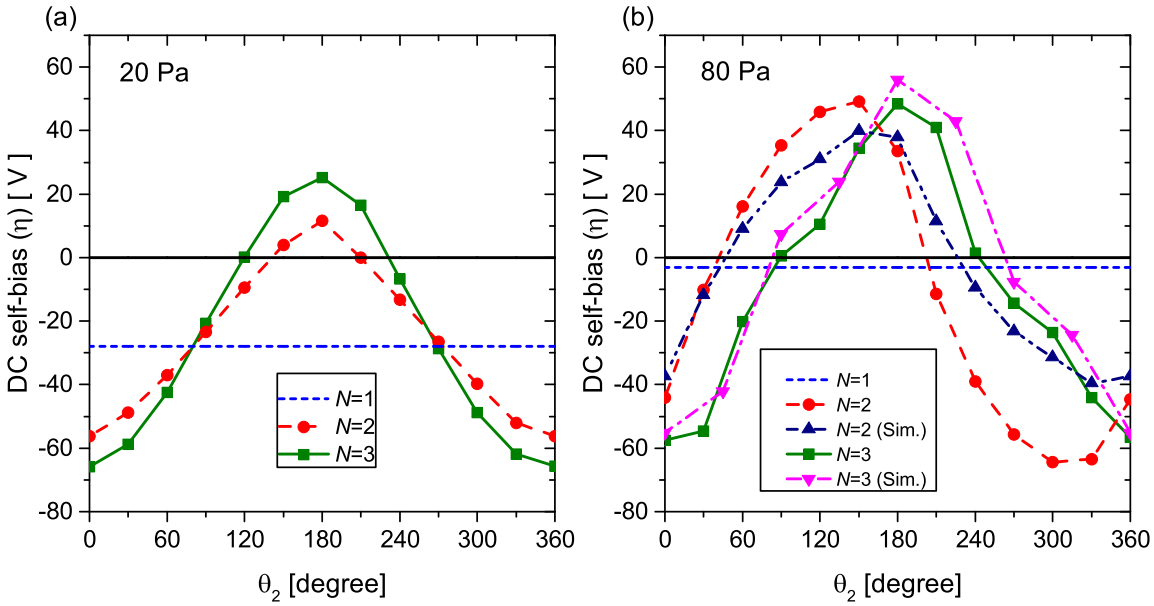

Figure 6.1: DC self-bias as a function of θ_2 for (a) 20 Pa (experimentally measured bias) and (b) 80 Pa (including both the experimentally measured bias and the bias obtained from the PIC simulation, a.k.a. "Sim.") for different numbers of applied harmonics, $N = 1, 2, 3$. Discharge conditions are: CF_4, $d = 25$ mm, $\phi_{\mathrm{tot}} = 210$ V, $\theta_{1,3} = 0°$. Figure provided from its original publication in Brandt *et al.*, Plasma Sources Sci. Technol. 25, 045015 (2016) [BS16].

not observed in the $N = 3$ case.

Figure 6.2 shows spatio-temporal plots of the different plasma parameters obtained from the experiment and the simulation, for $\theta_2 = 0°$ and $N = 3$. Figures 6.2(a) and (b) show the spatio-temporal excitation rate and the electric field obtained from the simulation at 80 Pa, while figures 6.2(c) and (d) show the excitation rate obtained experimentally at 80 Pa and 20 Pa, respectively. In the experiment, the excitation at the (bottom) powered electrode is enhanced with respect to the maxima observed at the grounded electrode due to the geometric asymmetry of the reactor. This does not happen in the simulation and, therefore, the excitation rate at the powered electrode is stronger in the experiment compared to the simulation. Nevertheless, good qualitative agreement is found throughout. The asymmetry of the discharge drastically changes between 20 and 80 Pa as the excitation maximum near the powered electrode moves towards the grounded electrode at higher pressures as the result of a heating mode transition. At 20 Pa, α-mode heating is dominant (see figure 6.2(d)), whereas Drift-Ambipolar mode heating is prevalent at 80 Pa (see figures 6.2(a) and (c)). This transition is caused by the low electronegativity (and collisionality) at 20 Pa and the high electronegativity (and higher collisionality) in combination with specific electron dynamics at 80 Pa. At this high pressure a strong excitation maximum is observed at the collapsing sheath edge close to the grounded electrode (see figure 6.2(a)), which originates from a strong drift and an ambipolar electric field caused by the high local electronegativity [59, 83–88]. The high local electronegativity is caused by a unique mechanism induced by the shape of the driving voltage waveform, which causes the sheath at the grounded electrode to be collapsed for most of the fundamental RF period. This does not happen at the powered electrode. Therefore, at the grounded electrode, negative ions can enter the sheath region, since the time-averaged electric field is very small and only weakly repels these ions from this region. Consequently, the local electron density and conductivity are depleted and a strong reversed electric field is generated by the high RF current which occurs during the sheath collapse [110]. This electric field causes an excitation maximum at the grounded electrode which is further analyzed in figure 6.3.

Figure 6.3(a) shows the reversed electric field and the presence of a potential well formed near the grounded electrode by the (floating) sheath electric field at the electrode during its sheath collapse and an ambipolar field at the bulk plasma side caused by the local slope of the electron density profile (see figure 6.3(b)) [83]. This peak in the electron density near the grounded sheath edge is generated near the time of sheath collapse around t = 12-17 ns and decays slowly throughout the RF period, as there is no sheath expansion to repel these electrons until around $t = 65$ ns. The peak in electron density and, by extension, the ambipolar electric field, persists throughout the RF period and appears prominently in the time-averaged electron density shown in figure 6.3(b). This peak in the electron density is due to the fact that the negative ion density in the sheath region is still prevented from reaching the electrode by the low mean sheath voltage at that electrode (see the CF_3^- and F^- densities near x = 23-24 mm in figure 6.3). Thus, during the phases of sheath collapse, these negative ions are insufficient to satisfy the charged particle flux-balance discussed in section 2.1, but the electron density in that region is normally depleted by attachment processes. Thus, an ambipolar electric field develops in this region between the positive and negative

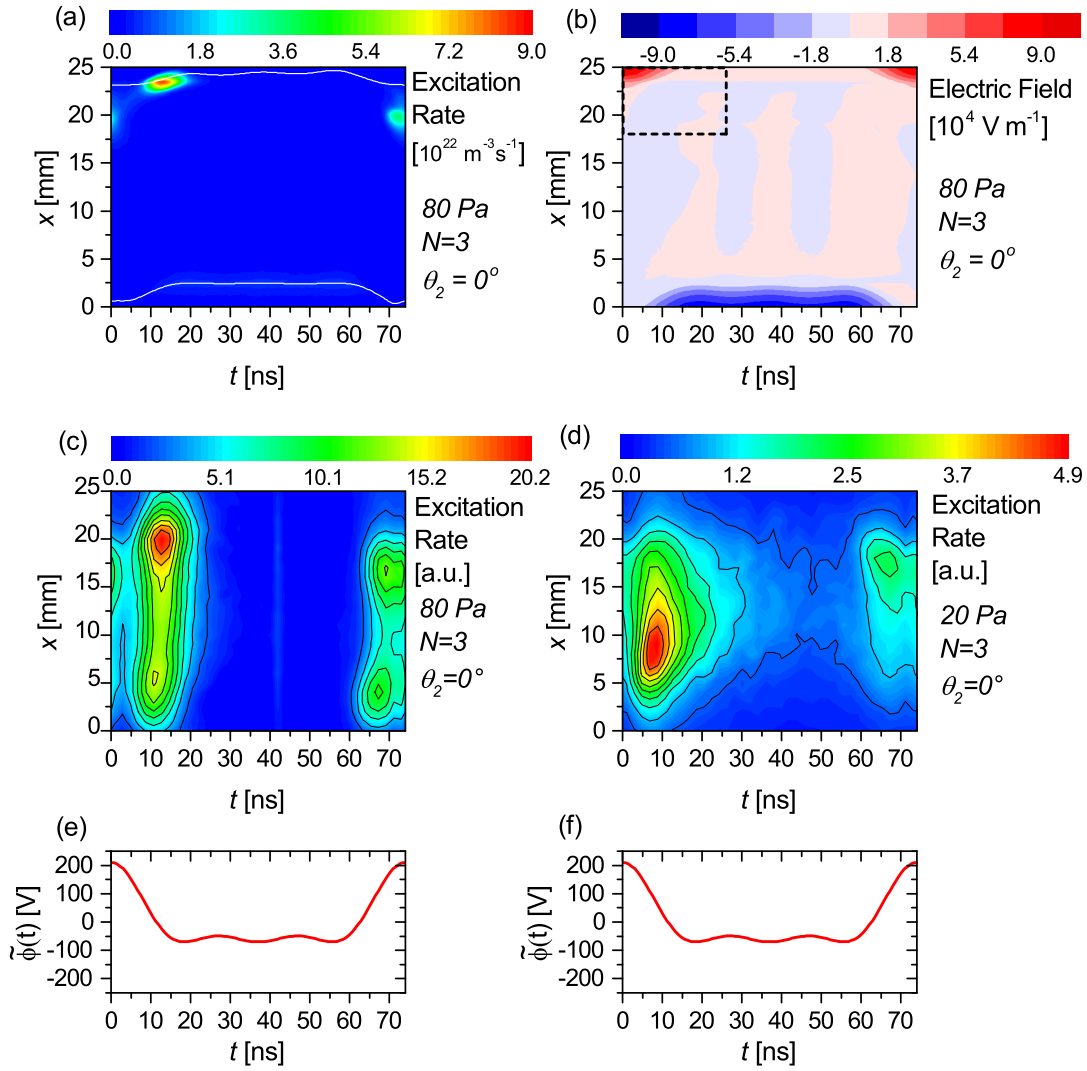

Figure 6.2: Spatio-temporal plots for $N = 3$, $\theta_2 = 0°$ ("peaks-type" waveform) of (a) the excitation rate at 80 Pa obtained from the PIC simulation with the sheath edges shown in white, (b) the electric field at 80 Pa obtained from the simulation, (c) the experimentally measured excitation rate at 80 Pa, and (d) the experimentally measured excitation rate at 20 Pa. The applied voltage waveform is shown in (e) and (f) for reference. Note that positive and negative values on the electric field's color scale correspond to an electric field in the $+\hat{x}$ and $-\hat{x}$ directions, respectively. The dashed region in (b) designates the region of high bulk electric field shown in figure 6.3(a). The powered electrode is situated at $x = 0$, while the grounded electrode is located at $x = 25$ mm. Discharge conditions are: CF_4, $d = 25$ mm, $\phi_{\text{tot}} = 210$ V, $\theta_{1,3} = 0°$. Figure provided from its original publication in Brandt *et al.*, Plasma Sources Sci. Technol. 25, 045015 (2016) [BS16]. ©IOP Publishing. Reproduced with permission. All rights reserved.

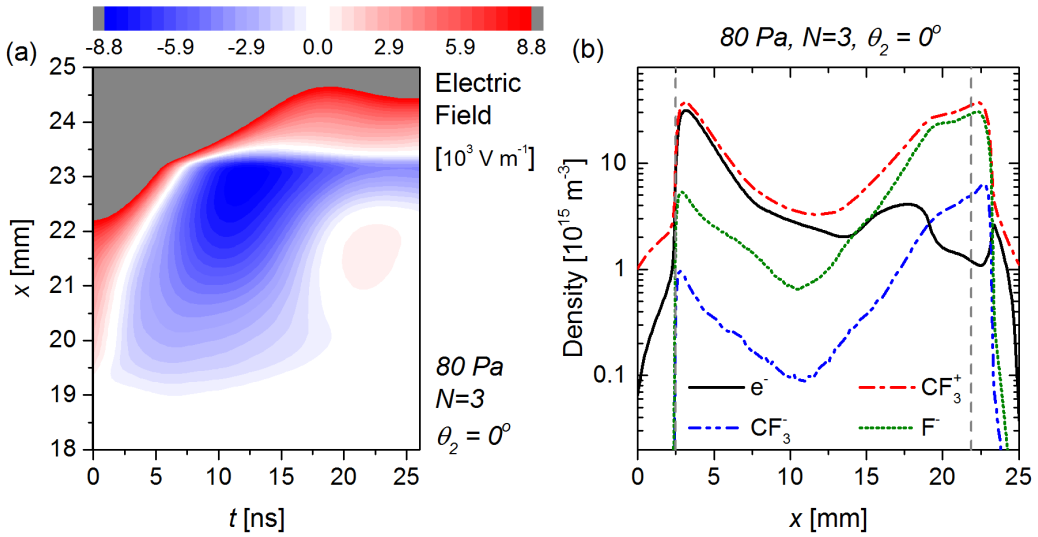

Figure 6.3: (a) Spatio-temporal plot of the electric field at the beginning of one fundamental RF period close to the grounded electrode for 80 Pa, $\theta_2 = 0°$ ("peaks-type" waveform, $N = 3$, $\phi_{\text{tot}} = 210$ V) obtained from the simulation, zoomed into the region of interest in figure 6.2. Note that positive and negative values on the electric field's color scale correspond to an electric field in the $+\hat{x}$ and $-\hat{x}$ directions, respectively. (b) Time-averaged density profiles from the PIC simulations for all charged species [BS16]. The dashed lines indicate the maximum sheath widths of the powered sheath (2.48 mm) and grounded sheath (3.13 mm). Discharge conditions are: CF_4, $d = 25$ mm, $\phi_{\text{tot}} = 210$ V, $\theta_{1,3} = 0°$. Figure provided from its original publication in Brandt *et al.*, Plasma Sources Sci. Technol. 25, 045015 (2016) [BS16].

ion densities which generates additional ionization and leads to the creation of this electron density peak (see section 2.4). After it is generated, the diffusion of this electron density peak is responsible for the ambipolar field seen in this sheath region.

Electrons are then accelerated by the reversed electric field in the bulk and are confined in this potential well. Depending on the energy of the electrons accelerated by the field reversal and those confined in this well, ionization (e.g., CF_3^+ generation) or attachment (CF_3^- and F^- generation) proceeds very efficiently, as shown in the marked regions of figure 6.4. Low energy electrons attach more efficiently compared to high energy electrons, due to the differences in the cross-sections (see figure 3.10). This mechanism leads to strong ionization and a source of negative ions inside the sheath region at the grounded electrode. In this way, an even stronger field reversal is generated due to a further local depletion of the conductivity. These effects are self-amplifying until the plasma stabilizes, making the effect self-sustaining (i.e., a closed loop). Consequently, this geometrically symmetric CCP becomes split into an electropositive (or weakly electronegative) half and a strongly electronegative half, due to the above mechanisms (see figure 6.3(b)).

Figure 6.4(a) also shows the presence of secondary electrons, which are accelerated in the sheath regions. However, they do not affect the ionization and attachment rates considerably (see figure 6.4(c)-(d)). Their contribution to the excitation also appears to be negligible in comparison to other power-coupling mechanisms (see figure 6.2).

The spatio-temporal excitation and electric field plots at $\theta_2 = 180°$ (see figure 6.5) mirror those at $\theta_2 = 0°$. The simulated excitation and electric field are exact mirrors of the $\theta_2 = 0°$ simulation results, as there is no geometric asymmetry there. The experimental PROES plots are affected by the geometric asymmetry in the experiment, but still closely mirror one another. Here, the region close to the powered electrode is electronegative, while the region close to the grounded electrode is electropositive (i.e., weakly electronegative), according to the simulation. An intermediate regime is found at $\theta_2 = 90°$ (see figure 6.6), where the applied waveform utilizes a non-optimized Slope Asymmetry Effect.

Several heating mode transitions can be observed as a function of θ_2 or pressure. Specifically, a clear transition from the α-heating mode to the Drift-Ambipolar mode occurs between 20 and 80 Pa for fixed harmonics' phases and voltage amplitudes (see figures 6.2, 6.5, 6.6), with the Drift-Ambipolar mode being favored at higher pressures due to the higher electronegativity and higher collisionality at higher pressures.

Figure 6.7 demonstrates that adding higher harmonics enhances the sheath expansion heating relative to the Drift-Ambipolar heating. This is due to an increase of the driving waveform's slope during sheath expansion, which increases the effectiveness of α-mode heating. For $\theta_2 = 270°$, this leads to more spatially symmetric excitation dynamics for $N = 3$, since the sheath expansion heating at the powered electrode is enhanced relative to the heating at the grounded electrode at about 28 ns. In terms of the symmetry parameter from equation (2.15), ε is less than unity for $N = 2$ and ε is approximately unity for $N = 3$ at $\theta_2 = 270°$. Thus, a negative DC self-bias is obtained for two harmonics at $\theta_2 = 270°$, and almost no bias

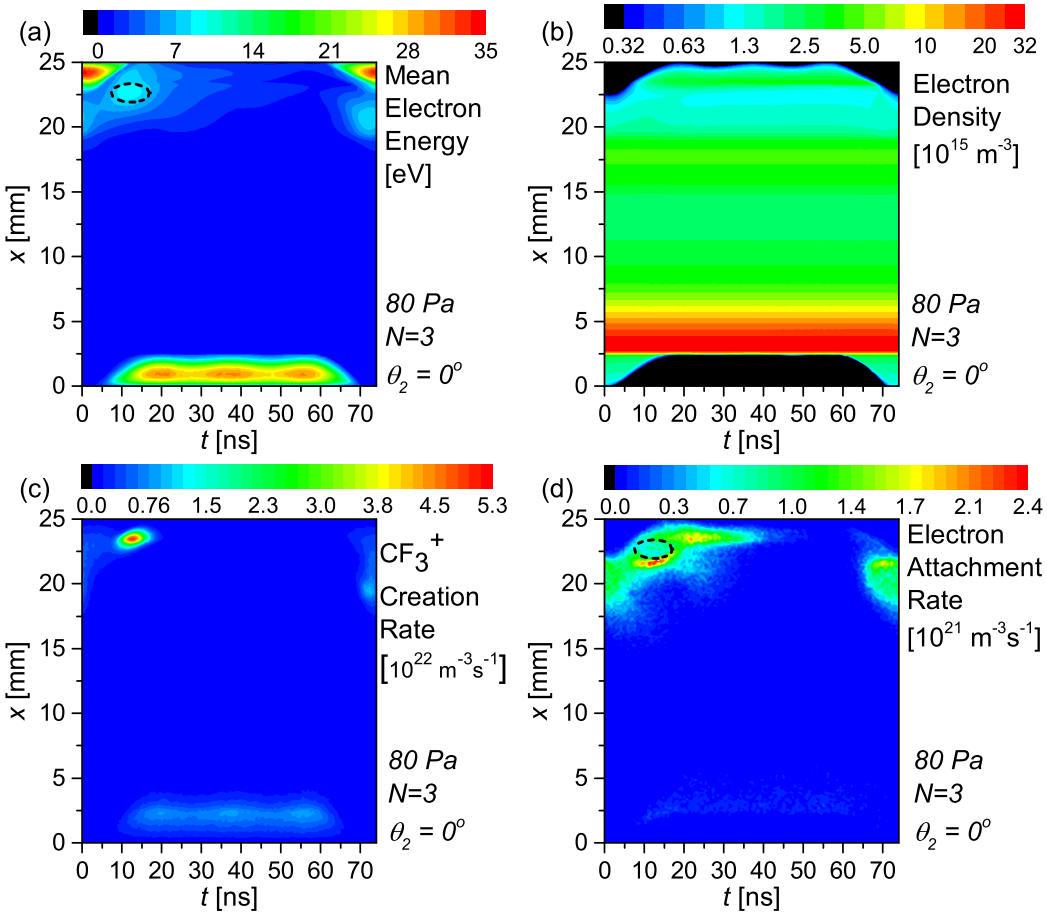

Figure 6.4: Spatio-temporal plots for 80 Pa, $\theta_2 = 0°$ ("peaks-type" waveform, $N = 3$, $\phi_{\text{tot}} = 210$ V) of (a) mean electron energy, (b) electron density, (c) rate of CF_3^+ creation, and (d) rate of electron attachment (i.e., CF_3^- and F^- creation), as obtained from the simulation. Discharge conditions are: CF_4, $d = 25$ mm, $\phi_{\text{tot}} = 210$ V, $\theta_{1,3} = 0°$. Figure provided from its original publication in Brandt *et al.*, Plasma Sources Sci. Technol. 25, 045015 (2016) [BS16].

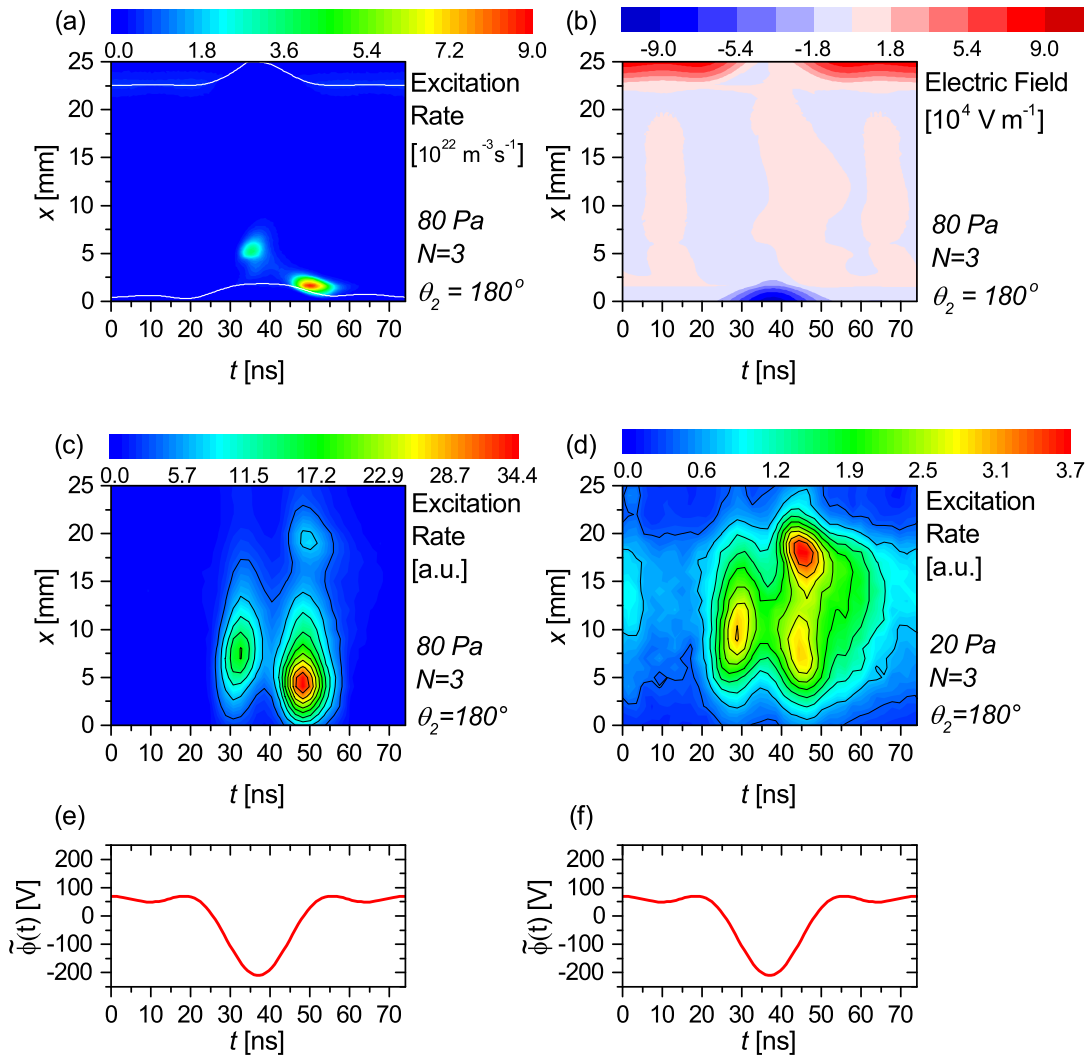

Figure 6.5: Spatio-temporal plots for $\theta_2 = 180°$ ("valleys-type" waveform, $N = 3$, $\phi_{\text{tot}} = 210$ V) of (a) the excitation rate at 80 Pa obtained from the simulation with the sheath edges shown in white, (b) the electric field at 80 Pa obtained from the simulation, (c) the experimentally measured excitation rate at 80 Pa, and (d) the experimentally measured excitation rate at 20 Pa. Note that positive and negative values on the electric field's color scale correspond to an electric field in the $+\hat{x}$ and $-\hat{x}$ directions, respectively. The applied voltage waveform is shown in (e) and (f) for reference. Discharge conditions are: CF_4, $d = 25$ mm, $\phi_{\text{tot}} = 210$ V, $\theta_{1,3} = 0°$. Figure provided from its original publication in Brandt *et al.*, Plasma Sources Sci. Technol. 25, 045015 (2016) [BS16].

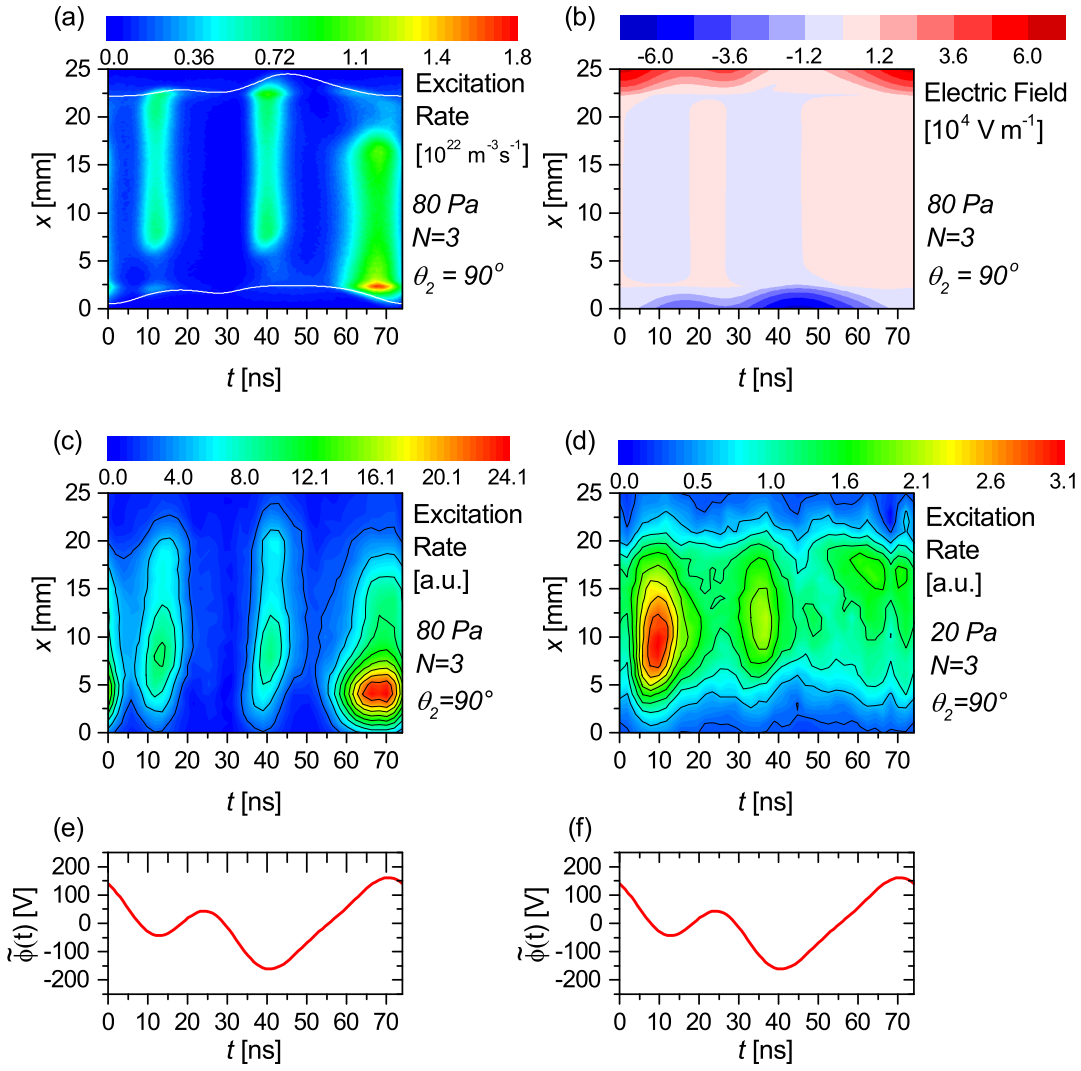

Figure 6.6: Spatio-temporal plots for $\theta_2 = 90°$ ($N = 3$, $\phi_{\text{tot}} = 210$ V) of (a) the excitation rate at 80 Pa obtained from the simulation with the sheath edges shown in white, (b) the electric field at 80 Pa obtained from the simulation, (c) the experimentally measured excitation rate at 80 Pa, and (d) the experimentally measured excitation rate at 20 Pa. The applied voltage waveform is shown in (e) and (f) for reference. Note that positive and negative values on the electric field's color scale correspond to an electric field in the $+\hat{x}$ and $-\hat{x}$ directions, respectively. Discharge conditions are: CF_4, $d = 25$ mm, $\phi_{\text{tot}} = 210$ V, $\theta_{1,3} = 0°$. Figure provided from its original publication in Brandt *et al.*, Plasma Sources Sci. Technol. 25, 045015 (2016) [BS16].

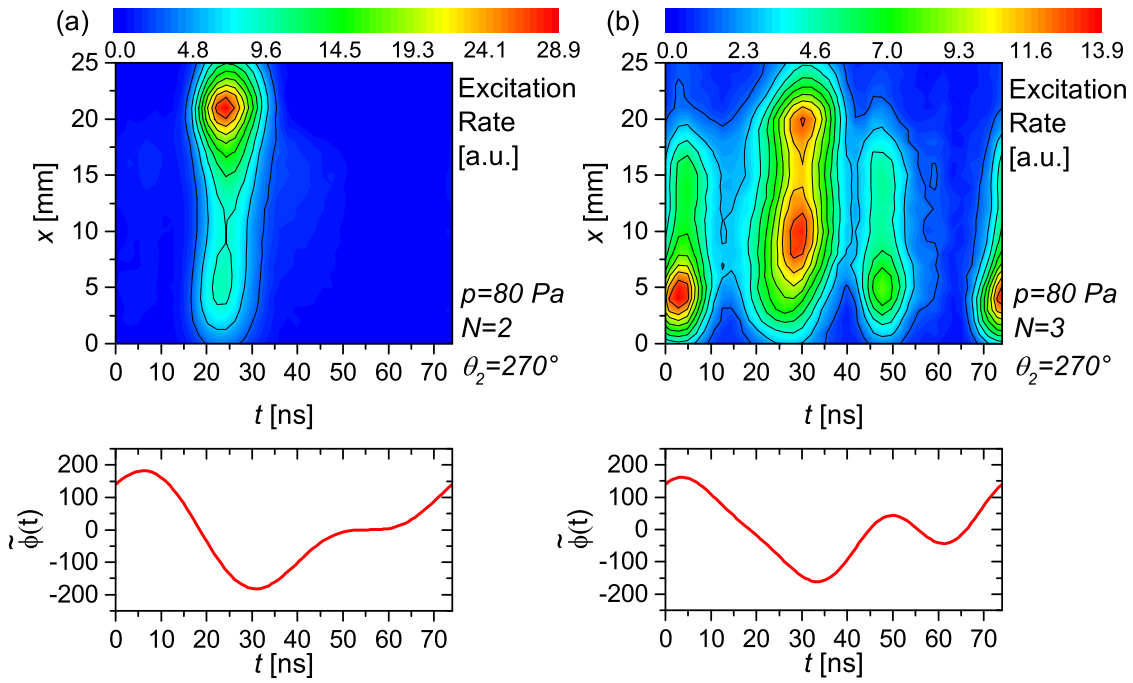

Figure 6.7: Spatio-temporal plots for $\theta_2 = 270°$ ($\phi_{\mathrm{tot}} = 210$ V) at 80 Pa of (a) the experimentally measured excitation rate for $N = 2$ and (b) the experimentally measured excitation rate for $N = 3$. Discharge conditions are: CF_4, $d = 25$ mm, $\phi_{\mathrm{tot}} = 210$ V, $\theta_{1,3} = 0°$. Figure provided from its original publication in Brandt *et al.*, Plasma Sources Sci. Technol. 25, 045015 (2016) [BS16].

is observed at the same phase for $N = 3$ (see figure 6.1). The strongly negative bias for $N = 2$ at this phase is caused by the SAE, although its effect is reversed compared to electropositive gases due to the presence of the Drift-Amipolar heating mode. In electropositive gases such as argon, positive DC self-biases are often observed for this phase [63–66].

6.1.2 Slope asymmetry in CF_4

The Sawtooth waveforms used here (see figure 3.3(c)) are realized with the fixed phases and amplitudes defined in section 2; these waveforms consist of three consecutive harmonics of $f = 13.56$ MHz, each with an amplitude according to equation (3.2). The amplitudes and phases of the Sawtooth Up waveform for $N = 3$ are: $\phi_1 = 138$ V, $\phi_2 = 69$ V, $\phi_3 = 46$ V, $\theta_1 = 0°$, $\theta_2 = 270°$, and $\theta_3 = 180°$. The Sawtooth Up waveform yields a fast sheath expansion at the powered electrode as a result of the fast transition from its maximum positive applied voltage to its maximum negative applied voltage, and a fast sheath contraction at the grounded electrode. Conversely, the Sawtooth Down waveform yields a fast expansion of the grounded sheath as the fast transition occurs from the maximum negative voltage to the maximum positive voltage. The $N = 3$ Sawtooth Down waveform has the same amplitudes and phases as listed above, with the exception that $\theta_2 = 90°$.

The experimentally obtained DC self-bias (η) for the Sawtooth waveforms is plotted as a function of pressure in figure 6.8. A significant geometric asymmetry is present, especially at lower pressures ($p \leqslant 30$ Pa), which prevents comparison of our experimental results to those of the PIC simulations. The bias changes drastically as a function of pressure as a result of the SAE and the geometric asymmetry of the discharge. No AAE can be present due to the identical global extrema in the driving voltage waveform. For the Sawtooth Down waveform, the sign of the self-bias changes as the pressure increases. In a geometrically symmetric reactor, this would also happen for the Sawtooth Up waveform. This reversal of the discharge asymmetry as a function of pressure is caused by a transition from the α-heating mode to the Drift-Ambipolar heating mode induced by increasing the pressure and thus increasing the electronegativity. Above 50 Pa, the self-bias stays approximately constant as a function of pressure after this mode transition. This is expected to be highly relevant for applications, as it completely reverses the role of the two electrodes with regards to the EAE. For example, a negative DC self-bias voltage corresponds to enhanced excitation at the grounded side, whereas, in electropositive plasmas, it corresponds to enhanced excitation at the powered side.

The Sawtooth Down waveform causes the grounded sheath to expand quickly and the sheath at the powered electrode to expand slowly, while for the Sawtooth Up waveform the situation is reversed. At 20 Pa, the discharge operates in the α-heating mode (see figures 6.9(a)-(b)). At this low pressure, the discharge is geometrically asymmetric. This results in an increase of the excitation rate at the powered electrode relative to that at the grounded electrode. For the Sawtooth Down waveform, the spatio-temporal excitation rate at the grounded side during the grounded sheath expansion is more visible compared to that

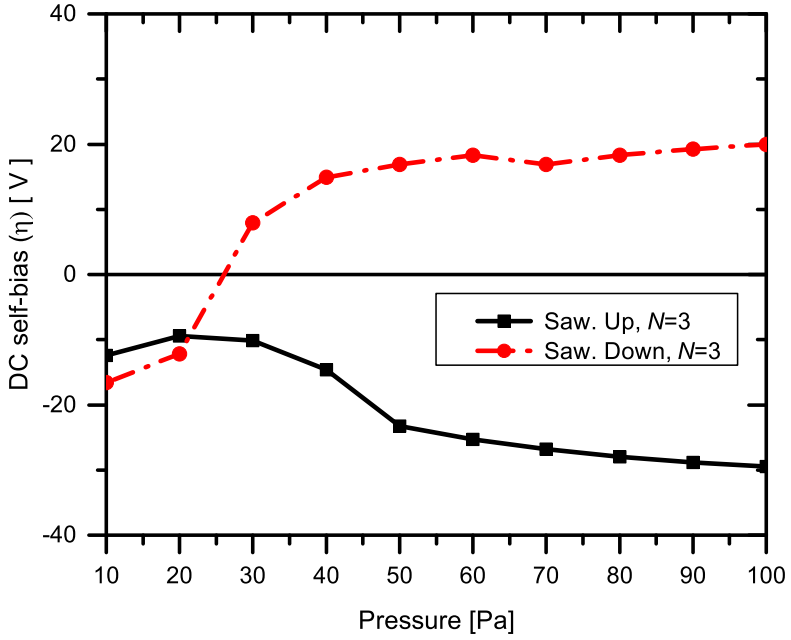

Figure 6.8: Experimentally measured DC self-bias voltage as a function of pressure for the $N = 3$ Sawtooth waveforms. Discharge conditions are: CF_4, $d = 25$ mm, $\phi_{\text{tot}} = 253$ V, $\theta_1 = 0°$. Figure provided from its original publication in Brandt *et al.*, Plasma Sources Sci. Technol. 25, 045015 (2016) [BS16].

measured for a Sawtooth Up waveform, as the grounded sheath expands very quickly once per fundamental RF period. Due to the geometric asymmetry of the reactor, the density in the powered sheath is still higher than that in the grounded sheath, i.e., $\bar{n}_{sp} > \bar{n}_{sg}$. Thus, according to equation (2.15), the symmetry parameter ε is relatively high for this situation, though it is still less than unity due to the geometric asymmetry. The self-bias is then weakly negative at low pressures, according to equation (2.14).

At higher pressures (50 Pa and 80 Pa, see figures 6.9(c)-(d) and figures 6.9(e)-(f), respectively), the discharge operates in the Drift-Ambipolar heating mode and there is strong excitation at the grounded/powered electrode for the Sawtooth Up/Down waveform, respectively, where the sheath collapses quickly once per fundamental RF period. This is caused by a mechanism similar to that described in subsections 4.1.1 and 4.1.2. The high negative-ion density leads to a local depletion of the electron density and a strong electric-field reversal at the edge of the rapidly collapsing sheath. The self-amplifying mechanism described before is only effective at one electrode for Sawtooth waveforms, where electrons are accelerated towards the electrode (i.e., towards the potential well) and not away from it (and its corresponding sheath). In combination with a reactor with better geometric symmetry, this leads to $\bar{n}_{sp} \gg \bar{n}_{sg}$ for the Sawtooth Down waveform, where $\varepsilon > 1$ and a positive bias is generated, and $\bar{n}_{sp} < \bar{n}_{sg}$ for the Sawtooth Up waveform, where $\varepsilon < 1$ and a

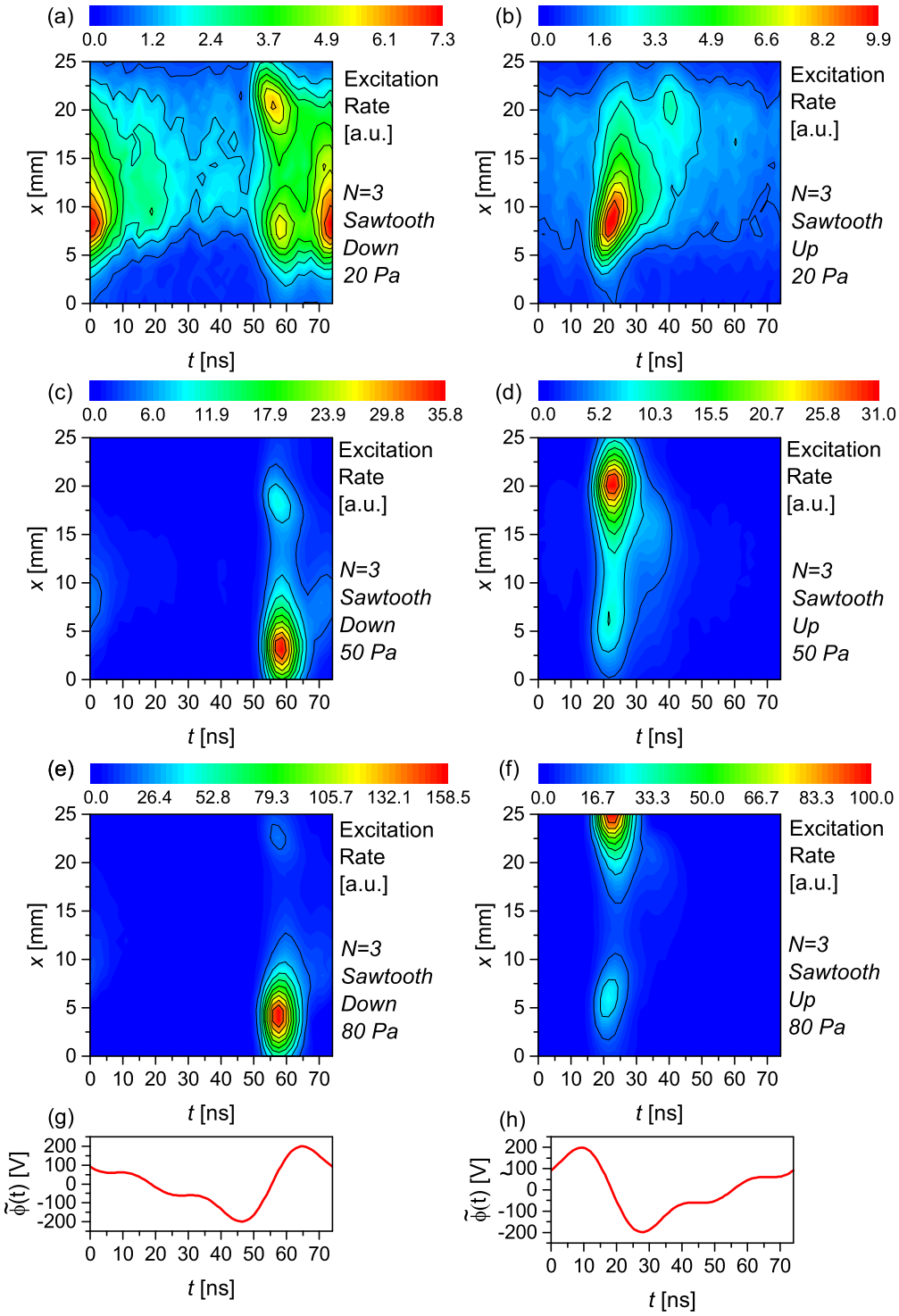

Figure 6.9: Experimentally measured spatio-temporal excitation rate for $N = 3$ Sawtooth waveforms at (a-b) 20 Pa, (c-d) 50 Pa, and (e-f) 80 Pa. The left column contains the Sawtooth Down ($\theta_2 = 90°$, $\theta_3 = 180°$) results, while the right column shows the Sawtooth Up ($\theta_2 = 270°$, $\theta_3 = 180°$) results. The applied voltage waveforms are shown in (g) and (h) for reference. Discharge conditions are: CF_4, $d = 25$ mm, $\phi_{\mathrm{tot}} = 253$ V, $\theta_1 = 0°$. Figure provided from its original publication in Brandt *et al.*, Plasma Sources Sci. Technol. 25, 045015 (2016) [BS16].

negative bias is generated. In conclusion, the change of the DC self-bias and the reversal of the discharge symmetry as a function of pressure for the Sawtooth waveforms can be explained by a transition to an electron heating mode characteristic of an electronegative plasma, which is induced by increasing the pressure.

6.2 Charged particle dynamics of capacitively coupled plasmas driven by tailored voltage waveforms in argon-CF_4 gas mixtures

As the effects of varying the Ar-to-CF_4 mixing ratio, and thus the plasma's electronegativity, on CCPs driven by tailored voltage waveforms are best understood by first examining the spatio-temporal dependence of the electron impact excitation/ionization rate, attachment processes, electric field, and the mean electron energy, the experimental and simulation results for these quantities are first discussed in subsection 6.2.1. These spatio-temporal dynamics and results of the analytical model are then linked to the DC self-bias evolution seen in both the simulations and the experiments in subsection 6.2.2. The simulations shown in this section are implemented and performed by the group of Zoltan Donkó and are analyzed in this work. This work is also published in Brandt *et al.* [BS19].

6.2.1 Spatio-temporal dynamics in argon-CF_4 gas mixtures

The global electronegativity (ζ) obtained from the PIC/MCC simulations is shown as a function of the argon content in the buffer gas for the "peaks-type" waveform at 20 Pa and 60 Pa in figure 6.10. For 20 Pa, the electronegativity is significant only in the pure CF_4 case and decreases dramatically with increasing argon content, until approximately 30% Ar, where it becomes negligible. The global electronegativity at 60 Pa exhibits a more complex variation across the 0-100% argon content interval in the simulations, moving from a low value for 0-20% Ar to a highly electronegative regime, which decreases with increasing argon content but remains significant even up to 90% Ar. The reduced values of ζ in the 0-20% argon content interval for 60 Pa are attributed to the fact that the plasma is divided into an electropositive and an electronegative region under these conditions, while it is electronegative in the whole discharge for 30-90% Ar (as will be shown below). This transition from a spatially asymmetric electronegative profile to a spatially symmetric electronegative profile occurs as a product of changing the spatial asymmetry in the attachment rate of electrons by increasing the electron power absorption from the α-mode as a function of increasing argon content. At very low argon content values, the generation of negative ions occurs primarily near the grounded electrode, like in section 6.1. As the argon content is increased, the enhanced α-mode heating increases the mean electron energy near the expanding powered sheath edge, i.e., in the other half of the discharge compared to the DA-mode heating, leading to an increased attachment rate in the discharge half adjacent to the powered electrode. Therefore, negative ions are

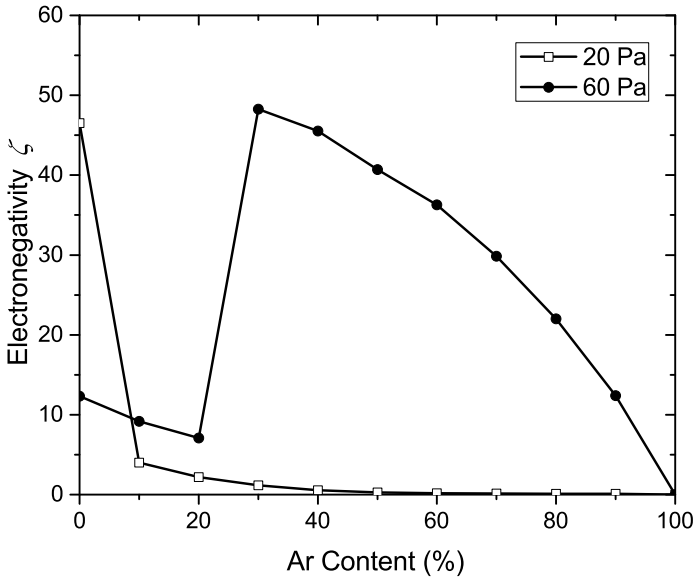

Figure 6.10: Global electronegativity ζ of the discharge obtained from the PIC/MCC simulation for the "peaks-type" waveform ($N = 3$) as a function of the argon content in the buffer gas at 20 Pa (open boxes) and 60 Pa (closed circles). Simulation conditions are: Ar-CF_4, $d = 25$ mm, $\phi_{\mathrm{tot}} = 150$ V, $\theta_k = 0° \; \forall \; k$. Figure provided from its original publication in Brandt *et al.*, Plasma Sources Sci. Technol. 28, 095021 (2019) [BS19].

generated near both electrodes and diffuse into the bulk, leading to an spatially symmetric electronegative regime. The presence of the electropositive region for 0-30% Ar reduces the global electronegativity. The physical origin of the strongly electronegative region adjacent to the grounded electrode at low Ar admixtures at 60 Pa is the formation of a potential well at the grounded electrode, which confines negative ions. This, in turn, is caused by the specific shape of the driving voltage waveform, which causes the sheath at the grounded electrode to be collapsed for most of the fundamental RF period and local maxima of the electron density at the position of the maximum sheath width. At the grounded electrode this leads to the formation of an ambipolar field that accelerates negatively charged particles towards this electrode. A potential well is caused by this ambipolar field and the floating potential at the electrode. The presence of the ambipolar electric field causes significant electron power absorption and, thus, a high mean electron energy at the time of high RF current, when the local sheath collapses. This enhances the attachment and, thus, the local negative ion density, which self-amplifies this effect. This phenomenon is discussed in detail in subsection 6.1.1 for a pure CF_4 discharge.

The spatio-temporal electron impact excitation rate for the 703.7 nm fluorine line obtained from the PIC/MCC simulation, which assumes a geometrically symmetric discharge, is shown in figure 6.11 for the "peaks-type" waveform at both 20 Pa (figures 6.11(a)-(c)) and 60 Pa

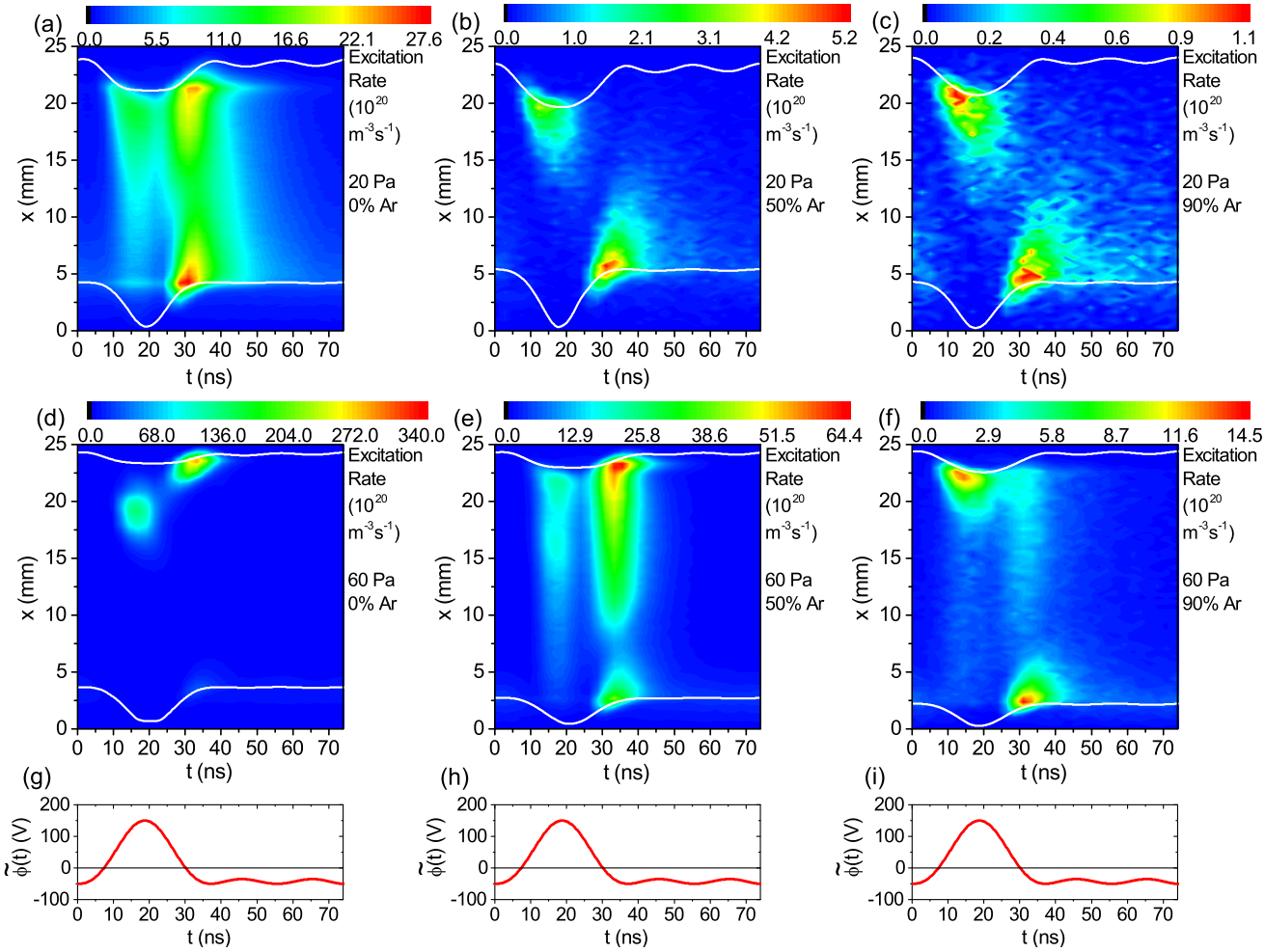

Figure 6.11: Spatio-temporal distribution of the electron impact excitation rate for the 703.7 nm fluorine line (excitation threshold energy: 14.56 eV) obtained from PIC/MCC simulations for the "peaks-type" waveform ($N = 3$) at 20 Pa (a)-(c) and 60 Pa (d)-(f), as a function of argon content in the buffer gas. The sheath edges are marked by the white lines based on the Brinkmann criterion [98]. The driving voltage waveform is shown for reference in (g)-(i). The powered electrode is located at $x = 0$ mm, while the grounded electrode is at $x = 25$ mm. Simulation conditions are: Ar-CF_4, $d = 25$ mm, $\phi_{\mathrm{tot}} = 150$ V, $\theta_k = 0° \; \forall \; k$. Figure provided from its original publication in Brandt *et al.*, Plasma Sources Sci. Technol. 28, 095021 (2019) [BS19]. ©IOP Publishing. Reproduced with permission. All rights reserved.

(figures 6.11(d)-(f)) for the 0% Ar, 50% Ar, and 90% Ar cases. The sheath edges are computed using the Brinkmann criterion [98] taking the presence of negative ions into account and are shown as white lines in each plot. The maximum absolute value of the excitation rate is observed to decrease both as the argon content is increased and as the pressure is decreased. In general, there are two separate mechanisms of electron acceleration that cause excitation maxima at different positions and times within the fundamental RF period: (i) α-mode excitation is caused by electron power absorption on the bulk side of the expanding sheath edge. (ii) DA-mode excitation maxima occur on the bulk side of the collapsing sheath edge and are caused by the local maxima of the electron density at the position of the maximum sheath width in electronegative CCPs. These cause ambipolar electric fields that accelerate electrons towards the adjacent electrode. Here, a transition from the DA power absorption mode to the α-mode is observed at both pressures as a function of increasing argon content. At 60 Pa, the mode transition has a different behavior with increasing argon content where the DA-mode heating is sustained to much higher argon content values. For example, the DA-mode heating remains dominant at 50% Ar (figure 6.11(e)) and remains relevant even for 90% Ar (figure 6.11(f)). This confirms the results shown in figure 6.10, where at 60 Pa the electronegativity (ζ) is about 40 and 15 for 50% Ar and 90% Ar, respectively. In the 0-20% Ar range at 60 Pa (e.g., figure 6.11(d) and figure 6.10), a highly localized DA-mode is observed with excitation maxima only at the collapsing sheath of the grounded electrode, similar to that observed in section 6.1 for pure CF_4. The change in the localization of the excitation/ionization in figures 6.11(d)-(f) from near the grounded sheath (DA-mode) to near the powered sheath (α-mode) is quite significant at 60 Pa in the simulations. It is thus easily conceivable that the symmetry parameter ε, which depends explicitly on the ratio of the ion density in both sheaths, would be dramatically changed by the mode transition with increasing argon content in the 60 Pa case (see later in figure 6.18(a)). At 20 Pa, a hybrid DA-α mode exists near 0% Ar and the discharge transitions to a pure α-mode near 30% Ar, in contrast to the DA-mode being sustained to almost 90% Ar for 60 Pa. The reduced change in excitation localization for 20 Pa implies that the symmetry parameter ε is expected to vary little with increasing argon content as a result (see later in figure 6.18(a)). The different behavior of the mode transition with increasing argon content at 20 Pa and 60 Pa is caused by the different electronegativity (see figure 6.10).

Figure 6.12 shows the results of the PROES measurements at 20 Pa (panels (a)-(c)) and 60 Pa (panels (d)-(f)) for the "peaks-type" waveform for 0%, 50%, and 90% argon content. Compared to the results of the simulations, performed for the same discharge conditions (see figure 6.11), good qualitative agreement between experimental and computational results is found. The differences in figures 6.11 and 6.12 are caused by the presence of a geometric asymmetry in the experiment, which is not included in the PIC/MCC simulations. In contrast to figure 6.11, the α-mode excitation near the powered electrode is significantly stronger than that at the grounded electrode even in the 60 Pa, 0% Ar case. This is caused by the presence a more negative DC self-bias in the experiment due to the geometric discharge asymmetry. This results in a smaller change in the localization of the excitation/ionization across the discharge in the experiment as the argon content is increased, in turn suggesting that any ε variation is also smaller in the experiment. The sustainment of the DA-mode to very high argon content values at 60 Pa seen in figures 6.11(d)-(f) is confirmed by the

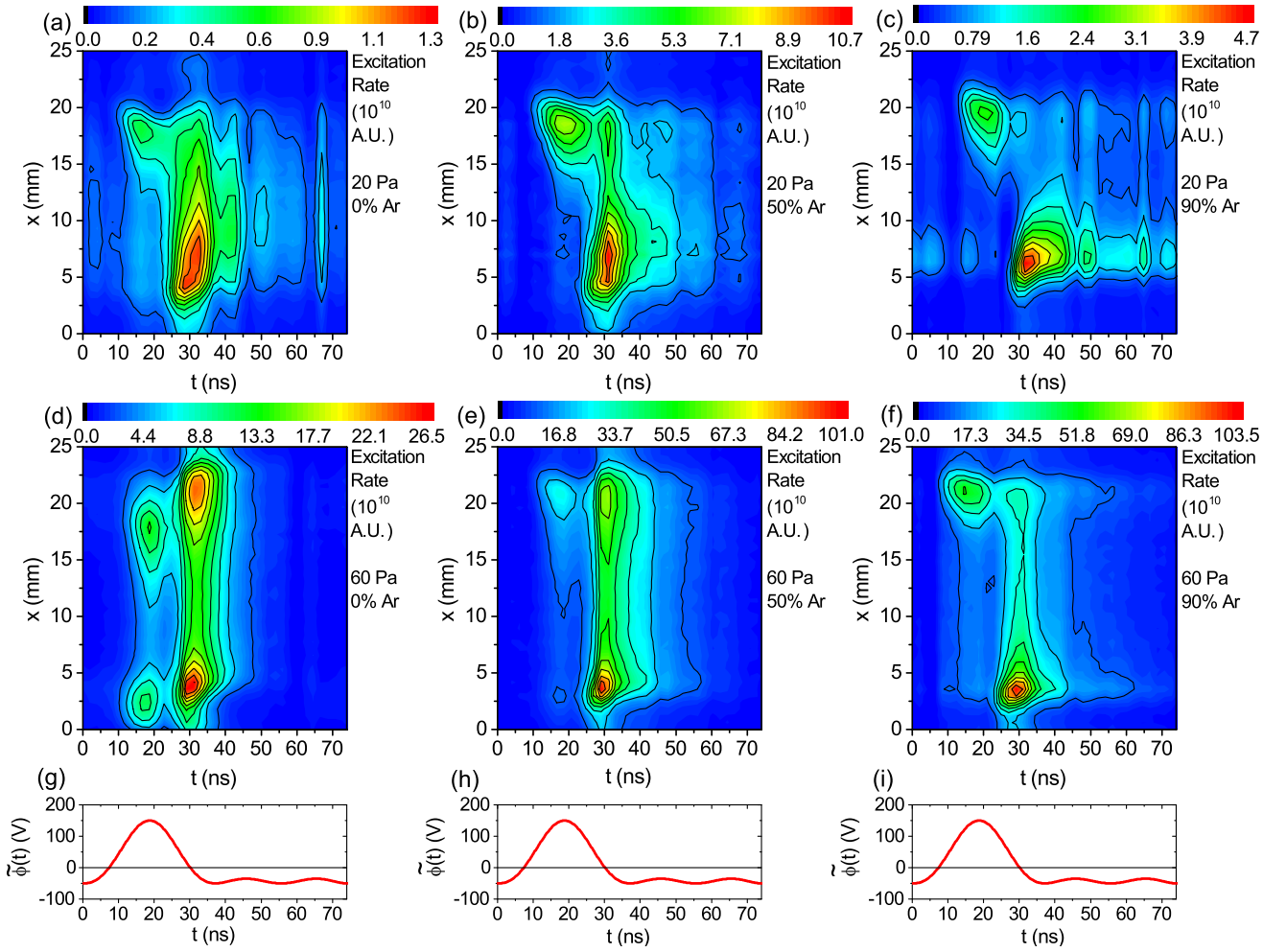

Figure 6.12: Spatio-temporal distributions of the electron impact excitation rate of the 703.7 nm fluorine line obtained via PROES in the experiment for the "peaks-type" waveform ($N = 3$) at 20 Pa (a)-(c) and 60 Pa (d)-(f), as a function of argon content in the buffer gas. The driving voltage waveform is shown for reference in (g)-(i). The powered electrode is located at $x = 0$ mm, while the grounded electrode is at $x = 25$ mm. Discharge conditions are: Ar-CF_4, $d = 25$ mm, $\phi_{\mathrm{tot}} = 150$ V, $\theta_k = 0° \ \forall \ k$. Figure provided from its original publication in Brandt *et al.*, Plasma Sources Sci. Technol. 28, 095021 (2019) [BS19].

experimentally measured excitation rates in figures 6.12(d)-(f). Similarly, at 20 Pa, the DA-α mode transition occurs at a smaller argon content value than that at 60 Pa, and the weaker mode transition should not significantly change the plasma symmetry.

The DA power absorption of electrons in the plasma bulk is caused by a significant density of negative ions in the bulk plasma and, thus, a depleted electron density. This leads to a reduced conductivity in the bulk and the generation of an enhanced bulk electric field required to drive the current. Consequently, electrons are accelerated to high energies in the bulk and cause excitation at the times of high current. Negative ion formation proceeds via collisional attachment processes, whose cross-sections are high only within an energy interval of 5-10 eV for CF_4 [101, 102]. The total attachment rate obtained from the simulation is shown for the "peaks-type" waveform at 20 Pa and 60 Pa for 0%, 50% and 90% argon content in figure 6.13. At 20 Pa (figures 6.13(a)-(c)), this rate is comparably much lower than for the 60 Pa cases throughout the discharge and becomes insufficient to sustain the DA-mode at a much lower argon content value due to the decreased mean electron energy at that pressure. This leads to a lower negative ion density, a less depleted electron density, lower electronegativity (as in figure 6.10), and thus a substantially weaker DA-mode for 20 Pa. This also constitutes the well-known phenomenon of the DA-mode being primarily induced at higher pressure in CF_4 [60, 89]. Conversely, at 60 Pa (figures 6.13(d)-(f)), the total attachment rate remains significant with increasing argon content, even up to 90% Ar, which supports the sustainment of the electronegativity and the DA-mode to high argon content values seen in figures 6.10, 6.11, and 6.12. The localized DA-mode at 60 Pa for 0% Ar in the simulations is further supported by the localized attachment rate maximum near the grounded electrode (see figure 6.13(d)) caused by a high local mean electron energy and the presence of a potential well that confines negatively charged particles to near the grounded electrode [BS16]. The α-mode heating, which increases with increasing argon content, is primarily responsible for generating attachment near the powered electrode for the "peaks-type" waveform, since it causes a local increase of the mean electron energy (see figure 6.16). Also, the DA- to α-mode transition leads to a breakdown of the localized negative ion density maximum at the grounded electrode (see figure 6.14(d) - (f)) and thus the "local" DA-mode as the argon content is increased. This is due to the α-mode heating generating a region of significant attachment close to the powered electrode, as can be seen for the 60 Pa, 50% Ar case in figures 6.11(e) and 6.13(e). These results imply that an increase of the electropositive gas content may actually lead to an enhanced discharge electronegativity for conditions where the attachment rate is dictated primarily by the DA-mode, e.g., for low electropositive content values in an Ar-CF_4 mixture. It also explains the jump from low to high global electronegativity observed in figure 6.10 due an increase in argon content from 20% Ar to 30% Ar.

The time-averaged densities of each charged particle species traced in the simulation for the "peaks-type" waveform cases are shown in figure 6.14. For 20 Pa, the negative ion and electron densities (i.e., the local electronegativity) remain spatially uniform in the plasma bulk. On the other hand, at 60 Pa, the discharge is split into two halves of strongly different electronegativity at 0% Ar according to the spatially asymmetric distribution of the attachment rate shown in figure 6.13(d). The plasma exhibits a spatially nearly uniform but still electronegative density profile near an argon content value of 30%. The electronegativity

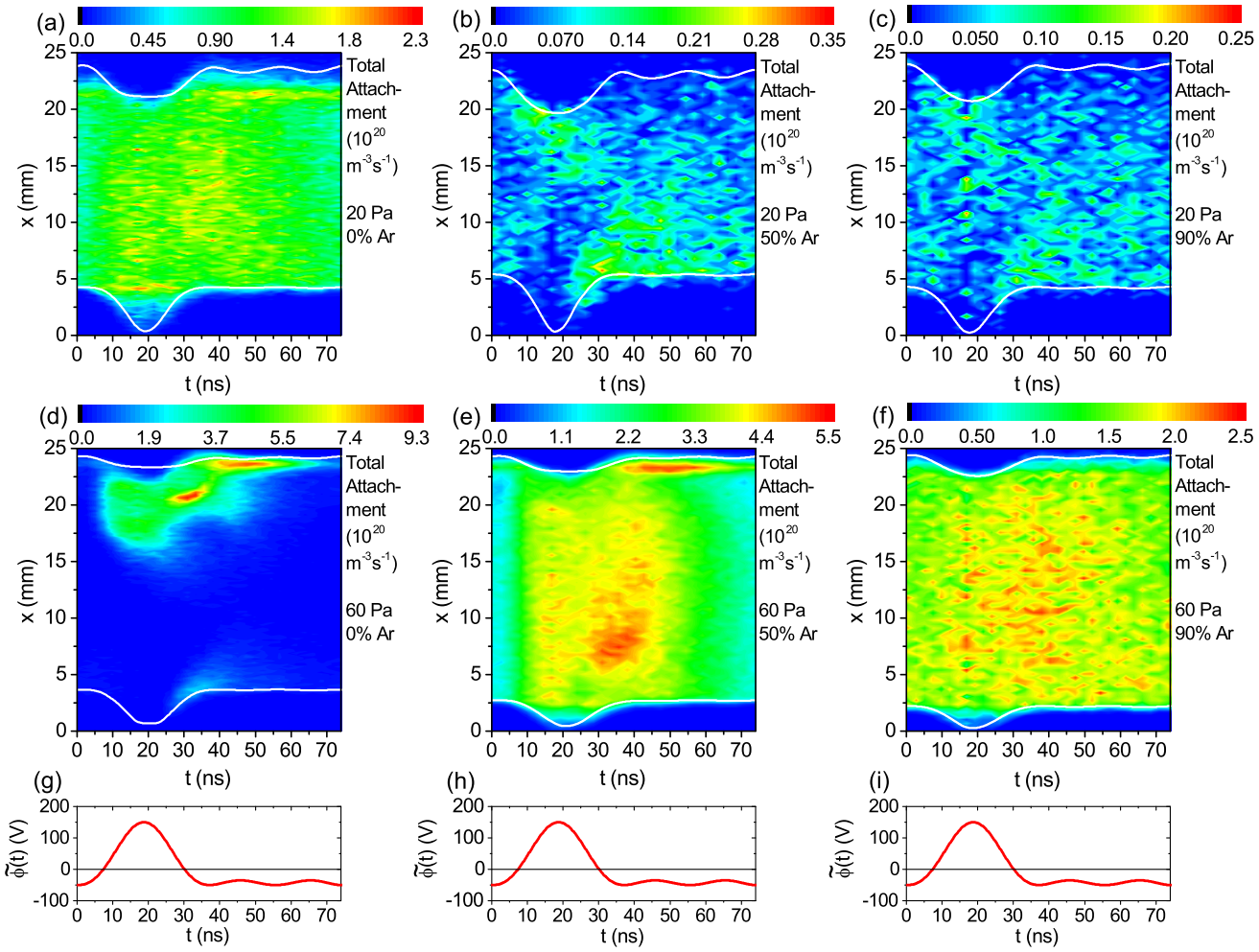

Figure 6.13: Spatio-temporal distributions of the total attachment rate from the simulation for the "peaks-type" waveform ($N = 3$) at 20 Pa (a-c) and 60 Pa (d-f), as a function of argon content in the buffer gas. The sheath edges are marked by the white lines based on the Brinkmann criterion [98] in each plot. The driving voltage waveform is shown for reference in (g)-(i). The powered electrode is located at $x = 0$ mm, while the grounded electrode is at $x = 25$ mm. Simulation conditions are: Ar-CF_4, $d = 25$ mm, $\phi_{\mathrm{tot}} = 150$ V, $\theta_k = 0° \; \forall \; k$. Figure provided from its original publication in Brandt *et al.*, Plasma Sources Sci. Technol. 28, 095021 (2019) [BS19]. ©IOP Publishing. Reproduced with permission. All rights reserved.

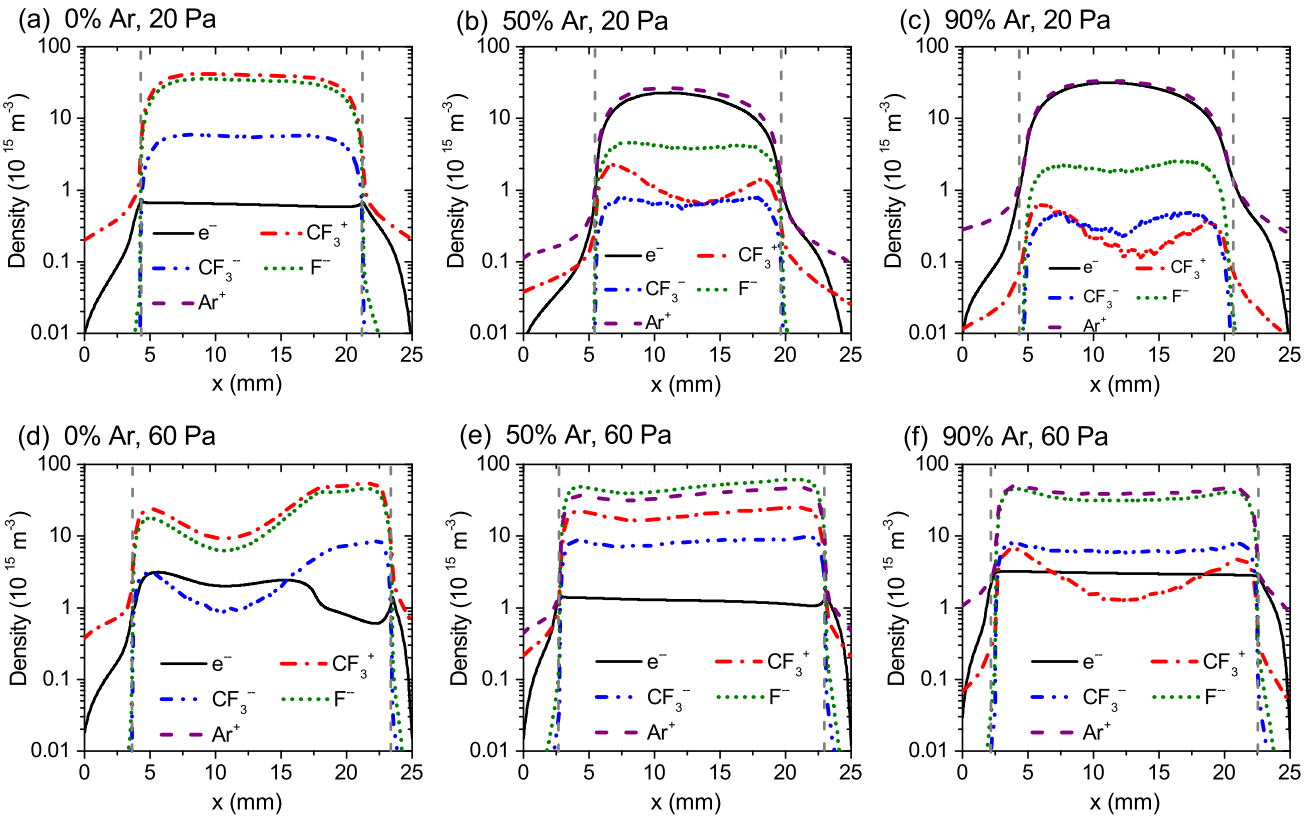

Figure 6.14: Simulation results for the time-averaged densities of each charged particle species traced in the simulation (CF_3^+, CF_3^-, F^-, Ar^+, and electrons) as a function of position x between the powered ($x = 0$ mm) and grounded ($x = 25$ mm) electrodes for the "peaks-type" waveform ($N = 3$) at 20 Pa (a)-(c) and 60 Pa (d)-(f), and as a function of argon content in the buffer gas. The maximum sheath widths are marked by the gray dashed vertical lines based on the Brinkmann criterion [98] in each plot. Simulation conditions are: Ar-CF_4, $d = 25$ mm, $\phi_{\mathrm{tot}} = 150$ V, $\theta_k = 0° \; \forall \; k$. Figure provided from its original publication in Brandt *et al.*, Plasma Sources Sci. Technol. 28, 095021 (2019) [BS19].

is still quite significant even for the 90% Ar case at 60 Pa, allowing for the presence of significant electric fields and DA-mode heating in the bulk plasma.

Spatio-temporal plots of the electric field determined from the simulation are shown in figure 6.15 at 20 Pa and 60 Pa for various argon content values. Under conditions of high electronegativity a strong drift field in the bulk and an ambipolar field at the grounded electrode are observed [59, 60, 79, 83–85, 103–105]. For 20 Pa, this bulk electric field disappears for high argon contents, i.e., above 30% Ar, as the discharge electronegativity and the attachment rate become negligible (figures 6.10 and 6.13(b)-(c)). In the 20 Pa, 0% Ar and the 60 Pa cases, though, significant electric fields are observed in the discharge bulk. The localized DA-mode present at low argon content values for 60 Pa is characterized by strong electric field maxima on the bulk side of the sheath edge at the grounded electrode, as shown in figure 6.15(d). The strength of this localized field is much higher than that of the almost homogeneous field typically observed in DA-mode plasmas [59, 60, 79, 83–85, 103–105], but it also occurs across a smaller spatial region. As this high local electric field oscillates within the fundamental RF period, it is associated with a significant displacement current. Notably, in the context of the global circuit model of section 2.2, the electric fields of the DA-mode in the bulk plasma effectively behave like a time-dependent capacitive circuit element which is the dominant source of $\phi_{\mathrm{b}}(t)$.

Figure 6.16 shows the spatio-temporal distribution of the mean electron energy for the "peaks-type" waveforms cases. The acceleration of electrons by the DA- or α-power absorption modes allows for efficient attachment at 60 Pa (figures 6.16(d)-(f)), as the mean electron energy in the bulk plasma is in the 5-10 eV energy range of the CF_4 attachment cross-sections [101, 102] resulting in the high attachment rates seen in figure 6.13. The DA-mode heating of bulk electrons and the reduction in attachment rate at 60 Pa and 90% argon (see figure 6.11(f) and figure 6.13(f)) lead to a small variation in the mean electron energy ($4 - 6$ eV) across the RF period (figure 6.16(f)). The distribution of electrons with energies required for generating reactive radicals may also change dramatically in space with increasing argon content, which could potentially lead to differing flux distributions of these radical species towards each electrode. These radical flux distributions could then potentially be adjusted as a function of the gas mixture for optimizing processes which require specific ion-to-radical flux ratios.

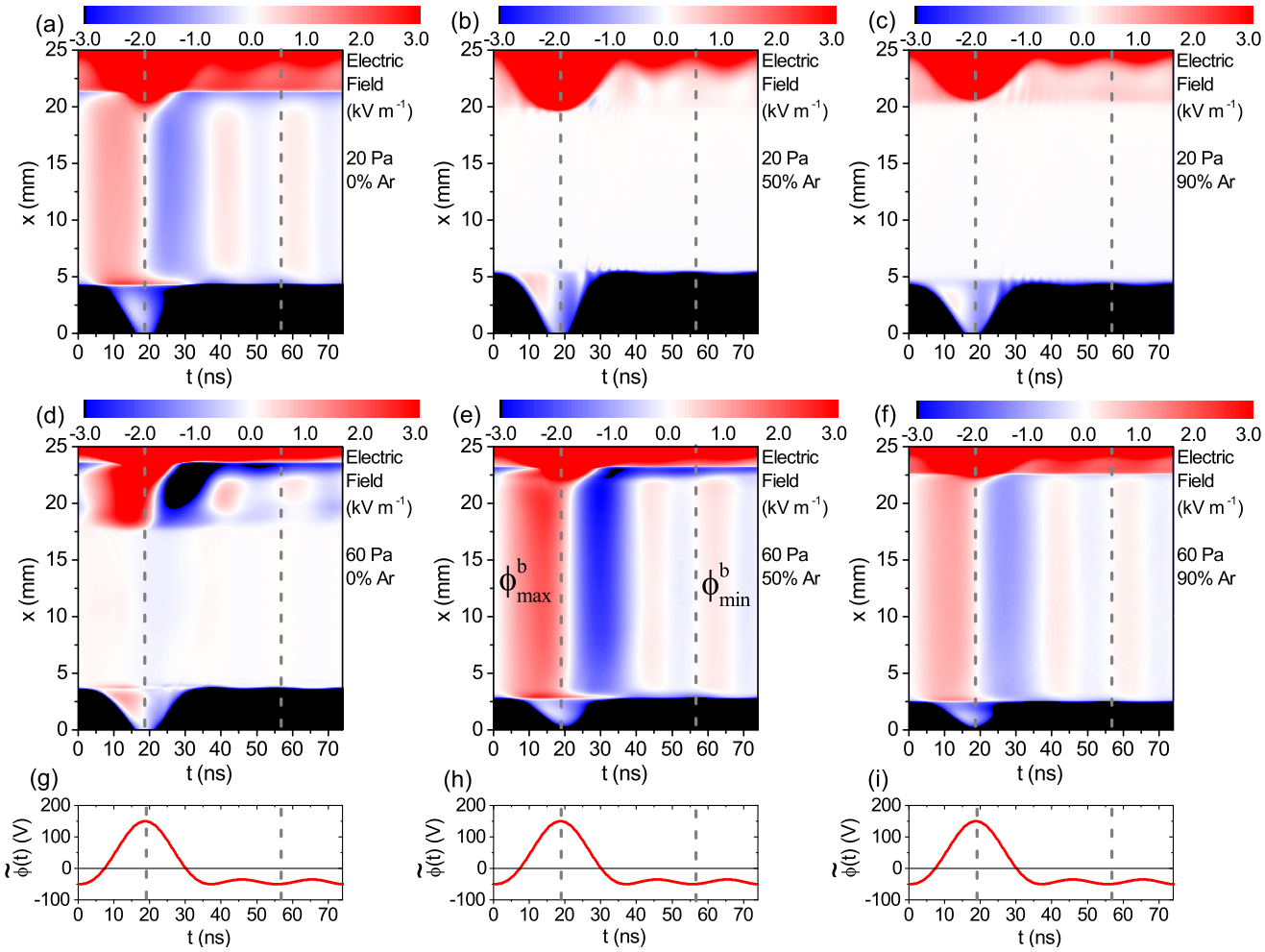

Figure 6.15: Spatio-temporal distribution of the electric field (kV m^{-1}) obtained from the simulation for the "peaks-type" waveform ($N = 3$) at 20 Pa (a)-(c) and 60 Pa (d)-(f), as a function of argon content in the buffer gas. The color scale is chosen in a way to make the electric field in the plasma bulk visible, with positive and negative values corresponding to electric fields in the $+\hat{x}$ and $-\hat{x}$ directions, respectively. The driving voltage waveform is shown for reference in (g)-(i). The dashed vertical lines indicate the times of maximum (at ≈ 19 ns) and minimum voltage (at ≈ 57 ns) of the driving voltage waveform at which $\phi^{\mathrm{b}}_{\mathrm{max/min}}$ are calculated. The powered electrode is located at $x = 0$ mm, while the grounded electrode is at $x = 25$ mm. Simulation conditions are: Ar-CF_4, $d = 25$ mm, $\phi_{\mathrm{tot}} = 150$ V, $\theta_k = 0° \ \forall \ k$. Figure provided from its original publication in Brandt *et al.*, Plasma Sources Sci. Technol. 28, 095021 (2019) [BS19].

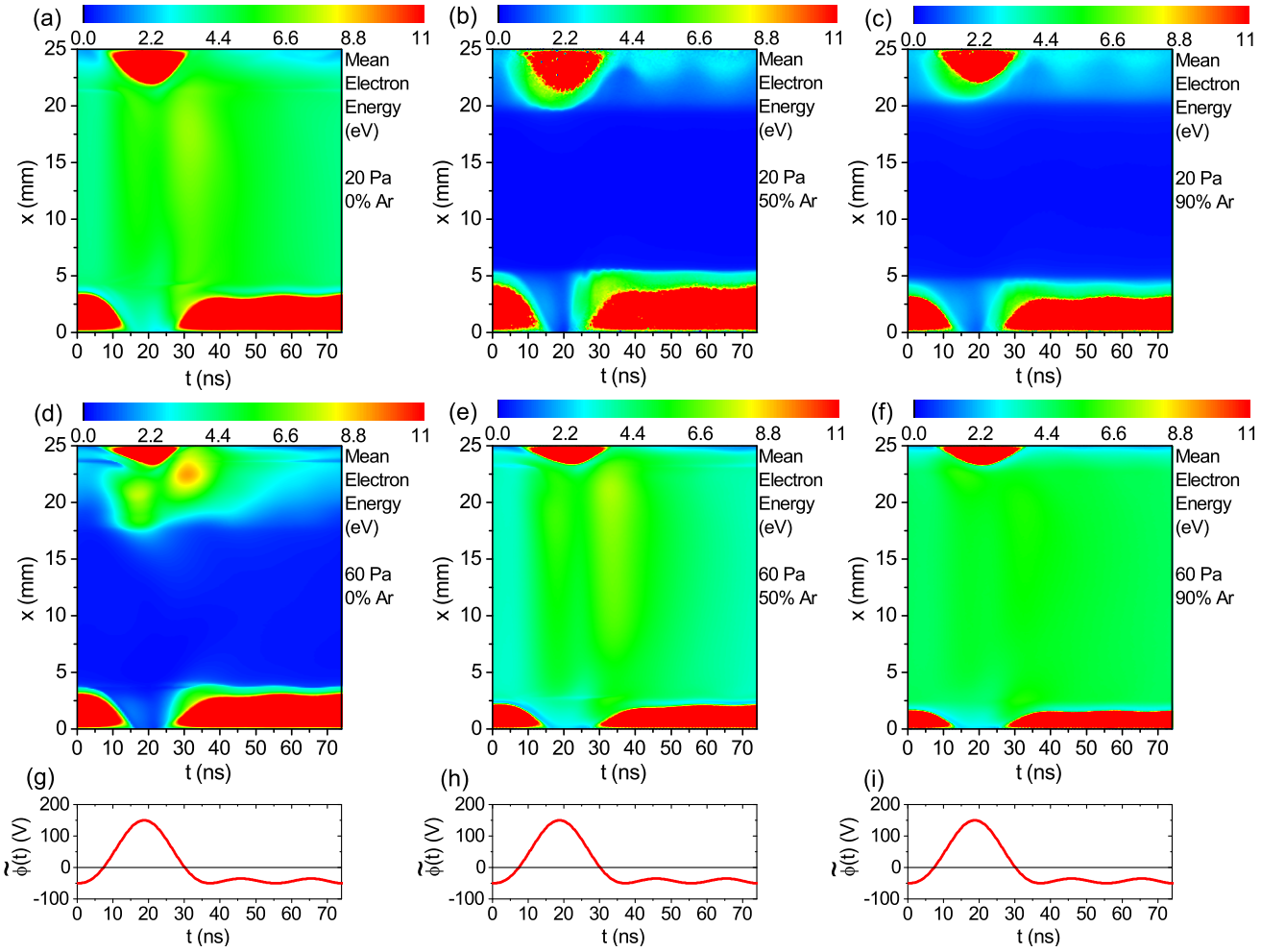

Figure 6.16: Spatio-temporal distribution of the mean electron energy obtained from the simulation for the "peaks-type" waveform ($N = 3$) at 20 Pa (a)-(c) and 60 Pa (d)-(f), as a function of argon content in the buffer gas. The driving voltage waveform is shown for reference in (g)-(i). The powered electrode is located at $x = 0$ mm, while the grounded electrode is at $x = 25$ mm. Simulation conditions are: Ar-CF_4, $d = 25$ mm, $\phi_{\mathrm{tot}} = 150$ V, $\theta_k = 0° \; \forall \; k$. Figure provided from its original publication in Brandt *et al.*, Plasma Sources Sci. Technol. 28, 095021 (2019) [BS19].

6.2.2 Effects of gas composition on generation of the DC self-bias

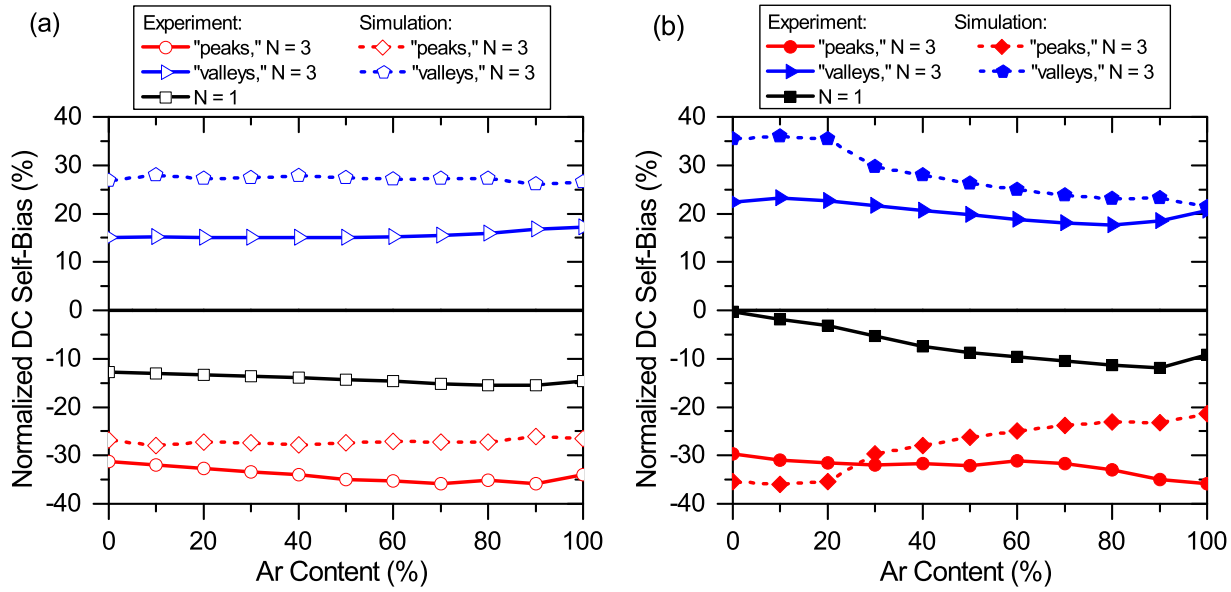

Figure 6.17: DC self-bias normalized by the total driving voltage amplitude as a function of the argon content in the buffer gas for single-frequency ($N = 1$) and triple-frequency ("peaks-type" and "valleys-type", $N = 3$) waveforms obtained from the experiment and the simulations at 20 Pa (a) and at 60 Pa (b). Discharge conditions are: Ar-CF_4, $d = 25$ mm, $\phi_{tot} = 150$ V, $\theta_{1,3} = 0°$. Figure provided from its original publication in Brandt *et al.*, Plasma Sources Sci. Technol. 28, 095021 (2019) [BS19]. ©IOP Publishing. Reproduced with permission. All rights reserved.

The understanding of the DC self-bias generation is important in applications since η influences both the ion FEDFs at plasma-facing surfaces and the electron power absorption dynamics. Figure 6.17 shows the DC self-bias as a function of the argon content in the buffer gas for single-frequency ($N = 1$) and triple-frequency ("peaks-type" and "valleys-type", $N = 3$) waveforms obtained from the experiment and the simulations at 20 Pa and 60 Pa. In the single frequency case, the experiment exhibits a normalized self bias (DC self-bias voltage divided by the total driving voltage amplitude) of approximately -15 % at 20 Pa, which is insensitive of the argon content. At 60 Pa, η is zero in a pure CF_4 discharge and its magnitude increases to about 12 % at high argon content. The DC self-bias is negative because of the presence of a larger grounded surface compared to powered electrode surface in the experiment. It is, however, zero in the simulations for N = 1 independent of the argon content, since no geometric discharge asymmetry is included and there is no electrical asymmetry.

For the triple frequency "peaks-/valleys-type" waveforms significantly different values of the DC self-bias are found compared to the single frequency case due to the presence of the EAE and the spatio-temporal electron dynamics described in the previous section. At 20 Pa good agreement between experimental and simulation results is obtained in terms of the

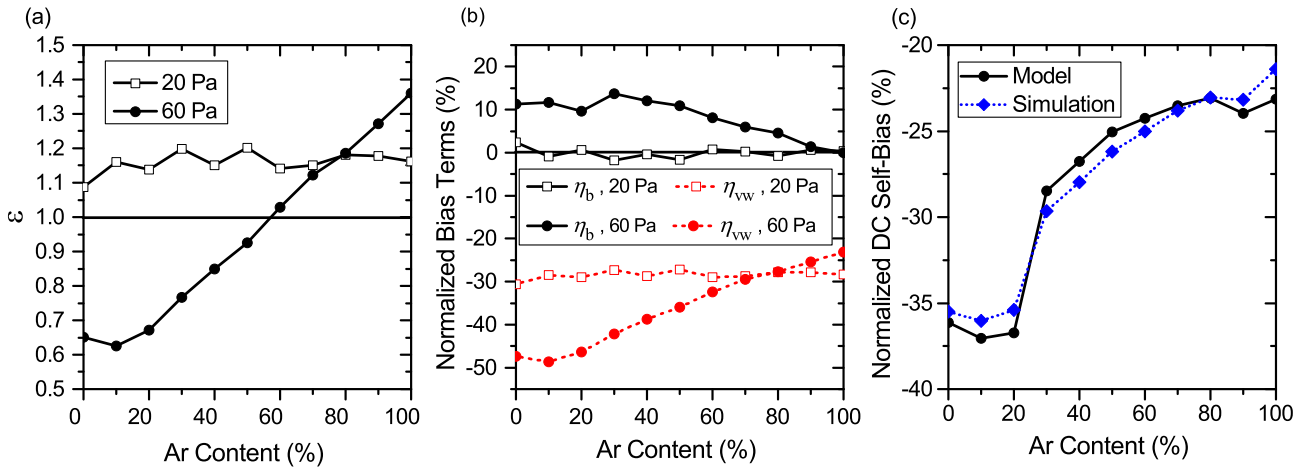

Figure 6.18: Symmetry parameter ε (a) extracted from the simulation as a function of the argon content in the buffer gas for the "peaks-type" waveform ($N = 3$) at 20 Pa and 60 Pa. DC self-bias terms, η_{vw} and η_{b} (b) calculated from the model using simulation data for the "peaks-type" waveform. DC self-bias for the 60 Pa, "peaks-type" waveform ($N = 3$) from the model and from the simulation (c). The data are normalized by the fixed total voltage amplitude of $\phi_{\mathrm{tot}} = 150$ V. Discharge conditions are: Ar-CF_4, $d = 25$ mm, $\phi_{\mathrm{tot}} = 150$ V, $\theta_k = 0° \; \forall \; k$. Figure provided from its original publication in Brandt *et al.*, Plasma Sources Sci. Technol. 28, 095021 (2019) [BS19].

dependence of η on the argon content. The only difference is an approximately constant shift caused by the geometric reactor asymmetry, which is only present in the experiment. At 60 Pa some deviations are observed. As will be explained later, these are also caused by the geometric discharge asymmetry in the experiment. For the "peaks-type" waveform the DC self-bias is negative at both pressures, while it is positive for the "valleys-type" waveforms. At 20 Pa it is independent of the argon admixtures for both waveforms, while its magnitude decreases as a function of the argon content at 60 Pa in the simulation.

In order to understand the dependence of the DC self-bias on the argon content at 20 Pa and 60 Pa the analytical model introduced in sections 2.2 and 2.3 is utilized. In the frame of this model, the DC self-bias is described by equations (2.14) and (2.15). It is determined by the sum of three terms: η_{vw} related to the applied voltage waveform, η_{f} due to the floating potentials at each electrode, and η_{b} resulting from the voltage drop across the bulk plasma. The floating potentials are neglected in our analysis due to their small magnitude.

In both terms, η_{vw} and η_{b}, the symmetry parameter, ε, plays an important role. Therefore, the behavior of ε obtained from the PIC/MCC simulation is analyzed as a function of argon content at both pressures for "peaks-type" waveforms (see figure 6.18(a)). In a geometrically symmetric discharge, which is the case in the simulation, the symmetry parameter is largely determined by the ratio of the mean ion densities in both sheaths. This ratio is, in turn, determined by the spatio-temporal dynamics of energetic electrons via their effects on the

ionization probed by the excitation here (see figures 6.11 and 6.12). At 20 Pa, the ratio of the maxima of the excitation rate at both electrodes does not change much as a function of the argon content. Thus, ε is independent of the argon content. At 60 Pa, however, by admixing more argon the mode of discharge operation is changed from the DA- to the α-mode. This causes the ratio of the excitation maxima adjacent to both electrodes and the symmetry parameter to change as a function of the argon content as well.

The dependence of ε on the argon content affects the two calculated self-bias terms, η_{vw} and η_{b}, in the model, which are shown in figure 6.18(b) as a function of the argon content for both 20 Pa and 60 Pa. Recall that, for a fixed applied voltage waveform, $\widetilde{\phi}_{\mathrm{max/min}}$ do not change, such that changes in η_{vw} are solely due to changes in the symmetry parameter (ε) due to the mode transition induced by the decreasing electronegativity with the argon content (figure 6.10).

The variation of η_{b} is a result of the change in ε and changes of the voltage drops across the plasma bulk at the times of maximum and minimum driving voltage, $\phi^{\mathrm{b}}_{\mathrm{max,min}}$. These voltage drops across the bulk are obtained from the simulations at the times indicated in figure 6.15. At 60 Pa, the presence of the oscillating drift electric field in the bulk implies a non-zero, time-dependent bulk voltage, $\phi_{\mathrm{b}}(t)$. In the presence of a "peaks-type" driving voltage waveform $|\phi^{\mathrm{b}}_{\mathrm{max}}| > |\phi^{\mathrm{b}}_{\mathrm{min}}|$ under these conditions, because the RF currents are different at these two characteristic times and, thus, different bulk electric fields are required to drive these currents. In combination with the change of the symmetry parameter as a function of the argon content this causes $\eta_{\mathrm{b}} > 0$ V at 60 Pa (see equation (2.14) and figure 6.18(b)). The voltage drops across the plasma bulk at the times of maximum and minimum applied voltage decrease as a function of argon content, since the discharge gets more electropositive and, thus, the drift electric field in the bulk decreases. At 20 Pa, the drift electric field in the bulk is lower, since the conductivity is higher compared to the 60 Pa case due to a lower electron-neutral collision frequency and a lower electronegativity for most argon admixtures. Moreover, ε is constant as a function of the argon content due to the absence of any strong mode transitions. Thus, η_b is essentially zero under these conditions.

Figure 6.18(c) shows the DC self-bias as a function of the argon content at 60 Pa obtained from the simulation and the analytical model. In the model, the DC self-bias is calculated as the sum of η_{vw} and η_{b}. Excellent agreement between the simulation and the model results is found. This shows that the floating potential term can indeed be neglected and that the model can be used to understand the generation of the DC self-bias as a function of the argon content under these conditions.

In order to obtain a more detailed understanding of the DC self-bias generation in this reactive electronegative RF-CCP, the evolution of the symmetry parameter, ε, for the "peaks-type" waveform at 60 Pa as a function of the argon content is investigated by calculating each individual term in equation (2.15) using simulation data as inputs to the model, assuming that the discharge is geometrically symmetric, i.e., $(\frac{A_{\mathrm{p}}}{A_{\mathrm{g}}})^2 = 1$. The results of this analysis can be seen in figure 6.19, where each term's variation with increasing argon content, as well as the ε reconstructed from the model calculations, are shown in figures 6.19(a) and

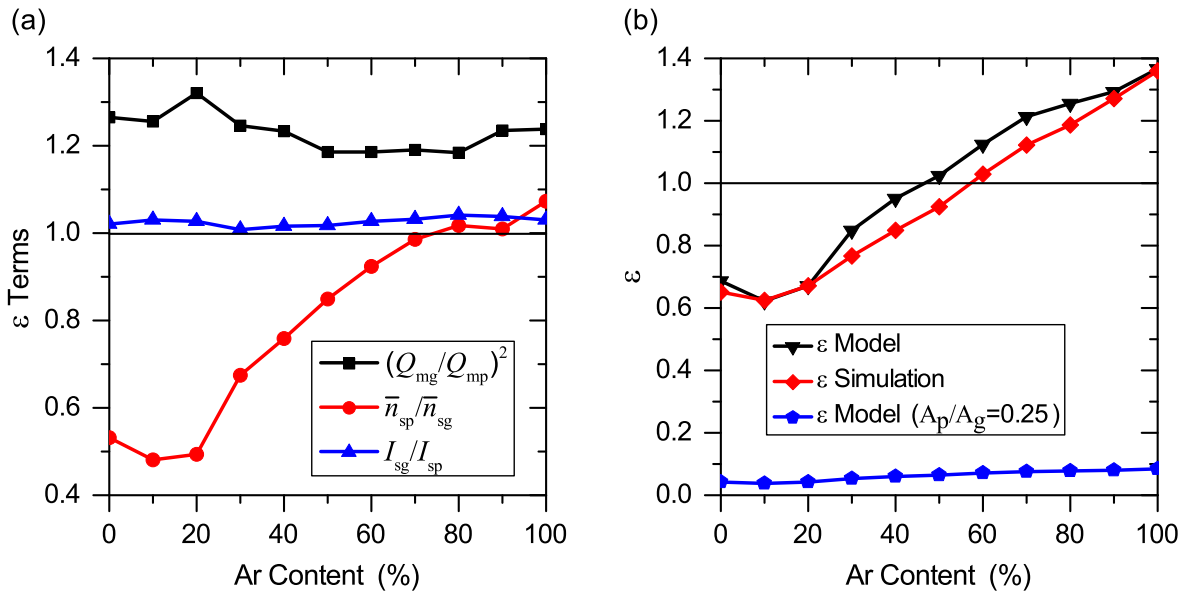

Figure 6.19: (a) Dependence of the individual ratios in equation (2.15), including the maximum uncompensated charges in each sheath (Q_{mg}/Q_{mp}), the sheath charged particle densities ($\bar{n}_{sp}/\bar{n}_{sg}$), and the sheath integrals (I_{sg}/I_{sp}) on the argon content in the buffer gas. (b) Variation of the symmetry parameter, ε, with the argon content in the buffer gas as obtained from the model using simulation data as inputs (black triangles), extracted directly from the simulation (red diamonds), and the same model results using an "artificial" geometric asymmetry factor of $\frac{A_p}{A_g} = 0.25$ (blue pentagons). Both (a) and (b) show results for the 60 Pa, "peaks-type" waveform ($N = 3$) cases. Discharge conditions are: Ar-CF_4, $d = 25$ mm, $\phi_{tot} = 150$ V, $\theta_k = 0° \; \forall \; k$. Figure provided from its original publication in Brandt *et al.*, Plasma Sources Sci. Technol. 28, 095021 (2019) [BS19]. ©IOP Publishing. Reproduced with permission. All rights reserved.

6.19(b), respectively. The changes in ε with increasing argon content are almost exclusively due to the strong increase in the sheath charged particle density ratio $\frac{\bar{n}_{sp}}{\bar{n}_{sg}}$, corresponding to the change in spatial localization of the discharge ionization as a function of the dominant power-absorption mode. The ratio of the maximum uncompensated charges in both sheaths as well as the ratio of the sheath integrals do not change much as a function of the argon content.

The symmetry parameter, ε, is calculated based on the individual terms in equation 2.15 from figure 6.19(a) and is compared to the ε directly provided as an output from the simulations in figure 6.19(b). Good agreement is found between the ε obtained from the model and that obtained from the simulation. The ε from the model is then calculated again, but with an "artificial" geometric asymmetry set at $\frac{A_p}{A_g} = 0.25$ in equation (2.15) to demonstrate the effect of a geometric asymmetry on the variation of ε qualitatively. This does not account for the changes in sheath density which would occur in the presence of such a geometric asymmetry, and the specific value of $\frac{A_p}{A_g}$ in the measurements, where a significant

geometric asymmetry is present, may not match this example value. The corresponding line in figure 6.19(b) demonstrates that the changes in ε are strongly damped by the presence of the geometric asymmetry. It is then expected that the variation of the η_{vw} self-bias term as a function of the argon content would similarly be reduced in the presence of a significant geometric asymmetry, leaving η_{b} to be the primary cause of changes in the total DC self-bias η in the experiment.

The evolution of the total DC self-bias in the experiments at high pressure with increasing argon content (shown in 6.17(b)) is primarily due to the presence of the bulk voltage term η_{b}, while the η_{vw} term's variation is suppressed by the geometric asymmetry's effect on ε. Therefore, the experimental DC self-bias η evolves due to the interaction of two terms: $\eta_{\mathrm{vw}} \approx$ constant, and a counter-acting $\eta_{\mathrm{b}} \to 0$ as the argon content increases to 100 %. The two effects together are responsible for the variation of the DC self-bias magnitude in each case in the experiment. This is most easily understood for the single-frequency ($N = 1$) case at 60 Pa (black solid line in figure 6.17(b)), where the negative DC self-bias generated due to the geometric asymmetry, represented by the 100% argon data point, is countered by the presence of a significant positive bulk voltage term η_{b} at 0% argon content, where the discharge operates in DA-mode. This results in a total DC self-bias very near zero for 0% argon content, despite the presence of the geometric asymmetry. As the argon content is increased, η_{b} decreases in magnitude towards zero, eventually restoring the negative DC self-bias caused by the geometric asymmetry at 100% argon. Similarly, for the "peaks-type" waveform, the negative bias from the driving voltage waveform (η_{vw}) is counter-acted by the presence of a positive η_{b} at low argon admixtures, which disappears as the $\mathrm{Ar}/\mathrm{CF}_4$ gas mixture is changed to pure argon gas. A similar albeit reversed situation is true for the "valleys-type" waveform, where a positive η_{vw} is counter-acted by a negative η_{b}, whose absolute value decreases to zero at 100% Ar. These effects minimally affect the total DC self-bias η as a function of increasing argon content at the lower pressure, because the electronegativity of the discharge is too low to induce significant DA-mode bulk electric fields and to significantly change the symmetry parameter ε.

At 60 Pa, the dependence of the DC self-bias on the argon content is different for the "peaks-type" and "valleys-type" waveforms in the experiment and in the simulation (see figure 6.17(b)). For the "peaks-type" waveform, the simulated DC self-bias retains a decrease in the magnitude of η_{vw} from ε, leading to the overall decrease in magnitude of the negative DC self-bias, despite the positive η_{b} decreasing to zero as the argon content approaches 100%. This stands in contrast to the experimental data, where the suppression of changes in η_{vw} allows the overall DC self-bias to increase in magnitude with increasing argon content. An analogous argument is valid for the "valleys-type" waveform. The dependence of this DC self-bias phenomenon on the discharge geometry, i.e., either geometrically asymmetric ($\frac{A_{\mathrm{p}}}{A_{\mathrm{g}}} < 1$) or geometrically symmetric ($\frac{A_{\mathrm{p}}}{A_{\mathrm{g}}} = 1$), implies that the discharge geometry becomes relevant when using an electronegative gas or admixture.

Chapter 7

Secondary electron emission at a changing plasma-facing surface

Secondary electron emission (SEE) is an essential plasma-surface interaction in many different types of plasmas and applications throughout plasma science, but is particularly relevant for plasma etching and plasma chemical vapor deposition processes. Secondary electron emission in such discharges is often caused by positive ions accelerated through a plasma sheath towards a plasma-facing surface of some material that, upon reaching the surface, ejects a "secondary" electron back into the plasma [175, 183, 190]. Other particles, such as fast moving neutrals, highly energetic electrons which overcome the sheath's potential, photons, and metastable atoms/molecules, can also be responsible for this phenomena [121, 122, 248]. For a given particle species, an incident energy-dependent coefficient known as the secondary electron emission coefficient (SEEC) describes the probability of a secondary electron being emitted upon an impact of that particle species with the surface as a function of the incident particle's kinetic energy and angle relative to the surface normal [174]. It is well known that different surface materials have different values for these various SEECs, with a particularly significant difference between metals and semiconductors [175, 183]. Furthermore, it has been shown that SEE has very significant influence over discharge operation and process-relevant plasma parameters, such as plasma and radical densities [31, 35, 175, 190]. However, the secondary electron emission coefficients are often assumed in both industry and academia to be fixed to some value or only be a function of incident-particle energy and ignore the possible dependence of SEECs on other discharge and plasma-facing surface conditions, despite the incredibly important precedent in etching/deposition processes that the surface material and surface profile (on a nm-scale) can potentially change dramatically over the course of a given process. A similar precedent exists for other types of discharges where electrodes eventually become worn over time, for example sputtering discharges, or contaminated between cleaning cycles. Therefore, it is necessary to develop a complete understanding of secondary electron emission interactions as a function of plasma parameters and surface conditions used in a given process.

In this chapter, phase-resolved optical emission spectroscopy measurements of an argon-neon CCP driven by single-frequency waveforms are presented at high pressures of 100-200 Pa, where the mean ion energy at a plasma-facing surface is low due to very high collisionality. The electrode gap is fixed at 30 mm for all cases. The experimental part of the γ-CAST technique explained in subsection 3.2.4 is utilized here in order to investigate the relationship between the changing surface conditions and the plasma's optical excitation"response" to different surface conditions. Aluminum disks of differing surface roughness, provided by the Lam Research corporation as part of an industry collaboration [228], are allowed to oxide by exposure to air and form aluminum oxide (Al_2O_3) films. The optical excitation intensity of the γ- power absorption mode described in chapter 2, which is explicitly seeded by secondary electron emission, is compared to the intensity of the α-mode excitation as a function of surface roughness for various aluminum and aluminum oxide surfaces. The ratio of these two excitation intensities is used as a qualitative measure for the plasma's optical excitation response to a changing secondary electron emission coefficient, from which qualitative conclusions about the dependence of SEE on surface conditions can be drawn as well as the impact this change has on the plasma itself.

In section 7.1, the dependence of this optical excitation intensity ratio on surface material, i.e., clean metal (aluminum) surfaces and "dirty" metal surfaces with semiconductor films (aluminum oxide), as well as the dependence on the thickness of these thin oxide films is investigated by examining the ratio of the optical excitation intensities of the γ- and α-mode for the 585.2 nm Neon line [197]. The results demonstrate that, qualitatively, the SEEC changes as a function of the surface material between "dirty" (aluminum oxide film) and "clean" aluminum metal surfaces, representative of a change between a semiconductor-like surface and a metal surface, which is consistent with previous works [175, 183]. The exact thickness of these films are not measured due to a lack of surface diagnostics. They can, however, be assumed to be within the range of 1-10 nm due to the logarithmic growth of such Al_2O_3 films observed in the work of R. K. Hart [196] and the previous works cited therein, as discussed in section 7.1. Comparisons of the PROES measurements of the "thick" and "thin" oxide films briefly demonstrate that the thickness of these thin films has significant influence over the value of the SEEC and the associated γ-mode heating, with very thin films (approximately 1-2 nm) behaving very similar to clean metal surfaces and thicker films (approximately 6-10 nm) behaving much closer to semiconductor surfaces. These findings are supported by other previous works [144, 176] on the quantum mechanical interaction that plasma particle species would make with a surface during SEE and is corroborated by recent experimental work [177]. While further research is required to confirm this phenomenon, particularly on quantitative/experimental measurements of the SEEC as a function of the surface material and film thickness, it has highly significant implications on the way plasma science should be studied in etching and deposition plasmas, where the removal and deposition of thin films is extremely common.

The dependence of the optical excitation intensity ratio on the physical profile ($S(\vec{x})$, where notably $\vec{x}$ refers to a position on the horizontal surface in this chapter) of a given surface is demonstrated and discussed in section 7.2. It is observed that as the surface roughness (measured in Ra using μm) increases, the optical excitation intensity ratio increases at

low Ra values but eventually becomes constant for higher Ra values. This phenomenon is hypothesized to be the result of a dependence of the low-energy SEE (Auger) processes on the incident particle's angle relative to the surface's normal, which itself may be dependent on the surface roughness. This hypothesis is supported by previous theoretical and experimental works [144, 178] but is dependent on the assumption that the surface roughness is functionally related to the slopes of the surface profile. The ensemble averaging of this effect across the surface further complicates the relationship between the surface profile and the observed results. Further research is also required to confirm this phenomenon, particularly into how the shape of the surface profile relates to the surface roughness and how the surface profile influences the "outgoing" secondary electron distribution. This qualitative result also suggests a second possibility of a surface-profile dependent SEEC existing at even smaller length-scales than those observed here, due to secondary electrons reflecting inside of a surface's "trenches". In particular, the influence of the surface profile would be highly relevant to etching applications, where many semiconductor etching processes which change the surface profile are performed on the nm-scale.

7.1 Dependence of optical excitation intensity ratio on surface material and film thickness

The experimental methodology outlined in subsection 3.2.4 examines the ratio of the excitation intensities of the α- and γ-excitation maxima, discussed in section 2.4, in order to qualitatively observe changes in the γ-heating mode indicative of different SEEC values due to different surface conditions at the powered electrode adjacent to the excitation maxima of these heating modes. The γ-mode excitation intensity, labeled as I_γ, is the result of an energetic electron avalanche produced by a Townsend-like, collisional electron multiplication process in the sheath, i.e., via ionization of the background gas in the sheath, which then subsequently collides with the background gas (90/10 gas mixture of Ar/Ne) and excites the 585.2 nm neon line. This excitation is therefore dependent on the electron multiplication process occurring in the sheath as well as the initial "seeding" distribution of secondary electrons emitted by a given surface during times of high sheath voltage in response to charged particle bombardment. The electron multiplication process, furthermore, is a function of the collisionality of the discharge, e.g., the electron-neutral collision frequency $\nu_{\mathrm{e-n}}$ which is dependent on gas pressure, and the reduced electric field in the sheath which accelerates these electrons to energies where such collisions with the background gas result in ionization and the production of additional free electrons inside the sheath. The distribution of fast electrons generated in this Townsend avalanche responsible for the γ-mode excitation peak seen in PROES therefore depends on the gas pressure p, the time-dependent sheath voltage $\phi_{\mathrm{s}}(t)$, and the distribution of secondary electrons emitted from the surface. This can be described by the proportionality $I_\gamma \propto M(p, \phi_{\mathrm{s}}(t)) * \text{SE-EDF}$, where $M(p, \phi_{\mathrm{s}}(t))$ represents the electron multiplication process which results in the fast electron distribution responsible for the γ-mode excitation peak, and the SE-EDF is the energy distribution function of the secondary electrons which seeded the electron multiplication process. The form of the

SE-EDF in this context and any spatial (across the disk's surface) or time dependence it may have is currently not well understood and is therefore not meant to be derived or estimated in this work. Rather, it is meant to conceptually motivate the results shown here.

The secondary electron energy distribution function (SE-EDF) may depend on a number of significant variables, particularly on the incident-particle (e.g., positive ion) energy distribution functions at the surface, but in this section, the relationship between the SE-EDF and the surface-dependent SEEC, denoted as $\gamma(X, Y)$ where X is the choice of surface material and Y is the film thickness of this surface material interacting with the plasma, is discussed and examined by measuring the γ-mode excitation intensity normalized to the α-mode excitation intensity as a function of pressure and surface material for a fixed surface roughness of 24 Ra (in μm). The SE-EDF is generated by the emission of secondary electrons in response to a bombarding ion flux-energy distribution through the probability described by the SEEC γ. Since this SE-EDF produces the electron avalanche responsible for the measured γ-mode excitation, qualitative changes in the excitation could potentially provide some insight to changes in the SE-EDF, and thus in γ, generated by different surface characteristics under otherwise identical discharge conditions. This is, however, complicated by the coupling between the γ-mode heating and ionization in the discharge, and subsequently the incident ion flux-energy distribution, as discussed later in this section. The mean incident ion energies for the pressures where the γ-mode is observed in our PROES measurements (i.e., 100-200 Pa) are generally assumed to be low (< 100 eV) due to the collisional nature of the plasma sheaths and therefore exist in a regime where the SEEC values change significantly between metal and oxide surfaces. Previous work performed by Phelps et. al. [183] demonstrates that clean metals generally have higher SEEC values when compared with "dirty", i.e., oxidized, metals at these low ion energies. It should be noted that this trend reverses for high ion energies, with oxidized metals having higher SEEC values, and thus any trends in the SEEC with surface characteristics must be carefully defined according to the energies of incident ions. The γ-mode excitation response associated with a specific SE-EDF, therefore, should also be sensitive to a change in the SEEC ($\gamma(X, Y)$) between different materials.

Figure 7.1 shows the ratio of γ- and α-mode excitation intensities (I_γ/I_α) as a function of pressure from 100 Pa to 200 Pa for two aluminum disks with surface roughness of 24 Ra. For each disk, the aluminum was allowed to oxidize, forming an aluminum oxide film on the surface. It was then placed onto the powered electrode and the setup was pumped down. PROES was then performed for this "dirty" metal surface for each plasma operating pressure. The surface was then cleaned via a sputtering process (outlined in section 3.4) and PROES was performed again for the clean metal surface at each pressure. From these PROES measurements, the I_γ and I_α excitation intensities are obtained from integration of the excitation rate across the respective region of interest in the spatio-temporal PROES measurement. The range of film thickness for these films is estimated based on the discussions presented by Hart [196]. These discussions clarify that the oxidation of a pure aluminum surface from exposure to dry air proceeds very quickly at first, resulting in a "thin" aluminum oxide film approximately 1-2 nm thick over the course of about 40 minutes, and then proceeds incredibly slowly after this thin film is present, with the oxide film growing potentially up to 10 nm given an extended period of time (i.e., several months). The process of placing

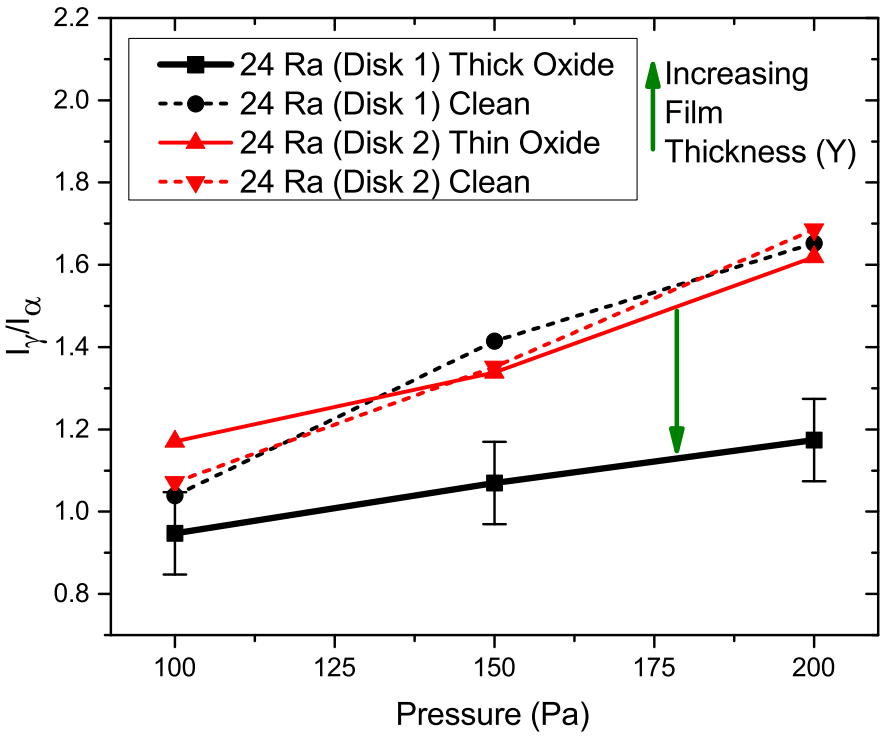

Figure 7.1: The experimentally measured optical excitation intensity ratio (I_γ/I_α) from PROES measurements is shown as a function of background gas pressure from 100 Pa to 200 Pa for two aluminum surfaces with surface roughness of 24 Ra (in μm). Each surface was exposed to air to form an aluminum oxide film, with one having a "thin" aluminum oxide film in the range 1-2 nm, labeled 24(a), and the other having a "thick" aluminum oxide film in the range 6-10 nm, labeled 24(b). Measurements of their clean metal surface counterparts are also shown for comparison. Discharge conditions are: Ar + 10% Ne, $d = 32$ mm, 13.56 MHz voltage waveform with $\phi_{\text{tot}} = 200$ V.

one aluminum disk into the vacuum chamber, performing the voltage calibration of section 3.2.1, and returning the chamber to vacuum conditions takes approximately one hour, and thus up to a few nm of Al_2O_3 film can assumed to be present for most "dirty" surface cases. An additional 24 Ra disk, which was allowed to continue oxidation for an extended period of around two months before being placed into the chamber, is similarly assumed to have a "thick" oxide film closer to 6-10 nm. Notably, the measurements of Hart [196] for dry oxygen over 7 days produce oxide films of approximately 3.5 nm, for context. Therefore, the associated PROES measurements are labeled as "thick" (approximately 6-10 nm) and "thin" (approximately 1-2 nm) oxide films in figure 7.1 and figure 7.2. These thickness values are thus only qualitatively estimated here. They are not quantitatively measured due to a lack of in-situ diagnostics (such as profilometry) in the vacuum chamber. This imposes limitations on the transport of the disks and thus the accuracy of any external diagnostics due to continued exposure to air outside the vacuum chamber resulting in further oxidation and changing the film thickness relative to when the PROES measurements are taken. A vacuum transport system could alternatively be implemented in future studies to avoid these limitations. Notably, this should emphasize the importance of designing such discharges when studying plasma-surface interactions such that in-situ surface diagnostics can be included and utilized with the plasma turned off but without the risk of opening the vacuum chamber and contaminating/oxidizing relevant surfaces.

Figure 7.1 demonstrates that the clean metal cases for both disks, and more importantly the thin oxide film case, are very similar and follow nearly the same increasing dependence with increasing gas pressure. The thick oxide film case, however, has a significantly lower intensity ratio compared to the other cases across the 100-200 Pa range and has a significantly smaller slope with increasing pressure. The slope of a I_γ/I_α versus pressure plot, as discussed in subsection 3.2.4, is qualitatively indicative of the increasing effectiveness of the electron multiplication process occurring in the sheath, but is also dependent on the SE-EDF and thus the SEEC values which generated the SE-EDF.

The reason behind different surfaces possessing significantly different slopes in figure 7.1 across the same pressure interval (100-200 Pa) can be qualitatively attributed to either: a) a change in the electron multiplication process, due to a significant change in the reduced electric field (E/N) in the sheath or a sudden change in collision processes, e.g., changing gas pressure implying a changing electron-neutral collision frequency ν_{e-n}, or b) a change in the SE-EDF, due to a change in the ion energy distribution of incident particles at the surface or a change in the SEEC. The changes described in option a) are not necessarily independent of the surface conditions but are associated with externally applied factors, i.e., the applied voltage waveform for the sheath's electric field and the fixed background gas pressure for the collisionality inside the sheath. Note that the collisionality generally does increase as the background gas pressure is increased due to the increase in the densities of colliding particle species [2, p. 80]. Furthermore, increases in pressure also generally decrease the maximum sheath width, as seen in the results of section 4.1. That said, it should be noted that an increase in γ (e.g., from a change in the film material thickness) will likely also increase the ion density n_i near or inside the sheath because of additional ionization (e.g., γ-mode ionization and ionization from electron multiplication in the sheath), resulting in an decrease

of the reduced electric field (E/N_i, where N_i is the number of particles (ions)) in the sheath, and could also affect the sheath width. This coupling between surface conditions and the properties of the sheath, and thus the sheath's role in electron heating, is therefore a highly significant complication which has only been addressed under certain conditions. Previous works, for example, demonstrate that the surface's SEE can impact the properties of the sheath in some cases, particularly for surfaces with a high SEEC value ($\gamma > 1$) [249, 250]. Notably, $\gamma > 1$ is easier to achieve when the surface temperature is very high (see section 2.6), but as the GEC reference cell utilizes electrode cooling [194], this is unlikely. Furthermore, the conditions here are unlikely to cause such a dependence as the measured SEEC values for argon ions impacting aluminum and aluminum oxide surfaces do not exceed a value of one even for kinetic SEE at high ion energies of thousands of eV [251]. The dependence of changes in option a) on γ does mean, however, that option b) is more likely to explain the difference in the trends in figure 7.1 as being primarily due to the changes in the SE-EDF since the externally applied factors, i.e., the applied voltage waveform and background gas pressure, are kept the same. None-the-less, it should be noted that this assumption is problematic and requires further investigation beyond the scope of the discussion here. The presence of the γ-mode ionization near the powered electrode does have significant influence over the plasma density, and thus positive ion density, near and inside the powered electrode's sheath, and therefore can influence the positive ion flux to the plasma-facing surface at these high pressures where the γ-mode is significant [31, 35, 175, 190]. This increase in plasma density in the sheath may also influence the reduced electric field of option a). However, it should be noted that the γ-mode ionization is also affected by a change in the SEEC itself, as it is seeded by the emitted secondary electrons. Therefore, the difference in trend between the "thick" oxide film case and the other cases in figure 7.1 is best explained by a significant difference in the material's SEEC value. This is conceptually supported by the work of Li *et. al.* [177], who examined the SEEC as a function of the oxide layer on an aluminum surface and observed significant changes in the SEEC for films up to 1 nm thick. Lee *et. al.* [179] examined a similar effect for magnesium oxide films in the 10-200 nm range. That said, additional measurements of the plasma density and the ion energy distribution function as a function of surface material and pressure are still necessary to fully account for the change in the positive ion flux from the γ-mode ionization which would affect the trends in figure 7.1. Furthermore, quantitative measurements on the surface's SEEC value as a function of the film thickness for various materials in the same manner as those seen in figure 2 of Li J *et. al.* [177] are also necessary to quantitatively relate these I_γ/I_α intensity ratios to a change in the SEEC value and confirm the above hypothesis.

Figure 7.2 shows the spatio-temporal excitation rates measured via PROES at 150 Pa for two separate aluminum disks with surface roughness of 24 Ra for the aforementioned "thick" (figure 7.2(a)) and "thin" (figure 7.2(c)) oxide cases and their associated clean surface cases (figure 7.2(b),(d)). The α- and γ-mode excitation peaks are denoted by the left and right boxes, respectively, displayed in each PROES plot in figure 7.2, and are also the regions of interest used to obtain I_γ and $/I_\alpha$. Figure 7.2 demonstrates a significant difference in the observed optical excitation intensity ratio (I_γ/I_α) between the thin and thick oxide films, with the thin oxide case (figure 7.2(c)) being remarkably similar to both of the clean metal cases (figure 7.2(b),(d)). The thick oxide case (figure 7.2(a)), however, is dramatically different, with

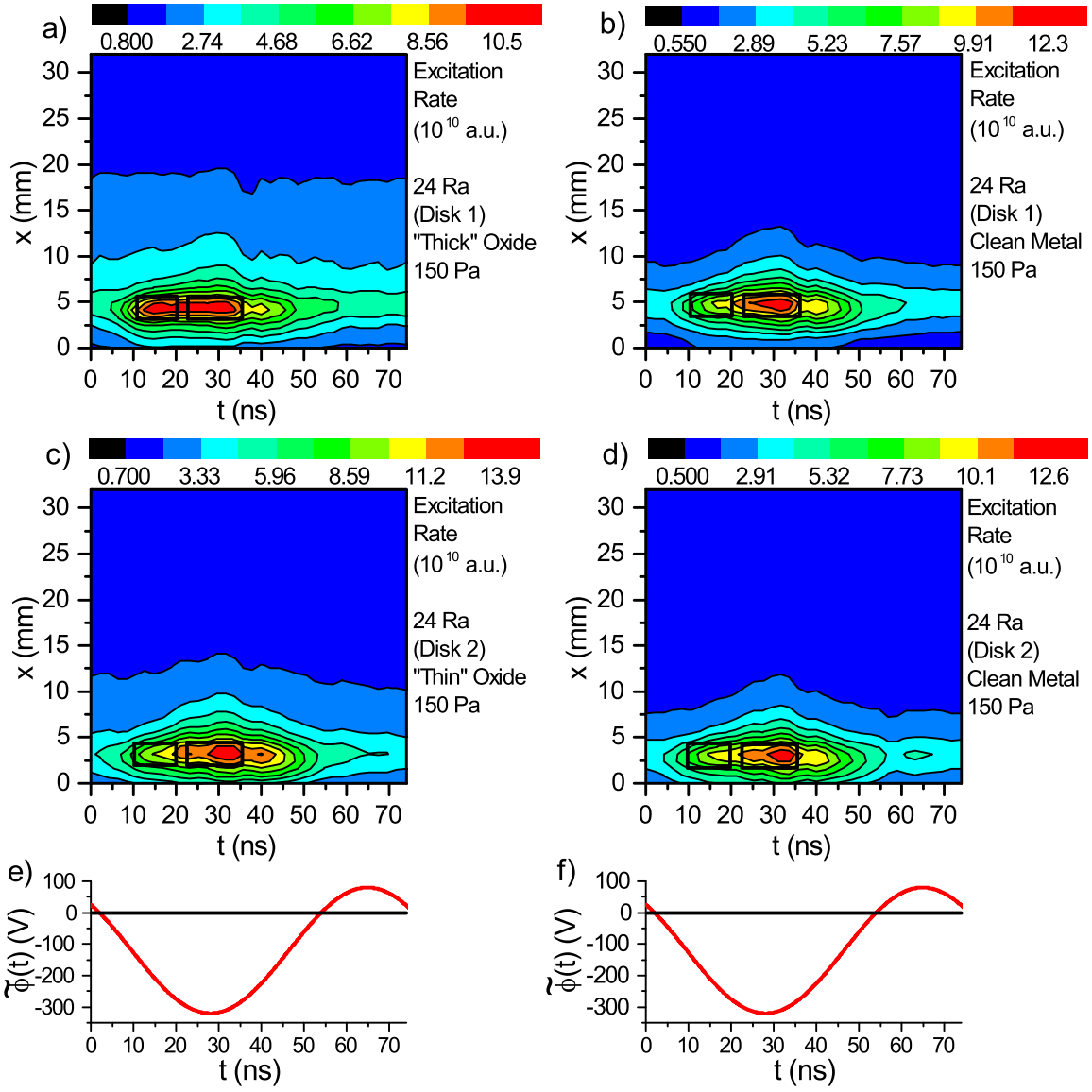

Figure 7.2: PROES measurements are shown for the (a) "thick" and (c) "thin" aluminum oxide film cases and their respective clean metal surfaces (b) and (d). The appropriate surface in each plot is located at $x = 0$, placed on top of the powered electrode. The applied voltage waveform is shown in (e) and (f) for reference. The regions of interest used to calculate the optical excitation intensity ratio I_γ/I_α are shown in each plot as black outlined boxes. Discharge conditions are: Ar + 10% Ne, 150 Pa, $d = 32$ mm, 13.56 MHz voltage waveform with $\phi_{\text{tot}} = 200$ V.

a comparably reduced γ-mode excitation intensity I_γ and a comparably increased α-mode excitation intensity I_α. This again qualitatively suggests that the SEEC is not just dependent on the surface material which interacts with the plasma, but also the thickness of that material (Y, in nm), as demonstrated in previous works [177, 179].

This dependence of the SEEC on oxide film thickness is best understood by considering the standpoint of solid-state electric band-gap structures and the electric potential curves that different structures produce relevant to the low-energy secondary electron emission processes, i.e., the Auger processes discussed in section 2.6 [144, 175, 176]. A more complete description of these Auger processes relevant to the SEE discussed here can be found in the work of Hagstrum [144]. These Auger processes are affected by a given surface's density of states influencing how surface electrons interact with the incident ion to achieve an exchange of energy which results in the emission of a secondary electron [144]. This can be accomplished using a few different interactions: i) resonance neutralization (an electron tunneling from the surface to the ion with enough energy to create an atom in a metastable state) followed by Auger de-excitation (metastable transitions to ground state, transferring energy to eject an electron from the surface), and ii) Auger neutralization (ion becoming a ground state atom via quantum Coulomb perturbations between two surface electrons, resulting in a transfer of energy to the surface which ejects an electron from the surface). Both of these processes are summarized in section 2.6. Notably, a change in the surface material could also be represented by a significant change in the surface's density of states and the potential profile associated with it for these Augur processes [175, 176].

Consider, then, a semiconductor film of a given thickness placed onto a clean metal. The surface material's band-gap, and thus its associated potential curve, could effectively be changed by the presence of the film. This suggests that, as such a film is grown (e.g., in a deposition discharge), the surface band-gap will change from a metal-like band-gap to a semiconductor-like band-gap as the film thickness (Y) is increased and thus the SEEC will be reduced for the mean incident ion energies seen in such discharges and for the conditions presented in this work [177, 183]. The exact film thicknesses over which such a transition would significantly impact plasma operation is not currently well-understood, but figures 7.1 and 7.2(a),(c) in addition to previous works like [177, 179] clearly demonstrate a significant change in the electron heating as a result of a changing film thickness (Y). This has dramatic ramifications for deposition discharges where such films are commonly generated, as the SEEC values may change during the deposition process as the surface material which interacts with the plasma changes. The effect this could potentially have on the γ-mode ionization, and thus the plasma density and other process-relevant plasma parameters could also therefore be significant. This kind of phenomena may also be relevant to etching discharges (albeit for kinetic SEE) for similar reasons. For example, the etching of a masking film in an etching process could affect the secondary electron emission processes of that surface, especially if the SEEC of the masking film is significantly different than that of the underlying substrate. It should also be noted that how the surface's electronic structure affects kinetic SEE is also highly relevant for other conditions with high incident particle energies, such as discharges used for material sputtering [176, 180–182].

The results presented here support the possibility of the SEEC having significant dependence on film thickness and thus discharge operation, as suggested by previous works [176, 177, 179]. However, further research on this hypothesis is essential to confirming this phenomenon and examining its ramifications on industrial plasma operation. Specifically, developing accurate theoretical models of secondary electron plasma-surface interactions and obtaining experimental measurements of the SEEC as a function of both surface material and surface film thickness are essential to understanding the relationship between SEEC and film thickness. Furthermore, in-situ experimental measurements of plasma parameters (plasma density, ion energy distribution functions, etc.) during processes where the surface material/film thickness is changed will be essential to fully understanding this phenomenon (e.g., consider the setup of [177] converted into an RF-CCP). The SEEC has also been shown to have other dependencies not explicitly considered here, such as the crystallinity of the film [180, 181] and the influence of the surface roughness on the electric properties of the surface, such as the work function of the surface [182]. Eastment and Mee [181] have also demonstrated that substrate thickness affects the anisotropy in the surface's work function by reordering crystalline orientations, implying that these dependencies may also be coupled together. The necessity of quantitative surface analysis as well as measurements of plasma parameters as a function of the surface material and film thickness should, however, be emphasized by the results presented here.

7.2 Dependence of optical excitation intensity ratio on surface profile

Figure 7.3 shows the the observed optical excitation intensity ratio (I_γ/I_α) as a function of increasing surface roughness (Ra, in μm) at 100 Pa, 150 Pa, and 200 Pa for both the clean and thin oxide film cases of each aluminum disk. Several trends can be observed happening simultaneously in figure 7.3, each of which are represented by an arrow of a given color. Firstly, the I_γ/I_α ratio generally increases at low Ra values (8-24 Ra) and later becomes constant at high Ra values (75-150 Ra), as represented by the purple arrow. Secondly, the separation between the clean metal and thin oxide film cases is indicative of the change in SEEC between these two materials noted by the green arrow, also seen in previous works [31, 35, 175–177, 183, 190] and shown in section 7.1. Lastly, the orange arrow denotes the trend seen with increasing gas pressure indicative of increasing electron multiplication in the sheath which increases I_γ/I_α and also amplifies the other trends observed in figure 7.3 as a result. The other trends are therefore best exemplified by the 200 Pa data in figure 7.3. As the green and orange arrows describe generally well-understood phenomena (different SEEC between different materials and electron multiplication in the sheath), this section will focus on the trend of I_γ/I_α as a function surface roughness (the purple arrow).

The dependence of I_γ/I_α on the surface profile $S(\vec{x})$, which in figure 7.4 and the following figures is described as a function of the surface roughness is not immediately obvious. Consider the example two-dimensional surface profiles shown in figure 7.4, each with increasing surface

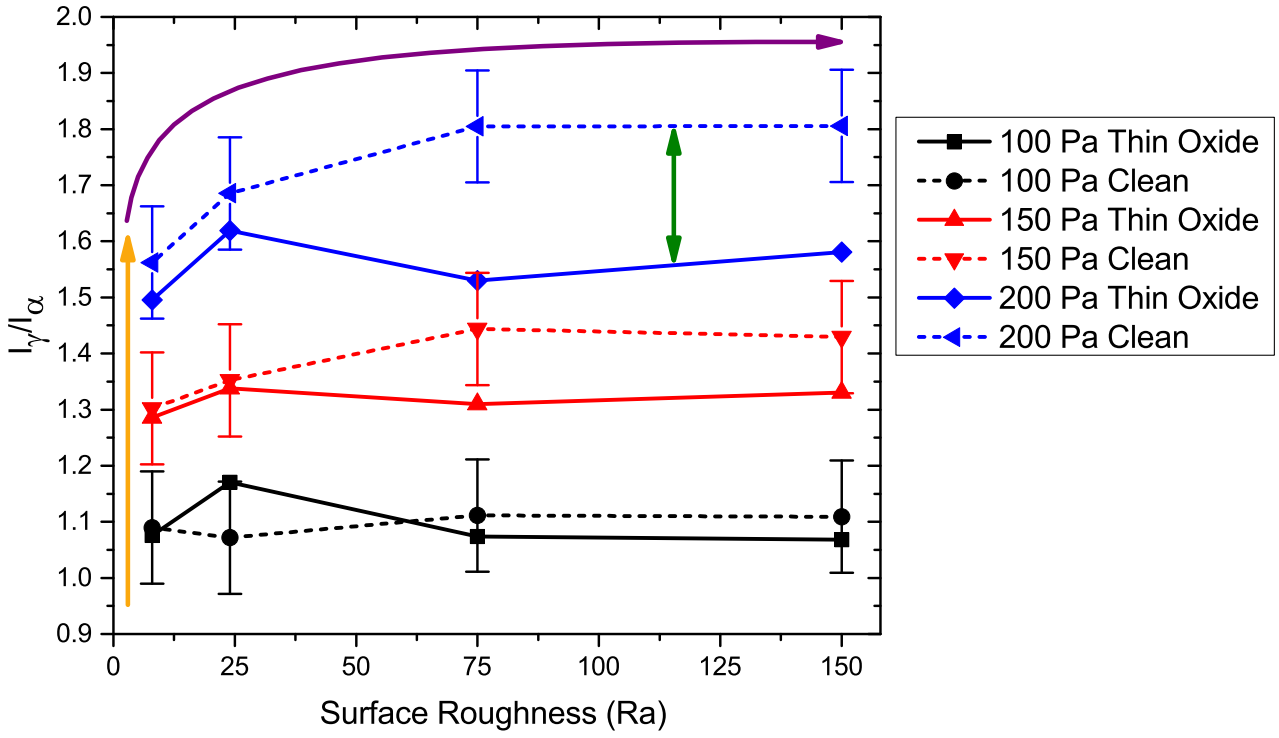

Figure 7.3: The experimentally measured optical excitation intensity ratio (I_γ/I_α) from PROES measurements is shown as a function of increasing surface roughness (8-150 Ra, in μm) of aluminum disks with and without a deposited thin oxide film for background gas pressures of 100 Pa, 150 Pa, and 200 Pa. Disks of 8 Ra, 24 Ra, 75 Ra, and 150 Ra are examined. The error bars seen on the clean cases apply to their respective thin oxide film cases also. The arrows in the figure represent the three primary trends observed from the measurements: the increase of I_γ/I_α with increasing background gas pressure (orange), the difference in I_γ/I_α between the thin oxide and clean metal cases (green, see section 7.1), and the increasing I_γ/I_α with increasing surface roughness which plateaus at high Ra values (purple). Discharge conditions are: Ar + 10% Ne, $d = 32$ mm, 13.56 MHz voltage waveform with $\phi_{\text{tot}} = 200$ V.

roughness. Note that for these example surface profiles we do not assume variations in the spacing between peaks (i.e., a surface "wavelength" λ_S for the spatial variation of the surface profile) and examine only an increasing mean deviation from the surface average, i.e., the surface roughness. The dependence of I_γ/I_α on the surface profile $S(\vec{x})$ comes from the dependence of the SEE probability on the incident particle angle shown as θ_{inc} in figure 7.4 which is defined from the surface normal for a given surface profile shape. Traditionally, due to the acceleration of positive ions across the plasma sheath, the velocity distributions of incident Ar^+ or Ne^+ ions are taken as strongly anisotropic and therefore unidirectional towards the surface normal in the case of a flat surface (downward in figure 7.4 for 0 Ra) [2].

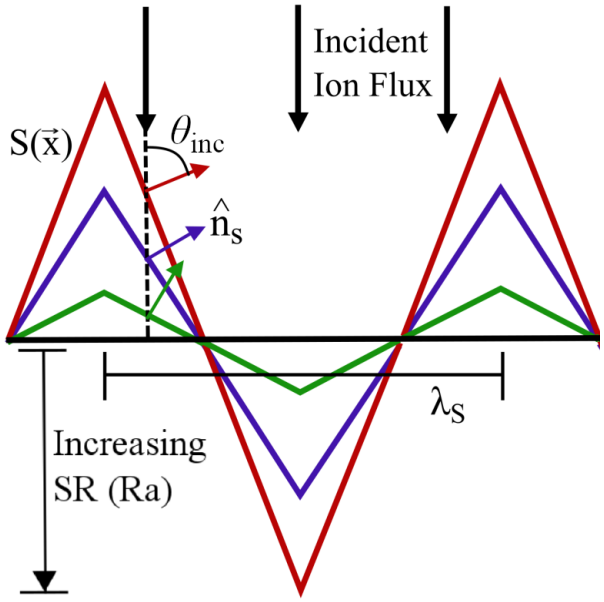

Figure 7.4: Example two-dimensional surface profiles $S(\vec{x})$ of increasing surface roughness (SR) and fixed spacing λ_S between peaks which demonstrates the increasing angle (θ_{inc}) of incident ions relative to the changing surface profile normal direction ($\hat{n}_S$). The incident ions are assumed to have velocities which are unidirectional and downward towards the surface material.

This incident particle angle dramatically changes for non-flat surface profiles, however, as the incident angle (θ_{inc}) is then defined relative to the slopes of the surface profile. This change is analogous to a rotation of a flat surface relative to the incoming flux of ions for each slope in the profile, with θ_{inc} increasing as the slope of a part of the surface profile increases. If the slope of the surface profile is itself dependent on the surface roughness (SR) and the surface variation's "wavelength" λ_S, as we might assume for the example cases shown in figure 7.4, then the slope at a given point ($\frac{\partial S(x)}{\partial x}$) increases with increasing surface roughness for a fixed λ_S according to the relationship $\frac{\partial S(x)}{\partial x} = \frac{\Delta \text{SR}}{\Delta x}$ where we can fix $\Delta x = \lambda_S/4$. It is then necessary to include any incident particle angle dependence that the SEEC may have for the relevant SEE processes. It should be noted that this precedent is also not a new consideration given that previous works have attempted to account for the surface roughness, such as the theoretical "smoothness" factor used by Vaughan [192] thirty years ago.

Castaldo *et. al.* [184], for example, have shown for helium and gallium ion beams that in the case of kinetic SEE, i.e., for high incident ion energies, the SEEC is maximum for "glancing" incident angles where a positive ion (e.g., He^+) is traveling nearly parallel to the surface interface, due to the reduced distance through the surface material an energized electron needs to travel to escape the surface. This incident angle dependence for kinetic SEE is outlined in section 2.6. In the case of a flat surface profile, such that $S(\vec{x}) = \text{constant}$, this dependence takes the form of a secant function when the incident particle angle is defined to be zero when the particle moves normal to the surface, i.e., $\gamma(\theta_{\text{inc}}) = \gamma_0 \sec(\theta_{\text{inc}})$ [184–187]. The SEEC therefore has the highest probability of emitting one or more secondary electrons

for an incident particle hitting the surface along the direction parallel to the surface (i.e., $\theta_{\text{inc}} = 90°$). This suggests an increase in the probability of an incident particle to cause a secondary electron to be emitted at parts of the surface profile which are nearly vertical in figure 7.4, i.e., parallel to the direction of the anisotropic ion flux. These nearly vertical surfaces can be correlated in this example to surfaces with very high surface roughness (large Ra), as the slopes increase with increasing Ra assuming the spacing between peaks λ_S remains the same. This type of incident particle dependence would therefore expect the effective SEE yield to increase with increasing surface roughness, similar to the observed trend at lower Ra values (8-75 Ra) in figure 7.3. The reduced variation for higher Ra values (75-150 Ra) could be related to a reduced change in the incident particle angle for the individual slopes as they slowly approach becoming perfectly vertical, i.e., at infinite surface roughness. This implies some interesting possible effects in the case of etching discharges, where vertical side-walls in an etched substrate are often ideal.

For the Auger processes which are most important for the low incident particle energies present for the conditions shown in this work, however, the incident angle dependence of the Auger processes is less clear because it is the product of quantum mechanical interactions. However, it can be inferred from the work of Hagstrum [144] that the incident particle's distance from the surface and the period of time it can interact with the surface through the Auger processes might be influenced by the particle's angle of incidence on the surface, which has also been noted in the past [193]. For example, a particle incident along the surface normal may be within the distance for Auger neutralization for a shorter time than a particle which is incident nearly parallel to the surface. This likely would imply that the particle moving parallel to the surface would, over the full course of its motion towards the surface, have a much higher probability of undergoing Auger neutralization and producing a secondary electron. A similar argument could be made for resonance neutralization followed by Auger de-excitation. Therefore, if the Auger processes exhibit incident particle angle dependence similar to that seen in Castaldo for kinetic SEE [184], the influence of the slopes in the surface profile also become relevant at low incident particle energies. The trend dictated by the purple arrow observed in figure 7.3 would therefore be attributable to the influence of the surface profile on the SEE processes. The work of Pierron *et. al.* [178] also significantly reinforces this hypothesis and provides excellent examples of the kind of results such phenomena might provide for SEE plasma-surface interactions that would be highly relevant to both industrial and academic discharges. In particular, SEE yield vs. incident energy curves as a function of incident particle angle such as those seen in figures 11 and 13 of [178] provide systematic evidence of this incident angle dependence across a large range of incident particle energies (10 eV - 1.8 keV), but may require additional research for the very low energies (< 10 eV) of interest to the results presented in this section.

The incident particle angle dependence of the SEEC may therefore be responsible for the trends with increasing surface roughness observed in figure 7.3, but this is currently only a hypothesis which requires a number of other assumptions/hypotheses to be confirmed. In particular, changes in the surface variation's "wavelength" λ_S across the surface will affect the slope of these surfaces and it may not be reasonable to assume a specific value or range of these wavelengths without extensive statistical analysis of surface slopes for

varying surface roughness values. This also means that the "randomness" or consistency of a surface profile's variations, i.e., the possibility of a changing λ_S or changing surface roughness with position $\vec{x}$ on the surface profile $S(\vec{x})$, may also play a factor when discussing the ensemble effect on discharge operation. The SEEC's dependence on the incident angle, furthermore, cannot be easily taken into account because of this ensemble averaging across the entire surface profile $S(\vec{x})$ from which the overall secondary electron emission related to the observed PROES measurements, i.e., the SE-EDF the plasma interacts with and thus the measured excitation maxima, is qualitatively estimated. The sputtering process used to clean the aluminum disks (see subsection 3.2.4) can also possibly impact these results if it were to significantly modify the surface profile, although this seems highly unlikely for surface variations on the order of μm. Highly detailed surface profilometry in addition to SEEC measurements are therefore necessary to fully understand this phenomenon at the scale of the surface interface, varying from nm to μm depending on the surface profile and discharge type, such as in semiconductor etching discharges where such small length-scales are highly relevant. PIC/MCC simulations which physically allow for non-uniform surface profiles and incorporate the angular dependencies of SEE processes may be necessary to properly correlate the trends in the observed excitation of the PROES measurements presented here with the changes in the surface's profile, such as increasing surface roughness, but this would likely be very time consuming to simulate.

An alternate possibility may be present for cases where the surface variation wavelength λ_S is small enough such that it is less than the mean free path of emitted secondary electrons λ_{mfp}, i.e., $\lambda_S \leqslant \lambda_{\text{mfp}}$. If an incident particle with a given energy strikes a given point $\vec{x}$ on one of these profiles and causes a secondary electron to be emitted, the angular probability distribution, which describes the probability of the secondary electron to be emitted at a given angle (see [144]), becomes relevant because there is now a limited range of angles, shown as $\Delta\theta_{out}$ in figure 7.5, where the emitted secondary electron escapes the surface profile and continues into the sheath. The range of angles $\Delta\theta_{out}$ is notably a function of both position on the surface profile, with the range being almost a full 180 degrees at the peaks of the profile and very narrow in the trenches of the profile, as well as the surface roughness of the profile, with profiles of higher roughness having steeper variations and more limited $\Delta\theta_{out}$ ranges at more positions under the assumption of fixed λ_S. However, for the conditions considered in this work, the incident particle energies are low and therefore the emitted secondary electrons are emitted with low kinetic energies (0-5 eV) [144, 175, 252]. The angular distribution of these emitted secondary electrons, furthermore, can be approximated to be narrow and focused around the angle which is normal to the surface profile at a given position [144]. Emitted secondary electrons are therefore increasingly likely to interact with another part of the surface after being emitted under these assumptions as the surface roughness is increased. The secondary electrons likely reflect when they interact with the opposing surface as they are emitted with low energies (0-5 eV) [252] at these incident particle energies. If the secondary electrons can traverse the distance between the surface's slopes before colliding, i.e., the secondary electron mean free path is greater than this separation and hence $\lambda_S \leqslant \lambda_{\text{mfp}}$, this can lead to a "ping-pong"-like confinement where the secondary electrons undergo multiple reflections inside the surface trench before finally escaping back into the plasma by reflection or by eventually undergoing an elastic collision with the background gas. This confinement of

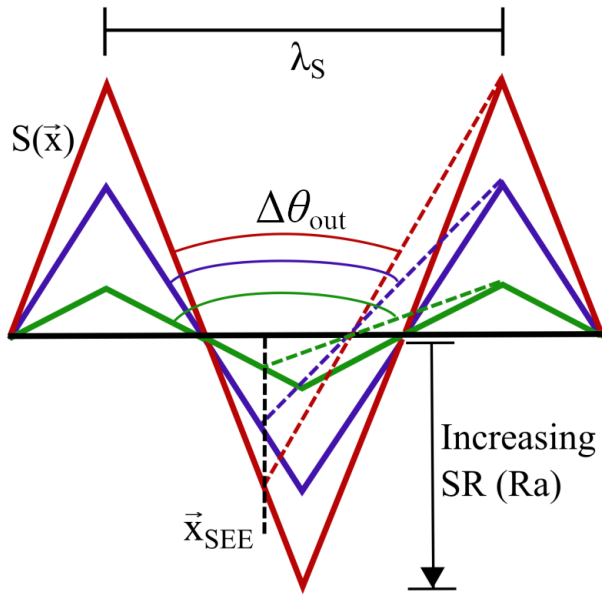

Figure 7.5: Example two-dimensional surface profiles $S(\vec{x})$ of increasing surface roughness (SR) and fixed spacing λ_S between peaks which demonstrate the changing range of angles for secondary electron emission $\Delta\theta_{out}$ at a given position $\vec{x}_{SEE}$ for which these secondary electrons can escape the surface profile without interacting with another part of the surface profile.

secondary electrons near the surface with increasing surface roughness could possibly reduce the SE-EDF that enters the plasma sheath during times of high sheath voltage and thus reduce I_γ/I_α. Notably, this would oppose the increasing trend for I_γ/I_α observed in figure 7.3, but could possibly counteract an increase in I_γ/I_α due to the increasing ion incidence angle θ_{inc}. It is currently unclear how important this hypothetical effect could be and requires further research to confirm its existence.

The confinement of secondary electrons by reflection would only occur under the assumption that the mean free path λ_{mfp} of these secondary electrons is sufficiently large such that they can reach the other surface before undergoing a collision, however. This also implies that the length-scale of the surface's variation λ_S must be sufficiently small to satisfy $\lambda_S \leqslant \lambda_{\text{mfp}}$. The length-scale of λ_S can likely be assumed to be within a few orders of magnitude of the variation in the surface's profile, i.e., the surface roughness in μm. Furthermore, the secondary electron mean free path inside the sheath is often not known due to its complicated nature compared to the bulk plasma. The low energies of emitted secondary electrons also make estimating their mean free path even more difficult. Thus, the above condition $\lambda_S \leqslant \lambda_{\text{mfp}}$ may not be satisfied for all pressures in this work and secondary electron confinement by reflection inside the surface trenches does not sufficiently explain the trend seen in figure 7.3. It should be noted that for lower pressure discharges, where the electron mean free path is increased, such as in etching discharges where the surface profile can vary on length-scales much smaller than the mean free path (e.g., nm compared to μm), this electron confinement by surface reflections could become relevant.

The presence of a strong sheath electric field can furthermore accelerate such secondary electrons towards the bulk plasma as they travel from one surface slope to another. Therefore, it is possible that these secondary electrons are accelerated upwards in figure 7.5 towards regions where the distance between two adjacent surface slopes at a given "height" is larger compared to that closer to the bottom. This effectively increases the range of $\Delta\theta_{\text{out}}$ for which electrons can escape the surface profile for a given emission location. It also strongly depends on the magnitude of the sheath electric field close to the surface, as this dictates the acceleration of these secondary electrons and thus the horizontal length-scale, denoted λ_{acc} here, over which enough velocity normal to the surface is obtained in order to escape the surface profile. Notably, this effect is also dependent on where the secondary electron is emitted ($\vec{x}$) for a fixed electric field strength as well as the number of times a given secondary electron traverses this electric field in the process of the confinement described above, particularly for surfaces where $\lambda_S < \lambda_{\text{acc}}$. It is not currently clear what range of electric field strengths or which length-scales would be most important for this acceleration, but for the conditions in this chapter, it is likely that $\lambda_{\text{acc}} \leqslant \lambda_{\text{mfp}} < \lambda_S$ under the assumptions that λ_S is on much larger (μm) length-scale than the others (see paragraph above), the sheath is collisional, and efficient acceleration of secondary electrons that results in electron multiplication and observed γ-mode excitation is achieved (see section 2.4). The time-dependent nature of the sheath electric field presents an additional complication to these considerations.

Further research is necessary to confirm these hypotheses, however, including quantitative surface profile measurements demonstrating the increasing surface area and increasing slopes of the profile alongside a changing SEEC value. The data and trends presented in this section do demonstrate, however, that the dependence of the SEE process on the shape of the surface profile may not always be negligible and therefore warrants further investigation. The confinement of secondary electrons by reflections inside the surface profile, while not likely under the conditions used in this work, could also be highly relevant for lower pressures or for surface profiles with small variations (i.e., small λ_S). This confinement is subject to the shape of the surface profile and the scale over which the profile varies due to the assumption that the secondary electron mean free path must be large enough to traverse the separation between the surface's slopes before a collision with the background gas occurs. The potential existence of these kind of effects demonstrates the importance of obtaining a complete understanding of plasma-surface interactions from both the quantum mechanical interpretation and the plasma science interpretation.

Chapter 8

Conclusions

The work of the previous chapters covers a few of the important topics in the study of RF-CCPs. These chapters draw several important conclusions regarding the operation of such discharges. Thus, the results and key conclusions demonstrated in the previous chapters are summarized in this chapter. These conclusions are ordered by chapter and section below.

The electron power absorption dynamics of low (3-5 Pa) and high pressure (200 Pa) electropositive argon RF-CCPs driven by customized multi-frequency ($N = 2, 3$) voltage waveforms are investigated in chapter 4. In section 4.1, the EAE, the DC self-bias, the electron power absorption dynamics, and the ion FEDF at the electrodes are all found to be controlled in the low pressure (3 Pa) discharge by adjusting the harmonic phases θ_k, with the largest control range of the DC self-bias and ion FEDF shape at each electrode being attainable by varying only θ_2 in the triple-frequency discharge. The spatio-temporally resolved electron impact excitation rate measured by PROES is correlated to the temporal evolution of the sheath voltages. This is utilized as the foundation to explain the effects of changing the shape of the voltage waveform on the electron power absorption, excitation, and ionization dynamics in the discharge. The low pressure discharge is found to operate in the α-heating mode, where the non-local interaction of electron beams with the opposing expanding/expanded sheaths dominates the discharge heating. The shape of the driving voltage waveform, controlled by the number of applied harmonics N, the relative harmonic phases θ_k, and the individual harmonic voltages at a fixed total voltage amplitude, is found to strongly impact the electron power absorption dynamics via the associated sheath dynamics, the dominant electron power absorption mode, and the ability to confine energetic electron beams for low pressure conditions. The EAE is found to be enhanced at higher N for fixed ϕ_{tot} due to the enhancement of the range of possible electrical asymmetries (i.e., via the AAE or the SAE) and corresponding DC self-bias values for voltage waveforms at higher N. Increased discharge ionization is also observed at higher N due to the enhancements in the electron power absorption, which causes the sheath to become thinner and less collisional leading to higher ion fluxes at energies near the mean sheath voltage. The shape of these ion FEDFs at both electrodes changes as a function of θ_2 in correlation to the corresponding

changes in the electron power absorption. Furthermore, it is demonstrated that PROES can be correlated to the ion flux to each electrode and could be used to monitor changes in the ion flux. These results are shown to be in good agreement with previous kinetic simulations.

The results of section 4.1.2 demonstrate that the EAE is strongly enhanced using $N = 3$ applied harmonics compared to using $N = 2$ applied harmonics in low pressure (5 Pa) argon RF-CCPs due to the enhancement of the EAE. The control range of the DC self-bias becomes larger at the same ϕ_{tot} and gas pressure compared to the $N = 2$ discharge. The shape of the ion FEDF is shown to be controlled by the enhancements of the α-mode electron heating, the associated ionization, and the DC self-bias as a function of the relative harmonic phases (θ_k). The total ion flux to the powered electrode is enhanced by the geometrical asymmetry of the experimental discharge. These results are in good agreement with previous computational simulations and experimental studies of the EAE for multi-frequency RF-CCPs.

In the high pressure (200 Pa) discharge of section 4.2, the γ-heating mode becomes significant and the measured excitation dynamics are dominated by local effects due to the higher discharge collisionality. Thus, excitation occurs primarily spatially and temporally close to where electrons gain energy from interactions with the sheath electric fields (i.e., α- and γ-mode electron heating). The γ-mode is found to dominate for a single-frequency 13.56 MHz waveform, but the strength of the α-heating mode is increased by increasing N for a fixed ϕ_{tot} leading to an observed γ- to α-mode transition. Similar transitions are also observed as a function of θ_2. These transitions are produced by altering the shape of the voltage waveform, the associated temporal evolution of each electrode's sheath voltage, and the relevance of each electron power absorption mechanism.

In section 2.5 and in chapter 5, the expanded global circuit model is utilized in conjunction with kinetic simulations to investigate the self-excitation of the PSR in single- and multi-frequency RF-CCPs. The self-excitation of the PSR is found to be strongly associated with the non-linear nature of the sheath charge-voltage relations and with a temporally varying bulk inductance in section 5.1. The strength of the PSR perturbations is furthermore observed to increase for asymmetric ($\varepsilon \neq 1$) discharges, but it is demonstrated that this asymmetry is not a requirement for the self-excitation of the PSR. Furthermore, $\beta(t)$ is found to vary significantly over the course of the RF period and its temporal dependence is shown to be necessary in the model in order to properly reproduce the current perturbations observed in the simulations. The PSR is also shown to be self-excited in symmetric ($\varepsilon = 1$) discharges, but only when both $a, b \neq 1$ and $\beta(t)$ are included. The strength of the PSR perturbations is furthermore seen to be enhanced for multi-frequency waveforms at higher N due to enhancements of $\beta(t)$.

The effects of the PSR on the electron power absorption dynamics in RF-CCPs driven by multi-frequency waveforms is subsequently investigated in section 5.2. The PSR is shown to be self-excited in geometrically symmetric discharges by applying symmetric and asymmetric $N = 4$ multi-frequency voltage waveforms for the same reasons as in section 5.1. Both effects, i.e., the additional cubic non-linearity of $\phi_{\text{sp}}(t)$ and $\phi_{\text{sg}}(t)$ and the temporal variation of $\beta(t)$, are found to be important in dictating the strength of the observed PSR current oscillations.

The shape of the voltage waveform, as a function of both N and the harmonic phases, is shown to strongly influence the evolution of $\beta(t)$. The self-excited PSR oscillations are furthermore demonstrated to affect the electron power absorption dynamics of the discharge and thus local plasma parameters by high-frequency modulation of the sheath dynamics and the generation of multiple energetic electron beams during sheath expansion. This non-linear electron resonance heating (NERH) enhances the total electron power absorption and can cause an additional spatial asymmetry in the electron power absorption in one half of the discharge. This spatial asymmetry is seen to be further enhanced when electron power absorption resulting from secondary electrons (i.e., the γ-mode) and electron cooling are included in the analysis of the simulations. The asymmetry in electron power absorption is not observed in the ionization profile or subsequent ion fluxes because of the non-local nature of the electron power absorption dynamics in low pressure argon discharges.

The electron power absorption dynamics in CF_4 RF-CCPs driven by tailored voltage waveforms is investigated via experimental measurements and analysis of kinetic simulations in chapter 6, with good qualitative agreement being found between the two. In section 6.1, the discharge pressure (spanning 10-100 Pa), the number of applied harmonics, and the harmonics' phases are varied systematically, with subsection 6.1.1 focusing on voltage waveforms utilizing the AAE and section 6.1.2 focusing on waveforms utilizing the SAE. At high pressures, the discharge operates in the DA-heating mode while at low pressure, the discharge operates in the α-heating mode. Mode transitions between the two modes are observed as a function of pressure, harmonic phases, and the number of applied harmonics. Furthermore, the presence of the DA-mode leads to unique spatio-temporal excitation/ionization dynamics which depend on the shape of the driving voltage waveform. For example, one strong excitation maximum can be produced at a collapsing sheath edge which remains collapsed for a large portion of the RF period, due to the creation of a potential well between the electric field of the (floating) collapsed sheath and the ambipolar electric field in the bulk plasma. The discharge is then divided into a strongly electronegative half at one electrode and a mostly electropositive half at the other electrode due to efficient attachment of electrons. Furthermore, the presence of the DA-mode is found to strongly impact the localization of the electron power absorption and therefore the associated ion density profile as a function of the neutral gas pressure (i.e., electronegativity) of the discharge. The EAE and the discharge asymmetry are seen to be altered by the dominant electron power absorption mode, as the location of the DA-mode ionization influences the discharge symmetry in a reversed fashion compared to that of the α-mode. A mode transition from the α-mode to the DA-mode also causes the DC self-bias to reverse in sign with increasing discharge pressure for sawtooth-type waveforms. This is again the result of the unique electron power absorption dynamics induced by the application of tailored voltage waveforms.

In section 6.2, the influence of the electronegativity on the charged particle dynamics and the EAE is experimentally and computationally investigated as a function of the gas mixture between electronegative CF_4 and electropositive argon for discharges driven by tailored voltage waveforms at low (20 Pa) and high (60 Pa) pressures. Triple-frequency "peaks-type" and "valleys-type" waveforms are utilized to examine the effects on the electron power absorption dynamics produced by a changing gas composition in subsection 6.2.1.

Mode transitions from the DA-mode to the α-mode are observed across the 0% to 100% argon content interval at both pressures. These transitions are found to occur at different argon admixtures at different pressures, with the mode transition being significantly less pronounced and occurring at smaller argon admixtures at 20 Pa compared to that observed at 60 Pa due to the persistence of high global electronegativity up to larger argon admixtures in the high pressure discharge. Furthermore, a significant increase in the global electronegativity is observed in the simulations at 60 Pa as a function of the argon admixture between argon content values of 20% and 30%. This counterintuitive finding is explained by the enhancement of α-mode heating caused by adding small admixtures of electropositive argon to electronegative CF_4, which influences the asymmetry in attachment rate and transitions the discharge from a strongly locally electronegative half and a locally electropositive half to an overall electronegative profile. The numerical simulations qualitatively reproduce the observed trends in the experimental spatio-temporal excitation dynamics and the measured DC self-bias. Differences between the experimental and computational results are found to be caused by the experimental setup's geometrical asymmetry, which is not accounted for in the simulations. A variety of plasma parameters provided by the simulations which could not be experimentally measured, such as the spatio-temporal attachment rate, the bulk electric field, and the mean electron energy, are discussed to clarify the charged particle dynamics. These insights provide a detailed fundamental understanding of the spatio-temporal electron dynamics and the mode transitions as a function of the argon admixture.

Based on this fundamental understanding of the plasma physics and an analytical global circuit model, the physical origin of the DC self-bias in an electronegative discharge is revealed as a function of the argon content for "peaks-type" and "valleys-type" waveforms in subsection 6.2.2. The changes in the electron power absorption mode induced by increasing the argon content in the buffer gas is found to affect the discharge symmetry and the voltage drop across the plasma bulk at high pressure (60 Pa). In the geometrically symmetric simulations, this causes a decrease in the magnitude of the generated DC self-bias as a function of increasing argon content at 60 Pa, while at 20 Pa the DC self-bias remains nearly constant. The experiment's geometrical asymmetry is found to suppress this variation of the discharge asymmetry as a function of the argon content, such that the DC self-bias remains approximately constant as a function of the argon content even at high pressure.

In chapter 7, the experimental methodology of the γ-CAST diagnostic [94] is utilized to investigate the dependence of the secondary electron emission (SEE) plasma-surface interaction on surface characteristics and the subsequent influence such dependence has on discharge operation. Through comparison of PROES excitation rate measurements spanning the 100-200 Pa range for various aluminum (Al) and aluminum oxide (Al_2O_3) surfaces of differing surface roughness, qualitative conclusions and hypotheses are made by drawing upon the model of SEE presented by Hagstrum [144]. The incident ion energies are assumed to be low due to high collisionality and thus only the quantum-mechanical SEE processes are discussed. Firstly, the γ-mode excitation maximum is found to comparably increase relative to that of the α-mode with increasing pressure due to increasingly efficient multiplication of electrons in the increasingly collisional sheath. Second, the measured excitation intensity ratio (I_γ/I_α) is seen in section 7.1 to increase faster with increasing pressure, indicating a

higher SEEC for clean Al surfaces compared to surfaces with Al_2O_3 thin films in accordance with previous work [183]. Measurements of an additional "thick" Al_2O_3 film surface suggests an even lower SEEC value. Therefore, it is hypothesized in section 7.1 that the SEEC of a given surface depends on both the surface material and film thickness, but this dependence is predicated on the assumption that the electronic structure of the surface changes as the film thickness increases.

Comparisons of the I_γ/I_α measurements in section 7.2 for surfaces with differing surface roughness imply a dependence of the SEEC and the associated γ-mode heating on the surface's physical profile. I_γ/I_α is seen to increase as the surface roughness is increased for lower surface roughness values (8-75 Ra) but eventually plateaus at higher surface roughness values (75-150 Ra). It is therefore hypothesized in section 7.2 that this dependence is a quantum-mechanical counterpart to the incident angle dependence seen for kinetic SEE processes which is produced by the changing slopes of the surface profile relative to the assumed anisotropic ion flux as the surface roughness is increased. This assumes that the overall surface profile does not vary significantly across the entire surface and the effect on the γ-mode excitation is an aggregated effect of all secondary electrons emitted from the surface. Therefore, any "randomness" in the surface profile is not accounted for by the observed "ensemble" trend seen in the I_γ/I_α measurements. A lack of surface diagnostics prevents confirmation of this hypothesis, however. The hypothetical considerations of section 7.2 also suggest the possibility of confinement of emitted secondary electrons within sufficiently small "trench-like" surface features whose length-scale of variation is smaller than the secondary electron mean free path. This confinement could be due to reflection of emitted secondary electrons at very low energies (1-5 eV) when they reach other points on the surface profile. It is unlikely such confinement exists in the experiments as the surface profile is assumed to vary on length-scales much larger than the particle mean free paths.

The results presented in this thesis therefore demonstrate the fundamental necessity of obtaining a fully complete understanding of how many industry-relevant factors, including customized charged particle dynamics via tailored voltage waveforms, the effects of plasma resonances (e.g., the PSR), the effects of gas admixtures and discharge electronegativity, and the consequences of plasma-surface interactions like secondary electron emission affect the operation of and process-optimization in RF-CCPs. Future research on these topics and on process-optimization therefore must be comprehensive and should not neglect any significant effects.

Chapter 9

Outlook for future research on capacitive radio-frequency plasmas driven by tailored voltage waveforms

The results of the proceeding chapters demonstrate several key conclusions which should not be neglected in future research on RF-CCPs, in addition to leaving several remaining open questions on the topics considered here. In the following paragraphs, the consequences and future relevance of each chapter are summarized.

The influence of customized voltage waveforms on the electron power absorption dynamics and the EAE explored for electropositive argon discharges in chapter 4 demonstrates several key factors for future research of multi-frequency RF-CPPs. First, the relevance of customized voltage waveforms using higher numbers of applied harmonics is shown to be improved by the substantial increase in the control ranges of various process-relevant plasma parameters such as mean ion energies at electrode surfaces. Therefore, optimization predicated on the use of the EAE is likely to be studied more for highly customized (high N) voltage waveforms in the future, particularly as the availability of better matching networks is improved. The same logic also applies to the idea of customizing waveforms in order to obtain specific electron heating or ionization dynamics, but this strongly depends on the dominant electron heating mechanisms for given conditions. Furthermore, the accessibility for significant control over the sheath dynamics by tuning only one or more control variables (i.e., the harmonic phases) may enable improved control over the charged particle dynamics in other kinds of discharges, such as RF-biasing in inductively coupled or magnetron plasmas.

The effects of the PSR on discharge heating and plasma properties discussed in chapter 5 demonstrate that such resonance effects may play a highly significant role for certain discharge conditions where they are self-excited. As noted in section 5.1, any future modeling of the PSR must include the cubic non-linearity in the sheath charge-voltage relations and the temporal variation of the bulk inductance to properly reproduce observed current

perturbations. Since these PSR perturbations are furthermore shown to be possible in symmetric ($\varepsilon = 1$) discharges and significantly influence electron heating in argon discharges, the range of discharge conditions which may self-excite the PSR may also increase in future studies. Furthermore, the model of section 2.5 could theoretically be utilized to search for conditions which self-excite the PSR in order to apply the PSR as a means of improving discharge heating and subsequent process rates, or alternatively as a secondary means of influencing the discharge's asymmetry.

The influence of gas admixtures and electronegativity on the charged particle dynamics and the EAE in RF-CCPs driven by tailored voltage waveforms explored in chapter 6 has numerous industry-relevant consequences. Firstly, section 6.1 demonstrates that the choice of the dominant electron heating mode can significantly impact, or even reverse, the electrical asymmetry of the discharge. Thus, the EAE effectively does not work identically in an electronegative discharge (i.e., in the DA-mode) compared to an electropositive discharge, as seen later in section 6.2. Future research and applications which use electronegative gases must therefore more carefully examine the influence of the gas admixture and electronegativity on the discharge dynamics. Furthermore, the unique, locally electronegative DA-mode observed at specific conditions in the simulations of chapter 6, in addition to the observed jump in global electronegativity as the discharge transitions away from this mode, presents an interesting case which could be further investigated in more detail in the future. It should be noted that the persistence of the global electronegativity at high (i.e $> 50\%$) argon admixtures in section 6.2 means that only a small admixture of electronegative CF_4 gas is needed at higher pressures to make electropositive argon discharges become significantly electronegative. Similar considerations may also be necessary for other electropositive-electronegative admixtures, but it is important to recall that the electronegativity of other electronegative gases may behave very differently (e.g., O_2 is more electronegative at lower pressures). Lastly, the damping influence of the geometric asymmetry on the overall discharge asymmetry in the DA- to α-mode transition may be highly relevant to other transitions where similar changes in asymmetry may occur, particularly those associated with changes in the plasma densities in the sheaths (i.e., $n_{\mathrm{sp}}/n_{\mathrm{sg}}$). These results in chapter 6 are expected to be highly important for plasma chemical vapor deposition discharges where similar conditions and phenomena are present.

The results of chapter 7 demonstrate the necessity of implementing more detailed SEE plasma-surface interactions into future modeling and simulations of RF-CCP discharges in which substantial heating or ionization caused by secondary electrons is known to be present. More thorough analysis of the dependence of secondary electron emission on surface characteristics and its subsequent influence on electron power absorption is necessary in order to obtain a complete understanding of when changes in the SEEC become significant during a given process. This is particularly important for many etching and film deposition applications, where plasma-facing surfaces commonly change in either surface material, film thickness, or surface profile throughout the course of a given processing cycle. Therefore, chapter 7 demonstrates the need for more extensive, in-situ surface diagnostics (e.g., profilometry, stoichiometry, etc.) in such discharges to monitor and optimize such processes. Since the measurements of chapter 7 only allow for hypotheses on the dependence of the SEEC on

surface characteristics, however, additional research using both experimental measurements and improved PIC/MCC simulations is likely necessary in order for these phenomena to be fully understood. Comparisons of measurements of such surface characteristics, the corresponding SEEC of differing surfaces, and further I_γ/I_α measurements are needed to properly correlate any changes in SEEC to the observed changes in electron heating and discharge operation seen in this chapter. Furthermore, all of these considerations will also need to be extended to future studies of secondary electron emission induced by species other than positive ions, e.g., that induced by electrons, photons, fast neutral atoms, and metastables.

The presence of various electric potentials near or at the plasma-facing surfaces in such RF-CCPs is an extremely important complication to the theory presented in section 2.6 and the hypotheses proposed in chapter 7. In the study of semiconductor devices, for example, it has been demonstrated that the electronic band gap structure can be modified by the application of external electric potentials (e.g., see the discussion in Achuthan and Bhat [253, p.475]). This phenomenon is referred to as the "field effect" and is important for the study of electronic materials and devices (see [254, 255] for a few modern examples). Furthermore, when considering the discharge as a circuit, the powered electrode surface is effectively one side of the capacitor that makes up the powered electrode sheath, and therefore there is a flow of charge, i.e., a populating of electrons in the conduction band, whenever the electric potential applied to this surface changes. A similar consideration needs to be addressed for floating potentials at such surfaces. This could even mean that the population of excited electrons in the conduction band associated with secondary electron emission could be time-dependent at one or both electrode surfaces due to the application of radio-frequency voltage waveforms. Therefore, the secondary electron emission at the powered electrode could be enhanced when the voltage applied to electrode is sufficiently high enough, i.e., during the times of a fully expanded sheath associated with the γ-mode excitation rate maxima, and potentially could be significantly different during sheath collapse. Furthermore, such effects may also be different between various materials with varying electronic structures and therefore further research into these effects on the basis of individual processes may be necessary. The effects of the electric potentials on the secondary electron emission at these surfaces must therefore be addressed and represent a critical obstacle to overcome in the proper modeling of secondary electron emission in RF-CCPs.

The topics discussed in this thesis and the considerations listed in this chapter should also reinforce the necessity of testing voltage waveform tailoring for various applications in production-like environments. That is, further research is needed to probe the consequences of utilizing VWT under identical conditions (including discharge geometry and gas composition) to industrial processes. The effects of customized voltage waveforms on the resulting film characteristics, etch rates, etch selectivity, or process uniformity in large scale reactors are currently not fully understood. The process of identifying all of the underlying plasma physics related to the application of VWT in such discharges may be arduous but is highly incentivized and could lead to significant improvements in such industrial applications.

List of Owned Publications

[BB15] B. Berger, S. Brandt, J. Franek, E. Schüngel, M. Koepke, T. Mussenbrock, and J. Schulze, "Experimental investigations of electron heating dynamics and ion energy distributions in capacitive discharges driven by customized voltage waveforms", J. Appl. Phys **118**, 223302 (2015).

[FJ15] J. Franek, S. Brandt, B. Berger, M. Liese, M. Barthel, E. Schüngel, and J. Schulze, "Power supply and impedance matching to drive technological radio-frequency plasmas with customized voltage waveforms", Review of Scientific Instruments **86**, 053504 (2015).

[SE15b] E. Schüngel, S. Brandt, Z. Donkó, I. Korolov, A. Derzsi, and J. Schulze, "Electron heating via self-excited plasma series resonance in geometrically symmetric multi-frequency capacitive plasmas", Plasma Sources Sci. Technol **24**, 044009 (2015).

[SE15a] E. Schüngel, S. Brandt, I. Korolov, A. Derzsi, Z. Donkó, and J. Schulze, "On the self-excitation mechanisms of plasma series resonance oscillations in single- and multi-frequency capacitive discharges", Physics of Plasmas **22**, 043512 (2015).

[BS16] S. Brandt, B. Berger, E. Schüngel, I. Korolov, A. Derzsi, B. Bruneau, E. Johnson, T. Lafleur, D. O'Connell, M. Koepke, T. Gans, B. J.-P., Z. Donkó, and J. Schulze, "Electron power absorption dynamics in capacitive radio frequency discharges driven by tailored voltage waveforms in CF_4", Plasma Sources Sci. Technol **25**, 045015 (2016).

[BS19] S. Brandt, B. Berger, Z. Donkó, A. Derzsi, E. Schüngel, M. Koepke, and J. Schulze, "Control of charge particle dynamics in capacitively coupled plasmas driven by tailored voltage waveforms in mixtures of Ar and CF_4", Plasma Sources Sci. Technol **28**, 095021 (2019).

Bibliography

[1] T. Makabe and Z. Petrović, *Plasma electronics: applications in microelectronic device fabrication* (Taylor & Francis, New York, 2006).

[2] M. A. Lieberman and A. J. Lichtenberg, *Principles of plasma discharge and materials processing*, 2nd (Wiley, New Jersey, 2005).

[3] V. M. Donnelly and A. Kornblit, "Plasma etching: yesterday, today, and tomorrow", J. Vac. Sci. Technol. A **31**, 050825 (2013).

[4] C. V. Falub, H. Rohrmann, M. Bless, M. Meduna, M. Marioni, D. Schneider, J. H. Richter, and M. Padrun, "Tailoring the soft magnetic properties of sputtered multilayers by microstructure engineering for high frequency applications", AIP Advances **7**, 056414 (2017).

[5] J. Rath, "Low temperature polycrystalline silicon: a review on deposition, physical properties and solar cell applications", Solar Energy Mater. Sol. Cells **76**, 431 (2003).

[6] L. Yu, B. O'Donnell, A. P.-J., S. Conesa-Boj, F. Peiró, J. Arbiol, and P. Roca i Cabarrocas, "Plasma-enhanced low temperature growth of silicon nanowires and hierarchical structures by using tin and indium catalysts", Nanotechnology **20**, 225604 (2009).

[7] E. V. Johnson, P. A. Delattre, and J.-P. Booth, "Microcrystalline silicon solar cells deposited using a plasma process excited by tailored voltage waveforms", Appl. Phys. Lett **100**, 133504 (2012).

[8] E. V. Johnson, S. Pouliquen, P. A. Delattre, and J.-P. Booth, "Hydrogenated microcrystalline silicon thin films deposited by rf-pecvd under low ion bombardment energy using voltage waveform tailoring", J. Non-Cryst. Solids **358**, 1974 (2012).

[9] B. Bruneau, M. Lepecq, J. Wang, J.-C. Dornstetter, J.-L. Maurice, and E. V. Johnson, "Effect of ion energy on microcrystalline silicon material and devices: a study using tailored voltage waveforms", IEEE J. Photovolt **4**, 1354 (2014).

[10] D. Hrunski, F. Mootz, A. Zeuner, A. Janssen, H. Rost, R. Beckmann, S. Binder, E. Schüngel, S. Mohr, C. U. Luggenhölscher, and G. Grabosch, "Deposition of microcrystalline intrinsic silicon by the electrical asymmetry effect technique", Vacuum **87**, 114–118 (2013).

[11] D. Hrunski, A. Janssen, T. Fritz, T. Hegemann, C. Clark, U. Schreiber, and G. Grabosch, "The influence of the electrical asymmetry effect on deposition uniformity of thin silicon film", Thin Solid Films **532**, 56–59 (2013).

[12] O. Vetterl, F. Finger, R. Carius, P. Hapke, L. Houben, O. Kluth, A. Lambertz, A. Mück, B. Rech, and H. Wagner, "Intrinsic microcrystalline silicon: a new material for photovoltaics", Sol. Energy Mater. Sol. Cells **62**, 97 (2000).

[13] E. Schüngel, R. Hofmann, S. Mohr, J. Schulze, J. Röpcke, and U. Czarnetzki, "Evaluation of the electrical asymmetry effect by spectroscopic measurements of capacitively coupled discharges and silicon thin film depositions", Thin Solid Films **574**, 60 (2015).

[14] P. K. Chu, J. Y. Chen, L. P. Wang, and N. Huang, "Plasma-surface modification of biomaterials", Materials Science and Engineering R **36**, 143 (2002).

[15] N. Gomathi, A. Sureshkumar, and S. Neogi, "Rf plasma-treated polymers for biomedical applications", Current Science **94**, 1478 (2008).

[16] D. B. Graves, "Low temperature plasma biomedicine: a tutorial review", Phys. Plasmas **21**, 080901 (2014).

[17] A. Fridman and G. Friedman, *Plasma medicine (1st edition)* (John Wiley and Sons Ltd., Oxford UK, 2013).

[18] G. E. Moore, "Cramming more components onto integrated circuits", Proc. IEEE **86**, 82 (1998).

[19] S. Samukawa, M. Hori, S. Rauf, K. Tachibana, P. Bruggeman, G. Kroesen, J. C. Whitehead, A. B. Murphy, A. F. Gutsol, and S. Starikovskaia, "The 2012 plasma roadmap", J. Phys. D **45**, 253001 (2012).

[20] H.-C. Lee, J.-Y. Bang, and C.-W. Chung, "Effects of rf bias power on electron energy distribution function and plasma uniformity in inductively coupled argon plasma", Thin Solid Films **519**, 7009 (2011).

[21] H.-C. Lee, J.-Y. Bang, and C.-W. Chung, "Collisionless electron heating by radio frequency bias in low gas pressure inductive discharge", Appl. Phys. Lett **101**, 244104 (2012).

[22] M. A. Sobolewski and K. J.-H., "The effects of radio-frequency bias on electron density in an inductively coupled plasma reactor", J. Appl. Phys **102**, 113302 (2007).

[23] J. Schulze, E. Schüngel, and U. Czarnetzki, "Coupling effects in inductive discharges with radio frequency substrate biasing", Appl. Phys. Lett **100**, 024102 (2012).

[24] B. Berger, T. Steinberger, E. Schüngel, M. Koepke, T. Mussenbrock, P. Awakowicz, and J. Schulze, "Enhanced power coupling efficiency in inductive discharges with rf substrate bias driven at consecutive harmonics with adjustable phase", Appl. Phys. Lett **111**, 201601 (2017).

[25] J. Schulze, E. Schüngel, Z. Donkó, and U. Czarnetzki, "Charge dynamics in capacitively coupled radio frequency discharges", J. Phys. D: Appl. Phys **43**, 225201 (2010).

[26] Z. Donkó, J. Schulze, U. Czarnetzki, A. Derzsi, P. Hartmann, I. Korolov, and E. Schüngel, "Fundamental investigations of capacitive radio frequency plasmas: simulations and experiments", Plasma Phys. Cont. Fusion **54**, 124003 (2012).

[27] J. Schulze, T. Gans, D. O'Connell, U. Czarnetzki, A. R. Ellingboe, and M. M. Turner, "Space and phase resolved plasma parameters in an industrial dual-frequency capacitively coupled radio-frequency discharge", J. Phys. D: Appl. Phys **40**, 7008 (2007).

[28] J. Waskoenig and T. Gans, "Nonlinear frequency coupling in dual radio-frequency driven atmospheric pressure plasmas", Appl. Phys. Lett **96**, 181501 (2010).

[29] T. Gans, J. Schulze, D. O'Connell, U. Czarnetzki, R. Faulkner, A. R. Ellingboe, and M. M. Turner, "Frequency coupling in dual frequency capacitively coupled radio-frequency plasmas", Appl. Phys. Lett **89**, 261502 (2006).

[30] S.-H. Song and M. J. Kushner, "Control of electron energy distributions and plasma characteristics of dual frequency, pulsed capacitively coupled plasmas sustained in Ar and $Ar/CF_4/O_2$", Plasma Sources Sci. Technol **21**, 055028 (2012).

[31] Z. Donkó, J. Schulze, P. Hartmann, I. Korolov, U. Czarnetzki, and E. Schüngel, "The effect of secondary electrons on the separate control of ion energy and flux in dual-frequency capacitively coupled radio frequency discharges", Appl. Phys. Lett **97**, 081501 (2010).

[32] X. V. Qin, Y.-H. Ting, and A. E. Wendt, "Tailored ion energy distributions at an rf-biased plasma electrode", Plasma Sources Sci. Technol **19**, 065014 (2010).

[33] M. M. Patterson, H.-Y. Chu, and A. E. Wendt, "Arbitrary substrate voltage wave forms for manipulating energy distribution of bombarding ions during plasma processing", Plasma Sources Sci. Technol **16**, 257 (2007).

[34] J. S. Townsend, *Electricity in gases* (Clarendon) pgs. 313-316, Oxford, 1915).

[35] J. Schulze, Z. Donkó, E. Schüngel, and U. Czarnetzki, "Secondary electrons in dual-frequency capacitive radio frequency discharges", Plasma Sources Sci. Technol **20**, 045007 (2011).

[36] T. Lafleur, "Tailored-waveform excitation of capacitively coupled plasmas and the electrical asymmetry effect", Plasma Sources Sci. Technol **25**, 013001 (2016).

[37] B. G. Heil, U. Czarnetzki, R. P. Brinkmann, and T. Mussenbrock, "On the possibility of making a geometrically symmetric rf-ccp discharge electrically asymmetric", J. Phys. D: Appl. Phys **41**, 165202 (2008).

[38] Z. Donkó, J. Schulze, B. G. Heil, and U. Czarnetzki, "Pic simulations of the separate control of ion flux and energy in ccrf discharges via the electrical asymmetry effect", J. Phys. D: Appl. Phys **42**, 025205 (2009).

[39] J. Schulze, E. Schüngel, and U. Czarnetzki, "The electrical asymmetry effect in capacitively coupled radio frequency discharges measurements of dc self bias, ion energy and ion flux", J. Phys. D: Appl. Phys **42**, 092005 (2009).

[40] U. Czarnetzki, J. Schulze, E. Schüngel, and Z. Donkó, "The electrical asymmetry effect in capacitively coupled radio-frequency discharges", Plasma Sources Sci. Technol **20**, 024010 (2011).

[41] S. Bienholz, T. Styrnoll, and P. Awakowicz, "On the electrical asymmetry effect in large area multiple frequency capacitively coupled plasmas", J. Phys. D: Appl. Phys **47**, 065201 (2014).

[42] E. Schüngel, J. Schulze, Z. Donkó, and U. Czarnetzki, "Power absorption in electrically asymmetric dual frequency capacitive radio frequency discharges", Phys. Plasmas **18**, 013503 (2011).

[43] J. Schulze, E. Schüngel, Z. Donkó, and U. Czarnetzki, "Excitation dynamics in electrically asymmetric capacitively coupled radio frequency discharges: experiment, simulation, and model", Plasma Sources Sci. Technol **19**, 045028 (2010).

[44] E. Schüngel, D. Eremin, J. Schulze, T. Mussenbrock, and U. Czarnetzki, "The electrical asymmetry effect in geometrically asymmetric capacitive radio frequency plasmas", J. Appl. Phys **112**, 053302 (2012).

[45] J. Schulze, E. Schüngel, Z. Donkó, and U. Czarnetzki, "The electrical asymmetry effect in multi-frequency capacitively coupled radio frequency discharges", Plasma Sources Sci. Technol **20**, 015017 (2011).

[46] A. Derzsi, I. Korolov, E. Schüngel, Z. Donkó, and J. Schulze, "Electron heating and control of ion properties in capacitive discharges driven by customized voltage waveforms", Plasma Sources Sci. Technol **22**, 065009 (2013).

[47] Y. Zhang, A. Zafar, D. Coumou, S. Shannon, and M. Kushner, "Control of ion energy distribution using phase shifting in multi-frequency capacitively coupled plasmas", J. Appl. Phys **117**, 233302 (2015).

[48] A. R. Gibson, A. Greb, W. G. Graham, and T. Gans, "Tailoring the nonlinear frequency coupling between odd harmonics for the optimization of charged particle dynamics in capacitively coupled oxygen plasmas", Appl. Phys. Lett **106**, 054102 (2015).

[49] B. Bora, "Effect of driving voltages in dual capacitively coupled radio frequency plasma: a study by nonlinear global model", Phys. of Plasmas **22**, 103503 (2015).

[50] B. Bora, "Studies on the effect of finite geometrical asymmetry in dual capacitively coupled radio frequency plasma", Plasma Sources Sci. Technol **24**, 054002 (2015).

[51] T. Lafleur, P. A. Delattre, E. V. Johnson, and J.-P. Booth, "Separate control of the ion flux and ion energy in capacitively coupled radio-frequency discharges using voltage waveform tailoring", Appl. Phys. Lett **101**, 124104 (2012).

[52] T. Lafleur, P. A. Delattre, E. V. Johnson, and J.-P. Booth, "Capacitively coupled radio-frequency plasmas excited by tailored voltage waveforms", Plasma Phys. Contr. F **55**, 124002 (2013).

[53] D. J. Coumou, D. H. Clark, T. Kummerer, M. Hopkins, D. Sullivan, and S. Shannon, "Ion energy distribution skew control using phase-locked harmonic rf bias drive", IEEE Trans. on Plasma Sci **42**, 1880 (2014).

[54] B. Bruneau, T. Lafleur, J. P. Booth, and E. Johnson, "Controlling the shape of the ion energy distribution at constant ion flux and constant mean ion energy with tailored voltage waveforms", Plasma Sources Sci. Technol **25**, 025006 (2016).

[55] E. Schüngel, Z. Donkó, P. Hartmann, A. Derzsi, I. Korolov, and J. Schulze, "Customized ion flux-energy distribution functions in capacitively coupled plasmas by voltage waveform tailoring", Plasma Sources Sci. Technol **24**, 045013 (2015).

[56] C. O'Neill, J. Waskoenig, and T. Gans, "Tailoring electron energy distribution functions through energy confinement in dual radio-frequency driven atmospheric pressure plasmas", Appl. Phys. Lett **101**, 154107 (2012).

[57] D. O'Connell, T. Gans, E. Semmler, and P. Awakowicz, "The role of the relative voltage and phase for frequency coupling in a dual-frequency capacitively coupled plasma", Appl. Phys. Lett **93**, 081502 (2008).

[58] P. Diomede, D. J. Economou, T. Lafleur, J.-P. Booth, and S. Longo, "Radio-frequency capacitively coupled plasmas in hydrogen excited by tailored voltage waveforms: comparison of simulations with experiments", Plasma Sources Sci. Technol **23**, 065049 (2014).

[59] E. Schüngel, S. Mohr, S. Iwashita, J. Schulze, and U. Czarnetzki, "The effect of dust on electron heating and dc self-bias in hydrogen diluted silane discharges", J. Phys. D: Appl. Phys **46**, 175205 (2013).

[60] J. Schulze, A. Derzsi, and Z. Donkó, "Electron heating and the electrical asymmetry effect in dual-frequency capacitive CF_4 discharges", Plasma Sources Sci. Technol **20**, 045008 (2011).

[61] E. V. Johnson, T. Verbeke, J.-C. Vanel, and J.-P. Booth, "Nanocrystalline silicon film growth morphology control through rf waveform tailoring", J. Phys. D: Appl. Phys **43**, 412001 (2010).

[62] E. Schüngel, S. Mohr, J. Schulze, and U. Czarnetzki, "Prevention of lateral ion flux inhomogneities in large area capacitive radio frequency plasmas via the electrical asymmetry effect", Appl. Phys. Lett **106**, 054108 (2015).

[63] B. Bruneau, T. Novikova, T. Lafleur, J.-P. Booth, and E. V. Johnson, "Control and optimization of the slope asymmetry effect in tailored voltage waveforms for capacitively coupled plasmas", Plasma Sources Sci. Technol **24**, 015021 (2015).

[64] B. Bruneau, T. Novikova, T. Lafleur, J.-P. Booth, and E. V. Johnson, "Ion flux asymmetry in radiofrequency capacitively-coupled plasmas excited by sawtooth-like waveforms", Plasma Sources Sci. Technol **23**, 065010 (2014).

[65] B. Bruneau, T. Gans, D. O'Connell, A. Greb, E. V. Johnson, and J.-P. Booth, "Strong ionization asymmetry in a geometrically symmetric radio frequency capacitively coupled plasma induced by sawtooth voltage waveforms", Phys. Rev. Lett **114**, 125002 (2015).

[66] B. Bruneau, T. Lafleur, T. Gans, D. O'Connell, A. Greb, I. Korolov, A. Derzsi, Z. Donkó, S. Brandt, E. Schüngel, J. Schulze, P. Diomede, D. J. Economou, S. Longo, E. Johnson, and J.-P. Booth, "Effect of gas properties on the dynamics of the electrical slope asymmetry effect in capacitive plasmas: comparison of Ar, H_2 and CF_4", Plasma Sources Sci. Technol **25**, 01LT02 (2016).

[67] F. Schmidt, J. Schulze, E. Johnson, J.-P. Booth, D. Keil, D. French, J. Trieschmann, and T. Mussenbrock, "Multi frequency matching for voltage waveform tailoring", Plasma Sources Sci. Technol **27**, 095012 (2018).

[68] J. Wang, S. Dine, J.-P. Booth, and E. V. Johnson, "Experimental demonstration of multifrequency impedance matching for tailored voltage waveform plasmas", Journal of Vacuum Science and Technology A **37**, 021303 (2019).

[69] Z. Donkó, A. Derzsi, I. Korolov, P. Hartmann, S. Brandt, J. Schulze, B. Berger, M. Koepke, B. Bruneau, and E. Johnson, "Experimental benchmark of kinetic simulations of capacitively coupled plasmas in molecular gases", Plasma Phys. Control. Fusion **60**, 014010 (2017).

[70] W. Xi-Feng, W.-Z. Jia, Y.-H. Song, Y.-Y. Zhang, Z.-L. Dai, and Y.-N. Wang, "Hybrid simulation of electron energy distributions and plasma characteristics in pulsed rf ccp sustained in Ar and SiH_4/Ar discharges", Physics of Plasmas **24**, 113503 (2017).

[71] O. V. Proshina, T. V. Rakhimova, D. V. Lopaev, V. Šamara, M. R. Baklanov, and J.-F. de Marneffe, "Experimental and theoretical study of rf capacitively coupled plasmas in Ar-CF_4-CF_3i mixtures", Plasma Sources Sci. Technol **24**, 055006 (2015).

[72] G. Fischer, K. Ouaras, E. Drahi, B. Bruneau, and E. V. Johnson, "Excitation of Ar, O_2, and SF_6/O_2 plasma discharges using tailored voltage waveforms: control of surface ion bombardment energy and determination of the dominant electron excitation mode", Plasma Sources Sci. Technol **27**, 074003 (2018).

[73] S. B. Wang and A. E. Wendt, "Control of ion energy distribution at substrates during plasma processing", J. Appl. Phys **88**, 643 (2000).

[74] T. Baloniak, R. Reuter, and A. von Keudell, "Fundamental aspects of substrate biasing; ion velocity distributions and nonlinear effects", J. Phys. D **43**, 335201 (2010).

[75] Z. L. Zhang, Q. Y. Nie, X. N. Zhang, Z. B. Wang, F. Kong, B. H. Jiang, and L. J. W. Mark, "Ionization asymmetry effects on the properties modulation of atmospheric pressure dielectric barrier discharge sustained by tailored voltage waveforms", Phys. Plasmas **25**, 043502 (2018).

[76] A. Gibson, Z. Donkó, L. Alelyani, L. Bischoff, G. Hübner, J. Bredin, S. Doyle, I. Korolov, K. Niemi, and T. Mussenbrock, "Disrupting the spatio-temporal symmetry of the electron dynamics in atmospheric pressure plasmas by voltage waveform tailoring", Plasma Sources Sci. Technol. **28**, 01LT01 (2019).

[77] J. Schulze, B. G. Heil, D. Luggenhölscher, R. P. Brinkmann, and U. Czarnetzki, "Stochastic heating in asymmetric capacitively coupled rf discharges", J. Phys. D: Appl. Phys **41**, 195212 (2008).

[78] J. Schulze, Z. Donkó, D. Luggenhölscher, and U. Czarnetzki, "Different modes of electron heating in dual-frequency capacitively coupled radio frequency discharges", Plasma Sources Sci. Technol **18**, 034011 (2009).

[79] B. Ph and J. P. Boeuf, "Transition between different regimes of rf glow discharges", Phys. Rev. A **41**, 4447 (1990).

[80] G. Gozadinos, M. M. Turner, and D. Vender, "Collisionless electron heating by capacitive rf sheaths", Phys. Rev. Lett **87**, 135004 (2001).

[81] M. Tatanova, B. Golubovskii Yu, A. S. Smirnov, G. Seimer, R. Basner, and H. Kersten, "Electron stochastic heating in a capacitively coupled low-pressure argon rf-discharge", Plasma Sources Sci. Technol **18**, 025026 (2009).

[82] B. G. Heil, J. Schulze, T. Mussenbrock, R. P. Brinkmann, and U. Czarnetzki, "Numerical modeling of electron beams accelerated by the radio frequency boundary sheath", IEEE Trans. on Plasma Sci **36**, 1404 (2008).

[83] J. Schulze, A. Derzsi, K. Dittmann, T. Hemke, J. Meichnser, and Z. Donkó, "Ionization by drift and ambipolar electric fields in electronegative capacitive radio frequency plasmas", Phys. Rev. Lett **107**, 275001 (2011).

[84] C. Küllig, K. Dittmann, T. Wegner, I. Sheykin, K. Matyash, D. Loffhagen, R. Schneider, and J. Meichsner, "Dynamics and electronegativity of oxygen rf plasmas", Contrib. Plasma Phys **52**, 836 (2012).

[85] G.-H. Liu, Y.-X. Liu, D.-Q. Wen, and Y.-N. Wang, "Heating mode transition in capacitively coupled CF_4 discharges: comparison of experiments with simulations", Plasma Sources Sci. Technol **24**, 034006 (2015).

[86] K. Dittmann, K. Matyash, S. Nemschokmichal, J. Meichsner, and R. Schneider, "Excitation mechanisms and sheath dynamics in capacitively coupled radio-frequency oxygen plasmas", Contrib. Plasma Phys **50**, 942 (2010).

[87] C. Killer, G. Bandelow, K. Matyash, R. Schneider, and A. Melzer, "Observation of x mode electron heating in dusty argon radio frequency discharges", Phys. Plasmas **20**, 083704 (2013).

[88] F. Tochikubo, T. Makabe, S. Kakuta, and A. Suzuki, "Study of the structure of radio-frequency glow-discharges in CH_4 and H_2 by spatiotemporal optical-emission spectroscopy", J. Appl. Phys **71**, 2143 (1992).

[89] O. V. Proshina, T. V. Rakhimova, A. T. Rakhimov, and D. G. Voloshin, "Two modes of capacitively coupled rf discharge in CF_4", Plasma Sources Sci. Technol **19**, 065013 (2010).

[90] D. A. Toneli, R. S. Pessoa, M. Roberto, and J. T. Gudmundsson, "A global model study of low pressure high density CF_4 discharge", Plasma Sources Sci. Technol **28**, 025007 (2019).

[91] G. H. Liu, L. Y.-X., B. L.-S., K. Zhao, and W. Y.-N., "Experimental investigation of mode transitions in asymmetric capacitively coupled radio-frequency Ne and CF_4 plasmas", Phys. Plasmas **25**, 023515 (2018).

[92] Y.-S. Liang, G.-H. Liu, C. Xue, Y.-X. Liu, and Y.-N. Wang, "Fluid simulation of species concentrations in capacitively coupled N_2/Ar plasmas: effect of gas proportion", J. Appl. Phys **121**, 203302 (2017).

[93] A. R. Gibson and T. Gans, "Controlling plasma properties under differing degrees of electronegativity using odd harmonic dual frequency excitation", Plasma Sources Science and Technology **26**, 115007 (2017).

[94] M. Daksha, B. Berger, E. Schüngel, I. Korolov, A. Derzsi, M. Koepke, Z. Donkó, and J. Schulze, "A computationally assisted spectroscopic technique to measure secondary electron emission coefficients in radio frequency plasmas", J. Phys. D: Appl. Phys **49**, 234001 (2016).

[95] U. Czarnetzki, "Analytical model for the radio-frequency sheath", Phys. Rev. E **88**, 063101 (2013).

[96] U. Czarnetzki, T. Mussenbrock, and R. P. Brinkmann, "Self-excitation of the plasma series resonance in radio-frequency discharges: an analytical description", Phys. Plasmas **13**, 123503 (2006).

[97] U. Czarnetzki, B. G. Heil, J. Schulze, Z. Donkó, T. Mussenbrock, and R. P. Brinkmann, "The electrical asymmetry effect - a novel and simple method for separate control of ion energy and flux in capacitively coupled rf discharges", J. Phys.: Conf. Ser **162**, 012010 (2009).

[98] R. P. Brinkmann, "The plasma-sheath transition in low temperature plasmas: on the existence of a collisionally modified bohm criterion", J. Phys. D: Appl. Phys **44**, 042002 (2011).

[99] J. W. Coburn and E. Kay, "Positive-ion bombardment of substrates in rf diode glow discharge sputtering", J. Appl. Phys **43**, 4965 (1972).

[100] M. A. Lieberman and S. E. Savas, "Bias voltage in finite length, cylindrical and coaxial radio-frequency discharges", J. Vac. Sci. Technol. A **8**, 1632 (1990).

[101] M. Kurihara, Z. L. Petrović, and T. Makabe, "Transport coefficients and scattering cross-sections for plasma modelling in CF_4-Ar mixtures: a swarm analysis", J. Phys. D: Appl. Phys **33**, 2146 (2000).

[102] R. A. Bonham, "Electron impact cross section data for carbon tetraflouride", Jpn. J. Appl. Phys **33**, 4157 (1994).

[103] F. Tochikubo, A. Suzuki, S. Kakuta, Y. Terazono, and T. Makabe, "Study of the structure in rf glow discharges in SiH_4/H_2 by spatiotemporal optical emission spectroscopy: influence of negative ions", J. Appl. Phys **68**, 5532 (1990).

[104] J. P. Boeuf and P. Belenguer, "Transition from a capacitive to a resistive regime in a silane radio frequency discharge and its possible relation to powder formation", J. Appl. Phys **71**, 4751 (1992).

[105] Q.-Z. Zhang, Y.-N. Wang, and A. Bogaerts, "Heating mode transition in a hybrid direct current/dual-frequency capacitively coupled CF_4 discharge", J. Appl. Phys **115**, 223302 (2014).

[106] E. Schüngel, I. Korolov, B. Bruneau, A. Derzsi, E. Johnson, D. O'Connell, T. Gans, B. J-p, Z. Donkó, and J. Schulze, "Tailored voltage waveform capacitively coupled plasmas in electronegative gases: frequency dependence of asymmetry effects", J. Phys. D: Appl. Phys **49**, 265203 (2016).

[107] T. Hemke, D. Eremin, T. Mussenbrock, A. Derzsi, Z. Donkó, K. Dittmann, J. Meichsner, and J. Schulze, "Ionization by bulk heating of electrons in capacitive radio frequency atmospheric pressure microplasmas", Plasma Sources Sci. Technol **22**, 015012 (2013).

[108] T. Gans, D. O'Connell, V. Schulz-von der Gathen, and J. Waskoenig, "The challenge of revealing and tailoring the dynamics of radio-frequency plasmas", Plasma Sources Sci. Technol **19**, 034010 (2010).

[109] C. M. O. Mahony, R. A. Wazzan, and W. G. Graham, "Sheath dynamics observed in a 13.56 mhz-driven plasma", Appl. Phys. Lett **71**, 608 (1997).

[110] J. Schulze, Z. Donkó, B. G. Heil, D. Luggenhölscher, T. Mussenbrock, R. P. Brinkmann, and U. Czarnetzki, "Electric field reversals in the sheath region of capacitively coupled radio frequency discharges at different pressures", J. Phys. D: Appl. Phys **41**, 105214 (2008).

[111] U. Czarnetzki, D. Luggenhölscher, and H. F. Döbele, "Space and time resolved electric field measurements in helium and hydrogen rf-discharges", Plasma Sources Sci. Technol **8**, 230 (1999).

[112] M. A. Lieberman and V. A. Godyak, "From fermi acceleration to collisionless discharge heating", IEEE Trans. Plasma Sci **26**, 955 (1998).

[113] M. Surendra and D. B. Graves, "Electron acoustic waves in capacitively coupled, low-pressure rf glow discharges", Phys. Rev. Lett **66**, 1469 (1991).

[114] A. Salabas, L. Marques, J. Jolly, and L. L. Alves, "Systematic characterization of low-pressure capacitively coupled hydrogen discharges", J. Appl. Phys **95**, 4605 (2004).

[115] D. Vender and R. W. Boswell, "Numerical modeling of low-pressure rf plasmas", IEEE Trans. Plasma Sci **18**, 725 (1990).

[116] T. Lafleur, P. Chabert, and J.-P. Booth, "Electron heating in capacitively coupled plasmas revisited", Plasma Sources Sci. Technol **23**, 035010 (2014).

[117] J. Schulze, E. Schüngel, A. Derzsi, I. Korolov, T. Mussenbrock, and Z. Donkó, "Complex electron heating in capacitive multi-frequency plasmas", IEEE Trans. on Plasma Sci **42**, 2780 (2014).

[118] J. Schulze, Z. Donkó, A. Derzsi, I. Korolov, and E. Schüngel, "The effect of ambipolar electric fields on the electron heating in capacitive rf plasmas", Plasma Sources Sci. Technol **24**, 015019 (2015).

[119] A. Proto and J. T. Gudmundsson, "The influence of secondary electron emission and electron reflection on a capacitively coupled oxygen discharge", Atoms **6**, 65 (2018).

[120] A. Proto and J. T. Gudmundsson, "The role of surface quenching of the singlet delta molecule in a capacitively coupled oxygen discharge", Plasma Sources Sci. Technol **27**, 074002 (2018).

[121] A. Derzsi, I. Korolov, E. Schüngel, Z. Donkó, and J. Schulze, "Effects of fast atoms and energy-dependent secondary electron emission yields in pic/mcc simulations of capacitively coupled plasmas", Plasma Sources Sci. Technol **24**, 034002 (2015).

[122] B. Horvath, M. Daksha, I. Korolov, A. Derzsi, and J. Schulze, "The role of electron induced secondary electron emission from SiO_2 surfaces in capacitively coupled radio frequency plasmas operated at low pressures", Plasma Sources Sci. Technol **26**, 124001 (2017).

[123] I. Korolov, A. Derzsi, Z. Donkó, and J. Schulze, "The influence of the secondary electron induced asymmetry on the electrical asymmetry effect in capacitively coupled plasmas", Appl. Phys. Lett **103**, 064102 (2013).

[124] M. M. Turner, "Collisionless heating in radio-frequency discharges; a review", J. Phys. D **42**, 194008 (2009).

[125] I. D. Kaganovich, "Anomalous capacitive sheath with deep radio-frequency electric-field penetration", Phys. Rev. Lett **89**, 265006 (2002).

[126] T. Mussenbrock and R. P. Brinkmann, "Nonlinear electron resonance heating in capacitive radio frequency discharges", Appl. Phys. Lett **88**, 151503 (2006).

[127] E. Kawamura, M. A. Lieberman, and J. Lichtenberg, "Electron heating in low pressure capacitive discharges revisited", Phys. Plasmas **21**, 123505 (2014).

[128] Y.-X. Liu, Q.-Z. Zhang, W. Jiang, L.-J. Hou, X.-Z. Jiang, W.-Q. Lu, and Y.-N. Wang, "Collisionless bounce resonance heating in dual-frequency capacitively coupled plasmas", Phys. Rev. Lett **107**, 055002 (2011).

[129] Y.-X. Liu, Q.-Z. Zhang, J. Liu, Y.-H. Song, A. Bogaerts, and Y.-N. Wang, "Effect of bulk electric field reversal on the bounce resonance heating in dual-frequency capacitively coupled electronegative plasmas", Appl. Phys. Lett **101**, 114101 (2012).

[130] O. L. Leroy, P. Stratil, J. Perrin, J. Jolly, and P. Bellenguer, "Spatiotemporal analysis of the double layer formation in hydrogen radio frequency discharges", J. Phys. D **28**, 500 (1995).

[131] T. Gans, V. Schulz-von der Gathen, and H. F. Döbele, "Spectroscopic measurements of phase-resolved electron energy distribution functions in rf-excited discharges", Europhys. Lett **66**, 232–8 (2004).

[132] M. M. Turner and M. B. Hopkins, "Anomalous sheath heating in a low pressure rf discharge in nitrogen", Phys. Rev. Lett **69**, 3511 (1992).

[133] E. Gogolides and H. H. Sawin, "Continuum modeling of radiofrequency glow discharges. i. theory and results for electropositive and electronegative gases", J. Appl. Phys **72**, 3971 (1992).

[134] M. Yan, A. Bogaerts, W. J. Goedheer, and R. Gijbels, "Electron energy distribution function in capacitively coupled rf discharges: difference between electropositive Ar and electronegative SiH_4 discharges", Plasma Sources Sci. Technol **9**, 583 (2000).

[135] V. Georgieva and A. Bogaerts, "Plasma characteristics of an $Ar/CF_4/N_2$ discharge in an asymmetric dual frequency reactor: numerical investigations by a pic/mcc model", Plasma Sources Sci. Technol **15**, 368 (2006).

[136] T. Kitajima, Y. Takeo, P. Z. Lj, and T. Makabe, "Functional separation of biasing and sustaining voltages in two-frequency capacitively coupled plasma", Appl. Phys. Lett **77**, 489 (2000).

[137] S. H. Lee, P. K. Tiwari, and J. K. Lee, "Control of ion energy distribution in low-pressure and triple-frequency capacitive discharge", Plasma Sources Sci. Technol **18**, 025024 (2009).

[138] P. C. Boyle, A. R. Ellingboe, and M. M. Turner, "Electrostatic modeling of dual frequency rf plasma discharges", Plasma Sources Sci. Technol **13**, 493 (2004).

[139] T. Lafleur and J.-P. Booth, "Control of the ion flux and ion energy in ccp discharges using non-sinusoidal voltage waveforms", J. Phys. D: Appl. Phys **45**, 395203 (2012).

[140] T. Lafleur, R. W. Boswell, and J.-P. Booth, "Enhanced sheath heating in capacitively coupled discharges due to non-sinusoidal voltage waveforms", Appl. Phys. Lett **100**, 194101 (2012).

[141] P. A. Delattre, T. Lafleur, E. Johnson, and J.-P. Booth, "Radio-frequency capacitively coupled plasmas excited by tailored voltage waveforms: comparison of experiment and particle-in-cell simulations", J. Phys. D: Appl. Phys **46**, 235201 (2013).

[142] F. Tochikubo, T. Makabe, S. Kakuta, and A. Suzuki, "Spatiotemporal optical emission spectroscopy of rf discharges in SF_6", J. Appl. Phys **73**, 2163 (1993).

[143] R. A. Gottscho, "Glow-discharge sheath electric fields: negative-ion, power, and frequency effects", Phys. Rev. A **36**, 2233 (1987).

[144] H. D. Hagstrum, "Theory of auger ejection of electrons from metals by ions", Phys. Rev. **96**, 336–365 (1954).

[145] V. A. Godyak, R. B. Piejak, and B. M. Alexandrovich, "Measurement of electron energy distribution in low-pressure rf discharges", Plasma Sources Sci. Technol **1**, 36 (1992).

[146] S. B. Radovanov, K. Dzierzega, J. R. Roberts, and J. K. Olthoff, "Time-resolved balmer-alpha emission from fast hydrogen atoms in low pressure, radio-frequency discharges in hydrogen", Appl. Phys. Lett **66**, 2637 (1995).

[147] B. M. Annaratone, V. P. T. Ku, and J. E. Allen, "Identification of plasma-sheath resonances in a parallel-plate plasma reactor", J. Appl. Phys **77**, 5455 (1995).

[148] V. P. T. Ku, B. M. Annaratone, and J. E. Allen, "Plasma-sheath resonances and energy absorption phenomena in capacitively coupled radio frequency plasmas part i", J. Appl. Phys. **84**, 6536 (1998).

[149] V. P. T. Ku, B. M. Annaratone, and J. E. Allen, "Plasma-sheath resonances and energy absorption phenomena in capacitively coupled radio frequency plasmas. part ii the herlofson paradox", J. Appl. Phys. **84**, 6546 (1998).

[150] T. Mussenbrock, R. P. Brinkmann, M. A. Lieberman, A. J. Lichtenberg, and E. Kawamura, "Enhancement of ohmic and stochastic heating by resonance effects in capacitive radio frequency discharges: a theoretical approach", Phys. Rev. Lett **101**, 085004 (2008).

[151] D. Ziegler, J. Trieschmann, T. Mussenbrock, R. P. Brinkmann, J. Schulze, U. Czarnetzki, E. Semmler, P. Awakowicz, D. O'Connell, and T. Gans, "The influence of the relative phase between the driving voltages on electron heating in asymmetric dual frequency capacitive discharges", Plasma Sources Sci. Technol **19**, 045001 (2010).

[152] M. Klick, W. Rehak, and M. Kammeyer, "Plasma diagnostics in rf discharges using nonlinear and resonance effects", Jpn. J. Appl. Phys. Part 1 **36**, 4625 (1997).

[153] Y. Yamazawa, "Effect of the resonant growth of harmonics on the electron density in capacitively coupled plasma", Appl. Phys. Lett **95**, 191504 (2009).

[154] J. Schulze, B. G. Heil, D. Luggenhölscher, and U. Czarnetzki, "Electron beams in capacitively coupled radio-frequency discharges", IEEE Trans. Plasma Sci **36**, 1400 (2008).

[155] D. Ziegler, T. Mussenbrock, and R. P. Brinkmann, "Nonlinear dynamics of dual frequency capacitive discharges: a global model matched to an experiment", Plasma Sources Sci. Technol **17**, 045011 (2008).

[156] J. Schulze, T. Kampschulte, D. Luggenhölscher, and U. Czarnetzki, "Diagnostics of the plasma series resonance effect in radio-frequency discharges", J. Phys.: Conf. Ser **86**, 012010 (2007).

[157] D. J. Cooperberg and C. K. Birdsall, "Series resonance sustained plasmas in a metal bound plasma slab", Plasma Sources Sci. Technol **7**, 96 (1998).

[158] T. Mussenbrock, D. Ziegler, and R. P. Brinkmann, "A nonlinear global model of a dual frequency capacitive discharge", Phys. Plasmas **13**, 083501 (2006).

[159] T. Mussenbrock and R. P. Brinkmann, "Nonlinear plasma dynamics in capacitive radio frequency discharges", Plasma Sources Sci. Technol **16**, 377 (2007).

[160] E. Semmler, P. Awakowicz, and A. von Keudell, "Heating of a dual frequency capacitively coupled plasma via the plasma series resonance", Plasma Sources Sci. Technol **16**, 839 (2007).

[161] M. A. Lieberman, A. J. Lichtenberg, E. Kawamura, T. Mussenbrock, and R. P. Brinkmann, "The effects of nonlinear series resonance on ohmic and stochastic heating in capacitive discharges", Phys. Plasmas **15**, 063505 (2008).

[162] Z. Donkó, J. Schulze, U. Czarnetzki, and D. Luggenhölscher, "Self-excited nonlinear plasma series resonance oscillations in geometrically symmetric capacitively coupled radio frequency discharges", Appl. Phys. Lett **94**, 131501 (2009).

[163] Z.-L. Dai and Y.-N. Wang, "Nonlinear plasma dynamics in electron heating of asymmetric capacitive discharges with a fluid sheath model", Chin. Phys. Lett **28**, 075202 (2011).

[164] B. Bora, H. Bhuyan, M. Favre, E. Wyndham, H. Chuaqui, and M. Kakati, "Measurements of time average series resonance effect in capacitively coupled radio frequency discharge plasma", Phys. Plasmas **18**, 103509 (2011).

[165] B. Bora, H. Bhuyan, M. Favre, E. Wyndham, and H. Chuaqui, "Theoretical approach for plasma series resonance effect in geometrically symmetric dual radio frequency plasma", Appl. Phys. Lett **100**, 094103 (2012).

[166] B. Bora, H. Bhuyan, M. Favre, E. Wyndham, H. Chuaqui, and C. S. Wong, "Measurements of plasma parameters in capacitively coupled radio frequency plasma from discharge characteristics: correlation with optical emission spectroscopy", Curr. Appl. Phys **13**, 1448 (2013).

[167] B. Bora and L. Soto, "Influence of finite geometrical asymmetry of the electrodes in capacitively coupled radio frequency plasma", Phys. Plasmas **21**, 083509 (2014).

[168] W. D. Qiu, K. J. Bowers, and C. K. Birdsall, "Electron series resonant discharges: comparison between simulation and experiment", Plasma Sources Sci. Technol **12**, 57 (2003).

[169] M. Klick, "Nonlinearity of the radio-frequency sheath", J. Appl. Phys **79**, 3445 (1996).

[170] R. P. Brinkmann, "Beyond the step model: approximate expressions for the field in the plasma boundary sheath", J. Appl. Phys **102**, 093303 (2007).

[171] C. Maplesoft Waterloo, *Maple*, version 16.01, 2012.

[172] J. Trieschmann, M. Shihab, D. Szeremley, A. E. Elgendy, S. Gallian, D. Eremin, R. P. Brinkmann, and T. Mussenbrock, "Ion energy distribution functions behind the sheaths of magnetized and non-magnetized radio frequency discharges", J. Phys. D: Appl. Phys **46**, 084016 (2013).

[173] T. Lafleur, P. Chabert, M. M. Turner, and J.-P. Booth, "Anomalous collisionality in low-pressure plasmas", Phys. Plasmas **20**, 124503 (2013).

[174] K. H. Krebs, "Electron ejection from solids by atomic particles with kinetic energy", Fortschr. Phys **16**, 419 (1968).

[175] M. Daksha, A. Derzsi, Z. Mujahid, D. Schulenberg, B. Berger, Z. Donkó, and J. Schulze, "Material dependent modeling of secondary electron emission coefficients and its effects on pic/mcc simulation results of capacitive rf plasmas", Plasma Sources Sci. Technol **28**, 034002 (2019).

[176] M. Bercx, B. Partoens, and D. Lamoen, "Quantitative modeling of secondary electrons from slow-ion bombardment on semiconductors", Physical Review B **99**, 085413 (2019).

[177] J. Li, B. Hoekstra, Z.-B. Wang, J. Qiu, and Y.-K. Pu, "Secondary electron emission influenced by oxidation on the aluminum surface: the roles of the chemisorbed oxygen and the oxide layer", Plasma Sources Sci. Technol **27**, 044002 (2018).

[178] J. Pierron, C. Inguimbert, M. Belhaj, T. Gineste, J. Puech, and M. Raine, "Electron emission yield for low energy electrons: monte carlo simulations for al, ag, and si", J. Appl. Phys **121**, 215107 (2017).

[179] J. Lee, T. Jeong, S. G. Yu, S. Jin, J. Heo, W. Yi, D. Jeon, and J. M. Kim, "Thickness effect on secondary electron emission of mgo layers", Applied Surface Science **174**, 62–69 (2001).

[180] E.-H. Choi, H.-J. Oh, Y.-G. Kim, J.-J. Ko, J.-Y. Lim, J.-G. Kim, D.-I. Kim, G. Cho, and S.-O. Kang, "Measurements of secondary electron emission coefficient (γ) of mgo protective layer with various crystallinities", Jpn. J. Appl. Phys **37**, 7015 (1998).

[181] R. M. Eastment and C. H. B. Mee, "Work function measurements on (100), (110), and (111) surfaces of aluminum", J Phys. F: Met. Phys **3**, 9 (1973).

[182] W. Li and D. Y. Li, "On the correlation between surface roughness and the work function in copper", J. Chem. Phys **122**, 064708 (2005).

[183] A. V. Phelps and Z. L. Petrović, "Cold-cathode discharges and breakdown in argon: surface and gas phase production of secondary electrons", Plasma Sources Sci. Technol **8**, R21 (1999).

[184] V. Castaldo, J. Withagen, C. Hagen, P. Kruit, and E. Van Veldhaven, "Angular dependence of the ion-induced secondary electron emission for He^+ and Ga^+ beams", Microscopy and Microanalysis **17**, 624–636 (2011).

[185] K. Ohya and J. Kawata, "Monte carlo study of incident-angle dependence of ion-induced kinetic electron emission from solids", Nucl. Instrum. Meth. B **90**, 552–555 (1994).

[186] E. Sternglass, "Theory of secondary electron emission by high-speed ions", Phys. Rev **108**, 1–12 (1957).

[187] J. Ferron, E. Alonso, R. Baragiola, and A. Oliva-Florio, "Dependence of ion-electron emission from clean metals on the incidence angle of the projectile", Phys. Rev. B **24**, 4412–4419 (1981).

[188] H. S. W. Massey and E. H. S. Burhop, *Electronic and ionic impact phenomena* (Oxford University Press, London, 1952), 610 ff. and 578 ff.

[189] G. K. Wehner, "Threshold energies for sputtering and the sound velocity in metals", Phys. Rev **93**, 633 (1954).

[190] M. Daksha, A. Derzsi, S. Wilczek, J. Trieschmann, T. Mussenbrock, P. Awakowicz, Z. Donkó, and J. Schulze, "The effect of realistic heavy particle induced secondary electron emission coefficients on the electron power absorption dynamics in single- and dual-frequency capacitively coupled plasmas", Plasma Sources Sci. Technol **26**, 085006 (2017).

[191] U. A. Arifov, *Interactions of atmoic particles with a solid surface*, 1st (Springer Science and Business, New York, 1969).

[192] J. Vaughan, "A new formula for secondary emission yield", IEEE Transactions on electron devices **36**, 1963–1967 (1989).

[193] V. P. Gopinath, J. P. Verboncoeur, and C. K. Birdsall, "Multipactor electron discharge physics using an improved secondary emission model", Physics of Plasmas **5**, 1535 (1998).

[194] P. J. Hargis, K. E. Greenberg, P. A. Miller, J. B. Gerardo, J. R. Torczynski, M. E. Riley, G. A. Hebner, J. R. Roberts, J. K. Olthoff, J. R. Whetstone, R. J. Van Brunt, M. A. Sobolewski, H. M. Anderson, M. P. Splichal, J. L. Mock, P. Bletzinger, A. Garscadden, R. A. Gottscho, G. Selwyn, M. Dalvie, J. E. Heidenreich, J. W. Butterbaugh, M. L. Brake, M. L. Passow, J. Pender, A. Lujan, M. E. Elta, D. B. Graves, H. H. Sawin, M. J. Kushner, J. T. Verdeyen, R. Horwath, and T. R. Turner, "The gaseous electronics conference radio-frequency reference cell: a defined parallel-plate radio-frequency system for experimental and theoretical studies of plasma-processing discharges", Rev. Sci. Instrum **65**, 140 (1994).

[195] See link for information about phase-locked multi-frequency generators and impedance matching.

[196] R. Hart, "The oxidation of aluminum in dry and humid oxygen atmospheres", Proceedings of the Royal Society of London, Series A, Mathematical and Physical Sciences **236**, 1204 (1956).

[197] J. Schulze, E. Schuengel, Z. Donkó, D. Luggenhoelscher, and U. Czarnetzki, "Phase resolved optical emission spectroscopy: a non-intrusive diagnostic to study electron dynamics in capacitive radio frequency discharges", J. Phys. D **43**, 124016 (2010).

[198] C. Böhm and J. Perrin, "Spatially resolved optical emission and electrical properties of SiH_4 rf discharges at 13.56 mhz in a symmetric parallel-plate configuration", J. Phys. D: Appl. Phys **24**, 865 (1991).

[199] A. Greb, A. R. Gibson, K. Niemi, D. O'Connell, and T. Gans, "Influence of surface conditions on plasma dynamics and electron heating in a radio-frequency driven capacitively coupled oxygen plasma", Plasma Sources Sci. Technol **24**, 044003 (2015).

[200] W. F. Meggers and Humphreys, "Interference measurements in the spectra of noble gases", J. Res. Natl. Bur. Stand. (U.S.) **13**, obtained from NIST Atomic Spectra Database (ver. 5.2),[Online]. Available: [2015 June], 293–309 (1934).

[201] W. Krötz, A. Ulrich, G. Ribitzki, J. Wieser, and D. E. Murnick, "Measurements of lifetimes and collisional rate constants for 3p levels in neon i, ii, and iv", Hyperfine Interact **88**, obtained from NIST Atomic Spectra Database (ver 5.2), [Online]. Available: [2015 June], 193–203 (1994).

[202] J. E. Chilton, M. D. Stewart, and C. C. Lin, "Electron-impact excitation cross sections of neon", Phys. Rev. A **61**, 52708 (2000).

[203] L. W. Wise, M. W. Smith, B. M. Glennon, K. Lidén, and N. A. Team, *Nist atomic spectra database*, (ver. 5.2), [Online]. Available: [2015, September 15]. National Institute of Standards and Technology, Gaithersburg, MD, 2014.

[204] D. Gahan, B. Dolinaj, and M. B. Hopkins, "Retarding field analyzer for ion energy distribution measurements at a radio-frequency biased electrode", Rev. Sci. Instrum **79**, 033502 (2008).

[205] S. G. Ingram and J. Braithwaite N. St., "Ion and electron energy analysis at a surface in an rf discharge", J. Phys. D: Appl. Phys **21**, 1496 (1988).

[206] C. Böhm and J. Perrin, "Retardingfield analyzer for measurements of ion energy distributions and secondary electron emission coefficients in low-pressure radio frequency discharges", Rev. Sci. Instrum **64**, 31 (1993).

[207] T. Baloniak, R. Reuter, C. Flötgen, and A. von Keudell, "Calibration of a miniaturized retarding field analyzer for low-temperature plasmas: geometrical transparency and collisional effects", J. Phys. D: Appl. Phys **43**, 055203 (2010).

[208] E. Schuüngel, S. Mohr, J. Schulze, U. Czarnetzki, and M. J. Kushner, "Ion distribution functions at the electrodes of capacitively coupled high-pressure hydrogen discharges", Plasma Sources Sci. Technol **23**, 015001 (2014).

[209] D. B. Medved, P. Mahadevan, and J. K. Layton, "Potential and kinetic electron ejection from molybdenum by argon ions and neutral atoms", Phys. Rev **129**, 2086 (1963).

[210] H. D. Hasselkamp, *Particle induced electron emission*, edited by G. Hoehler, 2nd (Springer, Berlin, 1992).

[211] M. M. Turner, A. Derzsi, Z. Donkó, D. Eremin, S. J. Kelly, T. Lafleur, and T. Mussenbrock, "Simulation benchmarks for low-pressure plasmas: capacitive discharges", Phys. Plasmas **20**, 013507 (2013).

[212] Z. Donkó, "Particle simulation methods for studies of low-pressure plasma sources", Plasma Sources Sci. Technol **20**, 024001 (2011).

[213] A. V. Phelps, "The application of scattering cross sections to ion flux models in discharge sheaths", J. Appl. Phys **76**, 747 (1994).

[214] W. H. Cramer, "Elastic and inelastic scattering of low-velocity ions: Ne+ in A, A+ in Ne, and A+ in A", The Journal of Chemical Physics **30**, 641–642 (1959).

[215] C. K. Birdsall, "Particle-in-cell charged-particle simulations, plus monte carlo collisions with neutral atoms, pic-mcc", IEEE Trans. Plasma Science **19**, 65 (1991).

[216] J. P. Verboncoeur, "Particle simulation of plasmas: review and advances", Plasma Phys. Control. Fusion **47**, A231 (2005).

[217] K. Matyash, R. Schneider, F. Taccogna, A. Hatayama, S. Longo, M. Capitelli, D. Tskhakaya, and F. X. Bronold, "Particle in cell simulation of low temperature laboratory plasmas", Contrib. Plasma Phys **47**, 595 (2007).

[218] V. Georgieva, A. Bogaerts, and R. Gijbels, "Numerical study of $Ar/CF_4/N_2$ discharges in single- and dual-frequency capacitively coupled plasma reactors", J. Appl. Phys **93**, 2369 (2003).

[219] V. Georgieva, A. Bogaerts, and R. Gijbels, "Numerical study of $Ar/CF_4/N_2$ discharges in single- and dual-frequency capacitively coupled plasma reactors", J. Appl. Phys **94**, 3748 (2003).

[220] V. Georgieva, A. Bogaerts, and R. Gijbels, "Numerical investigation of ion-energy-distribution functions in single and dual frequency capacitively coupled plasma reactors", Phys. Rev. E **69**, 026406 (2004).

[221] K. Nanbu, "Probability theory of electron-molecule, ion-molecule, molecule-molecule, and coulomb collisions for particle modellling of materials processing plasmas and gases", IEEE Trans. Plasma Sci **28**, 971 (2000).

[222] A. e. a. Ehlerding, "The dissociative recombination of fluorocarbon ions iii: CF^+_2 and CF^+_3", J. Phys. B: At. Mol. Opt. Phys. **39**, 805 (2006).

[223] R. A. Morris, A. A. Viggiano, J. M. Van Doren, and J. F. Paulson, "Chemistry of CF^+_n (n = 1-3) ions with halocarbons", J. Phys. Chem **96** (1992).

[224] K. Nanbu and K. Denpoh, "Monte carlo collision simulation of positive-negative ion recombination for a given rate constant", J. Phys. Soc. Jpn **67**, 1288 (1998).

[225] K. Denpoh and K. Nanbu, "Self-consistent particle simulation of radio frequency CF_4 discharge: effect of gas pressure", Jpn. J. Appl. Phys **39**, 2804 (2000).

[226] S. Rauf and M. J. Kushner, "Argon metastable densities in radio frequency Ar, Ar/O_2, and Ar/CF_4 electrical discharges", J. Appl. Phys **82**, 2805 (1997).

[227] R. Kollath, *Encyclopedia of physics*, edited by F. S, Vol. 21 (Springer, Berlin, 1956), p. 264.

[228] L. Research, *Company web-platform*, The aluminum disks used in chapter 7 were obtained as a part of a collaboration between WVU and Lam Research during 2017-2019., 2020.

[229] K. B. S. Eriksson and H. B. S. Isberg, "The spectrum of atomic aluminum, al i", Ark. Fys (Stockholm) **23**, 527–542 (1963).

[230] E. Kawamura, V. Vahedi, M. A. Lieberman, and C. K. Birdsall, "Ion energy distributions in rf sheaths: review, analysis, and simulation", Plasma Sources Sci. Technol **8**, R45 (1999).

[231] M. Prenzel, A. Kortmann, A. Stein, A. von Keudell, F. Nahif, and J. M. Schneider, "Bimodal substrate heating to control γ-Al_2O_3 deposition during reactive magnetron sputtering", J. Appl. Phys **114**, 113301 (2013).

[232] Y. Zhang, M. J. Kushner, S. Sriraman, A. Marakhtanov, J. Holland, and A. Paterson, "Control of ion energy and angular distributions in dual-frequency capacitively coupled plasmas through power ratios and phase: consequences on etch profiles", J. Vac. Sci. Technol **33**, 031302 (2015).

[233] L. Berry, H. Maynard, P. Miller, T. Moore, M. Pendley, V. Resta, D. Sparks, and Q. Yang, "Control of the radio-frequency wave form at the chuck of an industrial oxide-etch reactor", J. Vac. Sci. Technol. **18**, A2806 (2000).

[234] J. Schulze, E. Schüngel, Z. Donkó, and U. Czarnetzki, "Charge dynamics in capacitively coupled radio frequency discharges", J. Phys. D: Appl. Phys **43**, 225201 (2010).

[235] M. Klick, W. Rehak, and M. Kammeyer, "Plasma diagnostics in rf discharges using nonlinear and resonance effects", Jpn. J. Appl. Phys. Part 1 **36**, 4625 (1997).

[236] U. Czarnetzki, B. G. Heil, J. Schulze, Z. Donkó, T. Mussenbrock, and R. P. Brinkmann, J. Phys.: Conf. Ser **162**, 012010 (2009).

[237] J. Schulze, B. G. Heil, D. Luggenhölscher, R. P. Brinkmann, and U. Czarnetzki, "Stochastic heating in asymmetric capacitively coupled rf discharges", J. Phys. D: Appl. Phys **41**, 195212 (2008).

[238] D. Z-l and W. Y-n, "Nonlinear plasma dynamics in electron heating of asymmetric capacitive discharges with a fluid sheath model", Chin. Phys. Lett **28**, 075202 (2011).

[239] B. Bora and L. Soto, "Influence of finite geometrical asymmetry of the electrodes in capacitively coupled radio frequency plasma", Phys. Plasmas **21**, 083509 (2014).

[240] B. Bora, H. Bhuyan, M. Favre, E. Wyndham, H. Chuaqui, and M. Kakati, "Measurements of time average series resonance effect in capacitively coupled radio frequency discharge plasma", Phys. Plasmas **18**, 103509 (2011).

[241] B. Bora, H. Bhuyan, M. Favre, E. Wyndham, H. Chuaqui, and C. S. Wong, "Measurements of plasma parameters in capacitively coupled radio frequency plasma from discharge characteristics: correlation with optical emission spectroscopy", Curr. Appl. Phys **13**, 1448 (2013).

[242] E. Schuüngel, Z. Q-z, S. Iwashita, J. Schulze, L.-J. Hou, Y.-N. Wang, and U. Czarnetzki, "Control of plasmas properties in capacitively coupled oxygen discharges via the electrical asymmetry effect", J. Phys. D: Appl. Phys **44**, 285205 (2011).

[243] J. Schulze, T. Kampschulte, D. Luggenhölscher, and U. Czarnetzki, "Diagnostics of the plasma series resonance effect in radio-frequency discharges", J. Phys. Conf. Ser **86**, 012010 (2007).

[244] P. Kempkes and H. Soltwisch, "Plasma series resonance in e mode of low-pressure inductively coupled noble gas discharges", J. Phys. D: Appl. Phys **42**, 085206 (2009).

[245] M. Yan, A. Bogaerts, R. Gijbels, and W. J. Goedheer, "Spatial behavior of energy relaxation of electrons in capacitively coupled discharges: comparison between Ar and SiH_4", J. Appl. Phys **87**, 3628 (2000).

[246] J. Schulze, E. Schüngel, A. Derzsi, I. Korolov, T. Mussenbrock, and Z. Donkó, "Complex electron heating in capacitive multi-frequency plasmas", IEEE Trans. Plasma Sci **42**, 2780 (2014).

[247] M. Klick, M. Kammeyer, W. Rehak, W. Kasper, P. Awakowicz, and G. Franz, "Innovative plasma diagnostics and control of process in reactive low-temperature plasmas", Surf. Coat. Technol **98**, 1395 (1998).

[248] O. Braginsky, A. Kovalev, D. Lopaev, O. Proshina, T. Rakhimova, A. Vasilieva, D. Voloshin, and S. Zyryanov, "Experimental and theorectical study of dynamic effects in low-frequency capacitively coupled discharges", J. Phys. D **45**, 015201 (2012).

[249] M. D. Campanell, A. V. Khrabrov, and I. D. Kaganovich, "Absence of debye sheaths due to secondary electron emission", Phys. Rev. Lett **108**, 255001 (2012).

[250] M. D. Campanell and M. V. Umansky, "Strongly emitting surfaces unable to float below plasma potential", Phys. Rev. Lett **116**, 085003 (2016).

[251] A. Marcak, C. Corbella, T. de los Arcos, and A. von Keudell, "Note: ion-induced secondary electron emission from oxidized metal surfaces measured in a particle beam reactor", Rev. Sci. Instrum. **86**, 106102 (2015).

[252] J. Roupie, O. Jbara, T. Tondu, M. Belhaj, and J. Puech, "The study of electron emission from aluminum in the very low primary energy range using monte carlo simulations", J. Phys. D: Appl. Phys **46**, 125306 (2013).

[253] M. K. Achuthan and K. N. Bhat, *Fundamentals of semiconductor devices* (Tata McGraw-Hill Education, 2006).

[254] A. Ramasubramaniam, D. Naveh, and E. Towe, "Tunable band gaps in bilayer transition-metal dichalcogenides", Phys. Rev. B **84**, 205325 (2011).

[255] N. Zibouche, P. Philipsen, and A. Kuc, "Strong variation of electronic properties of mos2 and ws2 nanotubes in the presence of external electric fields", The Journal of Physical Chemistry C **123**, 3892–3899 (2019).

616 Apt 6 8th Street
Morgantown, WV, 26505

304-282-9620
sbrandt1@mix.wvu.edu
U.S. Citizen

Steven W. Brandt

Education	Bachelor of Science (Physics), Eberly College of Arts and Sciences, Honors Program, 3.8 GPA, West Virginia University, Morgantown, WV, Graduated 5/11/2014. Ph.D. (Physics), Eberly College of Arts and Sciences, 3.9 GPA, West Virginia University, Morgantown WV, expected graduation: 5/2020.
Work experience	West Virginia University, Morgantown, WV, 5/2014-present, Graduate Research Assistant under Dr. Julian Schulze, paid. • Ph.D. topic: Researched effects of industrial relevant conditions and phenomenon on the spatio-temporal dynamics and process control in low temperature capacitively driven plasmas. • Industry collaboration: Studied plasma-surface interactions (secondary electron emission) as a function of surface characteristics using plasma excitation dynamics. Proficient with vacuum systems, voltage waveform tailoring, and plasma diagnostics (optical excitation dynamics, PROES, Langmuir Probe, retarding field energy analyzer). Teaching Assistant for undergraduate physics laboratory, Fall 2014, Summer and Fall 2019.
Extracurricular activities	National Society of Leadership and Success, Spring 2011 – Present.
Volunteer experience / Other Skills	Undergraduate Introductory Physics Tutor, WVU, Morgantown, WV, Spring 2011 – Spring 2012. Journal of Physics D., Applied Physics, Peer Review, 2016 Proficient in IDL, MATLab, Fortran, LaTex, Word, Power-point, Excel.
Awards received	Eberly College Certificate of Achievement Award, Spring 2013 Presidential Award for Excellence and Scholarship, Spring 2012 Dean's List, WVU, Fall 2010-2014
References	Dr. Julian Schulze, +49-0234-32-23482, schulze@aept.ruhr-uni-bochum.de, Professor and Research Supervisor, Ruhr-University Bochum, Universitätsstraße 150, 44801 Bochum, Germany Dr. Mark Koepke, (304)-293-4912, mark.koepke@mail.wvu.edu, Professor and Research Co-adviser, West Virginia University, Department of Physics, Morgantown, WV, 26506 Dr. Paul Cassak, (304)-293-5102, paul.cassak@mail.wvu.edu, Professor, West Virginia University, Department of Physics, Morgantown, WV, 26506 Dr. D.J. Pisano, (304)-293-4886, djpisano@mail.wvu.edu, Professor and Undergraduate Adviser, West Virginia University, Morgantown, WV, 26506